



University
of Glasgow

Docherty, Robert Julian (2019) *Improving peripheral nerve regeneration: a multimodal approach*. PhD thesis.

<https://theses.gla.ac.uk/41141/>

Copyright and moral rights for this work are retained by the author

A copy can be downloaded for personal non-commercial research or study, without prior permission or charge

This work cannot be reproduced or quoted extensively from without first obtaining permission in writing from the author

The content must not be changed in any way or sold commercially in any format or medium without the formal permission of the author

When referring to this work, full bibliographic details including the author, title, awarding institution and date of the thesis must be given

Enlighten: Theses

<https://theses.gla.ac.uk/>
research-enlighten@glasgow.ac.uk



University of Glasgow

Improving Peripheral Nerve Regeneration: A Multimodal Approach

Robert Julian Docherty

MSci. Chemistry with Drug Discovery

October 2018

Submitted in fulfilment of the requirements for the Degree of
Doctor of Philosophy (PhD)

The Centre for the Cellular Microenvironment
Institute of Molecular, Cell and Systems Biology
College of Medical, Veterinary and Life Sciences
University of Glasgow

Abstract

Injury to the peripheral nerve system (PNS) is a relatively common occurrence and can have a devastating impact on quality of life. Currently, autologous nerve graft remains the gold standard for clinical nerve injury repair, although this approach leads to associated donor site morbidity. Alternatives are the use of nerve guidance conduits (NGC), which have shown some success over small defects. Research to improve NGC require a combined approach of increasing and applying the understanding of the underlying neuronal behaviour and signalling mechanisms, as well as scaffolding materials that are conducive to neuronal survival, axon outgrowth and guidance. Here both of these aspects are addressed separately to provide the basis for a future improvement to regenerative strategies for PNS repair.

The combination of growth factor therapy with designed NGC scaffolds first requires an understanding of the underlying signalling arising from both, exposure to nerve growth factor (NGF) and topographical cues. Original findings revealed that increasing NGF levels in media combined with linear topography produced less dorsal root ganglia (DRG) axon network sizes, in contrast to larger such networks on flat substrates. This trend was confirmed and determined to start between day four and six in vitro. The interaction between growth factor and topographical signalling was found to be exclusive to the NGF signalling pathway with FGFb, BDNF not being affected. Application of blebbistatin, a myosin II inhibitor, caused network sizes of high NGF cultures to increase on microgrooved surfaces, becoming comparable to that of low NGF concentrations. Myosin IIA intensity analysis of growth cones showed, that higher NGF concentrations result in blocking of myosin IIA similar to blebbistatin. Morphologically, high NGF promoted densely fasciculated axon growth, low NGF showed a low, ordered fasciculation and blebbistatin application caused no fasciculation and highly branched morphology. Taken together; myosin IIA is concluded to be involved in suppressing fasciculation. The NGF trend was concluded to occur from extensive fasciculation induced adhesion loss, arising from the combination of blocking myosin IIA mediated defasciculation, microgroove confinement and greater neurite outgrowth. The implications of these findings are that support with and dosage of NGF may not be straight forward to support regeneration, if topographic guidance is provided at the same time.

Cell therapy is suggested in combination with NGC to provide a long-term supportive environment. To enable structure and guidance akin to bands of Büngner, here a sonotweezer device was used to fabricate aligned strings of adipose-derived-stem-cells (ADSC) embedded in a collagen scaffolds and its effectiveness for 3-D neurite guidance assessed. Bands of ADSC were formed inside collagen I hydrogels during gelation with different spacings (185 and 375 μ m) and using two cell concentrations at seeding (12.5 and 25k). ADSC generated contraction of the collagen matrices and this produced collagen fibre alignment. Aligned bands of ADSC contracted the gels perpendicular to the direction of the banding pattern; the degree of organisation of the collagen gels was dependent on the ADSC seeding density. DRG axons, regenerating through these cell seeded gels, were directed by the ADSC pattern.

To create mechanically anisotropic, cell-free materials that supported regeneration locally silk fibroin microfibres were embedded in collagen I hydrogels. Regenerating DRG axons were not guided if the silk fibroin microfibres were aligned. The silk microfibres were also used as a means to deliver NGF. The NGF loaded silk fibroin microfibres incorporated into collagen scaffolds was shown to promote greater neurite outgrowth compared to untreated silk fibroin microfibres, when NGF was not supplied with media. This approach may provide a non-cellular, biocompatible and biodegradable way to deliver growth factors locally.

This work has three major findings that provide the basis for future improvements to regenerative strategies for PNS repair: A) growth factor delivery may not always be beneficial and that particular combined therapies need to be investigated for potential interactions; B) cell therapy, as an alternative to growth factor delivery, may benefit from patterning approaches such as the sonotweezers devices used here, to support directed outgrowth; C) growth factor supplied locally by gel embedded reservoirs supports robust regeneration at a level similar to systemic administration.

Contents

1.	Introduction	19
1.1.	General introduction.....	20
1.1.1.	The peripheral nervous system.....	20
1.1.2.	Anatomy of the peripheral nerve	21
1.1.3.	Extracellular matrix proteins	23
1.1.4.	Dorsal root ganglia	24
1.1.5.	Pseudo-unipolar neurons	25
1.2.	Peripheral nerve regeneration	26
1.2.1.	Injury classification	27
1.2.2.	Neuropathological survival response	28
1.2.3.	Wallerian degeneration.....	31
1.2.4.	Cell activity and assembly across the nerve bridge	32
1.2.5.	Axon extension and innervation.....	33
1.3.	The growth cone.....	33
1.3.1.	The structure of the growth cone.....	34
1.3.2.	Cytoskeletal dynamics	34
1.3.3.	Regenerating growth cone advance	36
1.3.4.	Growth cone turning	37
1.4.	Cell adhesion.....	39
1.4.1.	Cadherins and neural CAMs	39
1.4.2.	Integrins	40

1.5.	Neurotrophic growth factors.....	42
1.5.1.	Neurotrophic receptors.....	43
1.6.	Limits in nerve regeneration.....	47
1.7.	Nerve guidance conduit	48
1.7.1.	Functional requirements and design.....	48
1.7.2.	Substrate material	48
1.7.3.	Topographical cues.....	51
1.7.4.	Molecular support	52
1.7.5.	Supportive cells.....	53
1.8.	Improving peripheral nerve repair: a multimodal approach	57
2.	Synergistic or Antagonistic: An Investigation into the Interaction Between Topographical and Neurotrophic Growth Factor Signalling in Regenerating Dorsal Root Ganglia.	59
2.1.	Introduction	60
2.2.	Materials and methods.....	63
2.2.1.	PDMS 2-D substrate fabrication.....	63
2.2.2.	Substrate sterilisation and preparation	63
2.2.3.	Organotypic culturing of DRG explants.....	64
2.2.4.	Immunostaining	64
2.2.5.	Cell viability assay.....	66
2.2.6.	Data Analysis	67
2.3.	Results	72

2.3.1.	The interaction between topography induced signalling and NGF signalling Error! Bookmark not defined.	
2.3.2.	Myosin IIA inhibitory studies	80
2.3.3.	Growth Cone Analysis	95
2.4.	Discussion	104
2.4.1.	Topographical cues and NGF co-modulate axon outgrowth through Myosin II and fasciculation	104
2.4.2.	Blebbistatin inhibition of myosin II removes the reduced DRG outgrowths observed at excess NGF levels	106
2.4.3.	Excess NGF reduces myosin IIA amounts within the growth cone to comparable levels of blebbistatin application	107
2.4.4.	Myosin IIA blocking by NGF promotes excessive fasciculation on grooved topographies	108
2.4.5.	NGF may reduce substrate sensing	108
2.4.6.	The hypothesis of the observed NGF-topographical signalling trend ..	110
3.	Guiding Axons in 3-D: Fabrication of Arrayed ADSC- Collagen Hydrogel Scaffolds Using Octagonal Sonotweezers.....	113
3.1.	Introduction	114
3.1.1.	Hydrogels for peripheral nerve repair.....	114
3.1.2.	Cells to support peripheral nerve repair	115
3.1.3.	Acoustic patterning of cells.....	115
3.1.4.	Aligned cells - a suitable mimic for bands of Büngner?	116
3.2.	Methods	117
3.2.1.	Sonotweezer fabrication	117

3.2.2.	ADSC extraction, culture, differentiation and characterisation.....	119
3.2.3.	Collagen hydrogel creation	121
3.2.4.	Sonotweezer operation	122
3.2.5.	DRG/ ADSC collagen construct culturing.....	124
3.2.6.	Immunostaining	124
3.2.7.	Birefringence analysis of hydrogels.....	125
3.2.8.	Data analysis	126
3.3.	Results	127
3.3.1.	Method development	127
3.3.2.	Collagen embedded aligned ADSC behaviour within 3-D collagen (I) hydrogels	137
3.3.3.	Behavior of patterned dADSC in collagen I hydrogels	142
3.3.4.	Neurite guidance by collagen embedded, aligned ADSC.....	145
3.3.5.	A brief assessment of the potential for creating lumen of a NGC using sonotweezers.....	148
3.4.	Discussion.....	149
3.4.1.	Current Approaches to 3-D scaffold fabrication	149
3.4.2.	Challenges faced in 3-D patterning of ADSC within collagen during gelation	150
3.5.	Behaviour of patterned ADSC within a 3-D collagen matrix environment..	154
3.5.3.	Scaffolds in practice	159
4.	Guiding Axons in 3-D: Fabrication of Arrayed Silk Microfibre Hydrogel Scaffolds Using Octagonal Sonotweezers.....	163

4.1.	Introduction	164
4.1.4.	What are the physical limitations for sonotweezer alignment of silk microfibres?	165
4.1.5.	Is durotaxis a suitable way to guide regenerating nerve fibres?.....	165
4.1.6.	Can silk microfibres be used for localised NGF release?.....	165
4.2.	Methods	166
4.2.1.	Silk Fibre Production and Processing	166
4.2.2.	Analysis of particle alignment	168
4.2.3.	Preparation of NGF loaded silk microfibers (NGF-silk).....	169
4.2.4.	Enzyme-linked immunosorbent assay (ELISA) of NGF-silk	169
4.2.5.	Data analysis	170
4.3.	Results	173
4.3.1.	Silk Micro-Fibres Alignment Testing	173
4.3.2.	Aligned Silk Micro-fibres for Nerve Growth.....	178
4.3.3.	NGF loaded silk microfibers (NGF-silk).....	180
4.3.4.	Composite Alignment of uADSC and NGF-Silk for Nerve Regeneration	187
4.4.	Discussion.....	190
4.4.1.	Particle aligned scaffolds	190
4.4.2.	Sonotweezing of microparticles can be used to create anisotropic collagen hydrogel scaffolds	191
4.4.3.	Aligned silk fibre scaffolds in practice for nerve growth	195
4.4.4.	NGF-releasing silk microfibres to stimulate and direct axonal regeneration	196

4.5.	Investigating DRG neurite growth within NGF-silk/ collagen scaffolding ..	200
4.5.1.	NGF-loaded-silk microfibres promote DRG neurite outgrowth.....	200
4.5.2.	Reduced axon guidance in collagen gels with aligned NGF-loaded-silk microfibres	200
4.5.3.	Remarks on NGF-loaded-silk microfibres to support nerve regeneration 201	
4.6.	DRG outgrowth within uADSC/ NGF-silk composite- collagen scaffolds	201
4.6.1.	Initial prospect: uADSC guidance/ NGF-silk growth	201
4.6.2.	NGF-silk-microfibres do not interfere with ADSC mediated collagen contraction	202
4.6.3.	ADSC does not appear to differentiate when cultured with NGF-silk-microfibres for six days.....	203
4.6.4.	ADSC/ NGF-loaded-silk microfibre embedded collagen scaffolds promote and guide DRG outgrowth	204
4.6.1.	Excluded cultures in greater detail: directed growth by diametric pattern disruptions.....	204
5.	Final Discussion	205
5.1.	General Discussion	206
5.2.	Investigating the axon behaviour and signalling interactions arising from neurotrophic factors and topographical cues	207
5.2.1.	Myosin II mediates fasciculation.....	208
5.2.2.	The interaction is exclusive to NGF.....	209
5.2.3.	The interaction between NGF and topography signalling takes several days to establish.....	209
5.2.4.	Considering the experimental setup.....	210

5.3.	Ultrasonically aligned uADSC/ silk microfibers in collagen for nerve repair	210
5.3.1.	Comparative approaches to particle manipulation	211
5.3.2.	3-D patterning was seen to be in one plane	212
5.3.3.	Alignment of uADSC within collagen allows for controlled fibre alignment through contractile forces	212
5.3.4.	Scaffolds with aligned uADSC guide neurite outgrowth.....	214
5.4.	Silk fibroin microfiber scaffolds	215
5.4.1.	The sonotweezer allows for a unique approach to pattern silk microfibres within collagen I hydrogels	216
5.4.2.	Scaffolds with incorporated NGF loaded silk microfibres improves initial outgrowth.....	218
5.4.3.	Combined collagen scaffolds with aligned NGF-silk microfibres/ uADSC improve outgrowth and directionality or regeneration	220
6.	Future Work	221
6.1.	Antagonistic convergence of topographical and NGF signalling cascades..	222
6.1.1.	Target of key signalling mediators.....	222
6.1.2.	Substrate chemistry	223
6.1.3.	Investigation on how topography influences tension and promotes fasciculation.....	224
6.1.4.	Translation to a 3-D model.....	224
6.2.	Sonotweezer aligned scaffolding.....	225
6.2.1.	Use of other biomaterials	225
6.2.2.	Alternative to uADSC for alignment	225

6.2.3.	Improving NGF-silk	226
6.2.4.	Material reinforcement through silk fibre alignment	226
6.2.5.	Translation to in vivo models	226
6.2.6.	A spheroidal approach	227
7.	References.....	228

Acknowledgements

Firstly, I would like to thank Dr. Mathis Riehle, a truly exceptional supervisor whose immense, diverse knowledge is both helpful and inspirational. Through his guidance, support and friendship, my PhD was made much easier than it could have been and certainly more enjoyable. I am appreciative of his continued patience in teaching me the spelling of the bands of ~~bunger bungner~~ Büngner and his subtle efforts to cut my excessive waffling during presentations, it couldn't have been easy. I would also like to thank Dr. Anne Bernassau for her supervision, laughs and her perseverance in repeatedly fabrication and repairing of many sonotweezer devices following my blunderous handling. My thanks are also given to everyone at the Centre for Cell Engineering (CCE), now Centre for the Cellular Microenvironment, who provided a really fun atmosphere, comfortable environment and access to a wealth of advice and expertise. Particular thanks to Carol-Anne Smith who helped me countless times, Dr. Suzanne Thomson for her continuous provision of stem cells and laughs, Dr. Jemma Roberts for her banter at times when procrastination had to be achieved; Jake Cassin, Dr. Tom Hodgkinson and Dr. Monica Tsimbouri for their help and 'chit-chat'. Also, Dr. Jingli Yang, who really made the weekend work bearable and was always available for a round of biological questioning. Special thanks to: Dr. Gabriel Pemberton, for being companion since day one and a provider of intellectual and hilarious conversation throughout; Kseno Bondarenko for the "Jet Black Heart" sessions after a long day of dissections; and Ricky Unadkat who set up some rockin' poker nights and was party to some epic adventures at the 2017 Peripheral Nerve Repair conference in Barcelona.

I would also like to thank my collaborators at the University of Strathclyde for making it possible to carry out the research on silk fibroin: Dr. Philip Seib for his supervision, Thidarat Wongpinyochit for her training me in silk processing and Ms. Anne Goudie for her creation of silk hydrogels upon my request. Also, I would like to give a big thanks to Colin Hughes and all the animal house technicians, who always procured the rats on time, despite my late requests. I thank Dr. Manlio Tassierie, who carried out the rheological testing of my collagen hydrogels. Also, thanks are given to Immunotools GmbH, the company who provided me with a selection of growth factors upon the submission of my PhD research outlook.

I would like to thank my family Isobel, Laura and Mark for their love and support throughout my PhD and life, reminding me how far I have come. Thanks to my father: Richard who inspired and set me upon the path of University. You are my best friend.

I would like to thank my daughters: Jadey and Lilly -Faye who consistently and unwittingly drive me to aspire to be a better person and role-model. Kids definitely make the rollercoaster of life worth living.

Lastly, my greatest thanks go to my wife Valerie. You were there to care for me when I was most vulnerable, when times were dark. If we exist in a multiverse, I hope that you and I meeting are the only constant. I love you.

Author Declaration

I declare that, except where explicit reference is made to the contribution of others, that this dissertation is the result of my own work and has not been submitted for any other degree at the University of Glasgow or any other institution.

Robert Julian Docherty

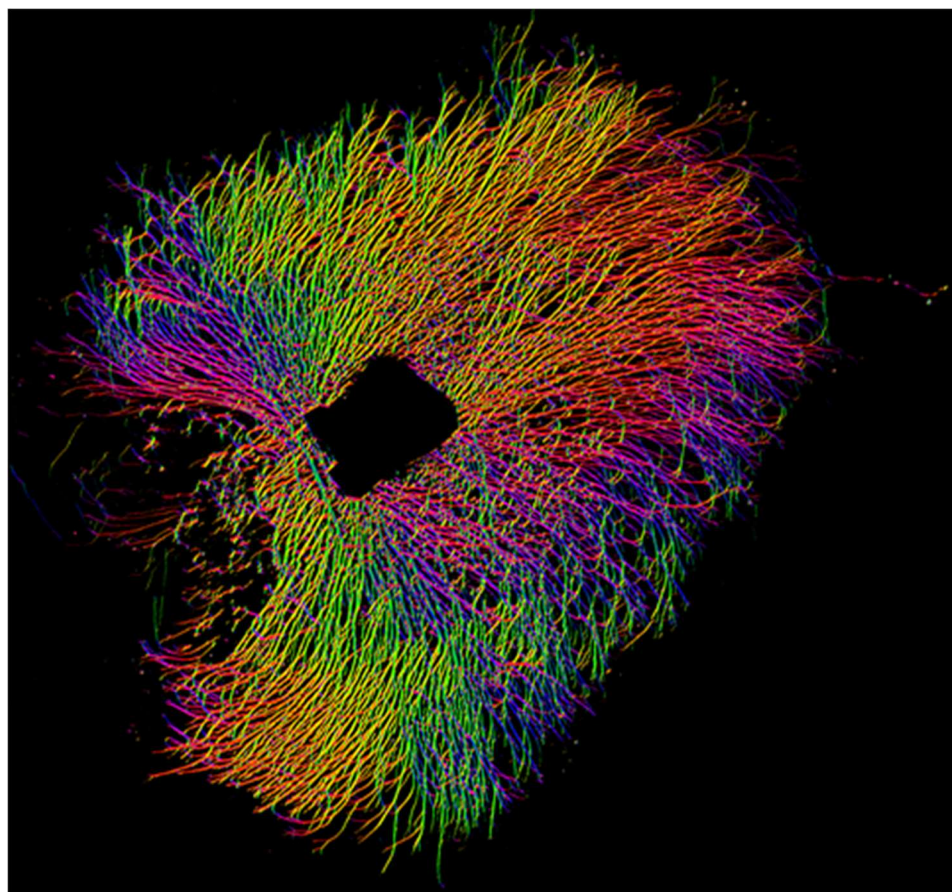
List of Abbreviations

AC	Alternating Current
ABS	Acetonitrile butadiene polymer wire
ADSC	Adipose derived stem cell
BDNF	Brain-derived neurotrophic factor
Blebb	Blebbistatin
BMMSC	Bone marrow mesenchymal stem cell
cAMP	Cyclic adenosine mono-phosphate
CNS	Central nervous system
CNTF	Ciliary neurotrophic factor
CREB	cAMP-response element binding protein
dADSC	Differentiated adipose derived stem cell
DRG	Dorsal root ganglion
ECM	Extracellular Matrix
EDF	Extended depth of field plugin
ERK	Extracellular signal-regulated kinase
ELISA	Enzyme-linked immunosorbent assay
EngNT	Engineered neural tissue
ESC	Embryonic stem cell
F-actin	Filamentous actin
FBS	Fetal bovine serum
FGFa	Acidic fibroblast growth factor
FGFb	Basic fibroblast growth factor
GC	Growth cone
GDNF	Glial derived neurotrophic factor

GGF	Glial growth factor, neuregulin-1
GFAP	Glial fibrillary protein
GF	Growth factor
L1CAM	L1 protein cell adhesion molecule
LIF	Leukemia inhibitory factor
MAP	Microtubule associated protein
MAPK	Mitogen-activated protein kinase
mRNA	Messenger RNA
MSC	Mesenchymal stem cell
mTOR	Mammalian target of rapamycin
N-CAM	Neural cell adhesion molecule
NGF	Nerve growth factor
NSC	Neural stem cell
NT	Neurotrophin
NP	Nanoparticle
PBS	Phosphate buffered saline
PCL	Polycaprolactone
PCR	Polymerase chain reaction
PDGF	Platelet-derived growth factor
PDMS	Polydimethylsiloxane
pH	Potential hydrogen
PI3K	Phosphoinositol-3-kinase
PLL	Poly-L-lysine
PNS	Peripheral nerve system
PNI	Peripheral nerve injury
PTEN	Phosphatase and tensin homolog

PTFE	Polytetrafluoroethylene
PZT	Lead zirconate titanate
Rac	Rho family GTPase
RAG	Regenerative associated gene
Rho	Ras homolog gene family
RNA	Ribonucleic acid
ROCK	Rho-associated kinase
S6K	Ribosomal s6 kinase
SC	Schwann cell
SDF1	Stromal cell-derived factor 1
STAT	Signal transducer and activator of transcription 3
TGF	Transforming growth factor
UK	United Kingdom
US	United States
UV	Ultra-violet
VEGF	Vascular endothelial growth factor

1. Introduction



“Gaining a sense of direction.” Orientation analysis of DRG explant network using Filament Sensor: eLoG directionality tool. DRG was cultured for a period of 6-days in 100 ng/ ml NGF, 50 μ M blebbistatin and grown on a flat substrate.

1.1. General introduction

Injury to the peripheral nerve system (PNS) is a relatively common occurrence and can have a devastating impact on quality of life (Tos et al., 2013). Despite being able to heal naturally without assistance, the outcome is never fully satisfactory due to nerve cell death, axons remaining disconnected and neuroma formation. Currently, autologous nerve grafts provide the best outcome (Deumens et al., 2010) although this procedure leads to associated morbidity to the areas supplying the nerves source. Consequentially, research into alternative treatment systems, capable of enhancing the intrinsic process of PNS regeneration is of vital importance. Success of treatment is dependent on the ability to promote greater numbers of axons migrating across the injury site and reaching the distal stump, achieved by encouraging axonal growth as well as guiding the direction of the regenerating neurons. The former is induced with supplied supportive cells and/ or drug treatment, whilst the latter; by a nerve repair scaffold that promotes guidance using surface topography (Allodi et al., 2012).

1.1.1. The peripheral nervous system

The prime function of the PNS is to serve as a connection between the central nervous system (CNS) and the peripheries e.g. limbs or organs allowing information to be conducted to and from the brain. The PNS is constructed from numerous conglomerates of electrochemically sensitive cells called neurons which are joined together by synaptic connections to create a neural network that is responsible for receiving and transmitting signals for sensory and motor function at a rapid rate. This network allows the information gathered at distant parts of the body to propagate and reach the CNS and conversely, relay the instructions from the CNS for distal muscle function. Generally, each neuron is comprised of a cell body called the soma which houses the nucleus and organelles responsible common cell functions such as: the supply of energy, production or packaging of peptides and proteins. The soma also extends into an axon which distributes signals, and dendrites, which are on the receiving side. Both structures are responsible for the formation of synaptic connections between neurons.

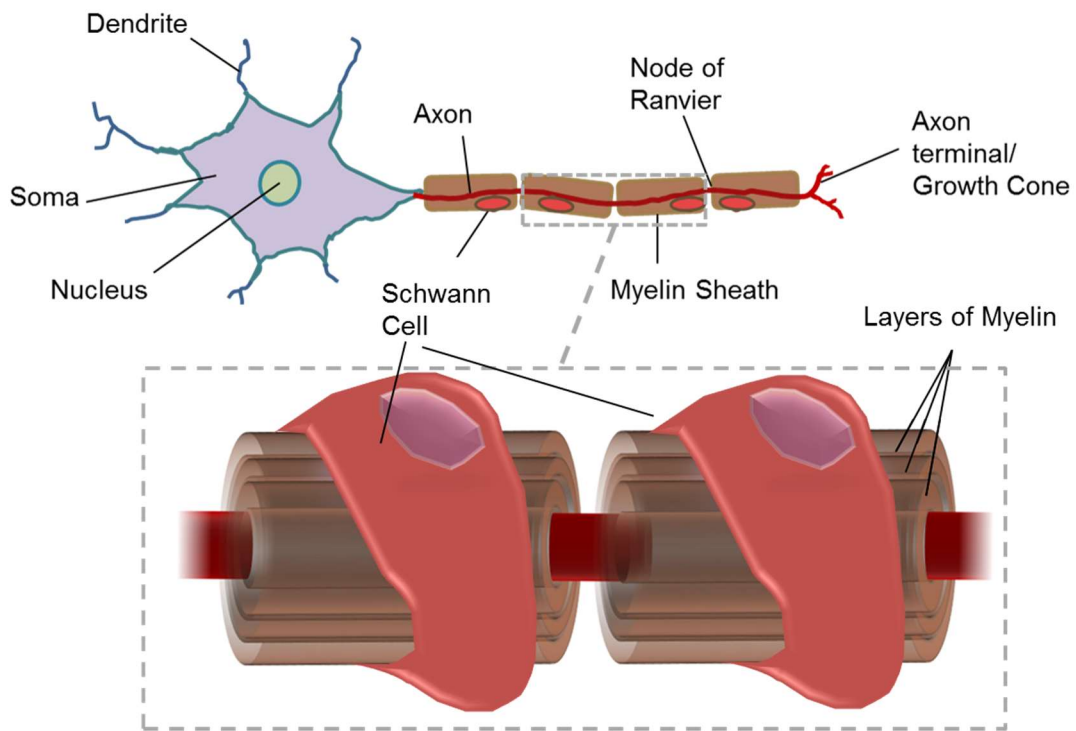


Figure 1: General schematic of the neuron. The neuron cell body, called the soma, contains the neuron nucleus and has an axon and a number of dendrites protruding from it. Signals are received by dendrites which are then transferred through the axon by action potentials communicating information to other connected neurons. Schwann cells reside along the axon, wrapping around it. These cells function by rotating around the axon to create layers of myelin and in doing so, form the surrounding myelin sheath that provides a layer of electrical insulation for fast and efficient signal transmission. Action potential propagation takes place at gaps in the myelin sheath termed “nodes of Ranvier” through allowing the exchange of sodium and potassium ions across the membrane of the axon. The axon terminal is the site of either organ innervation, synaptic connection to other neurons or in the case of regenerating axons; the growth cone (discussed later in section 1.3).

1.1.2. Anatomy of the peripheral nerve

There are two types of structure extending from the soma; dendrite and axon. Each soma can be to the outside via a number of inputs but always only one output. Dendrites are relatively small, thin, branching outgrowths, which constitute a receiving end of the axons from other neurons through synaptic connection. The axon is a cellular protrusion that can extend to macroscopic lengths (e.g. in humans the axons providing sensation of the toes can be ~1 meter in length) before reaching the organ targeted for innervation/ synapse formation. Encompassing the axon is a layering of myelin generated by Schwann Cells (SC) in their myelin forming phenotype. Each SC covers ca. 500µm of axon with a myelin sheath and is separated from the next SC along by a small gap, called node of Ranvier. The myelin sheath acts to electrically insulate the sheathed axon from its environment, allowing the rapid

(ca. up to 150 m/ s), non-degraded travel of action potentials in a saltatory fashion from one node of Ranvier to the next (Stoffel and Bosio, 1997). Surrounding the axon, SC and myelin sheath is an extracellular matrix (ECM) called the endoneurium. This ECM is similar to basal lamina and contains molecules such as collagen type IV, laminin and fibronectin providing the structural support to the axon and protection from the external forces acting on the PNS (King, 2013). A number of neighbouring axons are encapsulated together in bundles called fascicles and blood vessels by the perineurium. The perineurium is a connective tissue consisting of a dense ECM and a layering of flat perineurial cells that together give the nerve fascicles structural reinforcement and providing the blood-nerve interface (Peltonen et al., 2013). These perineurial cells regulate and protect the endoneurial microenvironment through secretion of ECM molecules that form a molecular diffusion barrier (Hill and Williams, 2002). The final connective tissue of the peripheral nerve is the epineurium. Mainly a collagenous construct, it holds the individual nerve fascicles separated in place and provides tensile strength to the nerve trunk (Barral and Croibier, 2009).

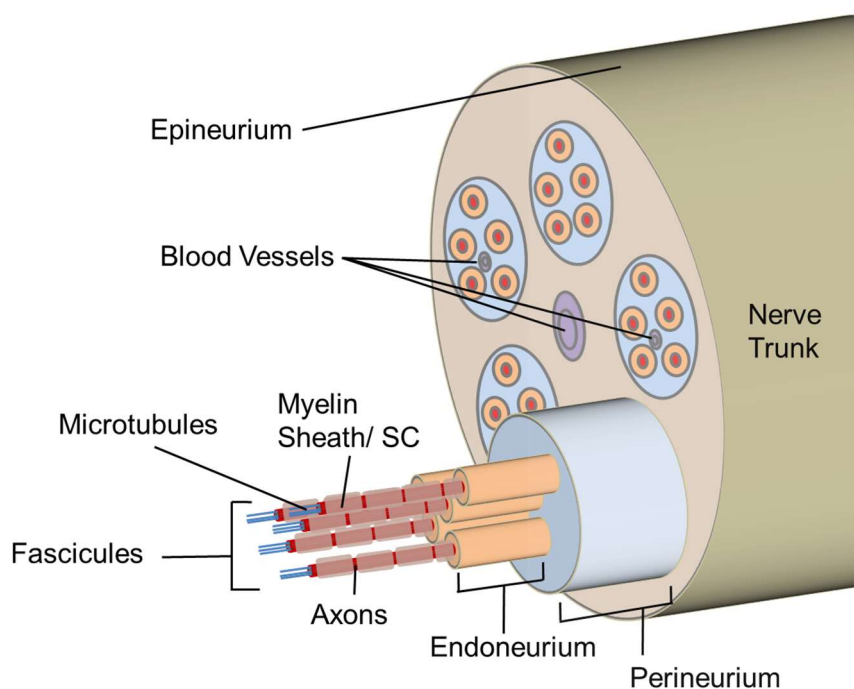


Figure 2: Structural model of the peripheral nerve. The three connective tissues of the peripheral nerve system provide structural support, external tissue barriers and the regulation of blood flow to the nerves. SC and myelinated axons are fundamentally embedded in an ECM called the endoneurium. Several axons (fascicles), endoneurium and blood vessels are bundled together further the perineurium. The outermost sleeve of the entire construct is termed the epineurium.

1.1.3. Extracellular matrix proteins

In the natural environment surrounding the neurites there are several key ECM molecules involved in adhesion and guidance by adhesions such as: collagen, netrin, fibronectin and laminin. On the other hand, other ECM molecules may negatively affect adhesion and repulse axon migration, observed by the repellent effect of Semaphorin-3A on neurite outgrowth (Orlova et al., 2007). It is important to consider that neurite guidance is achieved through both attractive and repulsive cues. Each has been thoroughly investigated in attempts to enhance nerve repair with all shown to provide a suitable surface for cell adhesion and promote outgrowth. Collagen in particular has likely attracted the most attention in tissue engineering due to its readily created 3-D matrix formation, tuneable mechanical/ structural properties and its biodegradability (Ahmed, 2015, Antoine et al., 2014).

Collagen type (I): secreted predominantly by fibroblasts and to lesser known extent Schwann and epithelial cells, is the most abundant ECM and connective tissue protein making up around one third of the total protein amount in the human body (Shoulders and Raines, 2009). Structurally it is a homo or heterotrimeric protein consisting of three α -helix chains, organised in triple helices which then undergo spontaneous cross-linking laterally giving stability and forming the supramolecular network fibril. The isoform composition impacts the fibril packing arrangement and the final superstructure of assembled fibrils (such as fibre) are responsible for producing the varied mechanical properties such as stiffness, elasticity and tensile strength exhibited across different types of collagen-based tissues (vitreous body, connective tissue, tendon and bone). Although numerous (~29) isoforms have been identified (Shoulders and Raines, 2009), a relatively small selection can be found in the PNS. The fibrillar types: I, III and V provide a flexible, supportive foundation of the epi/peri/endo-neurial tubes and are revealed to be required in Schwann cell myelination (Chernousov et al., 2006), while type IV is responsible for the formation of a two-dimensional layer essential in aggregating other ECM molecules together in the basement membrane (Koopmans et al., 2009).

1.1.4. Dorsal root ganglia

Neurons with axons present in the peripheral nervous system can be divided into groups depending on their function; sensory and motor. The somata of sensory neurons reside in dorsal root ganglia (DRG) residing on the dorsal root and with a pseudo-unipolar morphology, their axons extend to the sensory organs on one side and to the CNS terminating in the spinal cord or further up, on the other side. Sensory neurons receive information via axon terminal receptors before transmitting it on towards to the CNS (afferent signal flow). Motor neurons, however, are situated in the ventral horn of the spinal cord. These neurons instead receive instructions from the CNS and convey signals to muscles initiating and directing movement (efferent signal flow). The DRG (Figure 3) is a cluster of pseudo-unipolar afferent neurons, satellite glial cells (SGC), SC, fibroblasts, endothelial and macrophages. The SGC completely surround the soma of the sensory neuron, isolating it and preventing interaction with other neurons. This also loosely serves as a blood/ nerve barrier providing protection from toxic metabolites (Krames, 2014). Alongside this, there is evidence that SGC actively respond to neuroactive agents, environmental factors and injury signalling and are likely to play a role in relaying signals to their harboured neurons(Hanani, 2005). The DRG, its inhabiting neurons' soma and their protruded axons are encapsulated by the dorsal root, the structural component linking the CNS to the PNS.

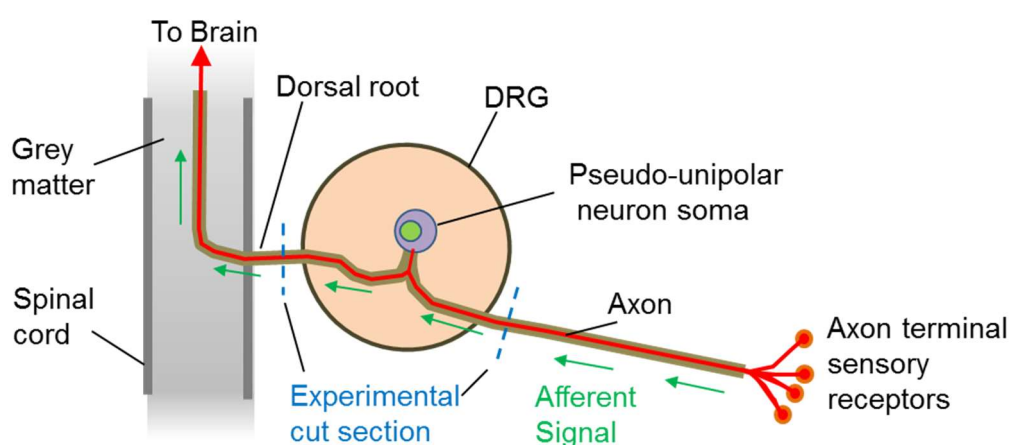


Figure 3: Diagram of the dorsal root ganglion. DRGs (~20) are situated adjacent to the spinal cord in the dorsal horn, connected by dorsal roots which encompass the DRG and axons that extend to both the CNS and the PNS. DRGs contain a number of different types of cells including the somata of pseudo-unipolar neurons. Pseudo-unipolar neurons are sensory neurons which have one axon that branches in two directions (CNS/ PNS). The afferent flow of signals (green arrows) that originate at the innervated target organ receptors are relayed through the axon and finally into the CNS where

they can be processed. The experimental method used in this project extract DRGs from the spine by the bilateral transection of the dorsal root at either side of the DRG as indicated by a blue dash.

The use of DRGs provides the advantage of a more relevant model to investigate neurite outgrowth than single neuron experiments as somata are still subjected to the inner DRG environment, maintaining contact with the natural ECM and the multiple cell types that inhabit (Corey et al., 2007). Following DRG extraction, an organotypic culture is produced, with fibroblasts, SC and macrophages migrating from the DRG during regeneration and surrounding the growing axons giving further mimicry of the natural regenerative components.

The DRG body has no surrounding capsular membrane and contains an abundance of vasculature. These aspects expose the sensory neurons housed inside the DRG to external factors, and thus are susceptible to toxic stimuli or drug delivery. As a result, the DRG has been focused on as a target for the treatment of neuropathic pain (Puljak et al., 2009, Yu et al., 2015). This is a contrast to other approaches targeting the CNS where drugs must first cross the blood brain barrier to take effect e.g. delivery of opioid analgesics (Witt and Davis, 2006).

1.1.5. Pseudo-unipolar neurons

Pseudo-unipolar neurons are a type of sensory neuron that has an axon which is split into two branches (Figure 4). One branch can terminate in the spinal cord to form synaptic connections with other neurons in the CNS (interneurons), or travel up to the brain, whilst the other branch is connected to the innervated tissue. Tissue innervation is diverse and may comprise of free nerve endings that sense temperature, pH, damage, or in specialised structures that aid in the sensation of muscle tension, specific touch modalities (i.e. vibration, shear or indentation) and also in hair follicles. Despite branching into a proximal and distal end, both branches act together as a single axon, relaying the signal uninterrupted from the periphery to the spinal cord of the CNS.

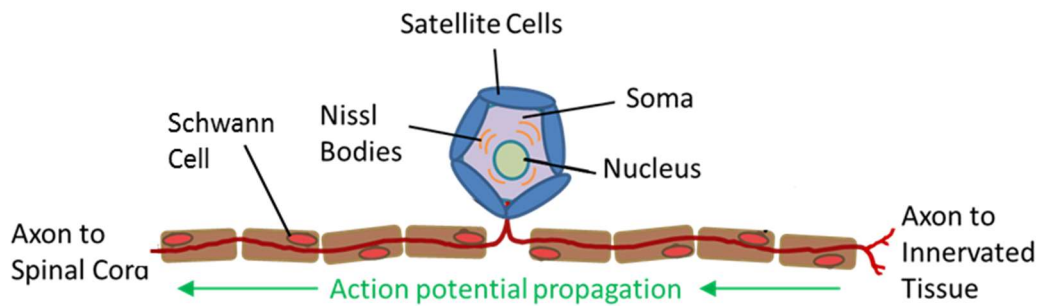


Figure 4: The pseudo-unipolar neuron. Similar to the typical neuron (as depicted in Figure 1), the pseudo-unipolar neuron has a soma containing an axon which is surrounded by SC and the myelin sheath. Approximately one SC can be found alongside each millimetre of axon. This neuron differs however in that its axon branches into two, each separating to connect to either the CNS or the PNS. Direction of action potential propagation is afferent moving from the PNS to the CNS exclusively.

Unlike other neurons (such as Figure 1), pseudo-unipolar neurons do not have dendrites. These neurons can be divided into three main types in accordance to their functioning;

- Proprioceptive neurons relay information on muscle tension and track limb position and orientation in space through synaptic connections with muscle spindles and Golgi organs within tendons (Oakley and Karpinski, 2002)
- Mechanoreceptive neurons provide information from touch, pressure, shear and vibratory stimuli through innervation of Merkel, Ruffini and Pacinian (respectively) cell complexes residing in the skin (Woo et al., 2015)
- Nociceptive neurons relay information of thermal or noxious stimuli

Pseudo-unipolar neurons possess the ability to regenerate axons following an injury provided the environmental conditions are suitable.

1.2. Peripheral nerve regeneration

The process by which injured neurons recover is a lengthy complex, multicellular sequence of events involving injury recognition, Wallerian degeneration, bands of Büngner formation, axon regrowth and eventually target re-innervation (Figure 5). Each stage is critical to successful regeneration and the difficulty of the task is strongly dependent on how extensive the nerve damage is.

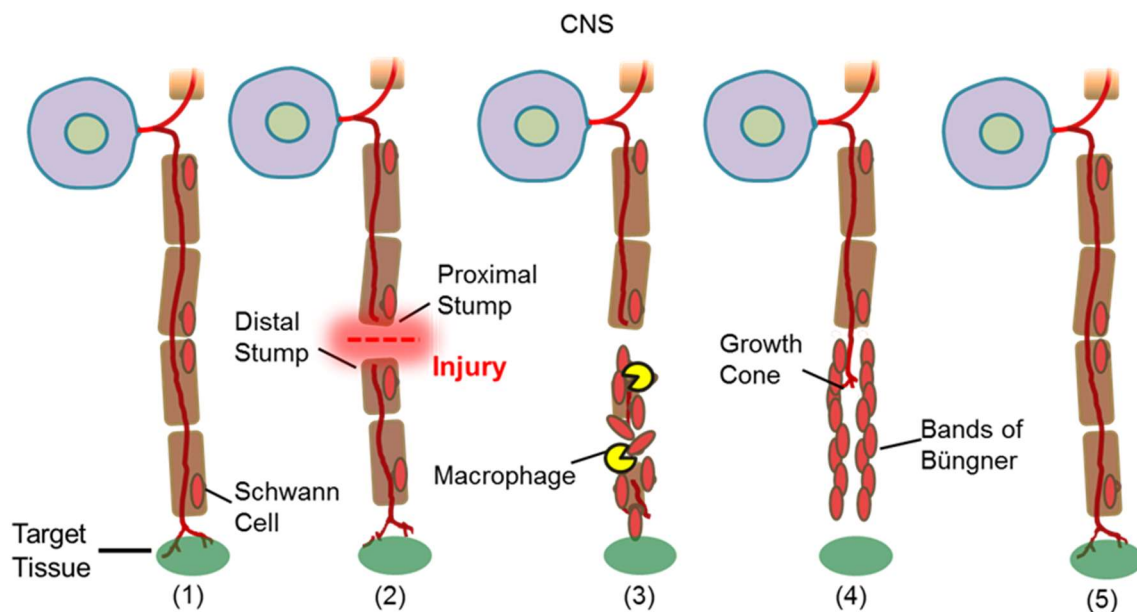


Figure 5: A brief overview of the nerve regeneration process. (1) Nerve before damage. (2) Nerve injury causing severance of axons. (3) SC migrate to the injury site to dedifferentiate into an immature state allowing them to promote the regeneration of axons. They then express cytokines prompting the recruitment of macrophages that cause phagocytosis of axon fragments at the distal stump in a process called Wallerian degeneration. (4) SC proliferate and align to form Bands of Büngner giving guidance to regenerating axons. The leading end of the axon of the proximal stump transforms into an actin rich, highly motile tip called the growth cone which contains numerous axonal sprouts. The growth cone senses the surrounding environment through netrin mediated chemotaxis of the secreted factors along the Bands of Büngner. (5) Providing successful regeneration, the target organ is reinnervated. SC disperse and switch to a myelinating phenotype causing reformation of the myelin sheath. Adapted from: (Navarro et al., 2007).

1.2.1. Injury classification

Although the PNS possesses an intrinsic ability for self-regeneration, even the best repair is very rarely complete, with success largely dependent on both the conditions of the patient (Kawabuchi et al., 2011) and the extent of the damage. Nerve injury can be divided into 3 main categories with further sub-categories in accordance with the Seddon and Sunderland classifications respectively (Ditty et al., 2015).

1.2.1.1. Neurapraxia: first degree injury

This injury is the least severe of the categories and occurs when a focused pressure is applied to the peripheral nerve. This force results in disruption of the myelin sheath in the proximity to a node of Ranvier and a conduction blockage at the site. No Wallerian degeneration occurs, and repair is completed naturally over a period of 1-3 months.

1.2.1.2. Axonotmesis: second-, third- and fourth- degree injury

Axonotmesis occurs following a sufficient force in which axons are damaged and the process of Wallerian degeneration distally will ensue. The degree of injury depends on the extent of damage to the supportive structures surrounding the axon: the endoneurium, perineurium and epineurium. If these structures remain intact, the injury is classified as a second degree and show the most promising prognosis due to the axon guidance being provided by endoneurial tubes. A third-degree injury occurs when the endoneurium is damaged however the perineurium and epineurium remain intact. This injury usually requires surgery due to the loss in neurite guidance and the likelihood of neuroma formation. When the only remaining structure is the epineurium, the injury is classed as fourth degree and has a very poor outlook for repair without surgical intervention.

1.2.1.3. Neurotmesis: fifth degree injury

The fifth degree is the most severe of injuries in which complete severance of axons and all supportive structures takes place. As a result, there is no possibility for nerve repair without surgery.

1.2.2. Neuropathological survival response

The first step towards regeneration is the recognition of injury. Following damage, a number of events and signals ensue at the cell body, the injury site and the distal terminus that contribute to some extent to the regeneration process (Figure 6). The combined effect of these signals can trigger activation of the regenerative phenotype or in apoptosis. The decision to undergo apoptosis rather than regeneration results in the death approximately 40% DRG neurons (Hall, 2005) following lesion.

1.2.2.1. Injury recognition: signalling and response

Injury signals can be divided into positive (increased presence of a factor) and negative signals (decreased presence of a factor) (Allodi, et al., 2012) and are described visually in Figure 6. Positive signals are initiated with the rapid influx of calcium ions through the open membrane into the axoplasm causing an intense burst of action potentials which can last for several hours until membrane resealing takes

place (Ahmed et al., 2001). Following resealing, high intracellular calcium ion levels continues to remain, leading to an increased cyclic Adenosine Mono-Phosphate (cAMP) concentration in the soma activating the cAMP-response-element-binding-protein (CREB) pathway, which is crucial to initiate the regenerative response (Rodger et al., 2005, Domeniconi and Filbin, 2005). The open membrane also leads to exposure of the axoplasm to exogenous signalling molecules such as FGF, NT-3 and CNTF that are expressed by local fibroblasts, SC and inflammatory cells. These normally extracellular molecules can activate signalling pathways such as the local translation of STAT-3 at the lesion site (Kirsch et al., 2003) which is then retrogradely transported by dynein and importin α 5 to the soma, where it effects to modulate neuronal survival (Ben-Yaakov et al., 2012).

Axon severance inhibits the retrograde transport, heavily diminishing the usual flow of signals that originate from the axon terminus. This absence of neurotrophic factors constitutes the negative injury signal and is believed to be the main source of injury recognition (Allodi et al., 2012). Research has shown that if support is maintained through a continuous exogenous supply of NGF during injury, the switch to a regenerative phenotype is delayed (Hirata et al., 2002, Gold, 1997a).

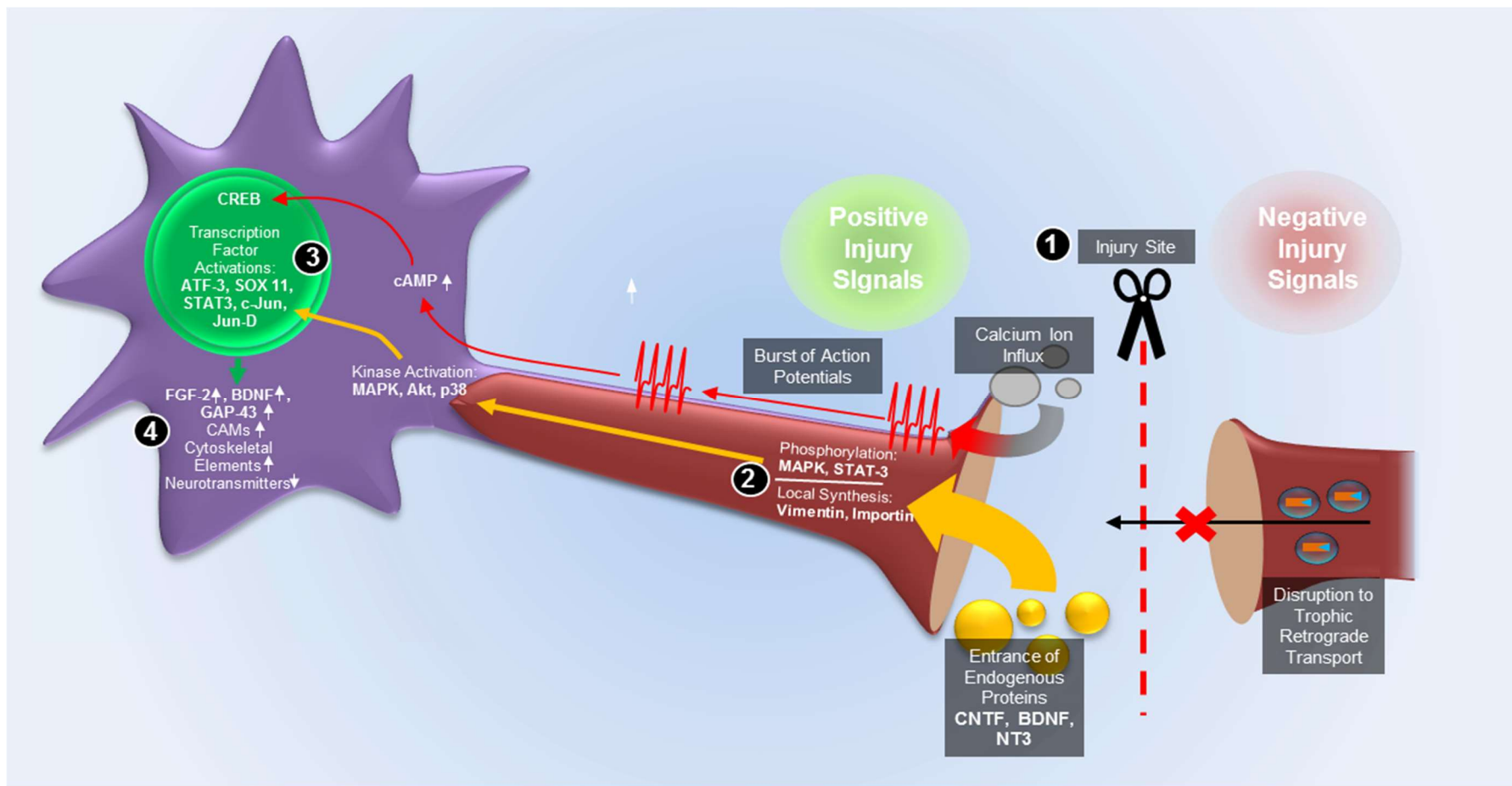


Figure 6: Injury signalling mechanisms of a PNS neuron. (1) The influx of calcium ions triggers a burst of action potentials. (2) Negative injury signals: Disruptions in the flow of retrograde signals such as NGF to the soma from the disconnected innervated organ. (3) Positive injury signals: phosphorylation of proteins such as MAPK, STAT-3 as well as uptake of exogenous proteins which are then moved to the soma through vimentin and importin. These mechanisms are essential for the alteration of the neuron phenotype from a signal transmission state to a regenerative state. This allows the activation of various transcription factors that regulate the expression of regeneration-associated proteins (5) essential for regeneration. Adaptation from: (Allodi et al., 2012).

At the lesion site, localised mRNA translation is triggered and production of importin and vimentin which upon complexation with the molecular motor dynein (Perlson et al., 2005), allow for the translocation and activation of intracellular signalling enzymes; extracellular signal regulated kinase (Erk1/2: MAPK), Akt, JNK and P38 (Donnelly et al., 2010). These signalling cascades elicit the early response in injury and contribute to neurite outgrowth (Michaevlevski et al., 2010, Lindwall and Kanje, 2005). Nuclear localisation and phosphorylation various transcription factors STAT-3, cJun, jun-D, ATF-3, Sox-11 (Allodi et al., 2012). Activation of these transcription factors leads to the upregulation of regenerative associated genes (RAGs) which are responsible for the transcription of cytoskeletal proteins; actin, tubulin, growth associated protein (GAP-43) and cell adhesion molecules such as integrins and CD44 (Kloss et al., 1999), which are important for growth cone advancement (Ma and Willis, 2015). The activation of these RAGs can also induce activity of CREB and p53 which are essential to a successful regenerative response. There is also a decrease in transcription of typical proteins involved in signal transmission irrelevant for regeneration. In addition, the adaptation to an injured state leads to morphological chromatolytic changes consisting of nucleus expansion, it moving off centre and the degradation of Nissl bodies.

The switch to the regenerative phenotype may simply be the first step following injury; however, its decisiveness in survival and speed of response overall determines the success of regeneration.

1.2.3. Wallerian degeneration

Wallerian Degeneration is a process which occurs following a second-degree injury or higher in which myelin and axons are disintegrated to allow the regrowth of axons emanating from surviving neurons. Immediately after injury, Wallerian degeneration occurs to the entire distal nerve as well as to the proximal end to the nearest node of Ranvier. This begins with the sealing of severed nerve endings via blood-clot formation which blocks the ante and retrograde flow through the axon causing an organelle build-up leading to axonal swelling (bulb formation). A loss of vascular flow to the injury site contributes to the development of a localised hypoxic condition, which aids in the attraction of macrophages via the release of VEGF by the cells within the hypoxic zone (Cattin et al., 2015).

The elevated intracellular calcium concentration, described above, activates calcium-dependent proteolytic enzyme calpain which acts to initiate the degradation of cytoskeletal components, mitochondria, endoplasmic reticulum and neurofilaments (Allodi et al., 2012). Within a day, Schwann cells begin to detach from dying axons, switching from a myelinating state to a regenerative one (Faroni et al., 2015). In this state, transcription of proteins relating to myelin (myelin basic protein, myelin-associated glycoprotein) are down regulated whilst RAGs begin to express (Jessen and Mirsky, 2016). Macrophages are recruited through the excretion of various interleukins (IL 1B, 6 10), leukemia inhibitory factor (LIF) and CCL2 chemoattractant molecule (Tofaris et al., 2002). Accompanied by this, SC begin to proliferate and resulting in a visible change to the morphology of the cell, where the cytoplasm and nucleus become enlarged caused by the inactivation of ATG7, which is responsible for autophagy (Jang et al., 2015). The combined efforts of SC and macrophages result in the phagocytosis of axonal debris and myelin sheath, remodelling the environment to accept the regenerating neurites (Figure 5).

1.2.4. Cell activity and assembly across the nerve bridge

In axonotmesis, a variable amount of structural integrity in the tissue between the proximal and distal stump of injury remains which is dependent on the extent of disruption to the layers of connective tissues, classed by the degree (described in section 1.2.1.2). During regeneration; however, this structure is reinforced through the construction of tissue between the stumps termed “the bridge” by resident perineurial cells and fibroblasts (Kucenas, 2015, Lewis and Kucenas, 2014). Following this, SC align to create neurotrophic gradients to promote axon growth across the bridge.

Previously, attention has focused on SC as the key player in cellular nerve guidance (Rodrigues et al., 2012, Verdú and Navarro, 1998) and this remains true (Jessen and Mirsky, 2016), however increasing evidence suggests that their regenerative ability is actually resultant of a multi-cellular concerted effort with a sequence of events involving fibroblasts, endothelia and macrophages (Cattin and Lloyd, 2016b).

In an injured and reconnected but not sutured mouse sciatic nerve this process begins with the recruitment of macrophages that release VEGF to guide angiogenesis across

the bridge which in turn serve as the structural support for cell adhesion. Neighbouring fibroblasts express ephrins (B/ B2) which attract SC into migration out of the nerve stump, along the vasculature to create bands of Büngner, for haptotactic guidance tracks for regenerating axons. SC direct axon pathfinding through cell adhesion molecule expression (L1CAM and NCAM) for adhesive anchorage and secretion of neurotrophic growth factors (NGF, BDNF, GDNF, bFGF and NT-3) to provide a chemotactic gradient to promote axon extension. Through these events, axons can cross the bridge to result in successful nerve regeneration in the PNS (Cattin et al., 2015, Cattin and Lloyd, 2016a, Cattin and Lloyd, 2016b).

1.2.5. Axon extension and innervation

During regeneration in humans, axon growth can reach rates of up to 1mm per day naturally when aided with the provision neurotrophic factors by supporting Schwann cell (Grinsell and Keating, 2014). To increase the chance of successful re-innervation, axons undergo arborisation in which a number of daughter axons sprout from the initial framework. This behaviour can be promoted by factors such as BDNF which has been shown to induce neurite branching (Cohen-Cory et al., 2010). Branching can be induced through increased neuronal cell death as there is a lack of uptake of growth factors arising from lower migrating axon competition. Over time the number of sprouts decrease as they fail to reach the target tissue and undergo atrophy to eventually disappear (Allodi et al., 2012). Moreover, if the axon leading edge termed the “growth cone” fails to reach its destination, it will likely lead to neuroma formation.

1.3. The growth cone

The growth cone of the axon can be described as a hand like structure, which functions to survey the local microenvironment and gain a sense of direction. It extends from the axon tip and is a highly dynamic structure that continually advances towards the innervation target. In the ideal case, reconnection to the original target of the neuron is accomplished through guidance cues from cells and the ECM via topographical structures, chemotaxis, haptotaxis and point contact mediated guidance by surface mechanical properties. On the other hand, negative feedback through contact mediated repulsion allows the avoidance of structures and negative

chemotaxis, when the growth cone turns away from chemo-repulsive factors (Brown and Bridgman, 2009).

1.3.1. The structure of the growth cone

The growth cone structure is, according to Bouquet and Nothias (2007), comprised of three regions (Figure 8), which are distinguished by their cytoskeletal components and function. These regions are the central domain (C-domain) situated at the end of the axon shaft containing microtubules, mitochondria and vesicles. The peripheral domain (P-domain) is the most motile part, rich in actin; here filopodia (bundled F-actin) and lamellipodia (supported by a tight meshwork of F-actin) emanate at the outer edge of the growth cone. Finally, there is the transition zone (T-zone), separating the C and P zones, which is populated by arcing actin filaments and myosin II rich region.

1.3.2. Cytoskeletal dynamics

As mentioned previously, the growth cone is a highly dynamic structure capable of retracting, remaining, turning and advancing through a complex cytoskeletal remodelling process (depicted in Figure 7). It has been shown that there is a continuous polymerisation and depolymerisation of F-actin at the leading (barbed) and trailing (sharp) ends respectively. The retrograde flow of actin in the growth cone result from myosin II contraction at the T-zone and the force exerted on the polymerising filament by the membrane (Medeiros et al., 2006, Lin et al., 1996) ensures that there is no endless advance. The combination of both the speed of the retrograde flow and the rate of polymerisation is a balance and will determine the behaviour of the growth cone. When the rates are at equilibrium, the result will be “tread-milling”, where the growth cone remains stationary. If the polymerisation is lower, the growth cone will withdraw and if higher, it will advance.

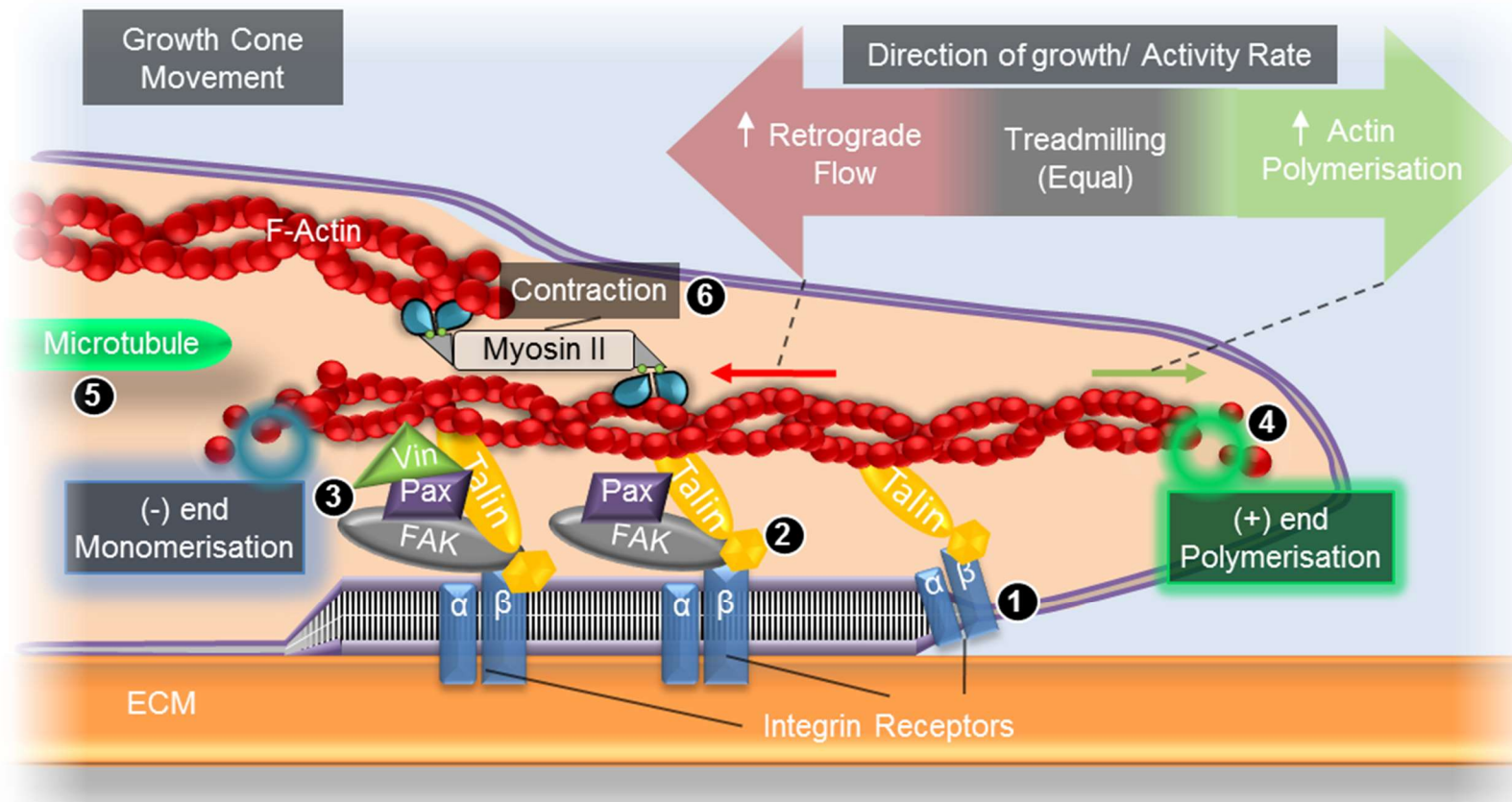


Figure 7: The mechanics of growth cone motility. The process begins with integrin binding to the ECM substrate surface ligand (1). Adaptor proteins are then recruited to form the integrin complex (2) with vinculin engaging the molecular clutch (3) and allowing actin polymerisation (green region, 4). This causes the extension of filopodia (green arrow) attributed to the protrusion stage and microtubule advance engorgement phase (5) (Fig1-8C). Myosin II then contracts the actin filaments pulling filopodia back and together with depolymerisation (blue region) is termed the retrograde flow (red arrow). Overall, the advance or retraction is dependent on the combined activities of polymerisation and retrograde flow. If both are balanced, “treadmilling” occurs and the growth cone remains static. Figure adapted from (Kerstein et al., 2015).

1.3.3. Regenerating growth cone advance

The mechanism by which the growth cone advances is a three-stage sequential process; protrusion, engorgement and consolidation (shown in Figure 8 and Figure 9). Primarily, protrusion begins with the binding of integrins to the ECM (collagens, laminin, fibronectin etc.), activating the molecular clutches vinculin and talin. This triggers the polymerisation of the filamentous actin resulting in extension of explorative filopodia and lamellopodia: the “fingers” of the growth cone “hand” structure. Engorgement, the second event occurs with invasion of C-zone microtubules into the P-zone. This brings the MTs into contact with the F-actin fibres and effectively expanding the C-zone towards the leading edge of the growth cone. This is achieved through a reactive phenomenon called dynamic instability, in which, the plus end of the MT undergoes a rapid disassembly (catastrophe) and recovery (rescue) allowing the agile remodelling of the C-zone observed in the engorgement stage. In the final stage; consolidation (Geraldo and Gordon-Weeks, 2009), myosin II contracts the actin filament arcs in the T-zone which compresses the MT, causing a restraint in their advance and leading to the formation of the new axon segment below the growth cone (Burnette et al., 2008). Overall, this results in axonal extension towards a positive cue,

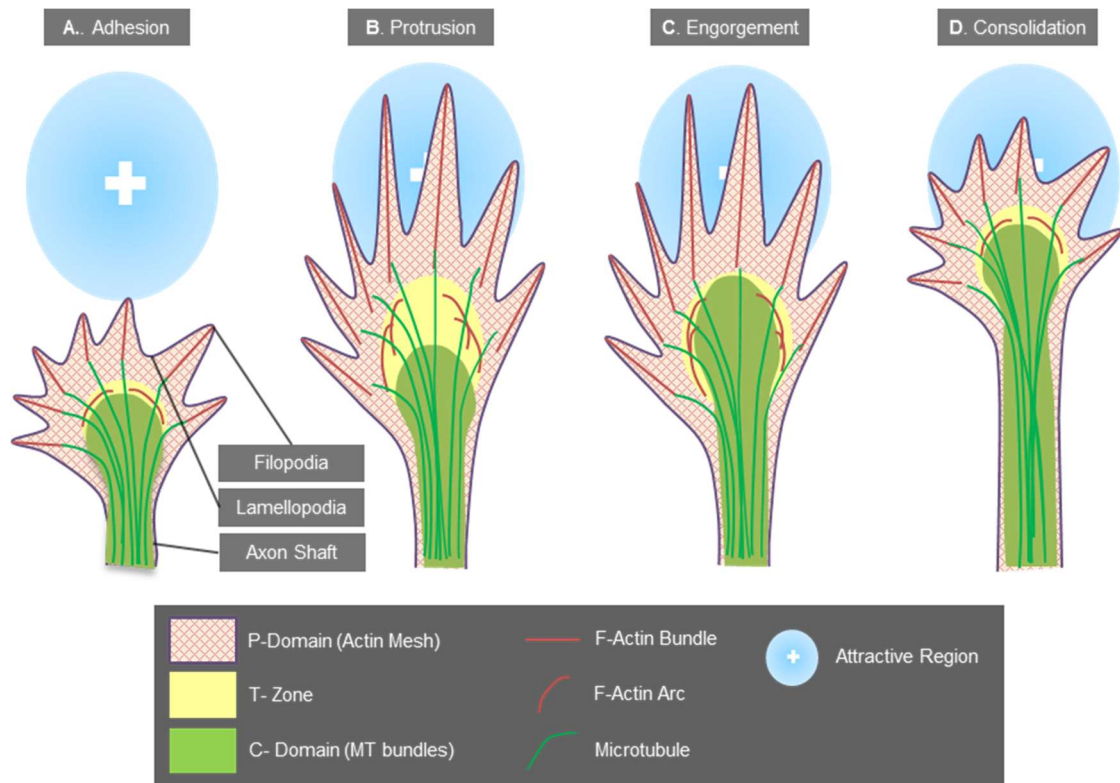


Figure 8: Cytoskeletal dynamics in growth cone extension. The growth cone consists of three regions as depicted by the (stasis) state: the peripheral (P)- domain, the transition (T)- zone and the central (C)-domain. Formation of the focal adhesion begins the advancement process with the binding of integrins to the substrate connecting the actin cytoskeleton to the substrate (A). This activates the polymerisation of F-actin in the P-domain leading to the protrusion of filopodia (bundle) and lamellipodia (mesh) structures (B). This clears the actin arcs in the T-zone providing a corridor for microtubules to cross into the C-domain and follow the filopodia extension in a process called engorgement (C). Lastly, there is the consolidation stage (D). Through myosin II contraction of actin, the growth cone structure tightens, compressing the microtubules and pushing the C-domain back halting the advance. This also results in some retraction of the P-domain and overall an extension of the axon shaft. Figure adapted from: (Lowery and Vector, 2009).

1.3.4. Growth cone turning

1.3.4.1. Repulsive cues

In order to navigation around surface objects, the GC is required to sense the environment and respond in a repulsive or attractive manner. Although the process of turning through repellent cues such as semaphorin-3A (Brown and Bridgman, 2009) is less well understood, evidence suggests that ipsilateral activation of Myosin II generates F-actin bundling and less protrusive potential (Orlova et al., 2007, Gallo, 2006). The general consensus is that upon contact with negative stimuli, there is a destabilisation of the filamentous actin super structure causing the loss of focal adhesions at the nearest edge (as depicted in Figure 9). This results in partial

collapsing of the growth cone creating an asymmetrical shape (Dent et al., 2011) in which there is an ebb (retraction) closest to, and a flow (extension) of lamellipodia at a region away from the repulsive cue, creating a recess in the GC shape. During advancement, microtubules reorganise avoiding and moving from the recess, into the majority region overall, effectively steering the axon direction (Zhou et al., 2002).

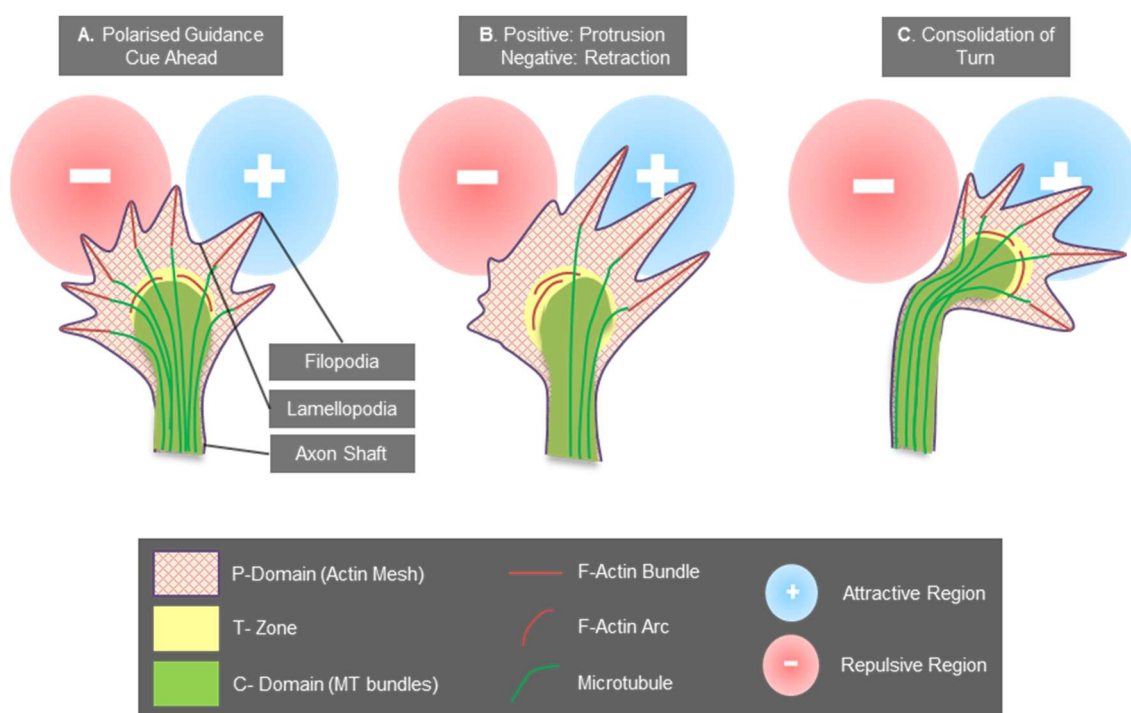


Figure 9: Cytoskeletal dynamics in growth cone turning. Upon reaching a polarized chemical stimuli (A), filopodia extend towards the positive chemical region sensed through FAK-src-Trk signalling (Figure 10). Negative stimuli (such as sema3A) result in retraction of filopodia through activation of ROCK pathway which promotes actin depolymerisation and myosin II activity. Mechanical stimuli such as stiffness in combination with actin traction modulate the force exerted on focal contacts which may result in loss or retention of adhesion (Kerstein et al., 2015). This results in the majority of F-actin bundles extending to the positive region, followed by microtubules to consolidate the turn (C).

1.3.4.2. Attractive cues

Chemoattractive surfaces can mediate axon pathfinding through activation of receptors at the plasma membrane of the growth cone edge to initiate intracellular signalling pathways involving cytoskeletal remodelling (Dent et al., 2011). This increases polymerisation nearest the gradient source resulting in an asymmetric, higher density actin region. Microtubules follow the abundance of actin (described below) resulting in a morphological shift in direction towards the positive cue. By this mechanism, substrate bound NGF, netrin-1 (Marsick et al., 2010) and BDNF (Song and

Poo, 1999) has been shown to increase protrusion whilst altering growth cone pathfinding. Local increases in intracellular calcium ion concentrations have shown to mediate the behaviour to molecular guidance cues in which the response to attractive signals can essentially “switched” to become repulsive (Hong et al., 2000) or vice versa. This example gives an insight into the complex fundamental behaviours of the axonal growth cone.

1.4. Cell adhesion

In cell adhesion, ECM proteins provide the surface to which transmembrane proteins; the cell adhesion molecules (CAM) can bind. Upon binding, signal transduction is initiated, transmitting information about the environment or cellular communication to the soma of the cell, which can initiate survival, or differentiation signals or cytoskeletal rearrangements (Horstkorte and Fuss, 2012). CAMs are one of the most heavily researched areas in molecular biology and there is an increasing number of CAMs being discovered, which are gathered into families ordered through function, structure and target. In the context of neurons, there are typically three relevant CAM superfamilies; cadherins and immunoglobulins (Ig) which form the cell to cell contacts points and integrins, which bind to the ECM.

1.4.1. Cadherins and neural CAMs

Neural-Cadherins (n-C) are a group of transmembrane proteins/ molecules responsible in mediating neuron- glial interactions (Fairless et al., 2005). N-C are calcium dependent, with their binding activity reliant upon extracellular Ca^{2+} concentration (Kim et al., 2011). Expressed in regenerating axons and Schwann cell, findings indicate that n-C are integral to the alignment and proliferation of SC (Gess et al., 2008), myelination by SC (Basak et al., 2015) as well as axon fasciculation and neurite outgrowth (Wanner and Wood, 2002). Neural CAMs are the next CAM superfamily involved in axon-cell adhesion, effective independently of calcium however. Neural-CAM (NCAM) and L1CAM are immunoglobulins which are known to be expressed in the neural growth cone, SC and fibroblasts during PNS regeneration and are associated with axonal growth, migration and neuron membrane excitability/ network action potential activity (Valente et al., 2016). Evidence indicates that both Ig and cadherin families can be influenced by neurotrophic factors such as NT- 3 and 4, shown to

differentially regulate the CAM expression (Thornton et al., 2008) and the heterophilic NCAM and L1CAM complexation to fibroblast growth factor receptor (FGF-R) to modulate several downstream signalling pathways (Walmod et al., 2004).

1.4.2. Integrins

1.4.2.1. Integrin complexation

Integrins are a family of transmembrane glycoproteins functioning fundamentally in the adherence, surveying and mechanosensing of the extracellular environment and in doing so trigger downstream pathways for events such as; gene expression, differentiation, protein synthesis and cytoskeletal rearrangements. This is achieved mainly through the external domain binding to particular moieties on ECM molecules (e.g. laminin, fibronectin and collagens) (Betz et al., 2009) as well as forming interior complexes such as focal contacts that connect to the actin cytoskeleton. Integrins are heterodimeric proteins existing in numerous (~24) configurations of both an alpha and a beta subunit (~18 and 8 known types respectively) (Campbell and Humphries, 2011). The variety in integrin complexes creates the selectivity required for specific recognition and binding to different ECM ligands.

1.4.2.2. Binding mechanics

Mechanistically, integrin complexes bind in two motifs: trans (ligand interaction) and cis (cytoskeletal proteins interaction). During trans- binding, both subunits participate together as active site for the ligand which can lead to their aggregation resulting in the clustering of integrins (Changede and Sheetz, 2017). However, during in-cis binding, integrins interact in a monovalent fashion with only the beta subunit. As a result of binding, signalling cascades are promoted for both inside- out and outside-in directions (Previtali et al., 2001). Inside-out signalling(cis) prompts an alteration of the integrin conformation, leading to an increase or decrease in binding affinity to the extracellular ligands, whilst outside-in signalling (trans) provides the cell with information about the ECM and may elicit morphological (re)organisation.

Integrin receptor occupation causes distancing between integrin subunits and conformational changes allowing intracellular associations with adaptor proteins,

signalling tyrosine kinases (FAK-1, src) (Tucker et al., 2008) and actin coupled structural proteins (talin, vinculin and paxillin) resulting in the reorganization of filamentous actin and formation of focal adhesions. Overall, evidence suggests, that this process is regulated by the Rho-family GTPases, specifically the small GTPases Rho-A and Rac modulation of actomyosin contraction (Gallo, 2006).

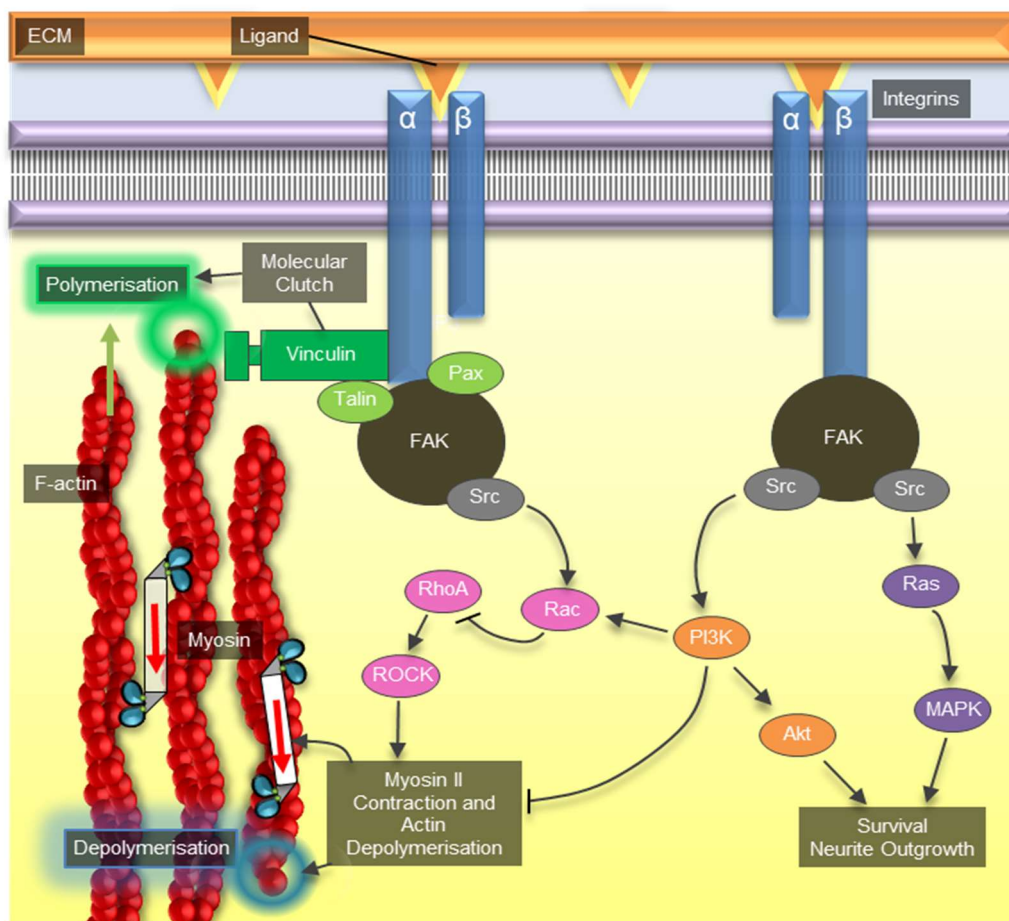


Figure 10: Signal transduction pathway initiated by integrins. Integrins function like molecular anchors that bind the cytoskeleton to components of the ECM or substrate causing the transduction of signals throughout the cell providing information on the external environment. Upon binding, the integrin complex (vinculin, talin, paxillin, FAK) serves as the molecular clutch allowing polymerisation of the barbed end and initiating protrusion. On coupling with Src, FAK plays a central role in regulating the substrate-cell response. Both Ras-MAPK and PI3k-Akt cascades may be activated resulting in cell survival. Also, the Rho GTPase Rac and PI3k can downregulate the ROCK pathway inhibiting axon retraction. ROCK is known to both phosphorylate myosin II for actin contraction-retrograde flow and as promoter for pointed end depolymerisation (Gary and Mattson, 2001, Tucker et al., 2008).

1.4.2.3. Integrin signalling

Generally, cell adhesion has been thought to lead mainly to cytoskeletal changes and axon migration however, there is an increasing amount of evidence that more is

achieved (Pollerberg et al., 2013, Kamiguchi, 2007). Integrin activation has been shown to be directly involved in Trk signal transduction with FAK serving as the key communication link between cell adhesion and Trk signalling cascades (MAPK, PLC γ , PI3K and effectors) (Rout, 2013). Gary and Mattson (2001) report that integrin activation initiates a neuroprotective response through FAK-PI3K/ Akt signalling (discussed later), a key cascade in neurotrophin signalling. On the other hand, inhibition of PI3K (Rac effector) has been shown to reduce growth cone protrusion (Orlova et al., 2007). Further to this, micro-topographical cues were seen to regulate mTOR activity, an upstream effector of PI3K signalling (Thomson et al., 2017). These findings provide a good example of the complex and interactive nature of mechanical-chemical signalling in nerve regeneration which is an aspect of the hypothesis investigated in Chapter 3.

The formation of focal adhesions, anchoring the axon growth cones to the basement membrane is required for growth and migration, with the majority of its focal adhesions residing at the leading edge (Betz et al., 2009), axon path finding relies on the activity of the actin-integrin complex. The combined tasks of probing stiffness gradients, acting as mechanosensors and informational transmission of environmental properties are essential in the axon path finding and growth cone motility.

1.5. Neurotrophic growth factors

A number of different GFs have been explored in attempts to improve both axonal growth during regeneration and regeneration rates. Neurotrophic growth factors are generally divided into two groups; neurotrophins (NGF, BDNF, neurotrophins -3/4/5) and other growth factors with neurotrophic actions (FGF, PDGF) (Allodi et al., 2012). The neurotrophins share similarities both structurally and in the cellular signalling pathways they activate whilst other neurotrophic growth factors can be structurally distinct, with pathways which may be different and/ or supportive to neurotrophin signalling transduction. Despite differences between these groups, there is overlap in their resultant effects that are aimed to support the survival, growth and differentiation of neurons.

These biomolecules are secreted by SC and fibroblasts following a nerve injury at the distal nerve stump and across the nerve bridge (explained in section 1.2.4).

Generally, in vitro neuronal cultures require an external GF supply to ensure survival and encourage outgrowth. It has been found that neurotrophic GF have additional effects such as modulation of nerve pain NGF, BDNF (Vögelin et al., 2006) or detrimental side-effects by causing psychiatric and neurodegenerative disorders (Mitre et al., 2017).

1.5.1. Neurotrophic receptors

Both GF groups have been shown to be important regulators of neuronal development, survival and axon migration however the neurotrophin family has received greater attention due to their presence during neural regeneration being a definite requirement for success (Ebadi et al., 1997). Initially synthesised as precursors, the pro-forms undergo cleavage to produce the bioactive molecular fragment. Neurotrophins work through interaction with surface receptor proteins: tropomyosin receptor kinase (Trk(a-c)) and p75, the former site holding selectivity for each neurotrophin (NGF, NT-3: a, BDNF, NT -3/4/5: b, NT-3: c) and the latter allowing either ligand. Although literature states that p75 is considered the lower affinity receptor (Gao et al., 2007), both have a relatively low affinity when acting independently (Covaceuszach et al., 2015), with Trk opting to dimerise upon ligand binding (Wang et al., 2014). Further, it is acknowledged that p75 can modulate the binding affinity and transient time of the Trk receptor (Jullien et al., 2002), with their association requiring lower NGF concentrations to initiate signalling responses (Horton et al., 1997). Despite these findings, it is not fully understood mechanistically how this is achieved, whether it is through direct interaction via a p75-Trk complex, an association inducing a conformational change or simply the passing of the ligand (Toni et al., 2014, Covaceuszach et al., 2015). In addition, binding interactions are reliant upon local concentrations, cellular location, retrograde transport and neuronal activity.

1.5.1.1. Endosome signal transduction

Following receptor binding of a number of different signalling cascades may be activated. First to consider is through dynein powered retrograde transport of the bound complex neurotrophin-(Trk or p75). Endosome formation is mediated through rac1/ rap1 endocytosis (Valdez et al., 2007, Harrington et al., 2011) and

transportation of the encapsulated bound ligand-receptor complex is powered through dynein motor proteins. The endosomes with their internalised ligands are moved to other regions in the membrane (York et al., 2000) or towards the soma activating various pathways such as ERK. This is accomplished through the binding of signalling proteins to available active sites on the Trk receptor complex in the endosomal membrane (Schmieg et al., 2014). Upon reaching the soma, the trk associated signalling influence transcription factors such as CREB or c-jun, an essential occurrence for cell differentiation and survival (Yano and Chao, 2000).

1.5.1.2. NTReceptor p75

The p75 receptor has long been implicated in neurons as a signalling of both cell survival and apoptosis however recently has been shown to influence cell migration and support myelination (Roux and Barker, 2002). With the help of adaptor proteins binding to the cytoplasmic domain (Hempstead, 2002), CASPASE-3 activated cell death is initiated through the JNK pathway with Rac1 also involved (Harrington et al., 2002), whilst NF- κ B elicits a survival response. Activation of p75 also shows involvement in cytoskeletal dynamics through modulation of RhoA which has been found to have an inhibitory effect on neurotrophin induced neuron outgrowth (Gehler et al., 2004b).

1.5.1.3. Tropomyosin receptor kinases

The Trk signalling cascades generally constitute the business end of the neuronal signalling, operating through 3 major signal cascades: PI3K/Akt, MAPK and PLC- γ 1. Following neurotrophic binding to the Trk Ig domain, trans-autophosphorylation of multiple tyrosine residues promotes the recruitment of adaptor proteins e.g. Src-homology-2 (SH2), Grb-2, sons of sevenless (SOS) and the docking protein FGF-receptor-substrate-2 (FRS2). The binding of these proteins mediates the selection and activation of signalling pathways. In the case of PI3K, cell survival and differentiation is controlled through Akt, and its downstream effector mTOR, which is also a mediator of cytoskeletal dynamics (Jaworski and Sheng, 2006). There are conflicted results on PI3k effects on axon arborisation, with Akt signalling shown to both inhibit (Higuchi et al., 2003) and promote (Schmidt and Rathjen, 2010) branching indicating that it may be dependent the neuron/ cell type with external influences such as GF

induction or substrate chemistries. Finally, PI3k shows involvement with the small GTPase family Rac and Cdc42, regulating cytoskeletal organisation and actin polymerisation (Hall and Lalli, 2010).

The second major pathway of Trk receptors is the MAPK cascade, stimulated through the membrane-associated G protein Ras. Ras actively phosphorylates several proteins including the proto-oncogene Raf, which then initiates MAP2K-MEK-ERK 1/2 cascade (Wang et al., 2013). ERK 1/2 can then enter the nucleus to alter the regulation of many transcription factors such as ELK1, ribosomal S6 kinase (S6k) and cyclic adenosine monophosphate response element binding (CREB), overall resulting in the pro-survival, differentiation and neurite outgrowth response (Wang et al., 2014).

The final neurotrophic signalling cascade to be discussed is PLC- γ 1 has attracted less attention due to previous opinion of a more indirect involvement in neurotrophic signalling (Reichardt, 2006). Nevertheless, opinion is changing with PLC- γ 1 retaining responsibility for mediating the Trk receptor-calcium ion channel signalling as well as in the regulation of transcription factors such as STAT-5 (Klein et al., 2005).

Mechanistically, Trk/ PLC- γ 1 signalling is carried out through docking of the PLC- γ 1 to the ligand bound Trk receptor, promoting the generation of IP3 and diacylglycerol (DAG) which alters activity of membrane proteins that interact with phosphatidylinositides producing effects in other signalling cascades (Chao, 2003). Increasing IP3 leads to Ca²⁺ release from cytoplasmic calcium stores whereas DAG can activate almost all protein kinase C isoforms (PKC) which are required for activation of NGF induced MAPK pathway activation (Corbit et al., 1999) and by extension, modulate transcription. Further, through protein kinase C activation, neurotrophin can exert the release of NRG-1 in sensory neurons, fibroblasts and (Esper and Loeb, 2009).

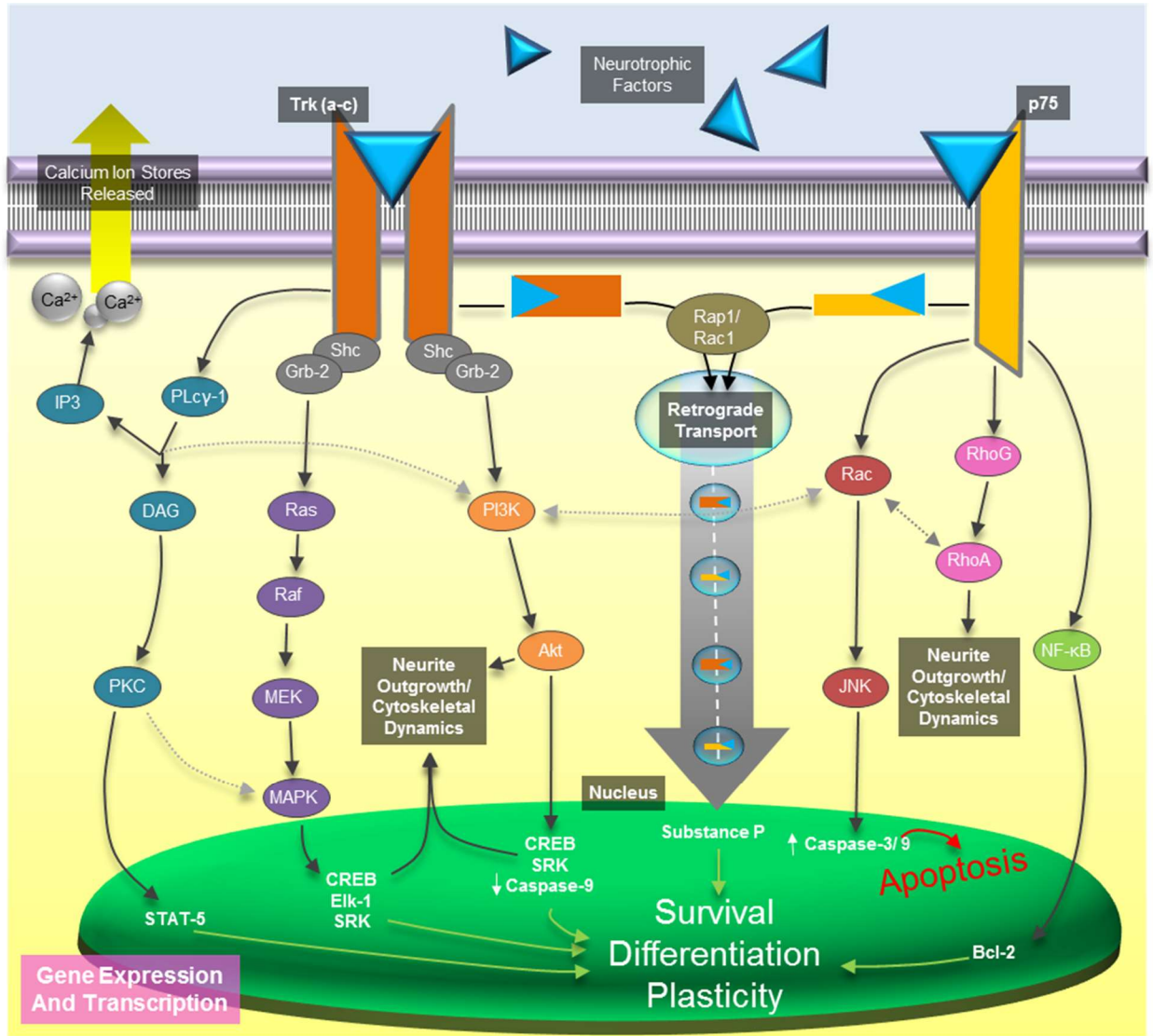


Figure 11: Neurotrophic growth factor signalling in neurons. Neurotrophic growth factors bind to both Trk (a-c) and p75 receptors although the latter with lesser affinity and selectivity. P75 receptor binding can lead to modulation of cytoskeletal dynamics through ROCK and both a pro-apoptotic and survival response. Apoptosis is regulated through JNK (c-Jun) in the presence of Rac1 whilst survival response is promoted by NF-kappaB gene activation and Bcl-2 transcription. On the other hand, Trk binding leads to a number of positive cell responses through PI3k/ Akt, Ras/ MAPK and PLCγ-1/ PKC signal cascades. As a result, the cAMP response element binding protein (CREB), ribosomal s6 kinase (S6K) and the ETS domain containing protein (Elk-1) are switched on proceeding to activate the transcription factors for neuron survival, growth and differentiation. Finally, a pro-survival and growth response (Substance P) is initiated also by the retrograde transport of the Neurotrophic GF-Trk complex inside endosomes to the soma and the nucleus through Rap1 and Rac mediated endosome encapsulation and dynein drivers. There is also a number of crosstalk sites between cascades (grey arrows) generally involving Rho GTPases indicating the interactive nature neurotrophic signalling and its complexities.

1.6. Limits in nerve regeneration

Although the intrinsic regeneration following nerve injury can be highly beneficial, it cannot be relied upon to consistently complete effective nerve repair. The overall success of natural regeneration depends on the injury classification (Gordon, 2015), size of nerve lesion and location (Zochodne). During the regenerative process, there are several occurrences that limit the outcome of recovery. One occurrence in particular which has a detrimental effect on regeneration is in scar formation. On these occasions, fibroblasts or SC produce collagen to excessive levels following injury and effectively barricade recovery resulting in neuroma formation (Floren et al., 2016; Qinwen Li, Chen, Chen, Cong, & Chen, 2016; Qinwen Li, Chen, Chen, Cong, & Chen, 2016; Monk et al., 2007) (Floren et al., 2016, Li et al., 2016, Monk et al., 2007). Other issues are in the speed of axon growth or misguided axon growth, resulting from lack of connective guidance tissue or neurotrophic support. Overall, these actions will amount to poor or incorrect target innervation and neuroma formation of “lost” neurites and eventual atrophy of the target tissue (skin, sweat glands, sensory organs etc.) arising from the lack of support (Gordon, 2015, Menorca et al., 2013).

Currently, the nerve autograft is the most successful approach to peripheral nerve injury capable of enhancing the repair across lesions of up to 5 cm (donor nerve transfer limit) (Arslantunali et al., 2014). There is however a number of drawbacks in its application such as donor site morbidity and function loss, mismatch of nerve dimensions (Wolford and Stevao, 2003) and neuroma formation. Another suitable alternative is through allograft transplantation, overcoming some limits such as inaccessibility of donor tissue although this also requires immunosuppression (Moore et al., 2011). The ideal solution is sought extensively with most efforts investigating the use of nerve guidance conduits (NGC), of which several are commercially available, readily producible scaffolding harnessing various guidance structures and supporting factors which will effectively aid nerve regeneration to reach new potentials.

1.7. Nerve guidance conduit

1.7.1. Functional requirements and design

General research targets for the development of NGC are focused on providing a readily accessible scaffold incorporating inductive elements for quick initiation of the PNS repair process with faster regeneration rates, more specificity in axonal growth and complete biodegradability following successful innervation (Allodi et al., 2012). Initiating the regenerative process early is a necessity, providing the optimal environment to promote axon growth with the ideal morphology is critical to success of treatment. This is largely dependent on substrate surface properties, selection of neurotrophic GFs used (Deumens et al., 2010) and the inclusion of support cells. The design of NGC must also account for permeability, to allow oxygen and nutrient exchange and mechanical flexibility/ strength to withstand demands of patient mobility (de Ruiter et al., 2009).

Micro- and nano-structured surface topographies have been shown to have a profound influence on nerve cell behaviour with microgrooved surfaces providing directional guidance, leading to a higher degree of axonal alignment and length resulting in more growth cones reaching the distal stump (Hoffman-Kim et al., 2010). Research suggests that topography does not lead directly to longer axonal growth; instead, regenerating axons need to be stimulated by GFs via endogenous supply or secretion of supportive cells. The choice of material selected for the substrate is paramount as its properties can affect the adhesiveness of cells, toxicity and biodegradability. The materials mechanical properties must be suitable, with sufficient robustness whilst also maintaining the optimal surface stiffness to serve as the structural guide for growing neurites and cells. As a result, a variety of materials, naturally biological and synthetic have been explored as discussed in detail below.

1.7.2. Substrate material

1.7.2.1. Transplanted tissues

Various tissues have been considered suitable substrate materials- cellular or decellularised; autogeneic, allogeneic or xenogeneic such as muscles and veins have

been examined (Brandt et al., 1999) utilizing their native structure and basal lamina like ECM to support regenerative capacity of the axons. For xenogeneic nerve grafts, decellularization of the tissue is a necessity prior to integration with the injured nerve in order to reduce the potential immunogenicity. In contrast, in allograft tissues, the abundance of SC contained in within may be harnessed with the provision of immunosuppressive drugs (Bain et al., 1988) however this becomes more complicated when applied in a clinical setting as immunomodulatory therapy brings associated morbidity (Mackinnon et al., 1984). The success of vascular scaffolds has been demonstrated to be effective for the repair of 1- 3 cm nerve gaps (such as in digital nerve injuries), or provide recovery where previous grafts were unsuccessful (Mackinnon et al., 1984, Chiu and Strauch, 1990, Terzis and Kostopoulos, 2010). However, vein tissue grafts for the inferior alveolar nerve were observed to have insufficient mechanical strength when exposed to the constant mobility and stresses at the region resulting in kinking and leading to structural collapse (Wessberg et al., 1982). To circumvent this, incorporating a grafted piece of muscle tissue filling the vein tissue has been used to increase structural integrity whilst also offering ECM proteins and the aligned structure of the muscle fibres to guide regenerating neurites, leading to promising results in nerve lesions as large as 6 cm (Glasby et al., 1986, Nectow et al., 2012). Despite the advantages and potentials of allogenic approaches, ultimately the immediate nerve autograft remains to be the superior choice for optimal recovery (Moore et al., 2011).

1.7.2.2. Biological materials

Other biological materials which have attracted interest for use in neural scaffolds are in soluble extracellular matrix proteins (e.g. fibronectin, laminin and collagen), serving as a filling for the lumen of the tube. NGC containing these biomaterials allow for a biomimetic approach, incorporating native components found in the PNS, harnessing the signalling directive and physical properties of ECM molecules found naturally in nerve growth and regeneration (Kubek et al., 2011) as well as unparalleled biocompatibility and also biodegradability.

Although laminin coatings (inner scaffold, collagen fibres) and gels (Cao et al., 2011) have shown to be effective in promoting neurite extension, the predominant biomaterial of choice for the lumen are collagen gels (Muheremu and Ao, 2015).

There is a vast body of research into the fabrication of collagen hydrogels enabling the design of reproducible and tuneable matrices of specific stiffness, fibre size and permeability (Shoulders and Raines, 2009). Furthermore, the drive to produce gels with anisotropic alignment of collagen fibres is key, as they have been shown to guide neurite outgrowth as well aligned SC and differentiated adiposed-derived-stem-cells (ADSC) (Georgiou et al., 2015, Dubey et al., 1999). SC incorporated into NGC intrinsically remodel the collagen gel structure further mimicking the natural system. A drawback of collagen hydrogels is in their mechanical strength and robustness (Hopkins et al., 2013). In practice, the concern is in the external forces applied to the scaffold as well as cellular contraction can rip and deform the gel impeding functional repair (Nectow et al., 2012). Attempts to increase tensile strength generally involve additives and/or increasing fibre diameter or reduced porosity which have adverse effects on gas and nutrient exchange and can in some cases may block the migration of regenerating nerves (Zhu and Marchant, 2011, Kim et al., 1993, Drury and Mooney, 2003). To circumvent this, various biomaterials are under investigation as alternatives such as alginate, chitin and silk fibroin although their combined collagen co-material is also proving an exciting route forward (Daly et al., 2012).

1.7.2.3. Synthetic materials

The final group of substrate materials which will be briefly discussed are synthetic biomaterials. The initial artificial nerve conduits for clinical use were non-resorbable tubes of silicone which were problematic due to chronic nerve compression and the necessity for a second surgical operation for their removal following repair. The reasoning as to why synthetic materials attract a lot of attention lies in the ability to modify them to have different chemical and physical properties such as elasticity, conductivity and bioactivity dependent on the application required. As a result, these materials find more application in in vitro research such as the polydimethylsiloxane (PDMS) used later in Chapter 3. This material is very convenient in that it is quick to produce, can be tailored to fit the parameters of the experiment (groove width, stiffness and total dimensions) although must first be treated to modify its inherent hydrophobicity. Overall, synthetic materials for clinical application are plagued with problems such as non- biodegradability, biodegradation into toxic molecules and poor biocompatibility due to inhibition of adherence by hydrophobic surface properties.

Despite this, there remains a strong research drive towards creating acceptable polymers which has resulted in some progress being made (Muheremu and Ao, 2015).

1.7.3. Topographical cues

Deliberately micro- and nano-structured surface topography has been shown to have a profound influence on general cell behaviour (Biela et al., 2009) giving rise to a large interest in investigating alternative patterns for use as substrate surface (Nikkhah et al., 2012). Both two dimensional substrates and the interior topographies of neural scaffolds designed with grooved surfaces have been well investigated, showing better directionality of axonal growth, support cell alignment and migration than flat surfaces and leading to a higher amount of axonal bridges (Lin et al., 2008, Faroni et al., 2015). Although studies have shown that the dimensions of microgrooves (height, width) are central to directional outgrowth, the angle of the approaching neurite to the groove-wall has been shown to determine axon pathfinding with perpendicular advance resulting in a crossing over the structure whilst lesser angles restricting growth to the confinements of the groove (Li and Folch, 2005).

Numerous varieties of scaffold interiors have been constructed with combinations of micro-tubes (Verdu et al., 2002), fibres and channels providing contact guidance cues three-dimensionally and so far have been found to be promising approaches in nerve repair (Spivey et al., 2012, Hoffman-Kim et al., 2010). Efforts include laminin coated polyester fibres, aligned collagen fibres (Georgiou et al., 2013), electrospinning of silk fibroin (Xue et al., 2017) are to name but a few exciting approaches. Despite this, natural ECM structures such as the decellularized nerve tissue allograft (Avance®) retain the highest standard of successful recovery (Spivey et al., 2012). Overall, current opinion is that the topography serves to focus the direction of outgrowth, mediating the nature of axon such as branching and axon-axon interactions but is not the predominant driving force for achieving faster outgrowth rates. Instead, the supply of chemotrophic growth factors retain responsibility in stimulating faster migration and overall outgrowth distance (Spivey et al., 2012).

1.7.4. Molecular support

Numerous different growth factors, cytokines and drugs have been investigated in efforts to understand and optimise the conditions for successful nerve repair (Raivich and Makwana, 2007). Currently, Tacrolimus (FK506) which induces immunosuppressive and neuroregenerative effects (Tung, 2015), is the only drug found to have any meaningful outcome in nerve regeneration (Gold, 1997b).

1.7.4.1. Neurotrophic growth factors

In general, nerve repair is aided with NGC incorporating the neurotrophins family (NGF, NT-3/4/5, BDNF and GDNF) which are not only essential to nerve regeneration through inducing axon outgrowth, survival, proliferation and cell differentiation but also retain a high degree of specificity, minimising side-effect occurrence (Pfister et al., 2007, Matheson et al., 1997, Ramburrun et al., 2014). Other GF with neurotrophic effects (PDGF, GGF, FGFa/b) are also relevant in neuroregeneration/ support cell response (Mohiuddin et al., 1996) and have proved to be highly beneficial when present in NGC. FGF-b has been found to be a key activator of CNS regeneration of zebra fish revealing a possible route to addressing spinal injuries (Goldshmit et al., 2012). Whilst a local administration of GF is effective for neurotrophic support, other positive therapeutic effects can also be induced. Autotomy was seen to be reduced in rats with nerve lesions when BDNF was administered indicating an analgesic applications (Vögelin et al., 2006) and NGF has recently been found to be a peripheral pain mediator with inhibitory agents undergoing clinical trials (Pezet and McMahon, 2006).

1.7.4.2. Growth factor delivery

Although the support of regeneration by growth factors is paramount, physiochemical properties are essential in ensuring that travel to the targeted site is achieved with high specificity and sufficient bioactivity for the promotion of axonal growth are equally important concerns that have to be met in clinical settings (Liu et al., 2013a). Recent research indicates that more attention should be directed to the optimisation of GF delivery systems (Vögelin et al., 2006) from findings that show a local sustained delivery of BDNF achieves faster rates of regeneration.

The foremost delivery strategy used currently is to incorporate the growth factors into the neural scaffold (embedded microspheres, NGC wall, inner lumen matrix) (Luca et al., 2015) allowing a sustained local release and generally has shown to be most effective (Whitworth et al., 1996). Although it is known that expression of neurotrophins is required for neural regeneration, it is not fully understood at which concentrations and at which specific timepoints various GFs provide this process with the optimum conditions for operation with the greatest efficiency. Current research also suggests that under some conditions, GFs may even have a detrimental effect on axonal outgrowth NGF can induce apoptosis (Mukai et al., 2003) or delay injury recognition (Gold, 1997a). The amount of supplied growth factor is a relatively unexplored issue (and a question addressed in Chp. 3) in which the optimal concentrations supplied is unknown especially when half-life and the pharmacokinetics are considered. Further to this, excess NGF has been shown to actually inhibit outgrowth (Conti et al., 1997) indicating that more attention needs to be focused on the quantities of external GF molecules which are used in support of nerve repair. In addition, combinations of GF may also result in adverse effects as seen in the case of BDNF and NT-3 which was seen to inhibit some of the growth promoting effects of NGF in specific subpopulations of neurons (Gavazzi et al., 1999).

1.7.5. Supportive cells

1.7.5.1. Schwann cells

In a natural setting, successful nerve regeneration is dependent heavily on the presence of SC at the distal stump and their supply of endogenous growth factors. This remains true in clinical treatment and as a result NGC have been constructed containing autologous SC. Evidence shows that the contribution of autologous SC (~6cm) effectively double the regenerative capacity over their absence (3cm) (Strauch et al., 2001). Recently, autologous SC incorporated in a sural nerve graft was used in human treatment of a 7.5cm sciatic nerve defect and showed evidence of recovery (Levi et al., 2016). However, the use of SC does have drawbacks in their low abundance, the damage to the source for harvesting and requirements for cell expansion (Lackington et al., 2017). Despite these limitations, SC possess unrivalled regenerative capacity, minimal immunogenic reaction, alongside their intrinsic

contribution and maintenance of the basal lamina and post regeneration myelination which provide solid reasoning for their continued use in constructs and transplants.

Genetically modified SC have been investigated with some success. SC modified to express NCAM may promote neurite migration with the alteration having no apparent effect on myelination after regeneration (Lavdas et al., 2006). SC with artificially increased expression of neurotrophins have also been investigated with upregulation of GDNF mRNA resulting in a better regeneration of sciatic nerve and survival of motor neurons in co-cultures (Li et al., 2006). Conversely, other research has shown that continual overexpression is actually detrimental to innervation overall (Santosa et al., 2013). Combined NGF and BDNF modifications yield effective approach to spinal cord repair with functional recovery increasing in comparison to controls (Feng et al., 2005).

1.7.5.2. The ADSC: a promising alternative

The ADSC is a mesenchymal stem cell (MSC) and has relatively recently been adopted in the field of regenerative medicine (Frese et al., 2016). ADSC provide substantial advantages over MSC from other sources (e.g. bone marrow or placenta (Hass et al., 2011)), they are relatively abundant (ca. 2% ADSC in fat versus 0.0001% of MSC in bone marrow), they are relatively easy to harvest from human adipose tissue, the harvest causes minimal donor morbidity and provide an accessible route for research that is effectively translatable to clinical applications. The regenerative potentials of ADSC have been assessed both in vitro and in vivo (Frese et al., 2016, Mohammadi et al., 2013). Transplantation of undifferentiated ADSC were shown to promote axon regeneration, myelin formation and atrophy to similar standards of SC, with cell population survival continuing for over 4 weeks (Sowa et al., 2016). Another group has suggest that ADSC stimulate faster neurite outgrowth indirectly through promoting SC proliferation at the distal stump however the 14-day culture ultimately showed insufficient amounts of viable cells by PCR (Erba et al., 2010). The interplay between undifferentiated ADSC and SC may be a major aspect in improving repair. Promising results (Xu et al., 2016) found ADSC/ SC co-cultures seeded in silk fibroin/ collagen scaffolds achieved comparable regeneration across a 1 cm gap to that of the autologous nerve graft with little inflammation at the injury site.

1.7.5.3. Differentiated ADSC

As a multipotent stem cell, ADSC are able to differentiate down a vast number of cell lineages including: hepatocytes, osteocytes, adipocytes, neural cells, vascular endothelial cells, osteoblasts, chondrocytes, cardiomyocytes, neural and finally glial cells (Bunnell et al., 2008). The latter being the key lineage for differentiated ADSC applications in peripheral nerve repair. Activation of a SC phenotype (dADSC) is attained through the culture with a growth factor cocktail (Forskolin, FGFb, GGF, PDGF) resulting in a relatively quick shift in phenotype (3 weeks) with rapid expansion potential. dADSC exhibit the distinctive spindle-like morphology, express the glial markers (S100, p75, GFAP) and secrete neurotrophins (NGF, BDNF, GDNF) of native SC (Xie et al., 2017). dADSC and SC were shown to provide similar increases to neurite count and length of motor neurons (Kingham et al., 2007). Further, spontaneous alignment of dADSC occurred when seeded into a tethered collagen construct akin to bands of Büngner which were seen to enhance neurite outgrowth over a 15mm sciatic nerve gap in comparison to the empty scaffold tube (Georgiou et al., 2015).

The most prominent pitfall in the use of dADSC lies in their rapid reversion to the progenitor state upon exclusion of the differentiation factors (Faroni et al., 2016) and therefore posing the requirement of sustained supply of the GF stimulants to the ADSC within the NGC in a clinical setting. There is also the possibility that this may be counteracted by 3-D culturing and the native production of neurotrophic support within the nerve microenvironment.

1.7.5.4. Cellular alignment

Although the choice of cell type is an important consideration in cell/ tissue engineering, the spatial formation of cells is known to play a role in determining their behaviour such as differentiation, ECM remodelling and protein expression. Alignment of cells into strings is one type of morphology, that occurs naturally when populations of cells elongate towards a specific direction in unison. This is essential in order to create the structures that function for various processes in the body such as the formation of the penetrating structures of the vascular system, anisotropic tendon tissue and neuroregenerative guidance by bands of Büngner (Dorta et al., 2018, Gigante et al., 2009, Weiss, 1934), naturally arising from cell-cell interaction,

chemotactic, or haptotactic guidance of anisotropic ECM tissue. Attempts have been made to mimic these alignments artificially through substrate topographies, chemical gradients, anisotropic materials or by placement of the cells. There are numerous fabrication techniques for these approaches involving polymer injection moulding (used for PDMS substrates in Chp. 2), 3-D printing, stereolithography or electrospinning and as a result, some control over cell behaviour has been achieved. An obvious example of this is in axon alignment provided by fibres and microgrooves which promotes neuronal survival and fasciculation ((Yu et al., 2008) and also shown in Chp. 2). Another is in the induced differentiation of BMMSC to tenocytes when aligned within anisotropic collagen scaffolds without the presence of differentiating factor BMP-2 (Kishore et al., 2012). In the case of scaffolds created by the group of James Phillips at UCL: engineered neural tissue (EngNT) (Georgiou et al., 2013), the alignment of SC or dADSC is self-imposed by their contractile behaviour, which remodels the collagen matrix into well-organised aligned fibres, this in turn promoted axon outgrowth and guidance (Georgiou et al., 2015, Georgiou et al., 2013). However, although these approaches instigate cellular orientation, they do not form strings, or bands of connected, aligned cells. For this reason, the spatial placement of cells, as detailed below, is a worthwhile and unique approach.

1.7.5.5. Patterning and alignment with ultrasound

The replication of intricate cellular formations within tissues remains a challenge; however, some progress has been made with strategies such as 3-D bioprinting, which has recently been shown to allow precise 3-D placement of different cells (human embryonic kidney cells and ovine MSCs) although, this was limited to a resolution of ca. 200 μm (Graham et al., 2017). Another method to achieve cell patterning is through optical manipulation; however, this is generally restricted to small cell numbers as energy requirements for higher populations would exceed technological limits and also result in photodamage to cells (Zhang and Liu, 2008). Acoustic manipulation is a non-invasive and high throughput alternative approach which can address these shortcomings, allowing the movement and trapping of thousands of cells, as aggregates or single cells within pre-defined patterns (Ren et al., 2015, Garvin et al., 2013). In Chps. 3 and 4, ultrasound manipulation is carried out using a sonotweezer device. This device functions by generating two oppositely travelling waves which upon interference, create a standing wave pattern, that drives particles

or cells to regions of lowest pressure. This device has been used previously to pattern SC, creating aligned bands that direct DRG neurite outgrowth (Gesellchen et al., 2014). In 3-D settings, acoustic manipulation is capable of levitating and trapping cellular aggregates (Kozuka et al., 2000, Bazou et al., 2008) and has recently been shown to an effective approach to engineering mechanically anisotropic muscle tissue through aligned deposition of myoblasts in a collagen hydrogel (Armstrong et al., 2018). As a result of these applications, sonotweezer devices are emerging as a reliable platform for non-invasive 3-D cell positioning and even tissue construction.

1.8. Improving peripheral nerve repair: a multimodal approach

Despite meaningful advances in treatment strategies to support repair after critical size nerve injury, none have produced a clinically viable rival to the gold-standard; autologous nerve tissue transplant. This suggests that improvements require:

Firstly: a deeper understanding of the neuronal response to individual and combinations of supportive factors such as the shape of the scaffold, growth factors and supportive cell types as well as the underlying neuronal signalling response.

Secondly: the ability to produce scaffolds optimised to offer a microenvironment (structure, adhesion and growth factors) supportive of peripheral nerve repair and regeneration.

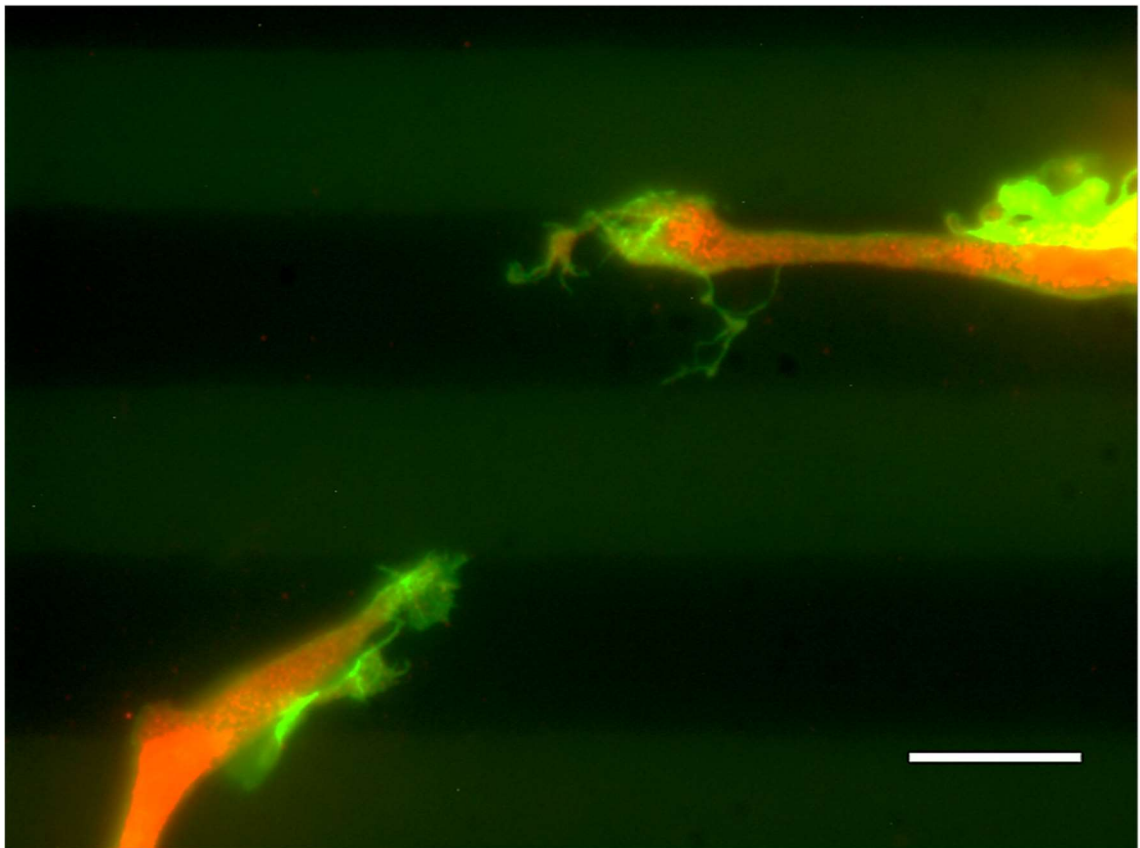
The work presented in this thesis was carried out with the aim to address these questions.

The first hypothesis is that the NGF signalling pathway, which has a wide range of effects, may intersect with the signalling induced by other external factors, here specifically aligned scaffolds or topographic patterns.

The second hypothesis is that NGC may be improved through a more controlled approach to their design. Here I aimed to develop protocols and designs that enabled precise control over all aspects of a scaffold to create artificial bands of Büngner and

a localised GF delivery system by incorporation of aligned NGF-loaded silk fibroin microfibres to the scaffold.

2. Synergistic or Antagonistic: An Investigation into the Interaction Between Topographical and Neurotrophic Growth Factor Signalling in Regenerating Dorsal Root Ganglia.



“Of all the grooves, on all the substrates, you had to go and cross into mine...” The interaction of two opposing growth cones from a DRG explant cultured in 10 ng/ ml NGF, 50 μ M blebbistatin, 12.5 μ m grooves. Green: Actin, Red: Myosin IIA Scale: 12.5 μ m

2.1. Introduction

Peripheral nerve injury is a relatively common occurrence (over 20 million sufferers in US alone (Grinsell and Keating, 2014)) caused by trauma or medical disorders, usually requiring surgery which often leads to unsatisfactory repair (Hirasawa et al., 1976). Despite the potential for fully functional recovery, there are some key occurrences which limit recovery. The first is the extent of damage; an injury comprising completely disrupted axons and neural connective tissues up to and including the perineurium have very low prognosis for recovery, prompting the need to improve scaffold design (refer to section 1.7 for more detail). Another problem lies in low regeneration rates and lack of directed growth, both of which generally lead to the absence of innervated target tissue/ organ, cell death and in combination with neuroma formation arising from scarring; the patient can be expected to experience acute pain, loss of sensation and function. Current efforts have attempted to address these limiting outcomes through employing scaffold micro/ nano-topographies for directional neurite guidance as a means to increase the number of reconnections to the distal stump tissue (Spivey et al., 2012, Hoffman-Kim et al., 2010, Chang et al., 2017). Elevation of the regeneration rates and cell survival have also been sought through the use of neurotrophic growth factors either by direct administration, incorporation into a scaffold for sustained release, or by transplantation of supportive cells which had been engineered to secrete these factors (Pfister et al., 2007, Catrina et al., 2013, Iwan et al., 2018, Dalby, 2005).

Although substrate chemical stimuli and mechanical cues are well known for inducing directed axon growth and elevating extension rates, leading to improvements in neuroregeneration-both clinically and in vitro (section: 1.7); there is some evidence that under certain circumstances they may actually impede regenerative potentials (Gu et al., 2012). Findings by Conti, et al. (1997) show that an excess of growth factor supplied (NGF) reduced the length of DRG axons in comparison to lower concentrations (range: 1-200 ng/ ml) with a maximum outgrowth was obtained when exposed to 10-20 ng/ ml NGF. Other findings implicate the potential for unwanted side-effects of GF supply as increased levels of NGF in serum have been linked mental disorders (Liu et al., 2014) and/ or increased pain (Hirose et al., 2016) which has led to a restriction in their use. These data highlight the need for more research directed

into finding the optimal concentrations at which neurotrophic factors could be of benefit in PNI. Further, there is a gap in the general understanding of the combined effects of topographical cues with differing amounts of trophic support. This may pose the issue that the outcomes may not simply equate to the sum of the parts: a discrepancy which this study aims to address. That topography and drug treatment to support nerve regeneration can interfere with each other has already been put forward by Thomson et al. (2017) who showed that immune suppression of the mTOR receptor Rapamycin, a downstream signalling cascade of PI3k/ Akt, reduces neurite sensitivity to topography which leads on to explain the disparate findings in the literature on the successful use of topographic guidance systems in the literature on the successful use of topographic guidance systems. When the immune system has been suppressed by Rapamycin, regeneration was poorer than through nerve guides with topographic guidance.

In recent work (Déjardin, 2013), a considerable reduction in neurite growth was observed when supplying high concentrations of NGF to DRG explants cultured on microgrooved surfaces. On the flat control, this was reversed with increasing NGF concentrations leading to larger network sizes. These findings suggested a mediation of the NGF signalling pathway through the mechanotransductive effects of the grooved topographies or possibly by axon-axon interactions arising from greater fasciculation on grooves. Further investigation through modification of the substrate stiffness confirmed that both physical characteristics and mechanical properties of the substrate are involved in modulating the NGF response. Higher NGF concentrations were seen to produce greater fasciculation and lower network sizes on stiffer substrates indicating that the observed trend was a result of complex signalling interactions involved with axon cytoskeletal tension. The hypothesis generated to explain this interplay is that the grooved topography forces GC to extend in a unidirectional forward advance which is not promoted on the flat topography. Upon this constricted extension, the cytoskeleton experiences an increase in the tension vector on grooves, whilst remains balanced through multidirectional GC spreading on flat. Overall, akin to mechanotransduction observed in other cell types (Dalby, 2005), it is believed that topographical induced tension differences have a central role in mediating the cytoskeletal dynamics response induced through differing quantities of NGF available.

The connection between axon tension levels in response to NGF concentration is gaining more scrutiny with recent studies investigating NGF induced changes to rates of retrograde flow (Turney et al., 2016, Shin et al., 2014). This places non-muscle-myosin II (hereby referred to as myosin II) as a prominent candidate for the key mediator of this interaction. Myosin II is a molecular motor protein which is largely responsible for tension within the cytoskeleton through actively pulling together two opposing actin filaments. Contraction and the build-up of tension is through a cycle of binding to, conformational shift in the myosin heavy chain and release of the actin filaments, powered by the hydrolysis of adenosine triphosphate (ATP) to adenosine diphosphate (ADP). Mechanical tension builds up as a vector sum over myosin II activity and the actin fibril orientation as a whole. Myosin II has two isoforms which bear significance to growth cone dynamics, myosin IIA and IIB. The former is believed to function to generate the contractile force for retraction through transverse actin bundling whilst the latter modulates axon extension through retrograde flow (Togo and Steinhardt, 2004). It remains unclear whether myosin IIA and IIB are solely exclusive to these roles; however, evidence suggests that it is determined by the ECM substrate (Turney et al., 2016). Our understanding of these details was through myosin II inhibitory studies using blebbistatin alongside myosin IIB knockout studies. Additionally, no studies investigate the impact extracellular guidance cues such as topography on myosin IIA or IIB activity, instead opting to observe NGF concentration modulations in relation to the ECM chemistry. It remains to be elucidated which isoform bears chief responsibility for the observed NGF/ topography interaction. Increased retraction or reduced extension?

The hypothesis was: Will the functionality of a NGC be affected by the modulation of growth factor concentration and substrate physical properties? This is to provide mechanistic insight into synergistic or antagonistic effects that may arise when the microenvironment of regenerating peripheral nerves is modified.

This can be investigated through observing the interaction between two commonly incorporated and well documented elements of a typical NGC: a microgrooved topography to provide alignment and the modulation of the regenerative environment by modulating and optimising the amount of GF delivered. This is tested through observing the outcomes of blocking the hypothesized increase in cytoskeletal tension

at higher NGF concentrations under the influence of grooves using blebbistatin and the quantifying the presence of myosin IIA activity.

The aims for this chapter of the thesis are to address the following questions:

- What is the nature of topography induced signalling in regenerating sensory DRG neurons?
- What is the basis for the interaction of NGF signalling and topography induced signalling?
- Could intracellular tension be the mechanistic link between topography and NGF signalling?

2.2. Materials and methods

2.2.1. PDMS 2-D substrate fabrication

A PDMS 184 polymer solution consisting of a silicon elastomer base (Sylgard® 184 Silicone Elastomer, Dow Corning, UK) mixed with a curing agent in a 9:1 (wt/wt) ratio respectively was added to a plastic cup and thoroughly mixed. Air bubbles arising from dissolved gas during mixing were then removed under vacuum for ~20mins. Flat substrates were created through pouring the PDMS solution onto a petri dish, settling to create a flat surface. Grooved substrates were created by injecting the mixture into a casting chamber containing a microgrooved (12.5µm wide, 5µm depth) SU8 wafer master. Following injection, the PDMS-chamber/ petri dish was cured in an oven for ~2 hours at a temperature of 85°C. The crosslinked PDMS was then removed from the chamber and allowed to cool before being cut into devices. Cutting was done using an 11mm diameter cork borer.

2.2.2. Substrate sterilisation and preparation

Samples were sterilized prior to seeding by immersing them in 70% ethanol for 30 mins followed by 2 washes in PBS and then dried with a flow of 0.22 µm filtered compressed air in a laminar flow cabinet to avoid contamination. Samples of PDMS were treated at for 1 min with air plasma generated using a Harrick Plasma PDC-002

cleaner at 29.6 W. After plasma treatment, the surfaces were coated in PLL solution for 30 mins at 37 °C. Each sample was rinsed 2x in PBS before seeding cells.

2.2.3. Organotypic culturing of DRG explants

For this study, thoracic DRGs were isolated from 1-3-day old neonatal Sprague-Dawley rats. DRG allow for an organotypic approach to studying nerve outgrowth through maintaining the natural ECM environment surrounding the soma of neurons whilst also providing the inclusion of satellite and migratory cells which support axons emanating from the DRG. It can be considered that the DRG offers an ideal 3-D microenvironment and a niche for the neurons. The substrates used here are fundamentally 2-D. The rat pups were euthanised by Euthatal[®] injection (500 mg/ Kg), carried out by an animal house technician in accordance with Home Office regulations followed by dissection and extraction of DRG. Upon extraction, DRG were transferred to an ice-cooled petri dish of nil NGF media and processed to remove excess roots emanating from the DRG body. The DRG were then seeded onto the middle of the prior treaded PDMS devices and grown for periods of up to 10 days, dictated by the experimental parameters. Culture was carried out in cell culture incubators providing a constant 37 °C, 5% CO₂, 100% humidity environment in 240 µl / 15 mm diameter well L15 media (Sigma, UK) supplemented with 10 % FBS, 50µg/ml n-acetyl-cystein, and 1% antibiotic mixture (L-glutamine, penicillin streptomycin and fungizone) (PAA p11-002, UK). NGF 2.5S (Invitrogen, UK) was added to the reach required concentration (2, 10, 50, 100 and 150 ng/ ml). Cultures were split/ fed 1:1 every day. For alternative growth factor cultures, NGF was substituted for either: rhBDNF (20 or 50 ng/ ml) or rrFGF-b (20/ 100 ng/ ml) (ImmunoTools). For inhibitor studies, blebbistatin was employed (Abcam). Blebbistatin was dissolved within the recommended minimal DMSO to form a 100mM stock solution, before addition to DRG culture media to a molar concentration of 50 or 100 µM (final concentration of DMSO was 0.1 or 0.2% respectively). DRG were allowed to attach onto the surfaces for 24 hours before the addition of blebbistatin to provide initial cell adhesion.

2.2.4. Immunostaining

Upon completion of the allotted culture period, DRG were fixed in 4% formaldehyde/PBS solution for 15 min at 37 °C. This was followed by a

permeabilisation stage through application of a buffer (per 100 ml PBS: 10.3g sucrose, 0.292g NaCl, 0.06g MgCl₂, 0.476g HEPES, 0.5% Triton X-100) for 2hrs, incubated at 4°C. This was then removed and blocking solution (1% BSA/PBS) was added at 37°C for 5 min. The blocking solution was then replaced with a 1 % BSA/ PBS containing primary antibodies: β 3-tubulin antibody (1:100, mouse anti-TU-20 Santa Cruz, California) and anti-S100B antibody (1:100 rabbit anti-S100 Abcam, UK). Samples were then incubated at 37°C for 6 hours. A wash step was then carried out involving 3 washes with PBS/ 0.5% Tween20 (Sigma, UK) solution. Following this, samples were then incubated for 2 hours in PBS/BSA solution containing biotinylated anti-mouse secondary antibody (1:50, Vector Laboratories) and Texas Red conjugated anti-rabbit antibody (1:50, Vector Labs). The previous wash step was then repeated. Fluorescein streptavidin (1:50, Vector Labs) in PBS/BSA was then added to the samples and incubated at 4°C for 1 hr before repeating the previous wash step for a third and final time. To image nuclei, a small drop of mounting medium containing DAPI-vectashield (Vector Labs) was dabbed on the surface of the substrate. For growth cone analysis, Myosin IIA was stained using anti-non-muscle-Myosin IIA antibody (1:200, rabbit polyclonal, Abcam) and actin was labelled with Oregon green phalloidin (1:200, ThermoFisher Scientific). All secondary antibodies and stains used were consistently ordered from the same manufacturer, have been previously validated for specificity and reliability on a variety of cell types including neuronal. A table of antibody combinations used is given below.

Samples were viewed on an Olympus BX51 fluorescent microscope using 2.5 (Zeiss, NA 0.15), 5x (Olympus, NA 0.3) and 100x oil immersion (Zeiss NA 1.3) objective lenses. Images were acquired using a high-resolution camera (QImaging, Retiga 2000i), an automated stage movement (Prior Scientific UK) combined with the auto- stitching of mosaic images with Surveyor Viewer software (Objective Imaging).

Target Protein	1 ^y Antibody/ Stain	2 ^y Conjugate/ Stain	3 ^y Conjugate/ Stain
Actin	Oregon Green Phalloidin (Thermo Fisher)	N/A	N/A
β3-Tubulin	Mouse anti-TU-20 (Santa Cruz)	Biotinylated anti-mouse secondary antibody (Vector Labs)	Fluorescein Streptavidin (Vector Labs)
S100 Protein	Rabbit anti-S100 (Abcam)	Texas Red conjugated anti-rabbit antibody (Vector Labs)	N/A
Non-Muscle Myosin IIA	Rabbit anti-non-muscle-Myosin IIA antibody (Abcam)	Texas Red conjugated anti-rabbit antibody (Vector Labs)	N/A
DNA/ Nuclei	DAPI (Vector Labs)	N/A	N/A

Table 1: Table of antibody combinations for immunostaining

2.2.5. Cell viability assay

Relative cell survival of the DRG population was carried out through the use of a Live/Dead™ Cell Imaging Kit (Cat. No: R37601, Invitrogen). This assay was comprised of a dual probe setup (live: calcein-AM, dead: ethidium homodimer-1) in a majority accordance with the Thermo Fisher protocol (L3224). Briefly, vials for each live/ dead probe were thawed and then combined through transference of live: calcein-AM vial contents to the vial containing dead: ethidium homodimer-1. To ensure complete transfer, the live vial was washed through filling with 1 ml of PBS and transference to the dead vial. The combined contents of the live/dead vial were then thoroughly mixed together by shaking to create a 1X stock solution. 50µl of the stock solution was then applied to each substrate and incubated for 10 mins within a cell culture incubator. Cells were imaged immediately, obeying the suggested time limitations of the assay (~2 hours).

2.2.6. Data Analysis

2.2.6.1. Manual size measuring

Composite images of DRG networks were assembled using Adobe Photoshop CS4. Size measurements of DRG networks were carried out using ImageJ-FIJI package (Schindelin et al., 2012) through a manual trace around the outer perimeter. An initial local contrast enhancement with the Contrast limited adaptive histogram equalization (CLAHE) plugin (Zuiderveld, 1994) was performed to identify the maximum amount of axons. In 2 situations, a small section of image was missing; edges were joined in this case from the two nearest points to complete the shape.

2.2.6.2. Image preparation

Prior to analysis with Filament Sensor (Eltzner et al., 2015) and WIS Neuromath (Rishal et al., 2013) software packages, images had to be prepared for maximum quality. This was a necessity to ensure minimal false positives, which could affect validity of the analysis (Figure 12). Preparation was limited solely to the images used for Filament Sensor and Neuromath analysis. These images were not used for intensity measurements. The preparation process was comprised of 3 steps, the first being to remove the “halo effect” of the DRG body fluorescence which results in an extremely high intensity background of the network surrounding these. This was achieved through the gradient brightness adjustment on Adobe Photoshop CamRaw program which allows the selective adjustment the brightest regions (surrounding the DRG). The second step was in the removal of debris which was conservatively limited to the outside of the network, i.e. no changes were made to axons or debris within the perimeter of the network. In the case of directionality analysis/ surface coverage, the DRG body was also completely removed due to its presence resulting in non-existent axonal data and thus skewing results. Finally, the last processing step was with an enhanced local contrast, provided by the CLAHE plugin (previously mentioned). Overall, this preparation step did not alter the actual analysis output but, served to reduce error and resulted in a better representation of the true network, by eliminating inconsistencies between images.

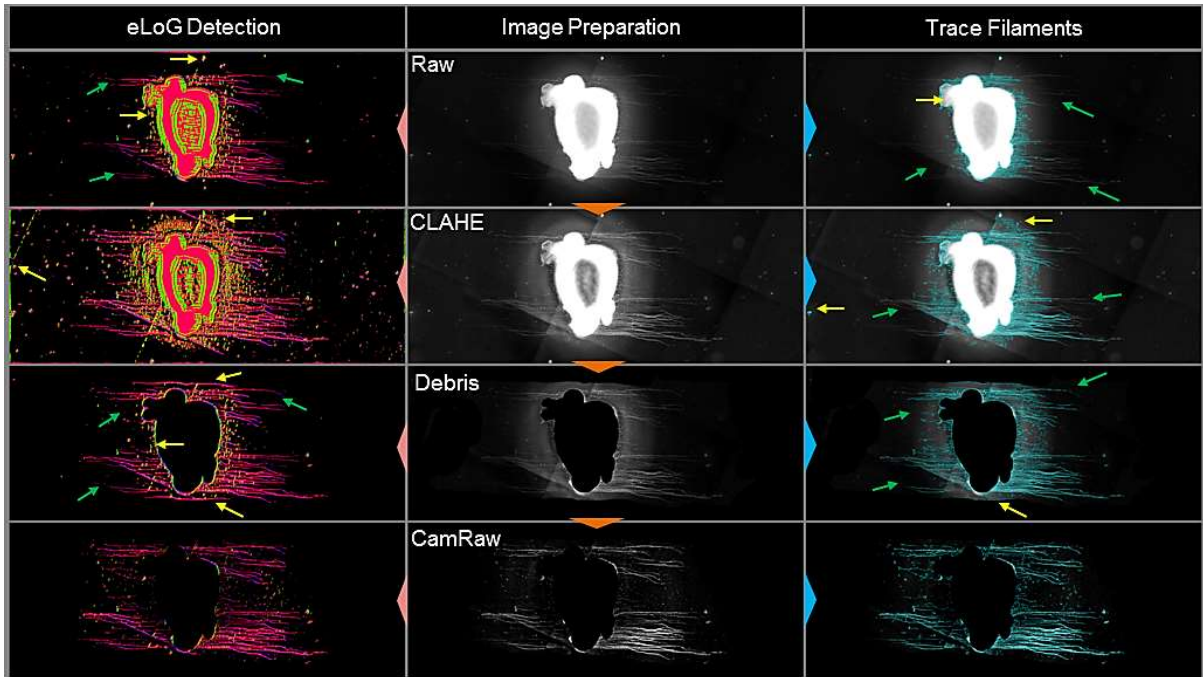


Figure 12: Image preparation for Filament Sensor analysis and comparison of outputs. Preparations of outputs were compared and validated. Each level of adjustment (orange) was performed as described in the running text. As can be seen, each level subsequent adjustments reduced the number of undetected axons (negative error: green arrow) but increase the amount of false positives (positive error: yellow arrows). Only with all adjustments was an accurate neurite detection achieved and by extension the results better represented the actual network structure.

2.2.6.3. Filament Sensor directionality analysis

Images were processed by the Filament Sensor Software (Eltzner et al., 2015) in batches for neurite tracing, network directionality, growth cone orientation and surface coverage measurements. For network directionality, images were first calibrated by rotation such that the grooved axis was in line with the image horizontal and in the case of flat, along the longest Ferret diameter of the DRG body. The “trace filaments” command was used under automatically detected/ default settings to produce the histographic output.

Growth cone orientation analysis began with a rotation calibration to ensure images of a GC were pointing in a specific direction (Figure 13). This was carried out through the midway point of the “neck” of the growth cone i.e. half of the angle between each side of the growth cone. This ensured that analysis was performed on the protrusion direction and growth cone shape, not whether the growth cone had simply turned or held course previously. The high degree of variation in GC shape and morphology made the comparison of the initial histograms difficult. To address this,

histograms were reduced from 18 to 3 bins for simplicity (Left: 0-60°, Straight: 70-100°, Right: 110-180°), providing the ability for comparison on the overall GC shape, and protrusion direction. For comparison purposes (Figure 33 and Figure 34), GC were classified to be actively protruding straight if the percentage of pixels in the straight bin was greater than 40%. Turning was determined if either a: the left or right bin was greater than 40% or b: the straight bin was lower than 40% combined with a left/right difference of over 5%. If the latter showed less than a 5% difference, the GC was deemed to be spreading.

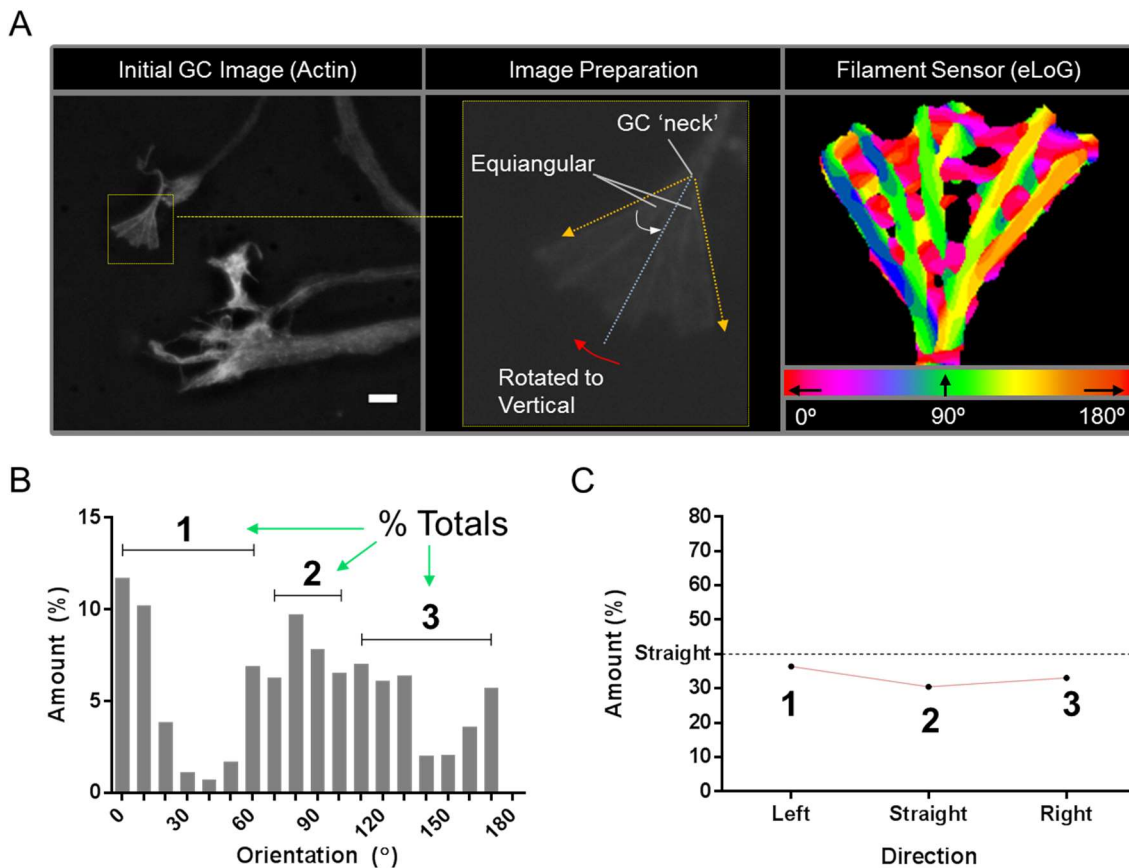


Figure 13: Schematic breakdown of GC directionality analysis methodology. Detailed images of the GC actin cytoskeleton were obtained (A: left) through a phalloidin stain followed by fluorescent microscopy at high magnification (x100). The GC image was then cropped to remove any irrelevant network not related and rotated to vertical axis through measurement of the midway angle between the angles of the ‘neck’ of the GC body (A: middle). This served to normalise the GC direction across all groups for Filament Sensor analysis (eLoG), with image output (A: right) and corresponding colour legend. The resultant histogram of the GC (B) bin count was then reduced to 3 groups comprising their total amount (%) (1: ‘Left’, $\leq 60^\circ$, 2: ‘Straight’, $>60^\circ$ and $<110^\circ$, and 3: ‘Right’, $\geq 110^\circ$) and put into a graph to reduce complexity and allow comparisons (C). From this direction graph, a simplistic insight GC directional morphology could be viewed, and the GC behaviour was deemed to be turning, straight or spreading based upon the ratios (amount (%)) between 1, 2 and 3 (described in detail within the running text). Scale: 5 μm

Complexity analysis, a method commonly employed to assess leaf morphology (Niinemets et al., 2006), was carried out on GC eLoG images. By FIJI ROI selection and measurement of the perimeter and area, the complexity of the circumference was calculated from the perimeter: area ratio.

For network surface coverage analysis, the Filament Sensor eLoG detection command was used again however, in this case on the whole network. The resulting eLoG image consisted of a very accurate tracing of the network with the same resolution as the initial image. This was then thresholded followed by the ROI selector command in Fiji, which was then measured to find the surface area that is covered by axons make for each substrate.

2.2.6.4. WIS Neuromath neurite count/ branch analysis

Counting the number of neurites was achieved with the WIS Neuromath software package (Rishal et al., 2013). In this, each image was manually assigned a mask encompassing the DRG which functions to provide the distance surrounding at which to begin the measurement count (100 μm around DRG). Neurite branch analysis was completed simultaneously, in which counts were carried out at pre-designated distances inside/ outside the mask (Number of in/out offsets: 3, distance between each offset: 5 μm). For neurite counting, the average count across all offsets was used. For branching/ fasciculation analysis; the averages of the 2 innermost offsets and always with reference to the images, the 2 outermost were calculated and the difference between the two determined whether axons were fasciculating or branching.

2.2.6.5. Cell viability analysis

As the soma of neurons remained within the housing of the DRG body, performing a simple count of living vs dead cells was not realistic. Instead, the integrated density of fluorescence of the DRG body was measured between live/ dead and combined in a ratio to give a relative idea of cell survival akin to the methodology used by (McCloy et al., 2014). This was carried out based on the assurance of assay quality controlled by which both probes produce the similar intensities for each emission for identical exposure settings. Further, this analysis is aimed at as a means to compare between

sample sets exclusive to this study. To further ensure reliability through normalisation, a background subtraction was performed for each image channel. This involved measuring the mean grey value at the same points between each channel, at 4 different points in the image. These values were then averaged and multiplied by the surface area of the measured DRG body, and finally subtracted from the integrated density to give the corrected total cell fluorescence value (CTCF). This was then presented as a percentage of the live: dead ratio.

2.2.6.6. GC measurements and myosin IIA intensity analysis

Myosin IIA intensity measurements within the GC (longitudinal and lateral) was carried out on raw images with Fiji, using the surface density plot command. Longitude measurements began from the proximal edge, through the GC and continuing out onto the substrate (~10 µm) whilst lateral went perpendicular to the GC with substrate either side (~10 µm). From the actin and myosin IIA plot profile, a baseline created for each, from the average of the substrate grey value at the same distance for both. Actin-myosin IIA distance difference (Figure 29) was then calculated from the beginning of the longitudinal peak. Intensity difference was calculated by subtracting the max peak height (actin- myosin IIA) of the latitudal plot.

Analysis of myosin IIA intensity at different regions in the GC (Figure 30 and Figure 31) was carried out via the FIJI plugin Filopodyan (Urbančič et al., 2017). Prior to this, a CLAHE enhancement was performed only on the actin channel (which was not being measured). This ensured the greatest amount of protrusion detected. The thresholding setting was kept in the Huang mode, with other settings for filopodia detection adjusted for each sample. Filopodia measures the mean grey value within each region whilst automatically creating a background subtraction from the surrounding region values. This software used the perimeter to measure filaments size and taking GC complexity into account, this serves as a proxy for the relative size/ shape of GC.

2.2.6.7. Statistical analysis

Graph creation and statistical analysis was performed using GraphPad Prism version 6 (GraphPad Software) by Two-way ANOVA with a Tukey post-hoc test for multiple

comparisons. Comparisons were made by the basis that each culture as a whole was an independent condition regardless of its constituents, with grooved and flat topographies nested within each culture condition i.e. column factor dictates culture condition across a particular topography whilst the row factor dictates between topographies. Results were gained from a minimum of 3 explants each from a different rat. Statistical significance was determined by $p < 0.05$, and presented by * $p < 0.05$, ** $p < 0.01$ and *** $p < 0.001$, all data is shown as well as the average (bar graph) and the standard deviation indicated by bars.

2.3. Results

2.3.1. The interaction between topography induced signalling and NGF signalling

2.3.1.1. DRG outgrowth on grooved and flat topographies at varied NGF concentrations

To address the questions about the nature of topography induced signalling in regenerating sensory DRG neurons and how this interacts with NGF signalling, one aspect of an earlier study was repeated. This was to ascertain whether the trend observed in this previous research was replicable and if DRG explant growths and responses were consistent across two independent studies undertaken years apart. In extension, a wider spectrum of NGF concentrations was investigated whilst restricting any variation in PDMS substrate stiffness or grooves width. The results of this initial study (Figure 14 and Figure 15) showed that the trend remained intact with respect to both axon morphology and outgrowth measurements. As expected, microgrooves were seen to cause a rectangular network with much greater directional outgrowth than those flat, which were radial and considerably more randomly orientated. Also, high NGF concentrations promoted higher surface areas on the flat control contrary to lower NGF concentrations which promoted higher length on grooved surfaces. Further to this, nil NGF provided similar (insignificant, higher average) network lengths as that of the highest NGF concentrations. The most ordered growth was seen with 10

ng/ ml NGF with an individualistic character whilst increasing NGF concentration gave rise to less ordered outgrowth with more heavily bundled, fasciculated morphologies.

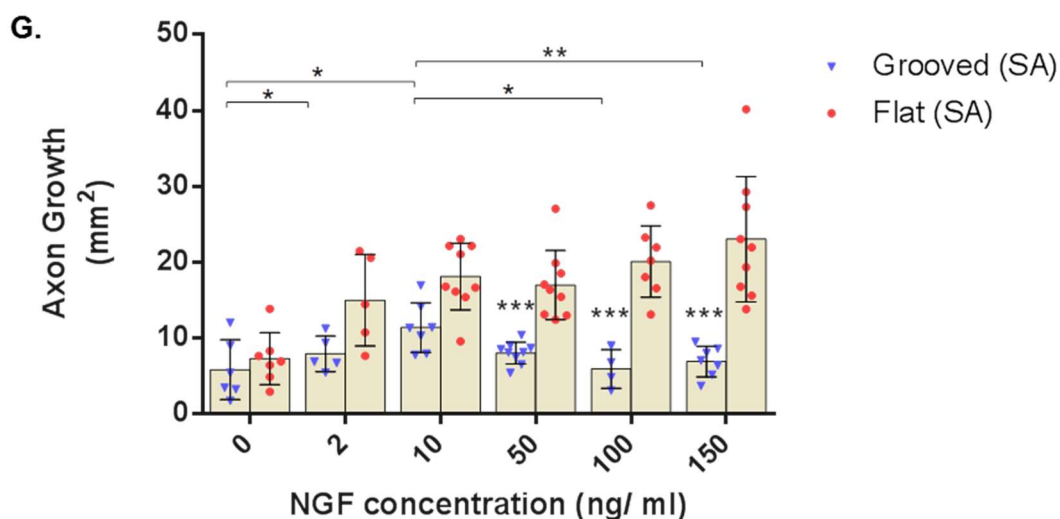
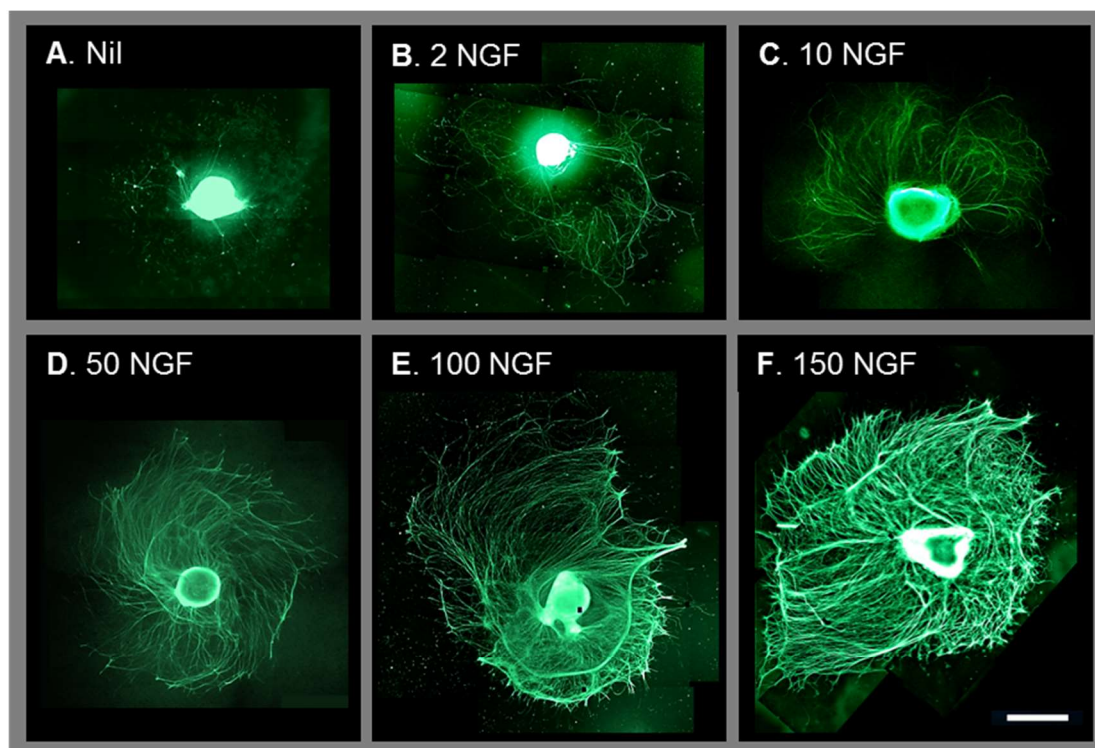


Figure 14: Surface area analysis of DRG networks cultured on PDMS with both flat and microgrooved topographies at increasing NGF concentrations for 10 days. Axons were immunolabelled using β 3-tubulin antibody and networks were measured manually via tracing the outer perimeter of the network. Images show flat networks at each concentration (A-F) and a graph for comparison (G). Surface area steadily increased with NGF concentration however, on grooves an optimal concentration of 10 ng/ ml yielded the largest network area. There was a large difference in surface area between grooved and flat which increases with deviation from 10 ng/ ml. These results conform to the predisposed trend. Greater NGF concentrations also resulted in greater; neurite count, fasciculation and network densities. Stars indicate significant differences between concentrations or topographies (stars above grooved). Significance was determined by two-way ANOVA with a Tukey post hoc test * $p < 0.05$, ** $p < 0.01$ and *** $p < 0.001$ where $n \geq 4$ biological repeats. The bars indicate standard deviation. Scale: 1mm

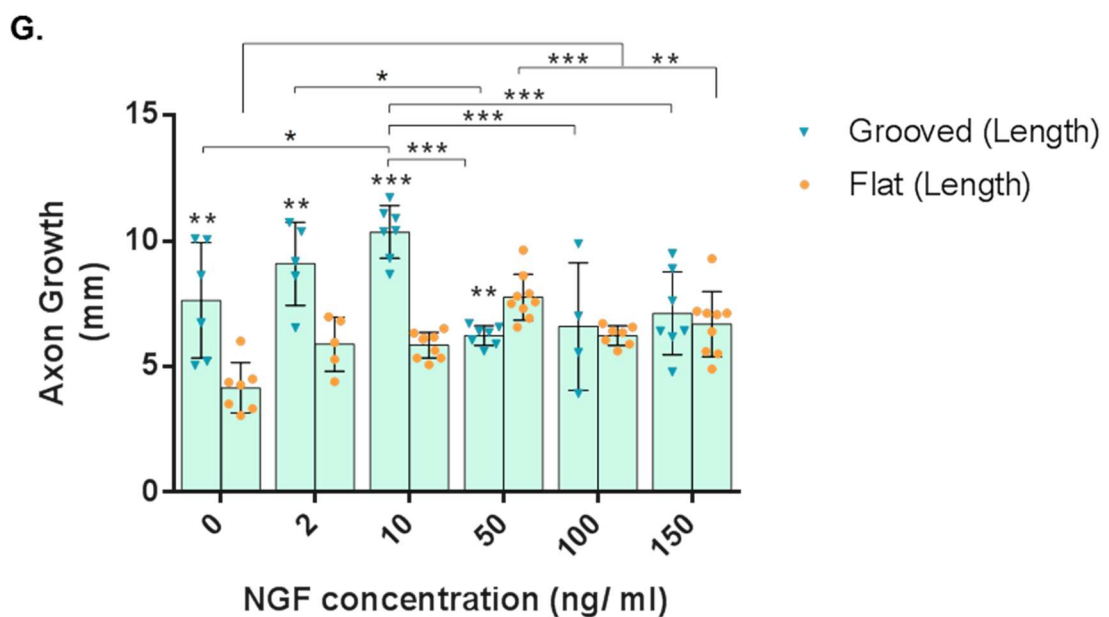
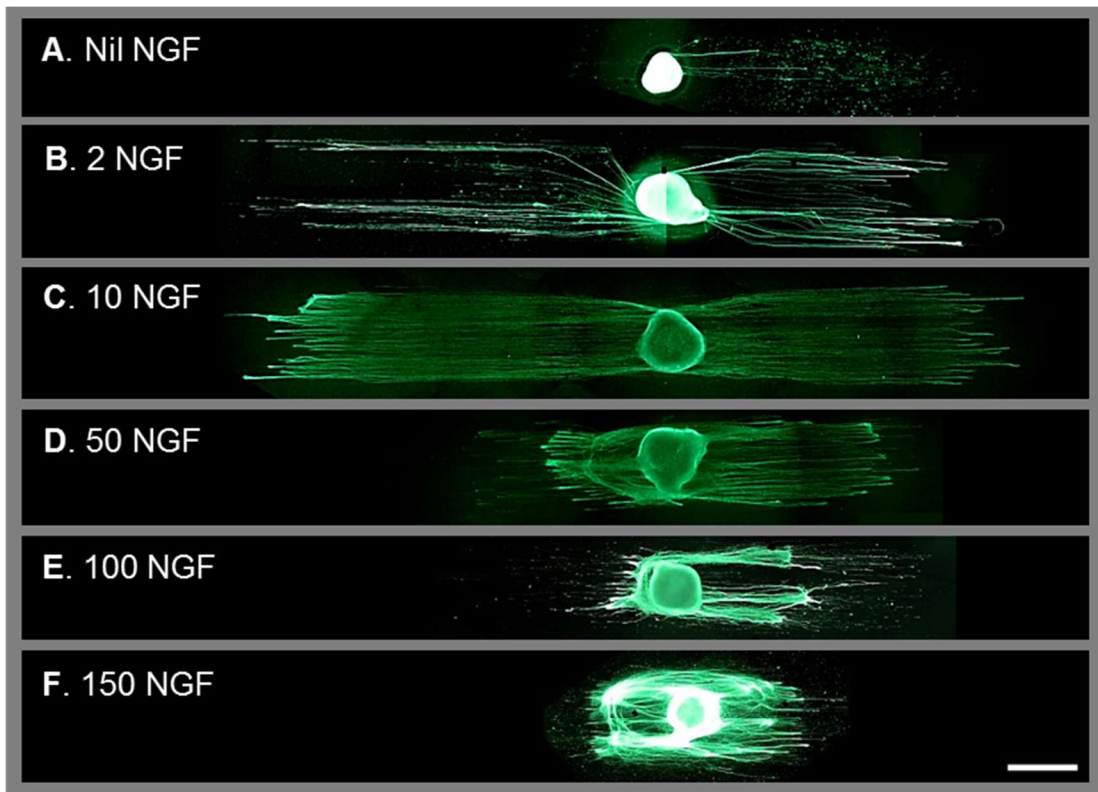


Figure 15: Network length analysis of DRG networks cultured on both flat and microgrooved topographies at increasing NGF concentrations for 10 days. Axons were immunolabelled using $\beta 3$ -tubulin antibody and networks were measured manually via tracing the outer perimeter of the network of which the Ferrets diameter was attained. Images show $12.5\mu\text{m}$ networks at each concentration (A-F) and a graph for comparison (G). Network length showed a significant decrease with on concentrations other than 10 ng/ ml whilst on flat, a general increase was apparent with higher concentrations. There was a large difference in length between grooved and flat at lower concentrations only but not at the highest concentrations. These results conform to the predisposed trend. Greater NGF concentrations also resulted in extremely different morphologies with extensive axon bundling contrasting the ordered networks of the lower concentrations. Stars indicate significant differences between concentrations or topographies (stars above grooved). Significance was determined by two-way ANOVA with a Tukey post hoc test $*p < 0.05$, $**p < 0.01$ and $***p < 0.001$ where $n \geq 4$ biological repeats. The bars indicate standard deviation. Scale: 1mm

2.3.1.2. Investigating other growth factors

The question arises if the interaction between topography induced signalling and growth factor signalling is unique to NGF therefore, it was investigated if the presence or absence of a grooved substrate influenced the efficacy of other neurotrophic growth factors. An initial test (n=2 biological repeats) was carried out on a selection of growth factors (FGF-a/b, BDNF, SDF1- α), chosen on the basis for their signalling pathways overlapping (BDNF) with or being different to that of NGF. BDNF and FGF-b were selected for further investigation based on their showing a difference in regenerative outgrowths comparing DRG grown on grooved or flat substrates (Figure 16). The selected 'low' and 'high' concentrations for each GF (FGF-b (Kelly et al., 2003, Goldshmit et al., 2012) and BDNF (Ji et al., 2010)) was based upon their effective working concentrations and use in previous studies and their respective use in previous studies. BDNF promoted branched morphologies with lower network sizes in comparison to nil GF controls regardless of topography. FGF-b was seen to result in very high network lengths on grooves and large network areas on flat substrates in comparison to nil GF controls, reaching similar sizes to that seen with optimal NGF concentrations. However, a lower number of neurites was observed when compared to NGF cultures. No significant difference was observed between concentrations of either BDNF or FGF-b indicating that the observed trend is resultant of NGF signalling.

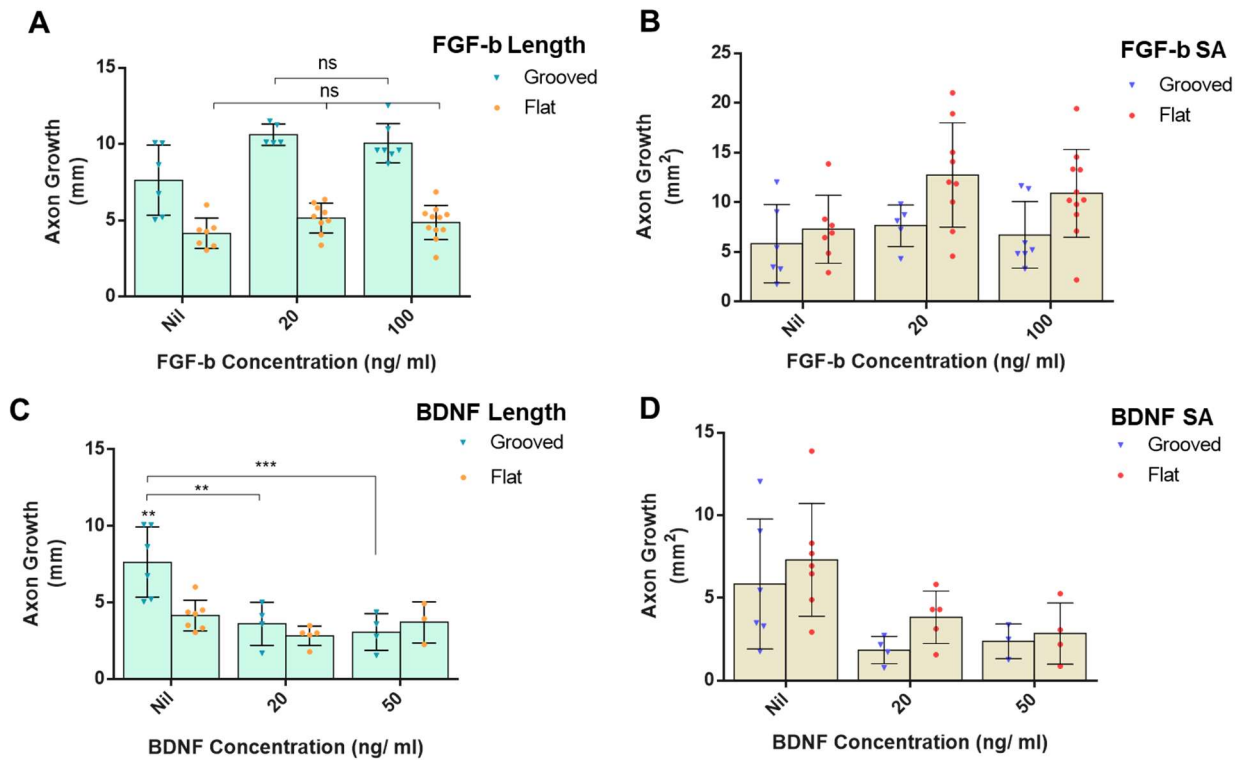


Figure 16: Investigation into topographical interactions with alternative neurotrophic growth factors: FGF-b and BDNF. FGF-b Network length and surface area (A, B) were found to be extremely high with no apparent differences between parameters indicating no apparent trend. Alongside this, a decrease in neurite numbers was observed resulting in very low network densities. BDNF showed low levels of outgrowth on both length and surface area (C, D) and no significant difference between each concentration and thus no conformity to the NGF- topography trend. In addition to these GFs, SDF-1a and FGF-a were also examined however the limited quantity of reagents restricted these to two biological repeats which indicated no trend adherence and were ultimately discounted for further study. Stars indicate significant differences between concentrations or topographies (stars above grooved). Significance was determined by two-way ANOVA with a Tukey post hoc test * $p < 0.05$, ** $p < 0.01$ and *** $p < 0.001$ where $n \geq (5: \text{FGF-b}, 3: \text{BDNF})$ biological repeats. The bars indicate standard deviation. Scale: 1mm

2.3.1.3. A time-course study

To determine the timeframe at which the interaction began to take effect, a time-course study was undertaken comparing two GF concentrations that lead to significantly different networks on grooved and flat substrates, 10 and 100 ng/ ml NGF (Figure 17). These concentrations were selected due to their significant difference in dimensions as well as morphologies as evident from the 10 day cultures (Figure 14 and Figure 15). The largest increase was found from 2 to 4-days with the trend becoming visible at 6-days.

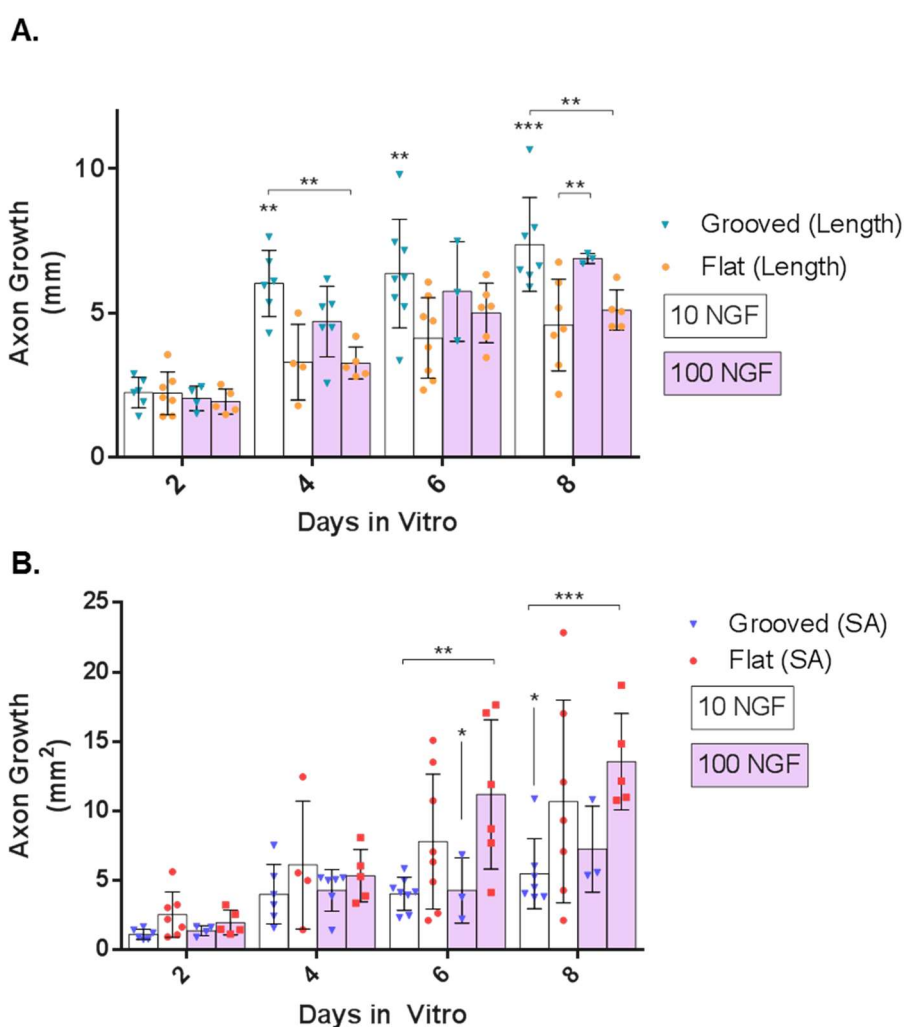


Figure 17: A time-course study of the outgrowth of DRG explants cultured with 10/ 100 ng/ ml NGF on both flat and grooved topographies. Both the length (A) and surface area (B) of all axon outgrowths showed a general increased with time. The trend appears to begin at 4 to 6-days, at which length on grooves and surface area on flat show differences between each NGF concentration. Significance was determined by two-way ANOVA with a Tukey post hoc test * $p < 0.05$, ** $p < 0.01$ and *** $p < 0.001$ where $n \geq 3$ biological repeats. The bars indicate standard deviation.

2.3.1.4. Axon network morphology analysis

The Filament Sensor eLoG tracer tool was used to further quantify the morphological nature of axon networks at differing NGF concentrations/ topographies. This allowed the measurement of the areas that axons actually covered the surface and so can provide a way in which to measure the axon density (Figure 18). Surface coverage was seen to exhibit the trend as NGF increased; coverage decreased on grooves but increased on flat. Density was seen to increase on both topographies with increasing NGF concentration. This analysis also served as a means to cross validate the manual measurements of axon networks carried out previously.

A significant correlation between lengths of outgrowth on grooves and network density was found (Figure 18) in which increasing NGF concentration showed shorter lengths and greater network densities. On closer examination between 10 and 100 ng/ml NGF, samples which exhibited shorter lengths was relatively proportional to greater network density at 100 ng/ml however this trend was not visible at 10 ng/ml.

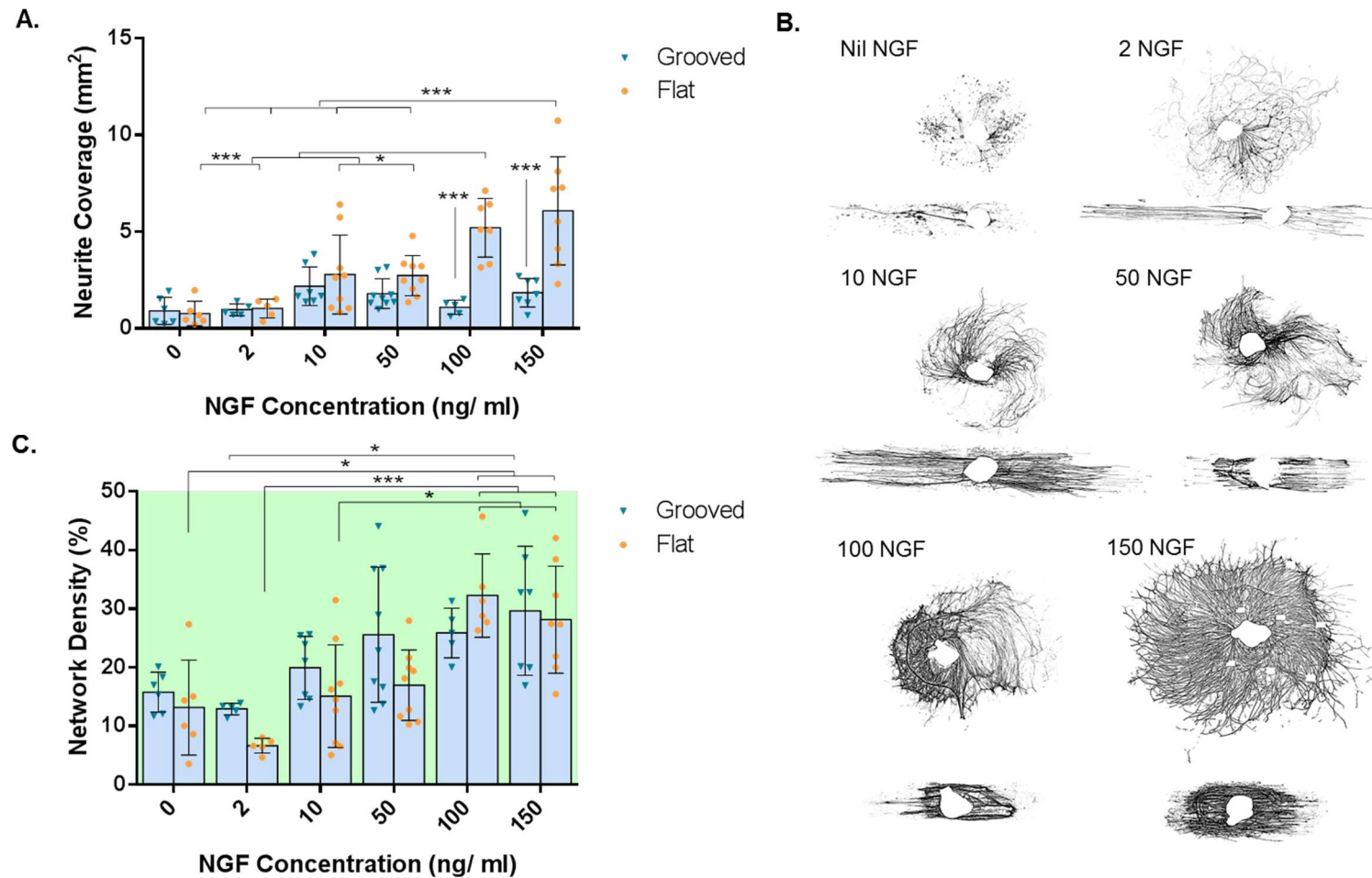


Figure 18: Axon surface coverage and network density of 10-day DRG cultures with increasing NGF concentration on grooved and flat substrates. Neurites were measured using Filament Sensor eLoG tracing tool and FIJI ROI threshold/ selection (B). Neurite Coverage (A) was in line with manual outer perimeter measurements with flat increasing significantly with higher concentrations; however, on grooves the decrease was less prominent. The network density (manual perimeter- network coverage) showed a significant increase in density with increasing concentration on flat and grooves to a lesser extent. Overall, on flat larger coverage was seen in combination with higher density whilst this was reversed on grooves. This can be visualised clearly from the eLoG trace images (B). Significance was determined by two-way ANOVA with a Tukey post hoc test * $p < 0.05$, ** $p < 0.01$ and *** $P < 0.001$ where $n \geq 5$ biological repeats. The bars indicate standard deviation.

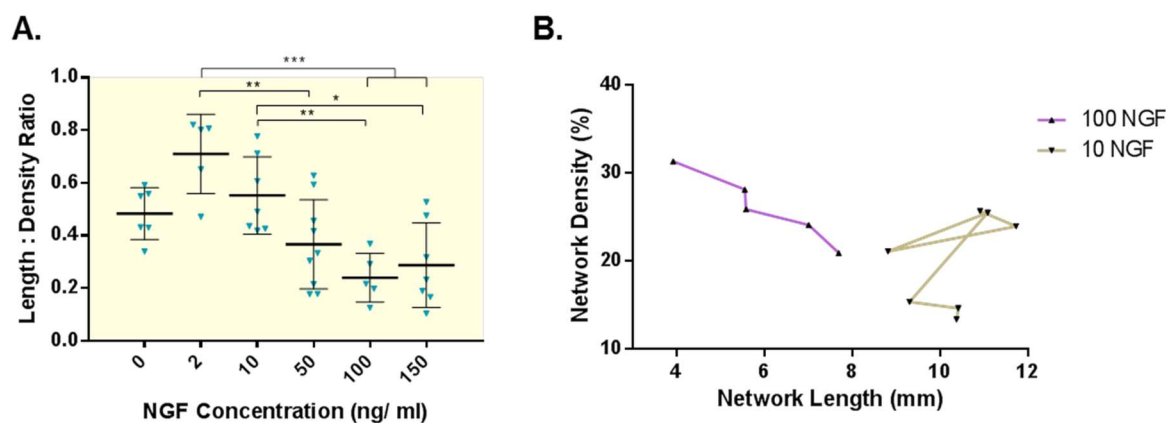


Figure 19: Investigation into the relationship between network length and density with increasing NGF concentration on microgrooves. Across all concentrations, a trend can be seen clearly with a significant decrease in length: density ratio as NGF concentration increases towards 100 ng/ ml following which the ratio reaches a plateau. A more detailed look at each explant network of 10 and 100 ng/ ml showed directly that a greater network density resulted in poorer overall network lengths on the higher whereas on the lower: no correlation was apparent. Significance was determined by one-way ANOVA with a Tukey post hoc test * $p < 0.05$, ** $p < 0.01$ and *** $P < 0.001$ where $n \geq 5$ biological repeats. The bars indicate standard deviation.

2.3.2. Myosin IIA inhibitory studies

The original hypothesis was based upon the theory that grooved substrates induced an increase in axon tension as the mediator of NGF induced outgrowth. For this reasoning, myosin II (responsible for actin contractility) was appointed as the target for inhibition. Blebbistatin; proven to be a highly selective inhibitor of myosin II whilst maintaining the least possible effect on cell adhesiveness, or alternative pathways (Kovacs et al., 2004) was employed. Despite this, there are known issues inherent to the use of blebbistatin which should be considered such as phototoxicity and photoinactivation (Kolega, 2004). Mechanistically, blebbistatin achieves inhibition through binding to myosin II in a fashion which renders the release the adenosine diphosphate and phosphate unfavourable and results in the inability to perform the conformation change for actin contraction. To reduce possible adhesion issues, blebbistatin was added after one day of culture.

2.3.2.1. Blebbistatin inhibition of 10 and 100 ng/ ml on both topographies for 4 and 6-day culture periods

Based on findings of the time series study (Figure 17), 4 and 6-day DRG culture periods were selected as culture timeframes for blebbistatin inhibition studies, although the former to a lesser extent. It was also feared that longer cultures would lead to more adhesion and toxicity issues. Within 6-day cultures (Figure 20 and Figure 21), the application of blebbistatin led to an increase in outgrowth, which occurred across all NGF concentrations/ topographies. In particular, the largest increase was seen at the high NGF concentration on grooves effectively normalising the length of outgrowth between 10 and 100 ng/ ml to the level of flat controls. At high concentrations of blebbistatin, a loss of adhesion was observed (visualised in eLoG trace, Figure 25). This was coupled with a drastic change in the network morphology which exhibited more individual axon growths with very little fasciculation. Another occurrence was the reduction of topographical sensing as axons began to deviate from the direction provided by the grooves. Finally, blebbistatin also caused numerous nodes along the axon (Figure 20: H), which showed intense myosin IIA aggregation, providing further evidence that successful inhibition was achieved (Gallo, 2006). In contrast, at the earlier timepoint, as seen in the 4-day cultures (Figure 22 and Figure 25), blebbistatin had no apparent effect on measured outgrowth other than a slight decrease at 100 μ M (most likely arising from adhesion issues).

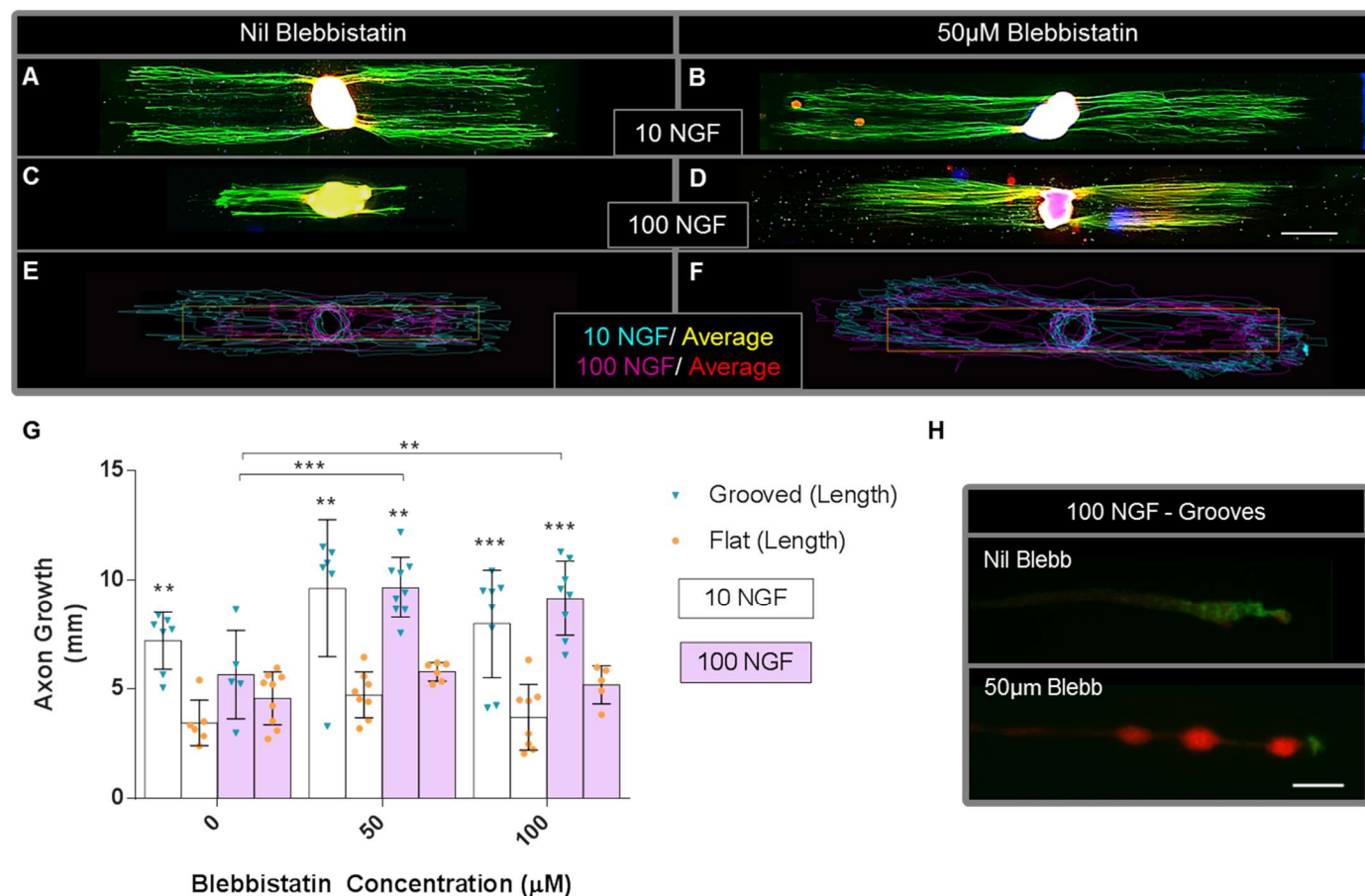


Figure 20: Analysis of network lengths of 6-day DRG explants at differing NGF and blebbistatin concentrations on grooved and flat surfaces. Network morphologies without (A: 10 NGF, C: 100 NGF) and with blebbistatin present (D: 10 NGF, F: 100 NGF) were imaged with immunolabeling of β 3-tubulin (green), S100 (Red) and nuclei (blue) revealing an average increase in length with blebbistatin, effectively normalising the growth between each NGF concentration. Reduced fasciculation and loss of substrate sensing was observed as neurites showed a greater degree of groove-crossing. A visualisation of the manual tracing outputs of each culture is depicted (Nil Blebb: E, 50 μ M Blebb F) shows the overall variation between NGF levels and the growth promoting effect of blebbistatin on grooves. A comparison of network lengths (G) showed that blebbistatin significantly increased the growth on grooves at 100 NGF whilst there was a minor change to the lengths on flat. At the highest blebbistatin concentration there was a high loss of adhesion giving lower outgrowth measurements. Closer inspection of axons (x100 obj) fluorescent images (H green: Actin, red: myosin IIA) blebbistatin also had the effect of forming numerous myosin IIA aggregate structures residing along the axon. Significance was determined by two-way ANOVA with a Tukey post hoc test * $p < 0.05$, ** $p < 0.01$ and *** $p < 0.001$ where $n \geq 5$ biological repeats. The bars indicate standard deviation. Scales: A-D: 1mm, H: 10 μ m

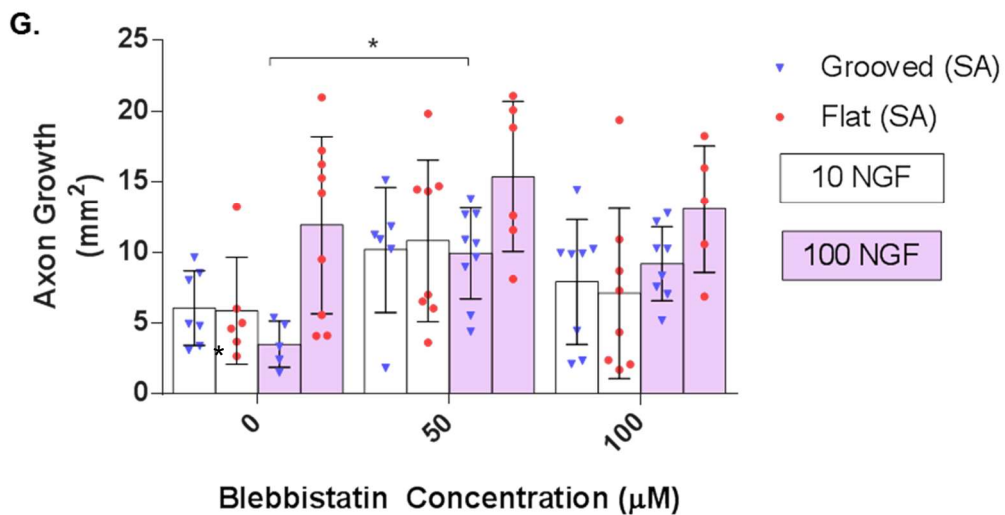
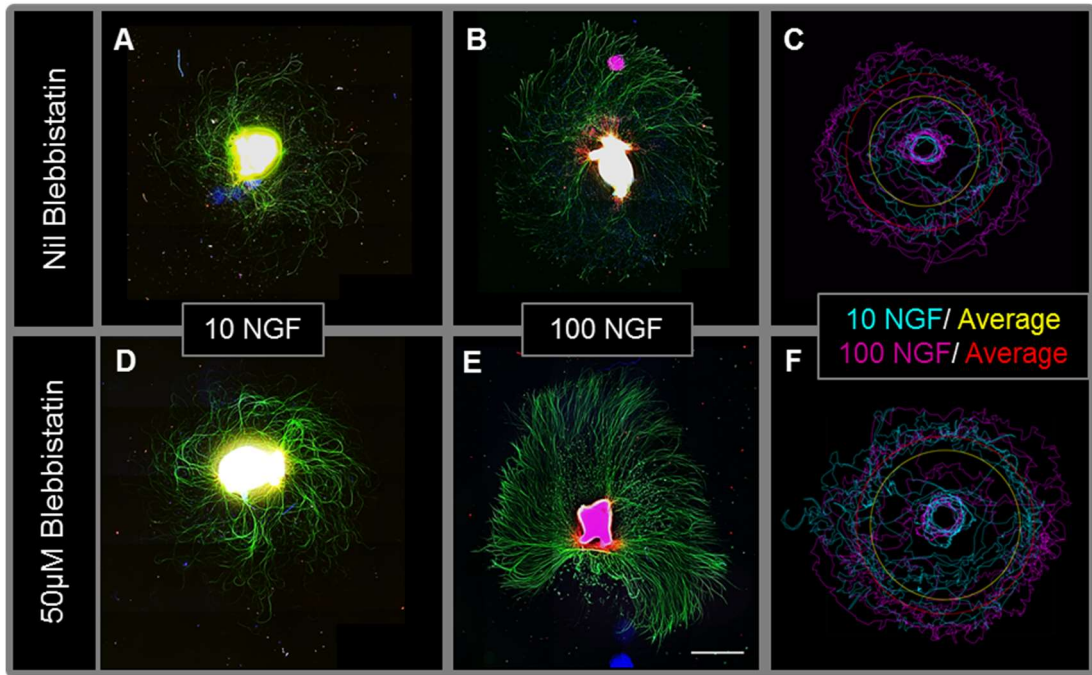


Figure 21: Analysis of network surface area of 6-day DRG explants at differing NGF and blebbistatin concentrations on grooved and flat surfaces. Network morphologies without (A: 10 NGF, B: 100 NGF) and with blebbistatin present (D: 10 NGF, E: 100 NGF) were imaged with immunolabelling of β 3-tubulin (green), S100 (Red) and nuclei (blue) and manually measured. On application of blebbistatin, the surface area was seen to increase however this remained proportionate with lower NGF concentration providing smaller network areas on average. Similar to grooves, reduced fasciculation with finer, individualistic growth of axons. A visualisation of the manual tracing outputs of each culture is depicted (C: Nil Blebb, F: 50 μ M Blebb) shows the overall variation between NGF levels and the growth promoting effect of blebbistatin on grooves. A comparison of surface areas (G) showed that blebbistatin significantly increased the growth on grooves at 100 NGF and all other cultures however due to high variance in surface areas, significance could not be achieved. The highest blebbistatin concentration was accompanied with a high loss of adhesion giving lower outgrowth measurements. Stars indicate significance between groups, above grooved dataset show significance between topographies for that concentration. Significance was determined by two-way ANOVA with a Tukey post hoc test * $p < 0.05$, ** $p < 0.01$ and *** $P < 0.001$ where $n \geq 5$ biological repeats. The bars indicate standard deviation. Scale: 1mm

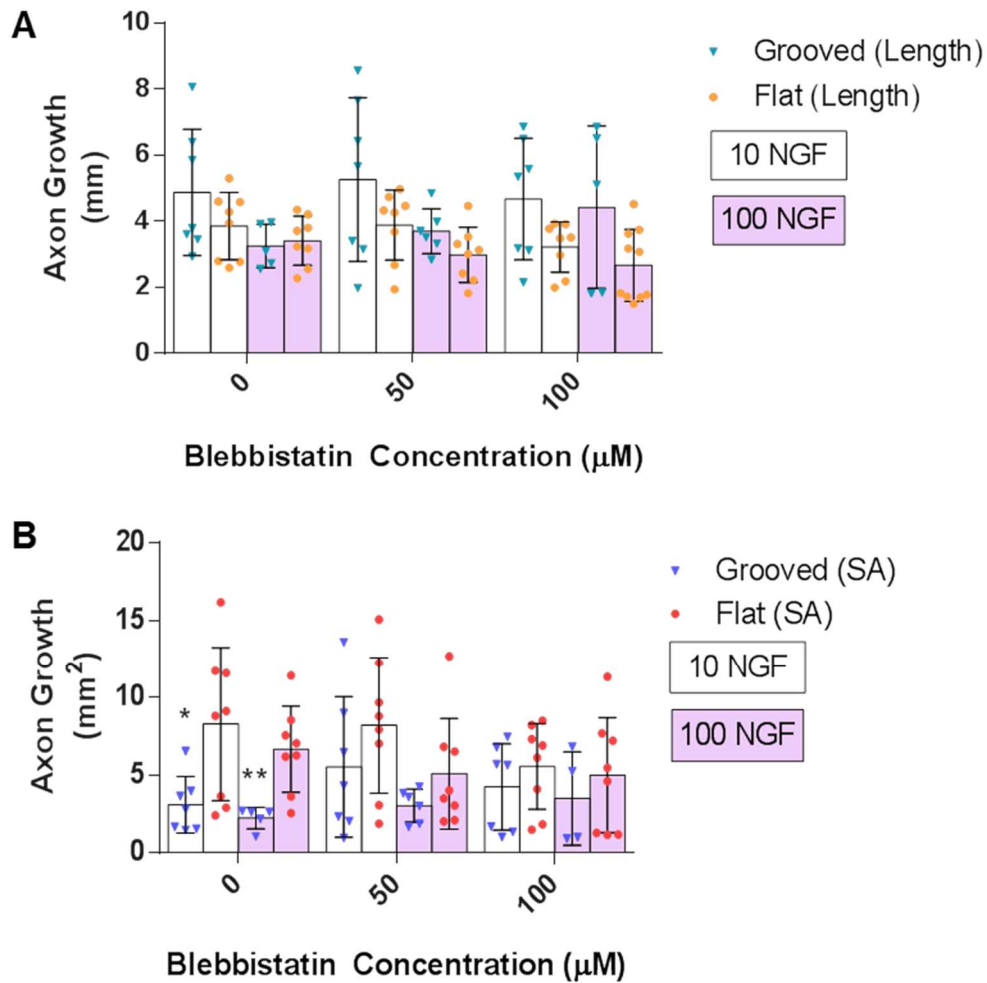


Figure 22: Network analysis of 4-day DRG cultures with varying NGF/ blebbistatin concentrations and topographies. Network length (A) and surface area (B) were measured manually for comparison. Difficulties arose imaging cultures of lower days in vitro as photo-bleaching from the DRG body encompassed the relatively small, thin calibre axon networks and the lower neurite counts leading to a larger sample variation. In spite of this, it can be seen that blebbistatin has very little effect on axon growth which is a stark contrast to that of 6-day. On top of this, adherence to the trend appears to be in the initial stages where the on grooves, the lower NGF concentration had a greater growth however on flat, outgrowths were similar. Stars indicate significance between groups, above grooved dataset show significance between topographies for that concentration. Significance was determined by two-way ANOVA with a Tukey post hoc test * $p < 0.05$, ** $p < 0.01$ and *** $P < 0.001$ where $n \geq 5$ biological repeats. The bars indicate standard deviation.

2.3.2.2. DMSO vehicle controls

As DMSO was used as a vehicle for the blebbistatin application and is a known to have cytotoxic effects at higher concentration (Zhang et al., 2017), a control experiment was carried out to assess the potential adversities on DRG outgrowth. This investigation was carried out in parallel to the experiments in this section by Kseno Bondarenko under supervision of Dr. Suzanne Thomson and was utilized as a means to

minimize the amount animals required. No adverse effects on DRG outgrow or support cell migration/ survival was found to occur through using 0.5% DMSO media, 2 to 5 times greater than the blebbistatin experiments used in this section (0.2/ 0.1% DMSO). This is also consistent with literature stating that cytotoxicity requires a minimum of 1% DMSO in culture (Penazzi et al., 2017).

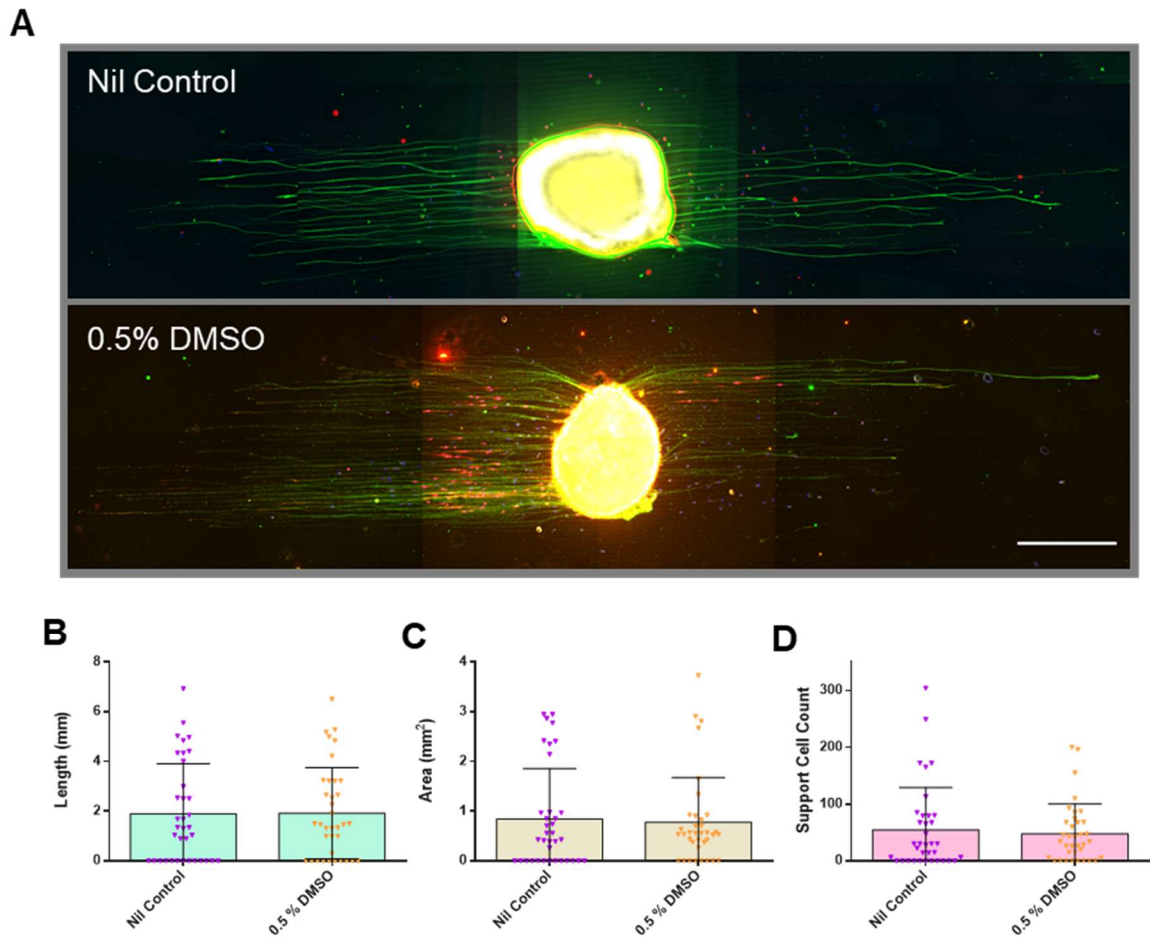


Figure 23: DMSO vehicle control experiment to assess potential cytotoxicity. Image-set A shows fluorescent labelled (Green: B3-tubulin (axons), red: S100 protein (Schwann cells) and blue: DAPI (nuclei)) DRG cultured within 10 ng/ml NGF-DRG media on microgrooves over 5 days. Analysis no significant (B, C) or visible difference to network sizes of cultures supplied in absence (purple data points) versus with DMSO to a concentration of 0.5% (orange data points). The populations of support cells (D) were also unaffected by DMSO. Significance was assessed through an unpaired, two-tailed Student's *t*-test with Welch's correction. No significant difference observed across all variants, bars indicate standard deviation. Experiments were carried out across 4-5 independent biological repeats. Scale: 500 μ m

2.3.2.3. Network directionality analysis of DRG cultured in blebbistatin

To quantify the effect blebbistatin had on substrate sensing, directionality analysis of the axon network was carried out. For this, the Filament Sensor software: “trace filaments” tool was used (Figure 24). In comparing 10 and 100 ng/ ml NGF on grooves without inhibition, average axon direction was found to be in line with the direction of the grooves (90°); however, at 100 ng/ ml NGF a slightly wider dispersion, arising from dense fasciculated bundles reaching across the grooves, was observed (Figure 26C). Upon addition of blebbistatin, the average orientation of neurites deviated from the direction of grooves by $\sim 7^\circ$. This deviation occurred across all NGF concentrations and was always a turn to the right, giving a consistent, chiral outgrowth (e.g. see Figure 24 B, D). Average flat networks showed no noticeable peaks or differences in any culture set.

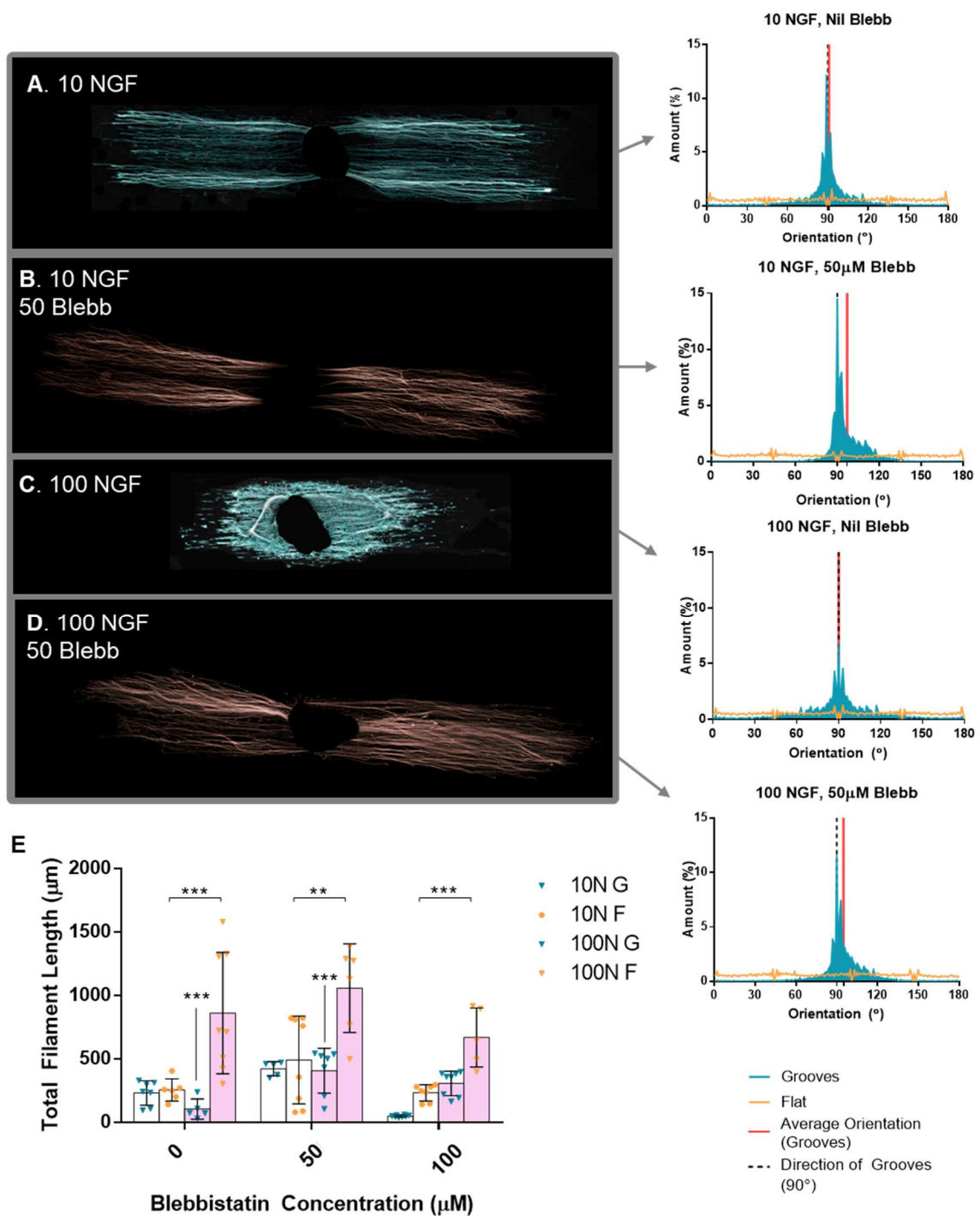


Figure 24: Network orientation analysis and total filament length estimation of 6-day DRG explants cultured in varied NGF and blebbistatin concentrations on grooved/ flat substrates. This analysis was carried out using Filament Sensor: trace filaments command which the final graphic output of the traced filaments can be seen A-D. For their respective concentrations, each histogram shows the average directionality as a percentage with an average orientation (red line). Across all concentrations, flat (yellow) showed no preference for direction in contrast to this, axons show a strong alignment along the direction of the grooves (turquoise). In absence of blebbistatin, 10 and 100 ng/ ml NGF showed an average orientation of 90° however, the lower concentration yielded a greater percentage aligned (10 NGF: 12.5%, 100 NGF: 7%), showing an overall narrower peak. In the presence of blebbistatin, there were two occurrences. The first was a greater percentage of 90° groove aligned axons (13-15%) and the second was a clear shift in the average orientation by 6-7%. This shift was observed across all samples and without exception showed a consistent turn to the right. To ensure the filament tracing was valid, the total filament lengths were measured and show a consistency with

*the manually measured networks. Stars indicate significance between groups, above grooved dataset show significance between topographies for that concentration. Significance was determined by two-way ANOVA with a Tukey post hoc test * $p < 0.05$, ** $p < 0.01$ and *** $p < 0.001$ where $n \geq 5$ biological repeats. The bars indicate standard deviation.*

Surface coverage and network density analysis of 4-day cultures showed very little change with the presence of blebbistatin. With 6-day cultures, an increase in surface area combined with a slight decrease in density was observed with the addition of blebbistatin (seen in Figure 25).

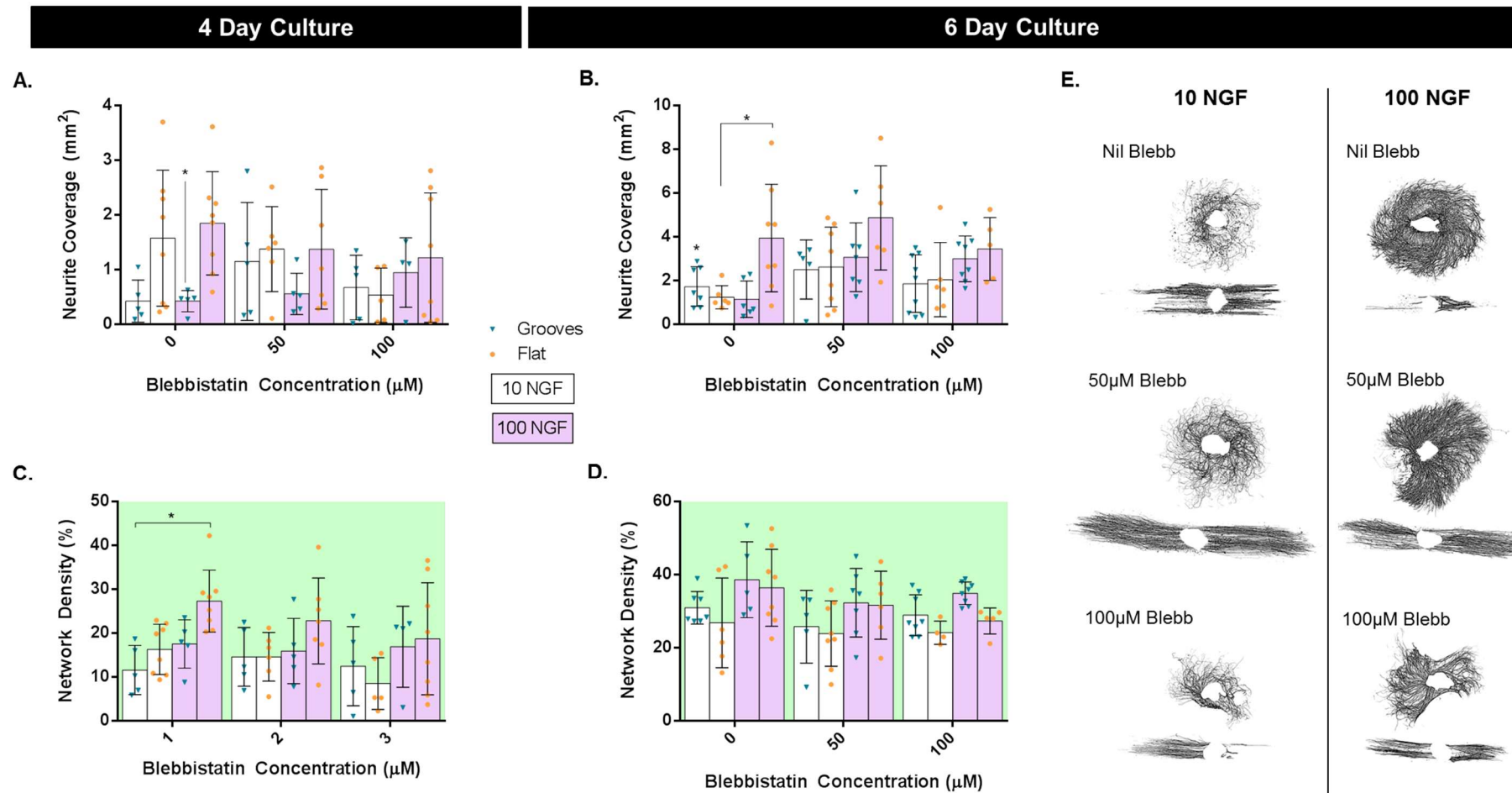


Figure 25: A comparison of surface coverage and neurite density of 4 and 6-day DRG explants cultured in varied NGF/ blebb concentrations and topographies. On 4-day cultures (A, C), the higher NGF concentration showed similar surface coverage levels but a greater average surface density. Application of blebbistatin was seen to have no significant effect on 4-day grooved cultures whereas on flat there was a consistent decrease in coverage and density although not statistically significant. On 6-day cultures surface coverage (B) was relatively consistent with manual measurements (Figure 20 and Figure 21). Surface density comparison (D) revealed the extensive quantity of axons per area on grooves at around 40%, the highest on average across all parameters with blebbistatin generally reducing mean density. At the highest concentration of blebbistatin there is very slight observed increase in density and can be seen to show a small degree of increased bundling in the eLoG trace images E.

2.3.2.4. Fasciculation analysis

To further analyse the fasciculating/ branching nature of the networks and gain an approximate/relative count for the number of neurites within each culture condition, WIS NeuroMath was used (Figure 26). Neurite counts on grooved substrates gave similar results regardless of concentration, generally arising from false negatives from extreme fasciculation at higher NGF cultures (e.g. see yellow arrows in Figure 27). On flat substrates, a more accurate representation of the number of migrating neurites was given, providing confirmation that high NGF concentration promotes greater amounts of growing neurites (~76) than lower NGF (~52). Analysis of branching/ fasciculation degree showed 10ng/ ml NGF to have consistent outgrowth with no fasciculation or branching on grooves, and a small amount of branching on flat substrates. On grooves, 100 ng/ ml NGF was found to promote fasciculation, with the largest decrease in neurite counts over a 30 μ m distance compared to all other groups. In contrast to this, flat surfaces with 100 ng/ ml NGF promoted the highest amount of branching. With the addition of blebbistatin, all grooved cultures experienced an increase in branching whilst flat showed no remarkable difference (with the exception of 100 μ M at 10 ng/ ml NGF due to adherence issues).

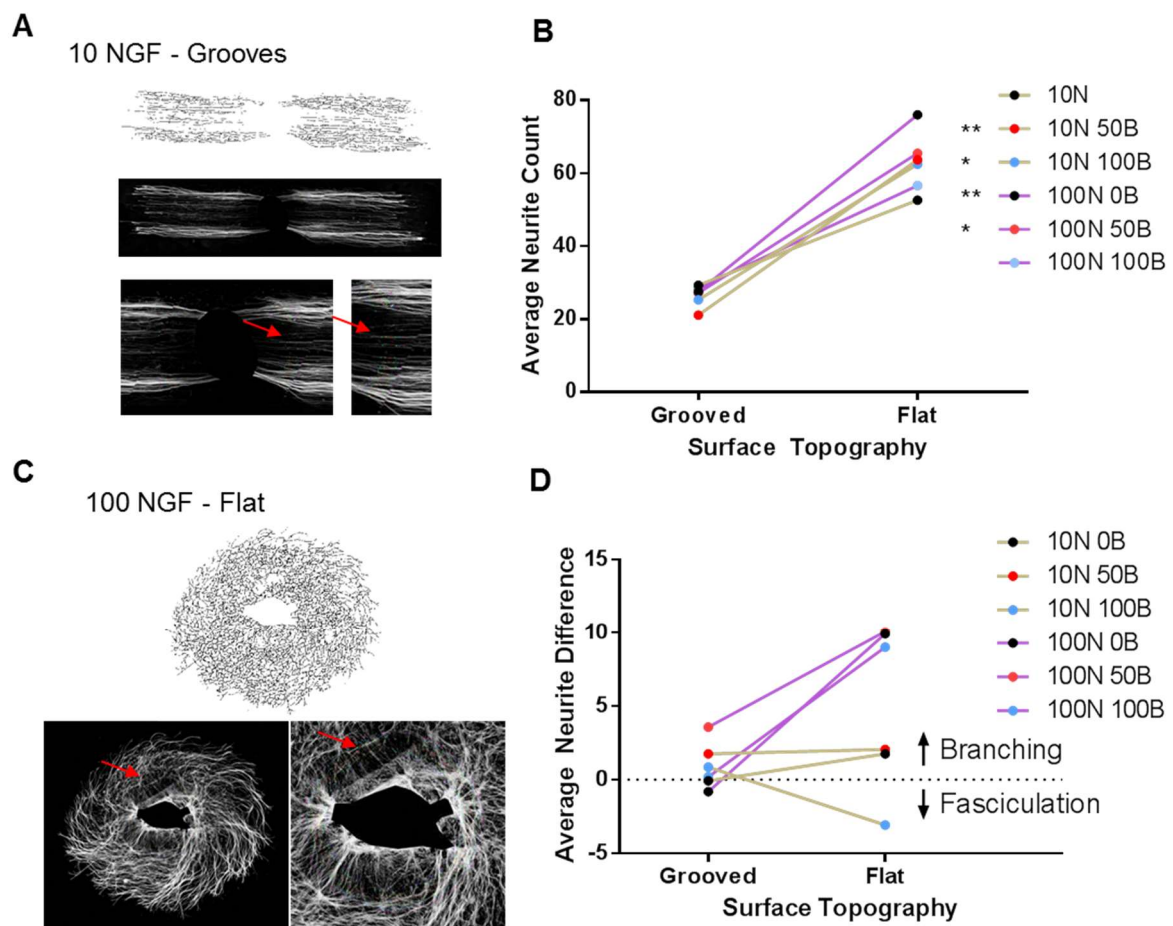


Figure 26: Neurite count and branch analysis of 6-day DRG explants grown with varying NGF/blebbistatin concentrations on grooved and flat topographies. This analysis was carried out on WIS-NeuroMath neuronal morphology tool. Tracing and count (red arrows/ coloured dots) for neurites can be seen (A: 10 NGF/ grooved, C: 100 NGF/ flat). From the neurite count (B), flat surfaces show an increase in the neurite numbers with higher concentrations of NGF which was significantly different to grooves in which the count showed similar numbers, likely due to insufficient detection on heavily bundled networks. Branching analysis across a distance of 30 μm showed lower NGF concentration an average of no branching or fasciculation on grooves with a small degree of branching on flat. In contrast to this, high NGF gave slightly more fasciculation on average with a vast increase of branching on flat. When blebbistatin is considered, average branching increased on all grooved groups however on flat showed very little difference (except 10 NGF, 100 μM blebbistatin fasciculation due to loss of adhesion and axon retraction). Stars indicate significance between topographies for that concentration. Significance was determined by two-way ANOVA with a Tukey post hoc test * $p < 0.05$, ** $p < 0.01$ and *** $p < 0.001$ where $n \geq 5$ biological repeats. The bars indicate standard deviation.

A time-lapse study was then carried out to gain an insight into the immediate outcomes of adding blebbistatin as well as how the axons extend under its influence (Figure 27). It should be considered that blebbistatin is both phototoxic and deactivated in the presence of blue light (Kolega, 2004) and thusly illumination during culture will have adverse effects in comparison to conventional cultures. This revealed an initial retraction, accompanied by a loss of adhesion followed by a burst

of growth, in which axons eventually 'met up'. Following this occurrence combined opposite growth and tension resulted in a lateral loss of adherence, constriction of the network and bundling of the axons around the DRG. Towards the end of the 4-day culture, a large majority of axons had on this occasion retracted or lost adherence. This resultant bundling of axons bears a resounding similarity to the morphological features found at high NGF concentrations on grooved substrates, wherein large fasciculated bundles can be seen to form perpendicular to the initial direction of outgrowth creating arc like fascicles (Figure 27B). This happens very slightly at lower NGF concentrations and is not generally seen with blebbistatin.

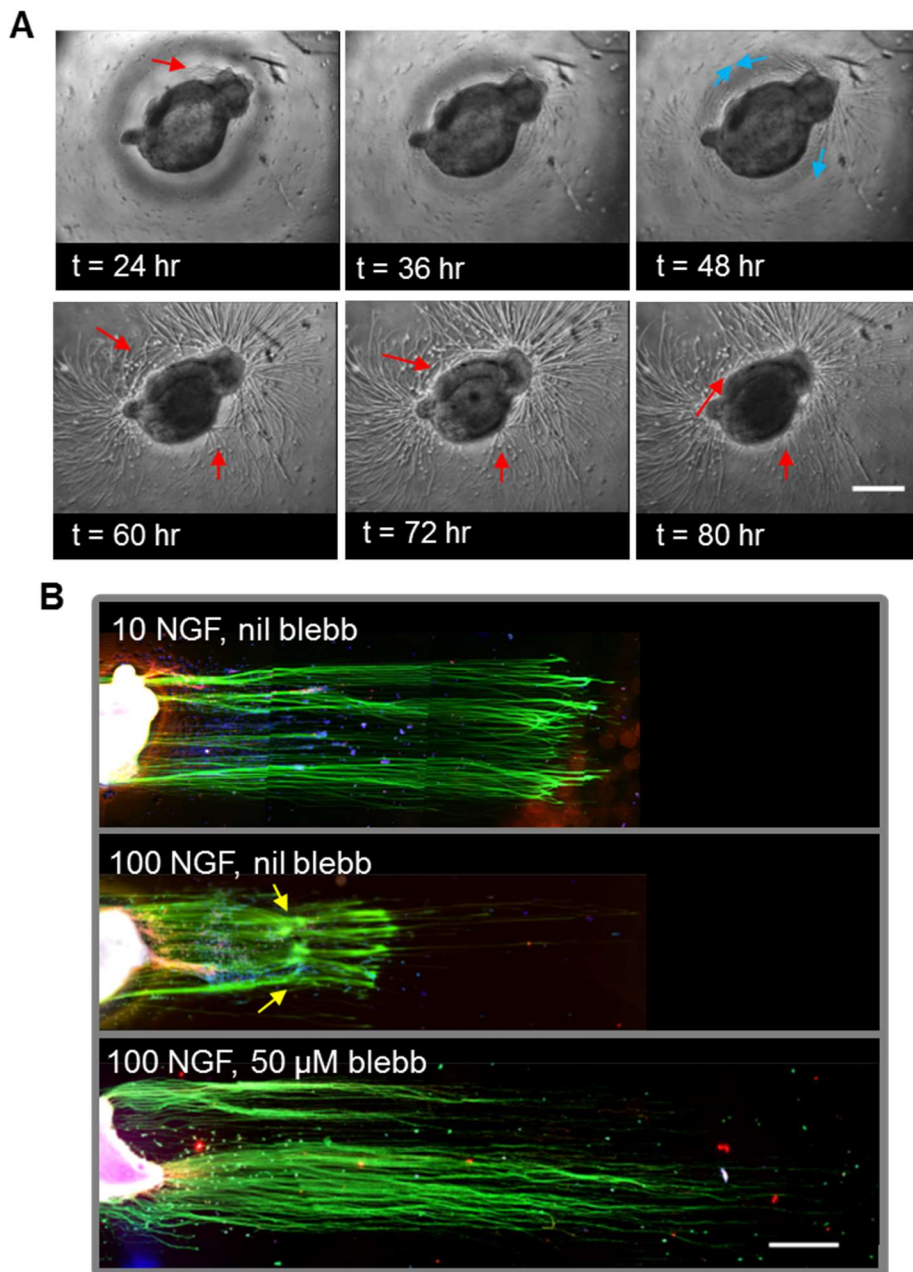


Figure 27: A study of the effects blebbistatin has on DRG network morphology. Figure A shows the image sequence of 12-hour segments from a recording of a DRG cultured with 100 ng/ml NGF on flat through a brightfield timelapse which begins from the addition of 50 μ M blebbistatin at the 24-hour point. The initial presence of blebbistatin serves to cause a retraction of axons (red arrow) however by 48 hrs the axon growth is re-activated and can be seen (blue arrows) around the DRG as well as outwards. Upon meeting axons can be seen to join/ fasciculate over one another (60 hr) and following this retraction of the network is seen creating high density axon bundles around the DRG (72 hr+). Image set B shows immunofluorescence of 6-day NGF/ blebbistatin cultured on grooves (green: B3-tubulin (axons), red: S100 protein (Schwann cells), blue: DAPI (nuclei)). The observed retraction/ condensing of the network from the timelapse bears a visual similarity to that of the 100 ng/ml morphologies which shows thick, groove-crossing bundles which look to constrict the network (B: yellow arrows). This occurred very slightly in 10 ng/ml NGF at the distal edges and not at all in the presence of blebbistatin which was seen to show more individualistic growth. The bars indicate standard deviation. Scale: 500 μ m

2.3.2.5. Cell viability analysis

To assess if the topographical cues influence the NGF survival signalling and whether blebbistatin, a known phototoxin had a detrimental effect on cell viability, a live/dead viability assay was carried out measuring the intensity ratio between the two. No statistical significance was found between groups indicating that blebbistatin had no presentable detrimental effects on neuronal survival over a period of 5-days; however, a consistent trend was observed in which grooves promoted ‘higher’ viability than flat. There was no variation in the extent of topographical increase between NGF or blebbistatin concentrations with exception of the high variance group: 100 ng/ ml NGF in combination with 50 μ M blebbistatin which showed no difference between topographies.

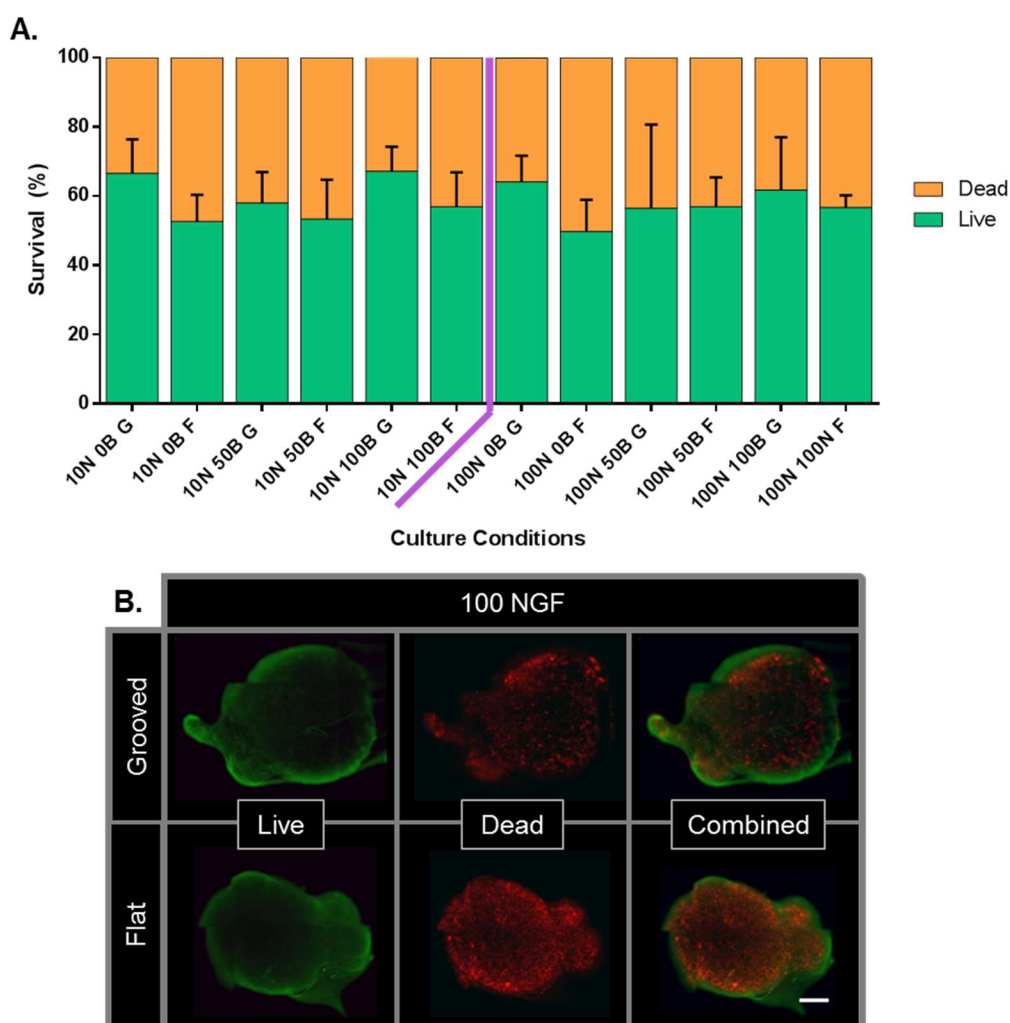


Figure 28: Viability analysis of 6-day DRG explants cultured in varying NGF/ blebbistatin concentration on grooved and flat topographies. Cell survival was determined through a ratio of the live and dead intensities (integrated density- Fiji) following a background correction. A comparison between each sample (A) showed similar survival regardless of concentration however, survival was seen to be

consistently higher on grooves than on flat although significance could not be reached. For visualisation, images are shown comparing grooved and flat survival differences (B). Significance was determined by two-way ANOVA with a Tukey post hoc test where $n \geq 3$ biological repeats. The bars indicate standard deviation.

2.3.3. Growth Cone Analysis

2.3.3.1. Growth cone myosin IIA intensity study

To further understand the effects both topography and NGF concentration has on contractility, analysis began to focus on the GC instead of the overall network morphology or dimensions. This was achieved through the use of myosin IIA and filamentous actin stains and microscopy at high magnification (100x). The GC intensity of myosin IIA relative to actin (as the control) was compared (Figure 29) across differing concentrations of NGF/ blebbistatin and the two surface topographies. This revealed that DRG explants cultured in high concentration of NGF had significantly lower GC myosin IIA intensities (with respect to actin) than low NGF concentration. Similar levels were seen between grooved and flat and there was no change with the addition of blebbistatin to grooved cultures. Blebbistatin presence on flat cultures resulted in a significant increase in myosin IIA intensity across both NGF concentrations. To gain an insight into possible activity of retrograde flow or GC retraction, the distance between the beginning of actin and myosin IIA peaks was measured following background normalisation (Figure 29B). High concentration of NGF (100 ng/ ml) was found to show a significantly longer distance between the actin and myosin IIA peaks than the lower concentration (10 ng/ ml), regardless of surface. Further to this, topography was seen to have no influence on the distance between the actin-myosin IIA peak intensity. Blebbistatin was seen to normalise the distance to ~ 0.2 μ m myosin IIA behind the actin edge, counteracting any noticeable effect NGF that the higher concentration exerted.

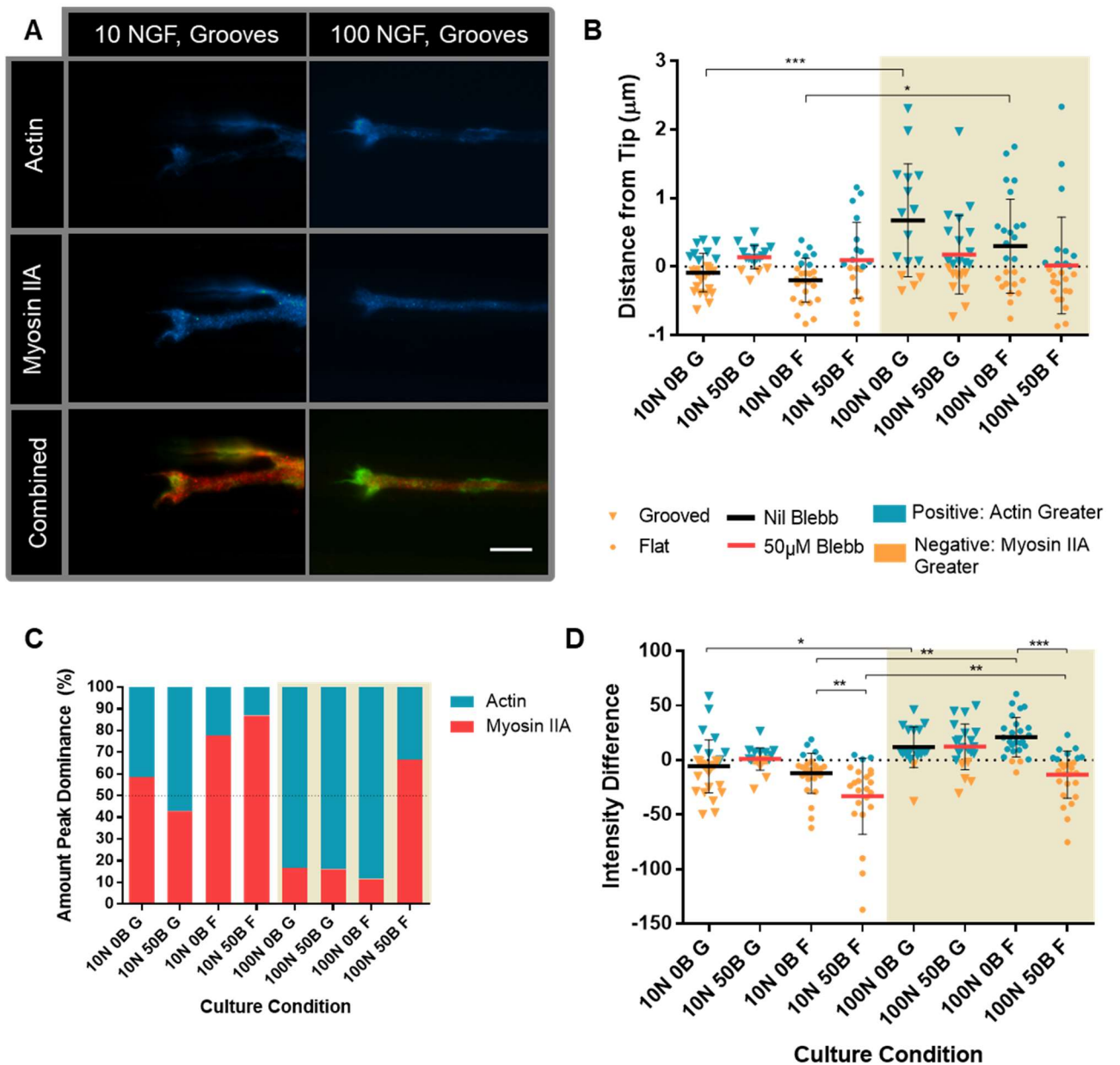


Figure 29: Myosin IIA/ Actin intensity analysis of growth cones from 6-day DRG cultured with varying NGF/ blebbistatin concentrations on grooved and flat topographies. Intensities through each GCs were quantified using FIJI surface density plot tool followed by normalisation between stains by background subtraction. Image set (A) shows a visual intensity comparison between immunolabelled myosin IIA (red) and actin (green) with each individual stain shown with a LUT for clarity. A greater intensity of actin can be seen within the filopodia of the GC with high NGF concentration whilst this is also accompanied by a lower intensity of myosin IIA throughout the GC which does not reach the GC tip. This was opposite to that of the low NGF concentration. The distance between myosin IIA and actin was quantified from the beginning of the surface plot peak for each stain (B *), revealing that 10 NGF produced significantly lower (actin-myosin IIA distances than 100 NGF GC (~1 μm). In addition to this, a lateral surface density plot showed the mean intensities for the growth cone as a total. The percentage of GCs with greater myosin IIA (red) or actin (green) peak area across each concentration is shown in C. GCs from the lower NGF concentration was seen to have greater amount of GC with myosin IIA peak dominance whilst in the higher NGF concentration the opposite occurred. The exception to this was on flat with blebbistatin which resulted in the highest quantity of myosin IIA dominant GC on both concentrations. Graph D shows the intensities for the lateral surface plot measurement revealing a significant difference in actin-myosin IIA intensity difference between 10 and 100 ng/ ml NGF. No apparent difference was observed with the addition of blebbistatin on grooved surfaces; however, on the flat resulted in a significant decrease on both concentrations. Stars

*indicate significance between topographies for that concentration. Significance was determined by two-way ANOVA with a Tukey post hoc test * $p < 0.05$, ** $p < 0.01$ and *** $P < 0.001$ where $n \geq 16$ (168 total) GCs spread across 3 biological repeats. The bars indicate standard deviation. *Two outliers were removed on the basis of flawed result (myosin IIA peak $> 1.3 \mu\text{m}$ in front of actin peak). Scale: $10 \mu\text{m}$*

2.3.3.2. Regional myosin IIA analysis with Filopodyan

Further investigation into the GC regional intensities of myosin IIA was carried out through analysis with the FIJI plugin: Filopodyan (Urbančič et al., 2017) (Figure 30 and Figure 31). In this, the GC was segmented into 4 regions (Figure 30A); the body (C/ T-zone, also described in section 1.3.1), the base of the filopodia, the filopodium protrusion, and the tip of the filopodium. Within the body of the GC, low NGF concentrations promoted significantly higher myosin IIA intensities than the higher NGF concentration. Consistent with previous results (size analysis in section 2.3.2), blebbistatin served to normalise the intensities across all parameters towards that seen with the high NGF concentration, resulting in a significant difference from the data for 10 ng/ ml NGF on grooved substrates. Within the protrusion region, NGF consistently seemed to reduce myosin IIA intensity at higher concentrations in all groups although not statistically significantly so. At low concentration NGF, the flat surface produced lower myosin IIA intensity compared to GC on grooves, if without blebbistatin.

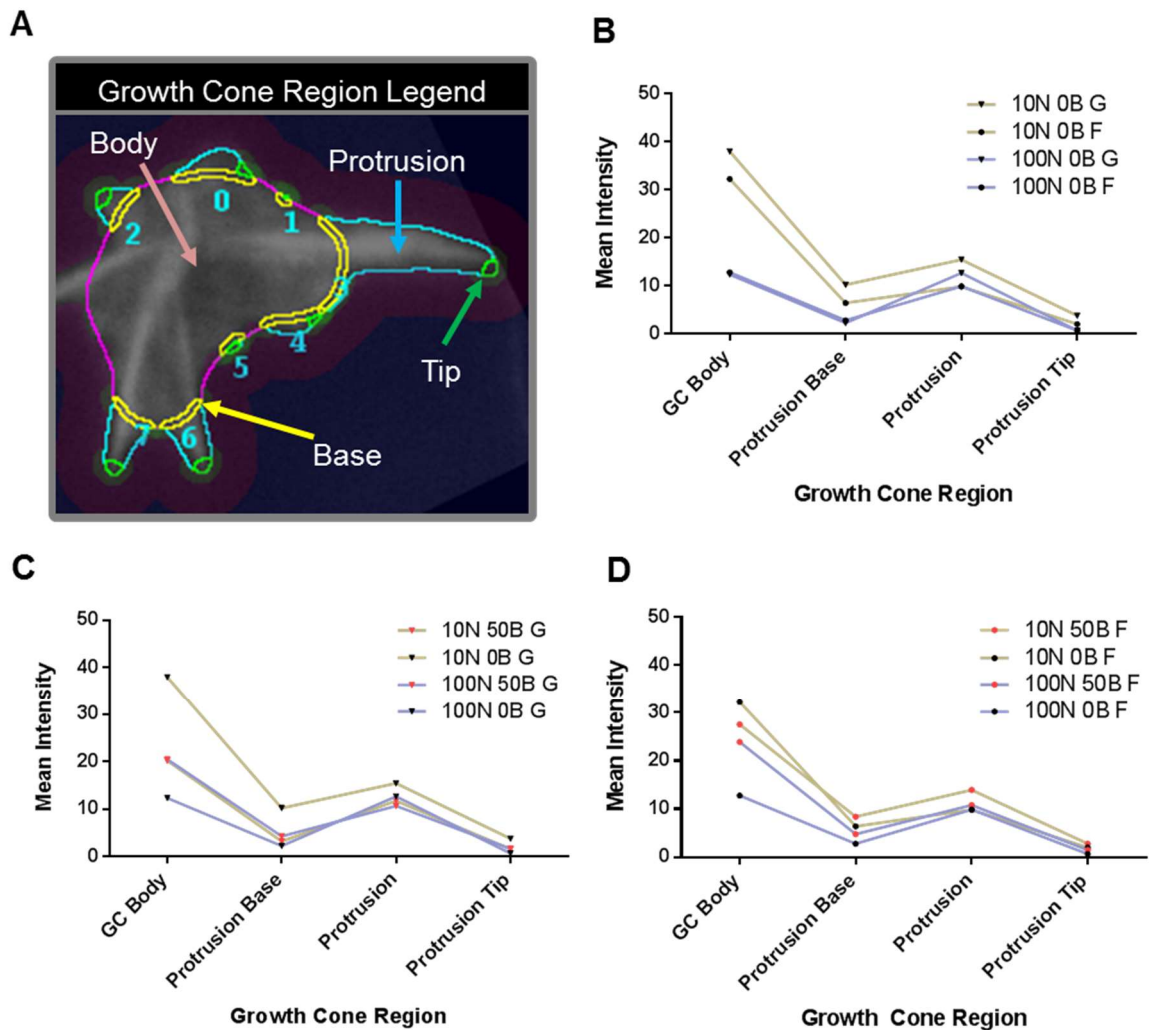


Figure 30: Intensity analysis of myosin IIA at different regions of growth cones from DRG cultured in varying NGF/ blebbistatin concentrations on grooved and flat topographies. A total of 105 GCs were analysed with FIJI plugin: Filopodyan with $n \geq 12$ spread across 3 biological repeats. Image A shows typical region segmentation of Filopodyan which measured the mean fluorescent intensity of myosin IIA within 4 regions: the body (pink), the base (yellow), the protrusion (blue) and the tip (green) following a background subtraction determined by the immediate area around each region. Graphs B-D show the average myosin IIA intensities within each region, at each culture condition. A comparison of 10 and 100 ng/ ml in the absence of blebbistatin shows that within the body (C/ T domain of GC) there is a greater intensity of myosin IIA at low NGF concentrations. Grooves showed higher myosin IIA levels than flat for 10 NGF in the GC body and, within the protrusion region this was also the case for both NGF concentrations. Blebbistatin was found to effectively normalise the myosin IIA intensity difference between each NGF concentration, providing similar results which lay between the two. The exception to this was within the protrusions on flat which was seen to be slightly higher.

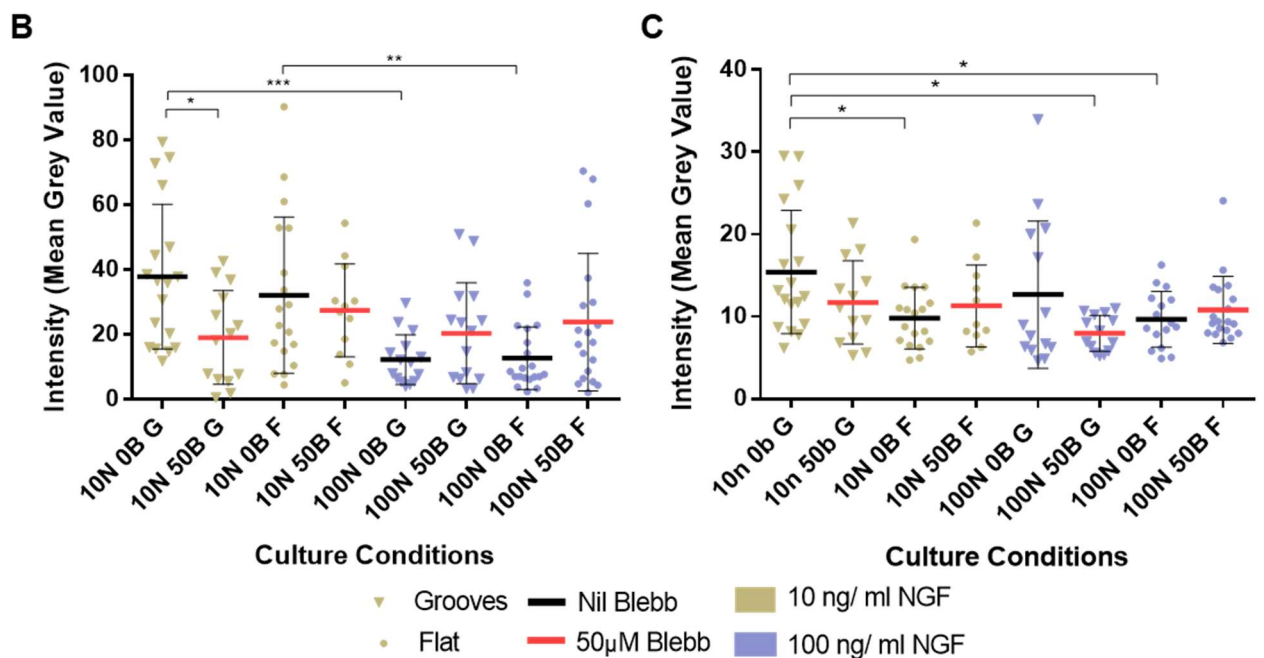
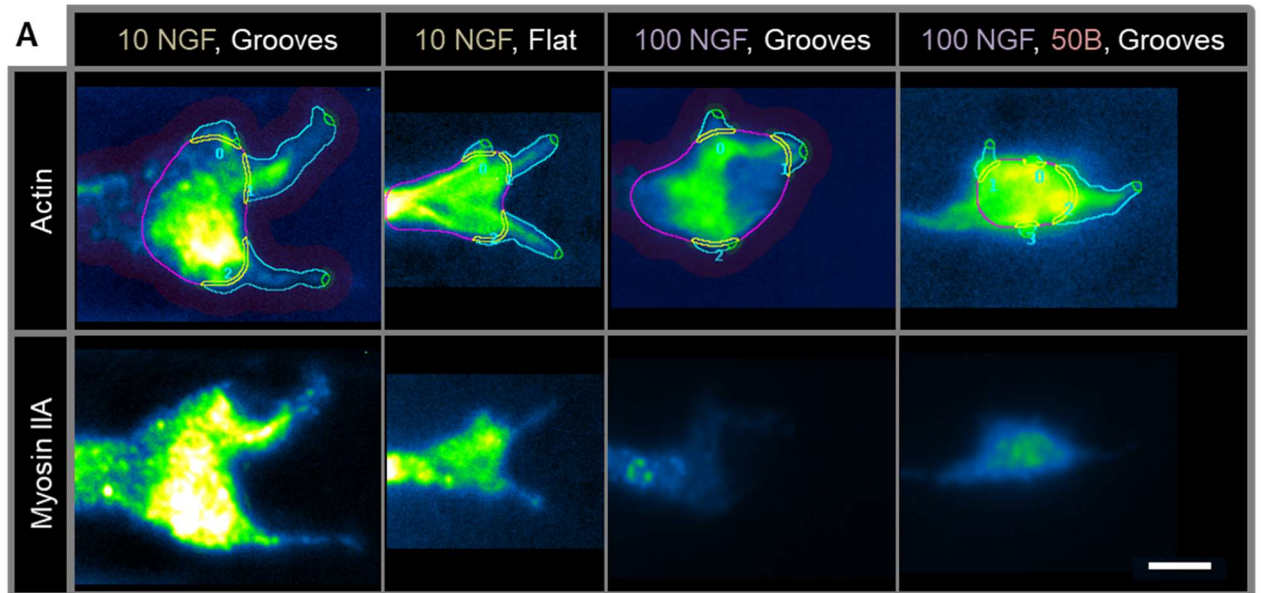


Figure 31: A closer examination of Filopodyan body and protrusion intensities from growth cones of 6-day DRG cultured in varying NGF/ blebbistatin concentrations and on differing topographies. GCs were immunolabeled with actin and myosin IIA (shown in LUTs for clarity) with typical results shown in the visual representation (A) serving to give an insight into the extent of contrast between 10 and 100 ng/ml NGF - myosin IIA levels. Graph B reveals a detailed comparison of myosin IIA intensities residing within the GC body region of which, 10 NGF/ nil blebb was found to be significantly higher on each topography than their respective 100 NGF counterparts. Additionally, blebbistatin was seen to provide similar levels regardless of NGF concentration, providing a significantly decreased the myosin IIA intensity of 10 NGF/ grooves. Within protrusions, 10 NGF/ grooves was found to be significantly higher than flat, and both 100 NGF/flat and 100 NGF/grooved/blebbistatin. Average intensity levels showed 100 NGF to be slightly lower than 10 NGF. Significance was determined by two-way ANOVA with a Tukey post hoc test * $p < 0.05$, ** $p < 0.01$ and *** $p < 0.001$ where $n \geq 16$ (103 total) GCs spread across 3 biological repeats. The bars indicate standard deviation. *Two outliers were removed on the basis of flawed result (myosin IIA extremely high: single data points 3 to 4-fold higher than mean). Scale: 3 μ m

2.3.3.3. Characterising the growth cone

Shape analysis of GC such as filopodia length (determined by Filopodyan, protrusion perimeter) showed no significant difference between culture conditions (Figure 32). The analysis of GC shape complexity (determined by perimeter/ area) gave an idea of the size and shape of the growth cone as a single number. Complexity was seen to increase with both: blebbistatin addition or placement on a flat substrate for all groups, although it was more prominent at a lower NGF concentration. These differences were significant if comparing 10 ng/ ml NGF on grooved substrates to 10ng/ ml NGF with 50 μ m blebbistatin on a flat substrate.

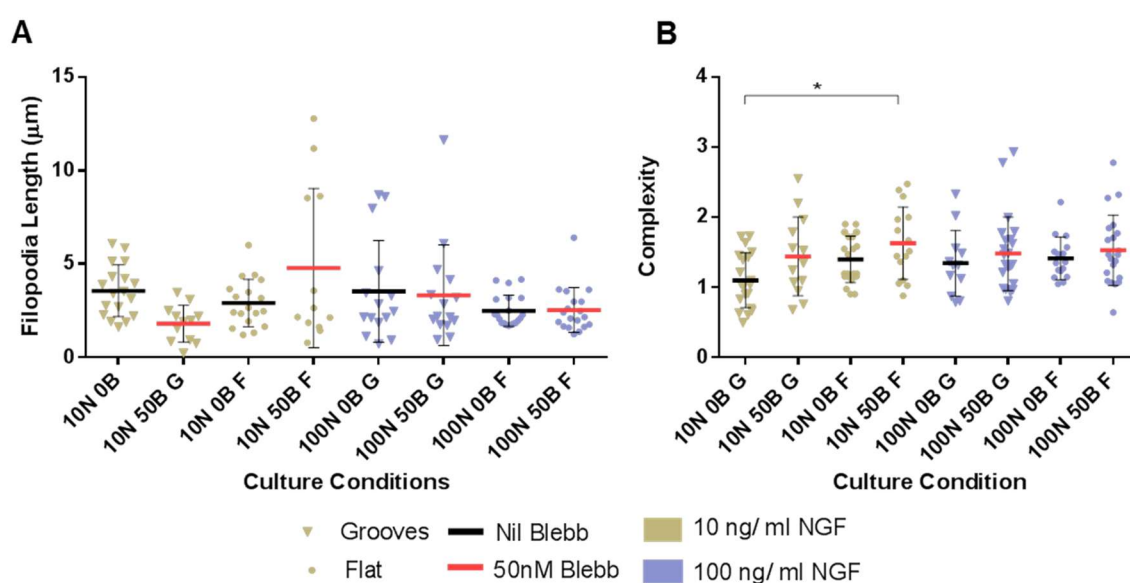


Figure 32: Length and complexity analysis of growth cone filopodia of DRG cultured in varied NGF/blebbistatin concentrations and grooved/ flat topographies. The effect of culture conditions on the length of filopodia is displayed in graph A, determined through measuring the perimeter of the protrusion with Filopodyan. Across all concentrations there was very little difference in protrusion length or count (not shown). On 10 ng/ ml, blebbistatin appeared to have a greater effect on the length however showing a decrease on grooves and a much higher potential for larger protrusions on flat causing a large variance. On grooves, 10 NGF/ 50 blebbistatin was found to produce significantly smaller filopodia lengths than both culture conditions: nil blebbistatin/ grooves and 50 μ M blebbistatin/ flat. Complexity analysis of (perimeter: area) the growth cone was carried out B as a means to provide a basic quantification of GC shape characteristics for comparison. Consistently across all sample groups, slight increases in complexity were observed from grooved to flat topographies and with the presence of blebbistatin. Significance was determined by two-way ANOVA with a Tukey post hoc test * $p < 0.05$, ** $p < 0.01$ and *** $P < 0.001$ where $n \geq 16$ (103 total) GCs spread across 3 biological repeats. The bars indicate standard deviation.

2.3.3.4. Growth cone directionality analysis

Directionality analysis of GCs (Figure 33) revealed grooved cultures without blebbistatin to yield the least disperse range of orientations and flat cultures; the most. Inhibition of myosin IIA was seen to increase the quantity of turning and spreading, but also heightened the potential amount for extremely straight GCs; overall resulting in a consistent increase in the number of straight GCs on average. The exception to this was with 10 ng/ ml NGF on a flat substrate, which experienced a decrease in dispersion, turning and spreading with the addition of blebbistatin. Upon comparing averages (Figure 34C), there was a clear increase in the average straight orientation comparing the data for the higher NGF concentration with that recorded for the lower NGF concentration.

Overall, the straightest GCs were observed for blebbistatin with 100 ng/ ml NGF on grooved substrates, whilst 10 ng/ ml NGF on flat substrates (with or without blebbistatin) promoted the greatest degree of turning and spreading. On comparing the percentage of GC assigned to either: straight, turning or spreading (Figure 34D) it is clearly visible that high concentration NGF increases the amount of straight GC (~/+25%). No change in the amount of turning was found across differing concentrations although increased spreading occurred on flat at 100 NGF. Blebbistatin showed near identical results regardless of concentration; however, with 100 NGF/ grooves, no visible change was identified from nil blebbistatin.

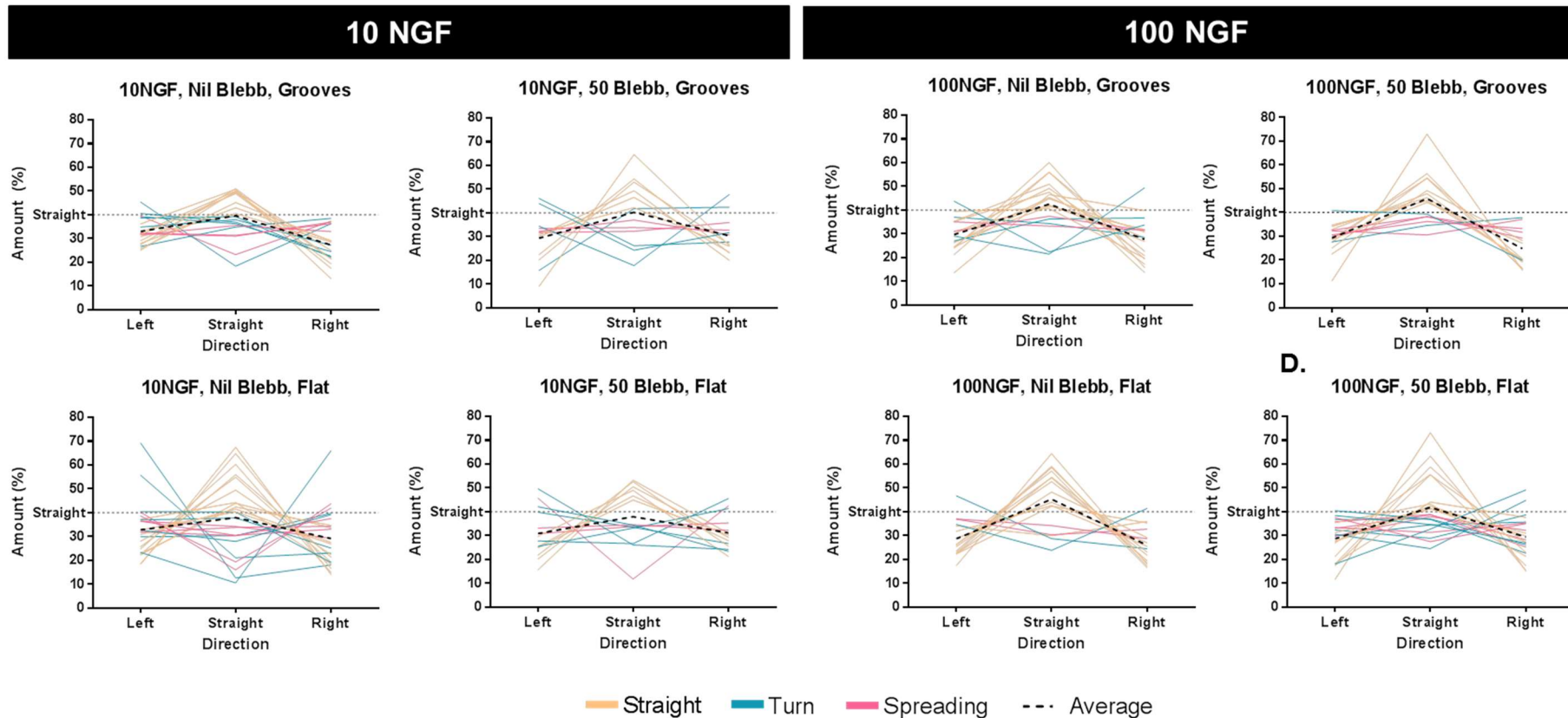


Figure 33: Growth cone directionality analysis of growth cones of 6-day DRG cultured with varied NGF/ blebbistatin concentrations and surface topographies. Analysis was carried out using Filament Sensor: eLoG tracing tool on pre-orientated GCs (mid-way between angles of GC 'neck') to create a percentage histogram split into three bins: left: 0-70°, straight: 70-110°, right: 110-180°. GCs were deemed to be straight (yellow) if above 40%, if this was not the case or left/ right was above 40%, the GC was considered to be either turning (blue) or spreading (red). Turning was decided on the demand of showing greater than 5% difference between left/ right which if not met, the growth cone was said to be spreading equally. Averages are marked by the black dashed line (discussed in more detail in Figure 34). On grooves, 10 NGF was found to have very low dispersion between straight/ turning and an average just below the threshold for straight category indicating a general spreading/ turning formation. On the other hand, 100NGF showed a majority above the threshold and less turning. Further, on flat the lower NGF concentration was seen to have a high variation in overall GC orientation, averaging below the straight threshold whilst at high NGF, there was less turning averaging above the straight threshold. Finally, the presence Blebbistatin had the effect of increasing the overall dispersion, generally increasing the average straight percent of each condition group except for 10 NGF/ flat which showed the highest variance across all sets.

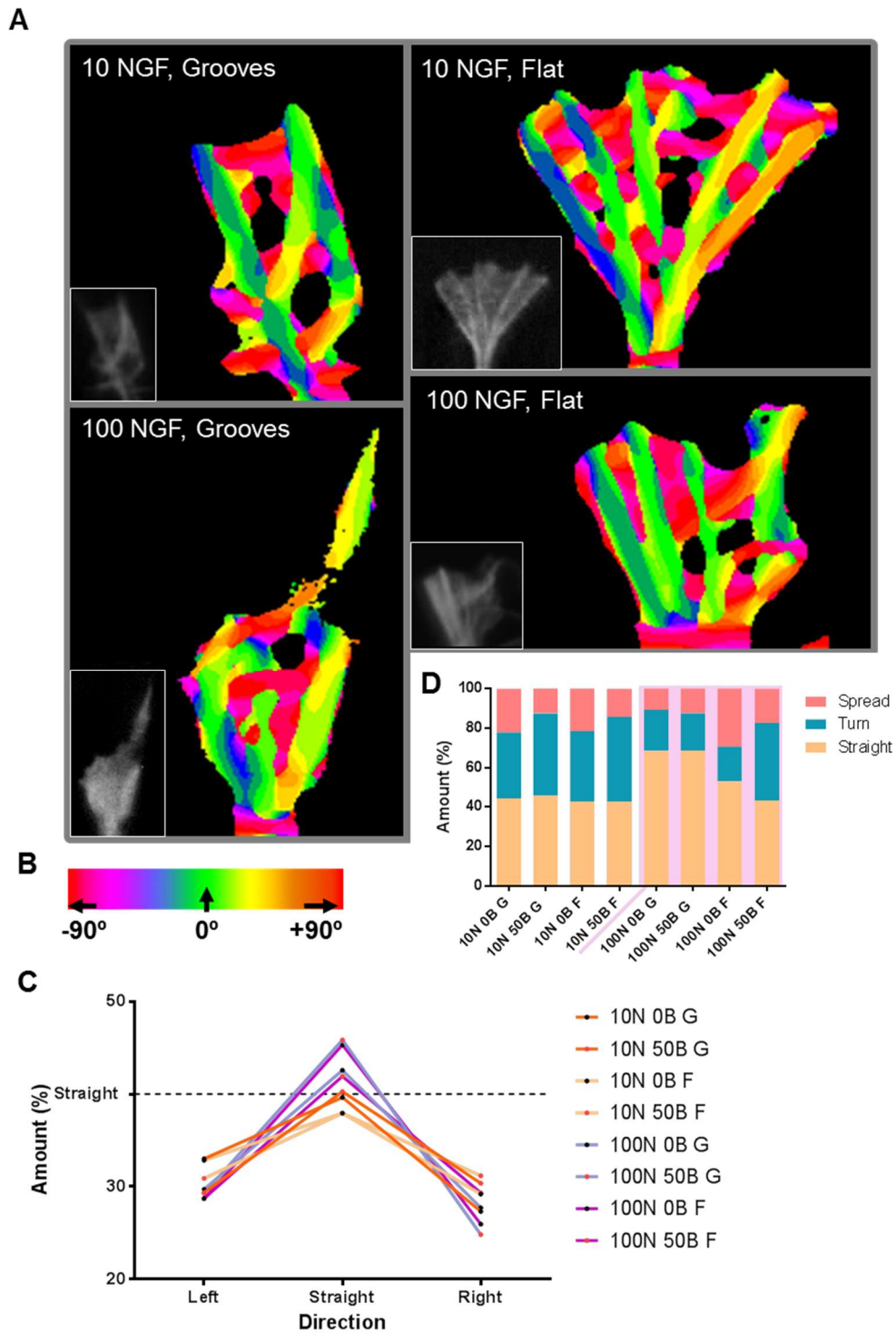


Figure 34: Average GC directionality of growth cones from 6-day DRG cultured in varied NGF/blebbistatin concentrations and differing topographies. Image set A shows the typical output of Filament Sensor eLoG analysis tool giving an insight to the typical nature of GC from each culture condition. A colour-direction legend (B) gives an understanding of the orientation each colour represents. Graph C (continued from Figure 33) shows the average direction of GCs from each culture set with a determination of which shows all high NGF cultures to be above the straight threshold and as a whole, significantly higher than the low NGF concentration. Graph D provides the percentage of GC orientation within each culture condition. Overall, due to the high degree of variation in growth cone shapes no individual statistical significance could be reached between each group. Significance was determined by two-way ANOVA with a Tukey post hoc where $n \geq 16$ (103 total) GCs spread across 3 biological repeats.

2.4. Discussion

2.4.1. Topographical cues and NGF co-modulate axon outgrowth through Myosin II and fasciculation

Consistent with the previous study by Theophile Déjardin (2013) flat surfaces created random, radial outgrowths contrary to grooved surfaces which caused rectangular, oriented outgrowth. Topographical cues strongly modulated the effects of NGF concentration on DRG neurite growth causing vast changes in size, morphology and density of axon networks. The trend observed was that increasing NGF concentrations increased network size on flat controls but produced shorter network lengths on grooves. Initially, the hypothesis was that grooves forced the axon to extend in a singular direction, increasing myosin II driven tension, promoting a modification in the NGF signalling pathway (shown in Figure 35), thus causing a decrease in growth. Excess NGF concentration has previously been found to produce less axon extension of DRG explants (Conti et al., 1997, Rutishauser and Edelman, 1980) on flat surfaces, going against the observed trend. The most likely explanation for this is with the mechanical or chemical properties of the surface, in which collagen or agar was used. More recently, synthetic polymers have been shown not to instigate this effect (Liu et al., 2002) whilst substrate stiffness has been shown to have a profound impact on general cell behaviour (Gu et al., 2012), as well as on neurite outgrowth at varying NGF levels (Déjardin, 2013).

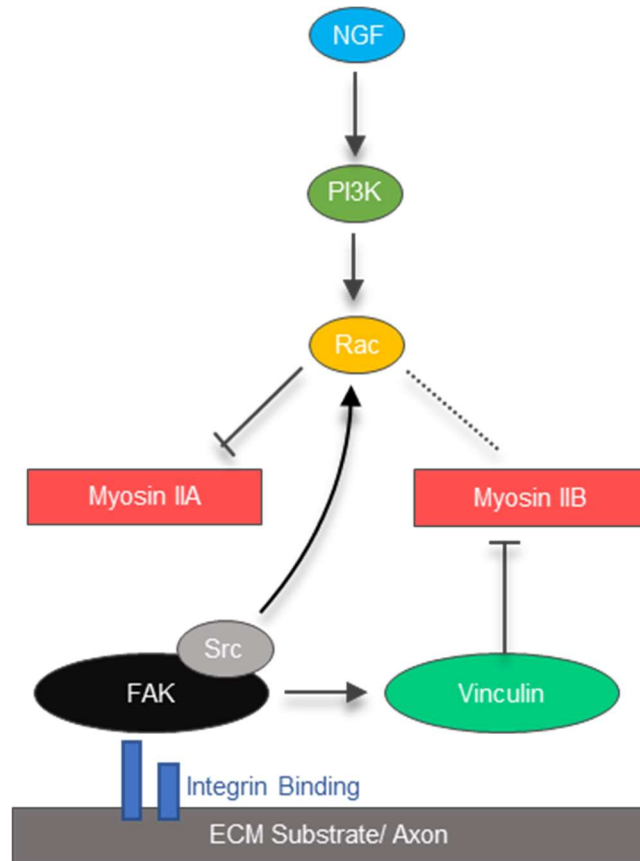


Figure 35: Simplified schematic of the convergence of each signalling pathway arising from NGF induction and substrate binding. NGF acts to modulate the GEF Rac and possibly others (RhoA, cdc42) to block myosin IIA activity and is likely to also have an effect on myosin IIB. Rac GEF action is also modulated through substrate binding and FAK-adaptor protein Src messaging and vinculin has been known to illicit actin polymerisation of the GC through restraint of myosin IIB (Turney et al., 2016). This is entirely dependent on substrate chemical and physical properties; however, generally permit the NGF signalling to produce axon elongation through negatively regulating myosin II. In excess, this process manifests as poorer network outgrowth as shown in this thesis and described overall in Figure 36.

Another explanation may be due to the use of embryonic DRG cultures in the studies by Conti et al. (1997), which aside from difference in cell behaviour, overall give spatial smaller area around the explant which these grow out (due to their smaller size), resulting in a large degree of fasciculation. This inherently, is the basis for their hypothesis of reduced growth, where increased fasciculation is the main effector of reduced growth with high NGF. This coincides with the observation of density- length studies (Figure 18 and Figure 19), in which higher NGF caused increased network density and this correlated with lower network lengths on grooves. These findings indicate fasciculation is likely a major contributor the observed trend in concordance with the reasoning of (Rutishauser and Edelman, 1980), in which axons growth over other axons increases the tension and rearward force experienced by axons beneath. Coupling this combined force by multiple fasciculating axons above with no

proportionate increase in traction force the underneath substrate-adhered axons can produce, provides the reasoning for the net result of reduced axon extension. This occurs extensively with the greater confinement provided by grooves, and to a much lesser degree on flat surfaces, where there is greater spatial freedom. This trend was seen to emerge between day 4 and 6 (Figure 17), as network density increased (Figure 25) and thus: fasciculation started to occur. Coinciding with (Conti et al., 1997) findings, reduced growth was exclusive to NGF (Figure 16), with no change in network size between concentrations and no visible axon fasciculation on either BDNF or FGF-b treated cultures, which possibly arises from the low neurite counts observed with these GFs. Although no trend was apparent within each alternate GF, vast differences of network sizes were apparent. Supplementation with BDNF resulting in extremely poor (comparable or less than nil GF controls) and FGF-b producing large networks comparable to that of the highest NGF induced outgrowth. This may be explained by the BDNF promotion of axon arborization (Cohen-Cory et al., 2010) whilst FGF-b is shown to play a supportive role in NGF signalling (Reuss and von Bohlen und Halbach, 2003) (which may be supplied by SC migrating from the DRG). These findings demonstrate that the supply of neurotrophins can be detrimental to outgrowth; however, these factors may be beneficial for other stages of regeneration such as target reinnervation. Overall, this indicates the need for further study into the spatial-temporal control of GF delivery and in their combined use in an NGC.

2.4.2. Blebbistatin inhibition of myosin II removes the reduced DRG outgrowths observed at excess NGF levels

The initial hypothesis proposed that axon tension increases on grooves and was a potential mechanical mediator for the NGF concentration dependent response on the grooves. To further investigate this, an inhibition of Myosin IIA, the molecular motor responsible for actin contractility and axon tension, was carried out using blebbistatin (section 2.3.2). Inhibition of myosin II with blebbistatin is well documented (Kovacs et al., 2004) and frequently used as the prime candidate due to its highly selective manner which has relatively minor or no impact on other processes (survival etc.). Both the A and B isoforms of myosin II are inhibited which are the main driving force involved in GC motility (Togo and Steinhardt, 2004). The general consensus is that myosin IIA instigates axon retraction with transverse actin bundling whilst myosin IIB

regulates the retrograde flow of actin thereby controlling filopodia extension rates (Turney et al., 2016). There is however still debate on whether each isoform is solely exclusive to these roles and recent evidence suggests that their modality is highly dependent on the ECM or the specific chemical properties of the substrate (Turney et al., 2016). From the present study, blebbistatin (50 μ M) inhibition resulted in an increase in growth across all NGF concentrations and topographies but the largest increase was observed for the high NGF concentration (100 ng/ ml) on grooves which effectively normalised any NGF effect on growth (Figure 20 and Figure 21). It is inconclusive if this was normalised due to reaching the maximum potential outgrowth rate or if this blocked the NGF induced signalling, although the latter appears to be the case when considering that a similar effect was observed by Shin *et al.* (2014). The relatively small increases in length on flat, but the larger increases on grooves provided by inhibition of both myosin II isoforms, indicates that there may be an increase in tension on grooves and that is likely as result of myosin IIB activity, reasoned from the low myosin IIA intensities described below and shown in Figure 29. A higher blebbistatin concentration (100 μ M) lead to axon adhesion issues on all groups and thus; results were discredited from comparative analysis and largely excluded from discussion.

2.4.3. Excess NGF reduces myosin IIA amounts within the growth cone to comparable levels of blebbistatin application

From the myosin IIA intensity analysis, increasing NGF concentration produced a significant decrease in myosin IIA abundance within the growth cone in all regions, showing similar levels or lower than with blebbistatin inhibition (Figure 29 and Figure 30). This is in agreement with literature, where it had been shown that NGF downregulates myosin IIA through the ROCK pathway (Loudon et al., 2006, Shin et al., 2014, Turney et al., 2016) to suppress retrograde flow and initiate axon extension. This regulation can be overruled by the blebbistatin blocking of myosin IIA, effectively removing the NGF influence on the signalling channel. This may help to explain the normalising of myosin IIA intensities across all concentrations observed in Figure 31, instead of a compound decrease from the combination of high NGF with blebbistatin. In addition, myosin IIA inhibition has also been shown to reduce adhesion strength (Cai et al., 2006, Wylie and Chantler, 2001). Loss of adhesion is most likely a major

effector in the induced reduction in axon growth induced by excess NGF, which can be seen in the time-lapse study and with the high NGF concentration network morphologies (Figure 27). Networks developed here have large fascicles arcing over and across the grooved topographies which may be the result of two or more axons meeting and initiating fasciculation.

2.4.4. Myosin IIA blocking by NGF promotes excessive fasciculation on grooved topographies

Since the application of blebbistatin for three days, as seen in the four day cultures led to very little or no change (Figure 22), increases in network size induced by inhibition for five days in six day cultures (Figure 20 and Figure 21) are likely to have been a result of trend effector inhibition, rather than the reduction in the rate of retrograde flow, or a combination of the two. On examination of the network morphologies, high concentration NGF resulted in the greatest amount of fasciculation and blebbistatin: the least (Figure 25, Figure 26 and Figure 27). Taking this into account in combination with findings of Liu *et al.* (2013c) which pinpoints that fasciculation is modulated by myosin II, it can here be proposed that fasciculation is mediated by myosin IIB. Further, since myosin IIA is responsible for GC retraction, it is defasciculation that is modulated by myosin IIA reasoned by the inability of fasciculating axons above to deviate from axons beneath as evidence from the fasciculated networks at the high NGF concentration (100 ng/ ml). Applying this thought process to the observed trends, blebbistatin results in neither defasciculation nor fasciculation, low NGF allows defasciculation whilst high NGF inhibits defasciculation. This gives an explanation for increased NGF concentration promotion of fasciculation observed in this and other studies (Houle and Johnson, 1989, Rutishauser and Edelman, 1980).

2.4.5. NGF may reduce substrate sensing

Another factor to consider is the effects of Myosin II inhibition on both the orientation of growth cone motility and overall axon network directionality. Generally, blebbistatin increased dispersion, likely arising from collapsed lamellopodia giving stronger intensities of filopodia. A percentage amount of GC orientation (straight, turning, spreading) across each culture condition (Figure 33 and Figure 34) revealed

high NGF concentration provides straighter GC with in general, a 50% decrease in turning. No difference in the percentage of GC turning, or straight among groups however there was a treble increase in spreading at 100 NGF on flat. In contrast to the average orientation, blebbistatin was seen to increase the amount of GC turning on all cultures except 100 NGF/grooves. This indicates that although directionality of blebbistatin as a whole is straighter however due to retraction lamellar retraction and GC collapse, the directionality analysis is likely being heavily influenced and thus; comparison between +/- blebbistatin cultures does not have enough reliability for a solid comparison. Overall, topographies may influence the amount of GC spreading (flat: greater spreading); however, the amount of turning is instead regulated by the NGF concentration (high: less turning). Increased NGF produced on average a straighter shape of GC on both surfaces. This is in agreement with both the myosin IIA intensity analysis and current consensus that myosin IIA is a key mediator in growth cone turning, a process by which is carried out filopodia retraction. The complexity of growth cones was seen to increase across three parameters (Figure 32); higher NGF concentrations, flat surfaces and with blebbistatin although this was not deemed statistically significant. Despite this, these trends are likely attributed to increase filopodia length (Gehler et al., 2004a), greater spreading (Figure 34), and GC collapse (Liu et al., 2013b).

On examination of network directionality (Figure 24), blebbistatin was seen to have reduced sensing to physical cues with average deviation from the grooves by ~7%. This was a consistent polar deviation to the right, resulting in a largely chiral shape which is difficult to explain. It may possibly be related to an uninhibited molecular motor or possibly to do with the DRG body itself and an axial tension created perpendicular to the grooves. High concentration NGF may also be seen to show less commitment to the confines of the microgrooved topography with the overall network shape bearing similarity to that of flat surfaces although it is unclear if this is due to fasciculation or substrate sensing. If the latter, myosin IIA inhibition at high levels of NGF is likely to be a key contributor to the reduced sensing of topographical cues through the inability to perform myosin IIA mediated filopodia retraction on meeting the side-wall of the groove.

The cell viability assay indicated that toxicity from excessive NGF supplied was not causing the observed reductions to outgrowth (Figure 28). This is further confirmed by

the greater numbers of neurites at higher NGF concentrations (Figure 26). Grooves were found to increase cell survival over flat surfaces which is consistent with our current knowledge of mechanical/topographical promotion of viability (Qi et al., 2013, Muhammad et al., 2015). Another explanation for this could lie in the SC or axon area distribution which was not measured. SC have been shown to secrete supportive growth factors such as, but not limited to BDNF and NGF, which promote neuronal survival and differentiation (Reynolds and Woolf, 1993); logically it can be surmised that grooves would promote a greater amount of SC/ axon co-localisation and thus, increase survival and extension.

2.4.6. The hypothesis of the observed NGF-topographical signalling trend

Condensing the results of this study into a hypothesis as to why the observed trend in which excess NGF levels and grooved substrates results in smaller DRG network sizes (Figure 36). This placed the extreme-fasciculation of axons as the key driving force, caused by the confinements of topographical grooves coupled with the antagonistic effects of excess NGF on myosin IIA activity. A higher NGF concentration results in larger neurite counts as well as inhibition of myosin IIA mediated defasciculation. These factors result in a greater elastic tension experienced by the axons underneath combined with a decrease in myosin IIA mediated focal adhesion strength. Also, with the increased number of axons crossing grooves, the potential for the conjoining of separate axons rises, creating fascicular arcs that transverse across the grooves. Fascicular arcs may then act to form a barrier to upcoming axons (yellow arrows, Figure 27). More importantly, with the opposite growth direction within these fascicular arcs, it is probable that a much greater lateral tension will be exerted on the axon and the growth cone. Of which; myosin IIA would be (if not NGF inhibited) the primary defence due to its function as the key component for transverse actin bundling. Overall this results in a critical loss of adhesion to large sections of the axon network and very poor network sizes.

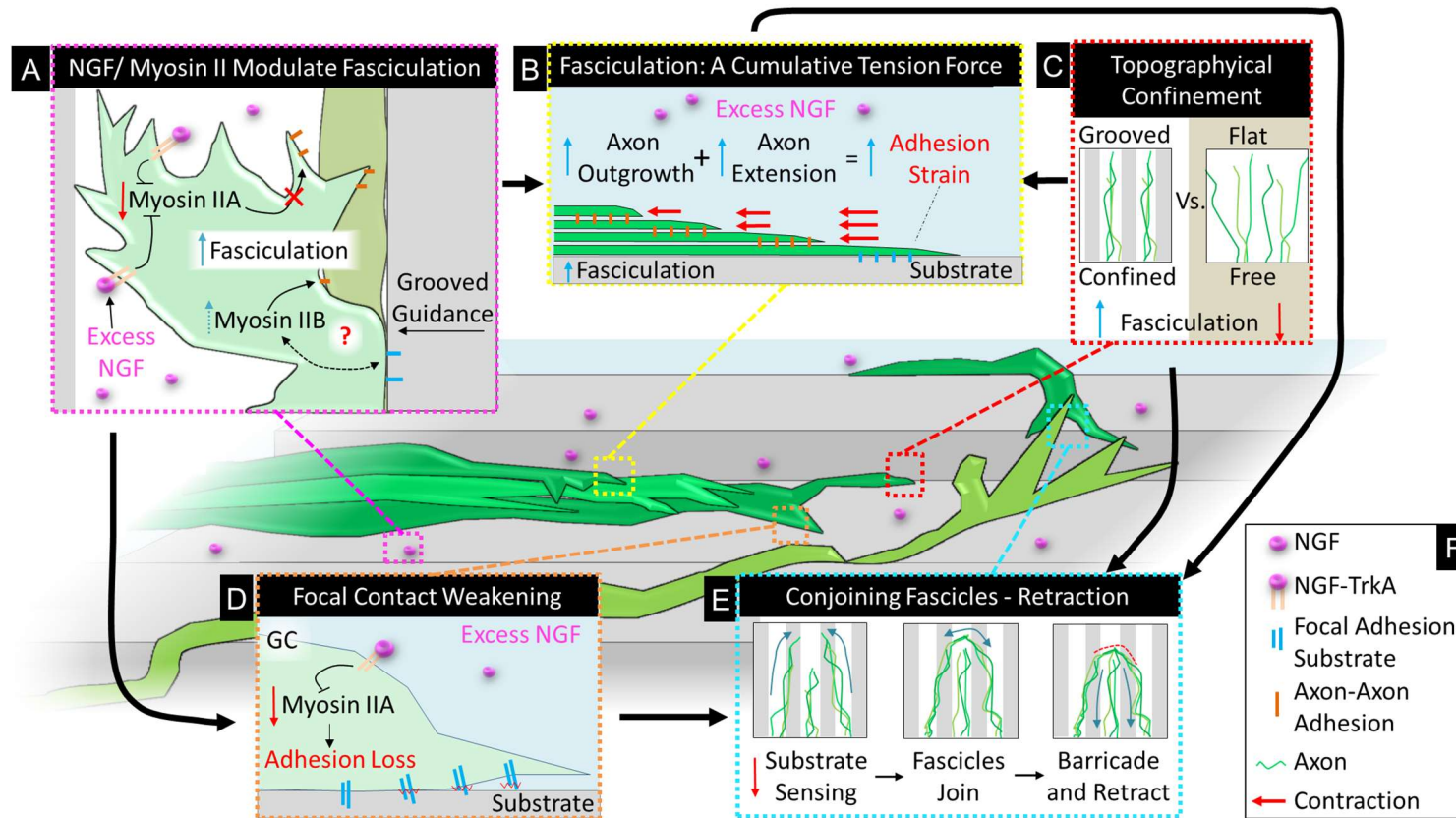
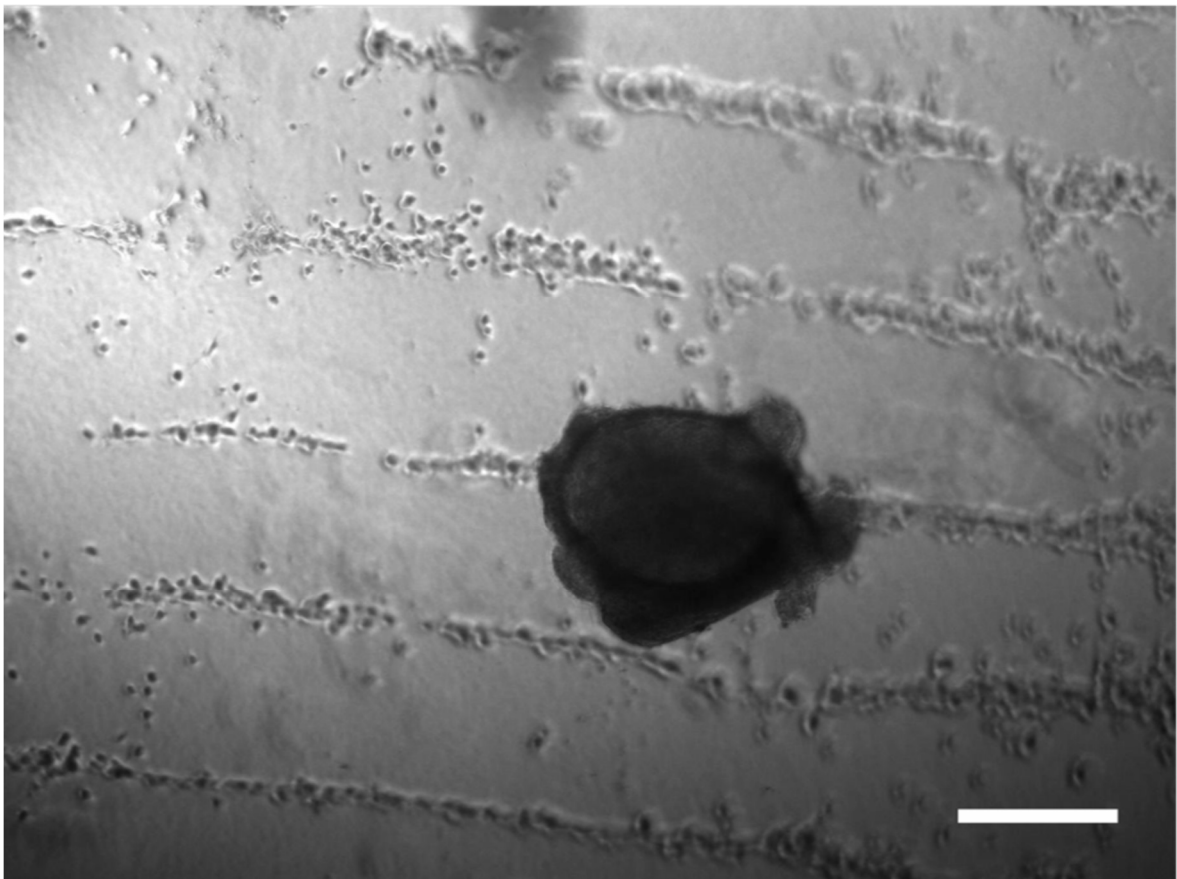


Figure 36: The hypothetical explanation for reduced DRG network size at high NGF concentrations on grooved substrates. This hypothesis implicates the antagonistic convergence of various factors instigated by the combined actions of topography and excessive NGF signalling, as the basis for the reduced outgrowth trend. As shown in (A), the excess of NGF in supply downregulates myosin IIA, which reduces axon-axon decoupling and thus promotes fasciculation. Additionally, the unidirectional axon extension caused by the topographical guidance may promote myosin IIB activity, a possible mediator for fasciculation. From event (B), NGF increases outgrowth and topography confines axons to narrower available surfaces; but of which cause further fasciculation. Altogether, these events contribute to the formation of multiple fasciculating axons which, under elevated axon extension rates provided by higher NGF concentrations (B), exhibit a cumulative tension force on underlying axons. As a result, the focal contacts of the bottom axons experience extraordinary strain. In contribution, the binding affinity to the substrate, regulated by myosin IIA is also reduced through NGF modulation (D). Overall, axons extend at a slower rate and lose adhesion, causing retraction. As fasciculating axons are not attached to the substrate, but the underneath axons, they also retract and thereby creates the highly dense, small networks observed at high NGF concentrations. The final occurrence which takes place is in the conjoining of separate fascicles, which causes adhesion loss as described but also effectively barricade or constrict preceding axons, heavily impacting resulting network size.

This hypothesis does not negate the possibility of topographical induced tension crosstalk mechanism as projected by the initial theory, which remains to be elucidated. In fact, this still remains an additional possible contributor to the above events. Finally, if there is a microgrooved induced increase tension, it is almost certainly not as a result of myosin IIA contractility, leaving myosin IIB to be the most probable culprit. Further validation of this hypothesis would be extremely beneficial to gain a true understanding of each active member which produces the reduced growth trend. Many routes remain available which could involve knockout studies of either myosin IIA/ B, inhibitory studies of the key signalling mediators such as Rac and other cytoskeletal components such as dynein, the microtubule motor protein. This is discussed in greater detail within section 6.1.1. The implications of the findings in this study are profound in the context of designing the optimum setup for nerve injury repair. This research proves that NGF concentration and topographical cues do not work in synergy but instead, may be antagonistic, despite their positive effects separately, highlighting the importance for further research into growth promoting interactions. Yet this study still only touches the surface of the clinical challenge as the addition of substrate mechanics and chemistry may have further widespread differences in combination.

3. Guiding Axons in 3-D: Fabrication of Arrayed ADSC- Collagen Hydrogel Scaffolds Using Octagonal Sonotweezers



“Pulling together for the greater good!” The beginnings of a uADSC aligned collagen hydrogel for the guidance of DRG outgrowth. Brightfield image of 375 μm alignment width, 25k uADSC conc. 25k and DRG explant. Scale: 300 μm

3.1. Introduction

Emerging nerve regeneration research bears an increasing focus on the use of 3-D approaches or incorporating them to some degree, as a means to investigate and improve current repair strategies (Petcu et al., 2018a, Cirillo et al., 2018). This shift from 2-D, has been encouraged following observed differences in cell behaviour between 2/3-D environments, a greater degree of similarity to the natural neuronal surroundings/ factors and a more translatable results, which impact on clinical application (Edmondson et al., 2014). Fundamentally, the choice of biomaterial is crucial, with successful nerve repair relying heavily on both physical and chemical properties of the conduit or scaffold. Mechanical requirements on the conduit encompass robustness to withstand compression, flexibility to allow movement, permeability to provide nutrient/waste exchange and biodegradability (Nectow et al., 2012). Furthermore, the internal lumen structure of the typical conduit should promote cell survival, directional guidance and rate of axon regrowth. Generally, these outcomes are achieved through material biocompatibility and permeability, physical cues and supplied neurotrophic growth factors or supportive cells respectively.

3.1.1. Hydrogels for peripheral nerve repair

Hydrogels are an interesting type of biomaterial which have rapidly gained widespread attention for applications in cell and tissue engineering (Drury and Mooney, 2003). Typically consisting of predominantly water (~90%), their low cost, tune-ability, convenience of production and biocompatibility provide adequate incentive for their use (Ahmed, 2015). Within a nerve repair context, hydrogels ranging from collagen, silk fibroin and alginate have been a suitable choice (Mosahebi et al., 2003, Xu et al., 2016, Hopkins et al., 2013). Particularly, collagen has been shown to improve directional guidance when aligned fibres are employed (Georgiou et al., 2013) and alterations to pore size, stiffness, fibre size have been investigated intensely although mechanical robustness of such gels is a recurring issue (Antoine et al., 2014).

3.1.2. Cells to support peripheral nerve repair

A number of different cell types have been investigated such as SC, ESC NSC ADSC (refer to 1.7.5 and 1.7.5.2) to be included as a supportive cell. ADSC are remarkably easily collected with minimal patient impact by isolation from fatty tissues (i.e. liposuction aspirate) and provide a beneficial influence on the regeneration of nerves. A study by Mohammadi, et al. (2013) showed that further improvements can be made by prior differentiation of ADSC to a glial lineage, which is readily accomplished in culture with the supplementation of selected growth factors for three weeks. Following this, elevated expression of neural markers (S100, nestin, p75, GFAP) and exhibit the morphological characteristics to SC (elongated, spindle shape) (Kingham et al., 2007, Tse et al., 2015). These similarities to SC continue through to cell function and behaviour, with dADSC shown to promote neurite length and outgrowth of motor neurons in culture, with comparable levels to SC. A recent in vivo study revealed recovery standards NGC incorporated dADSC to reach similar levels of of glial-differentiated bmMSC but lower than SC (di Summa et al., 2010). However, recently dADSC-EngNT scaffolds improved repair of sciatic nerve lesions over hollow NGC controls (Georgiou et al., 2015). In this, an anisotropic collagen matrix was formed containing aligned strands of dADSC along collagen fibres akin to bands of Büngner which, in conjunction, together produced highly directed neurite outgrowth, with greater numbers of neurites reaching the distal nerve stump. Under consideration of these studies, ADSC were selected as the candidate support cell used in this study with the strategy of forming artificial bands of Büngner suspended within collagen hydrogel scaffolds using acoustic induced cell patterning.

3.1.3. Acoustic patterning of cells

From a design viewpoint, current strategies have provided vague environmental cues for promoting directionality and rate of neurite outgrowth. This study aimed to address this vacancy through the creation of precisely fabricated cellular arrays suspended in collagen hydrogels using sonotweezers. This technique for particle manipulation has previously been employed mainly in 2-D setups (Bernassau et al., 2014); with applications in nerve regeneration shown through promotion of directional DRG growth with aligned SC (Gesellchen et al., 2014). Acoustic manipulation of cells and particles with sonotweezers has been possible in 3-D for almost 20 years (Bazou

et al., 2008, Kozuka et al., 2000) and is emerging as a valid platform for practical 3-D tissue engineering approaches. These have involved alignment of myoblasts in collagen to form mechanically anisotropic muscle tissue (Armstrong et al., 2018) or in the formation of vascular networks by endothelial patterning also in collagen (Garvin et al., 2013). To current knowledge, this is the first case of 3-D neural scaffold creation using the sonotweezer device.

The underlying principle of the sonotweezer device is to harness the ultrasonic waves generated by piezoelectric plates: lead zirconate titanate (PZT) which are activated during supply of A.C. voltage using a wave generator. This enables the non-invasive trapping of cells and micro-particles allowing the possibility of forming relatively complex patterns. Briefly; this is accomplished through the production of acoustic travelling waves that interact (de)constructively to create region specific pressure differentials which act on the suspended particles or cells. Pressure regions are generally controlled through thickness (determining the resonant frequency), positioning and activation (voltage applied) of the PZT transducer wave source and medium's compressibility and density.

The sonotweezer device used in this study used oppositely positioned transducers which were activated in-phase to create a standing wave within the medium, here: collagen at pre-gelation state. This results in the formation of linear bands of pressure voids (at points of zero wave amplitude) termed “nodes” that cells line up at and remain trapped in, creating the aligned pattern. The distance between aligned particles can be modulated by the PZT thickness determining the resonant or fundamental frequency and harmonics (integer multiples of the fundamental frequency). Additionally, the pressure force (and vortex in 3-D) applied on particles can be controlled by the voltage supplied.

3.1.4. Aligned cells - a suitable mimic for bands of Büngner?

Bands of Büngner, are strings of SC that act to guide regenerating axons and result from Wallerian degeneration (outlined in 1.2.3). Here, building on previous work in the group (Gesellchen et al., 2014), it was hypothesised that strings of cells could be formed in 3D using an acoustic sonotweezer and that these artificial Bands of Büngner would be able to guide regenerating axons. The formation of 3D hydrogels in the

setting of a sonotweezer device limited the choice to relatively fast setting collagen gel mixtures. Suitable alternative cell-reconfigurable materials typically consist of peptide-polyethylene glycol (PEG) hydrogels (Gjorevski and Lutolf, 2017, García, 2014); however, in comparison these are not as easily accessible and are more costly. With translation in mind and as SC are not easy to isolate, provision of these for repair of peripheral nerve in humans would require sacrificing nerve tissue and would require the use of immunosuppressants, ADSC were chosen as the appropriate alternative. The aims for this chapter are to address the following questions:

- Is it possible to reliably manipulate and trap cells within collagen hydrogels during gelation using sonotweezers?
- Will the behaviour of (d/u) ADSC, embedded in a 3-D hydrogel, differ between randomly distributed and acoustically aligned cells?
- Are collagen hydrogels with aligned ADSC potentially useful as constructs for the enhancement of nerve repair?

3.2. Methods

3.2.1. Sonotweezer fabrication

The sonotweezer devices used in this project were created by Dr. Anne Bernassau-Herriot-Watt University, for detailed instructions to the design and construction of the acoustic tweezer device please refer to: (Bernassau et al., 2014, Bernassau et al., 2013). Three devices were used for exploring these aims: (a) heptagonal cavity (with angled travelling waves: 154°), (b) octagonal cavity (travelling waves opposite to each other's) and (c) 3-D printed device with larger and shallower cavity (travelling waves opposite to each other) shown in Figure 37.

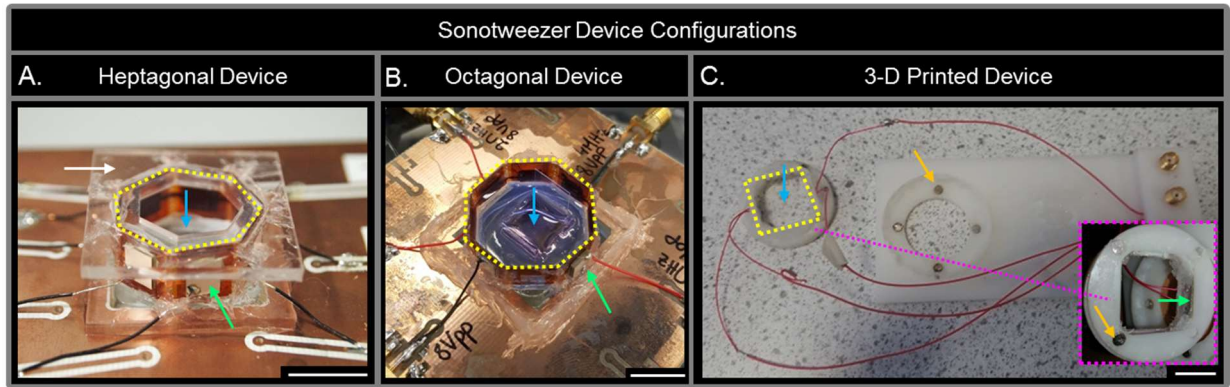


Figure 37: Overview of sonotweezer device configurations. Camera images of each device annotated to show: the cavity for acoustic field (blue arrow), the shape of cavity/ transducer formation (yellow dashes and PZT shown by green arrow). Image A displays the heptagonal device which had the smallest cavity (blue arrow), a lid for structural support (white arrow, not required in other devices) and also had transducers that were not oppositely placed (154° shape-heptagon). Image B displays the octagonal device, with oppositely placed PZT) in an octagonal formation (yellow dashes). Image C shows the 3-D printed device which had oppositely placed transducers in a square shape. This device was constructed in two parts with the transducer part remaining relatively free (purple dash) and during action, inserted into the petri dish that sits within the circular base, held together by magnets (yellow arrow). Scale:

The heptagon device offers a quick manufacturing as it is based on 7 lead zirconate titanate plates (PZT; NCE51, Noliac ceramics) that are directly bonded to a flexible printed circuit board (PCB), or flex circuit (Flexible Dynamics Ltd., Ipswich, UK) and forming it into a heptagon. When exciting 2 transducers simultaneously, two acoustic travelling waves are generated in the medium and an acoustic standing wave is formed where the 2 travelling waves interfere. One of the disadvantages of this device is that the trapping/patterning region is small (ca. 4x4mm).

For the octagon device, the PZT (NCE51 Noliac ceramic) plates were first treated with alumina loaded epoxy matching layers. These matching layers were a means to inhibit resonances which could create unwanted standing waves within the purposefully created nodal positions.

For both devices, the PZT plates were 5x5 mm with a thickness of 0.5 mm. The flex circuit was a ribbon of 10 mm width and 95 mm length, each face of the heptagon was 10 mm long. As mentioned above, the PZT plates were bonded to a flexible kapton ribbon or also called flexible printed circuit board (Flexible Dynamics Ltd, Ipswich UK) using super glue which was then folded into a heptagon or octagon. This was then attached to a perspex bottom in order to visualise the alignment and

provide a sterilisable containment. Following this, a custom design metal circuitry board containing a centre hole was attached with wire connections soldered into onto the PZT. The complete device was then further sealed with aquarium glue, see Figure 37.

In the case of the 3-D printed device, the design was modelled on that of (Courtney et al., 2011), making small modifications to the PZT size (10x2 mm) relative to the heptagonal and octagonal, in effort to create a wider field pattern. Using Autocad Software (Autodesk) the design was designed and then exported to a STL file, read into Ultimaker Cura software for slicing and realised in polymer on an Ultimaker II 3-D printer using acrylonitrile butadiene styrene. Neodymium magnets (2x1 mm) (First4Magnets) were attached to the transducer arm and dish holding chamber. PZT were bonded to the transducer arm and soldered to wires to connect to the frequency generator. The device was then sealed with aquarium glue for protection and to cover cracks which the collagen may enter.

The PZT layer thickness determines the resonant frequency of the device and thus the distance between adjacent pattern nodes (i.e. the pattern width). Here, the PZT plates were 0.5 mm thick, making a resonant frequency of 4 MHz ($F_r = \text{frequency constant of the material} / \text{thickness of the plate}$). For the heptagon and the octagon, at this frequency (4 MHz), the wavelength of the sound waves in water is $\lambda = 375 \mu\text{m}$.

For the heptagon, the distance d between the nodes can be calculated by $d = \lambda / 2 \sin(\theta / 2)$, where θ is the angle formed by the normals to the planes of the two sides with the active transducers.

3.2.2. ADSC extraction, culture, differentiation and characterisation

3.2.2.1. ADSC isolation

For this project, ADSC were isolated through processing of the fatty tissues removed from the groin area of matured Sprague-Dawley rats. These cells were isolated, differentiated, characterised and cryopreserved by Dr Suzanne Thomson (Thomson, 2018) who also granted access to these for this research. Briefly: euthanasia by

Euthatal® injection (500 mg/ Kg) was carried out in accordance with Home Office regulations by animal technicians. Upon tissue extraction, the fat pad was minced into cubes <1mm using a scalpel blade before being enzymatically dissociated using 30mg collagenase type I (ThermoFisher Scientific) dissolved in 15ml of HBSS, Gibco, UK with 0.5ml of penicillin Streptomycin (GE Healthcare) under incubation for 1 hour at 37°C. This was then passed through a 70µm filter to remove any dissociated tissue remnants and then diluted with ADSC media (disclosed below) to reduce collagenase action. The cell suspension was then centrifuged at 800xg for 5 minutes following which; the surface adipose lumps and lipid layer were gently aspirated leaving the stromovascular pellet. The pellet was then re-suspended within ADSC media which was then added to a T75 culture flask at a concentration of ca. 10k cells/ cm².

3.2.2.2. ADSC culture

ADSC culture was carried out in incubation providing a constant 37°C, 5% CO₂ within ADSC media consisting of: Gibco α-MEM [+ GlutaMAX, -Ribonucleases, DNAases] (ThermoFisher, UK), supplemented with 10 % FBS, and 1% antibiotic mixture (L-glutamine, penicillin streptomycin and fungizone) (PAA p11-002, UK). Cells were maintained at sub-confluent levels through a split/feed every ~three to four days using trypsin/EDTA (Invitrogen, UK) and used up to a passage of seven. Cell counting was carried out manually by haemocytometer and the cells diluted to be incorporated into the gel/device at a concentration of (12.5k or 25k per 25µl).

3.2.2.3. Differentiation to dADSC

ADSC were induced to an SC lineage following the protocol developed by Kingham *et al.* (Kingham *et al.*, 2007) through initial supplementation of 1mM β-mercaptoethanol (Sigma Aldrich) for one day followed by 35 ng/ ml all-trans-retinoic acid for three days. Complete differentiation was achieved after 18 days through the encouragement of a differentiation media containing of standard ADSC media plus: (14µM Forskolin (Sigma Aldrich, UK), 250 ng/ ml hNRG-1 (R & D Systems), 10ng/ ml FGF-b (ThermoFisher, UK), 5ng/ ml PDGF (Millipore, UK).

3.2.2.4. Characterisation of ADSC

The state of ADSC before and after differentiation towards a Schwann cell phenotype was assessed by Suzanne Thomson using morphometric analysis, immunolabelling and RT-PCR, briefly described below.

Stemness was confirmed by culturing ADSC for 48 hrs on glass coverslips followed by immunostaining of cell surface markers which are essential for categorisation as MSC. These consisted of positive: CD90 (ab225), CD105 (ab11414) and CD73 (ab175396) but negative for CD45 (ab10558) (antibodies sourced from Abcam).

The multipotent potential of the ADSC to form bone, fat and a SC like phenotype was assessed. After exposure to osteogenic media (StemProOsteogenesis: 100µg/ml ascorbate, 0.1µM dexamethasone and 10mM β-glycerophosphate) for 18-days the ADSC formed bone nodules positive for alizarin red. For adipogenesis, the development of and incorporation of fat storing vesicles within the cells after treatment with adipogenic media (Adipogenesis Differentiation Kit: low glucose DMEM, 1µM dexamethasone, 0.5mM isobutylmethylxanthine (IBMX), 10µg/ml insulin, 100µM indomethacin) for 21-days were shown by oil-red - O staining.

For SC differentiation characterisation, cell aspect ratio was measured to confirm spindle like shape in dADSC and even-spread in uADSC. RT-PCR indicated positive gene expression for SC markers S100, GFAP and p75 in dADSC alongside this, expression for the production of neurotrophic factors NGF, BDNF, GDNF and VEGF-A was seen in dADSC but not uADSC. Immunocytochemistry further confirmed differentiation by intense fluorescence of S100, p75 and GFAP in dADSC but not uADSC.

3.2.3. Collagen hydrogel creation

Soft and stiff hydrogels were created based on the protocol developed by Natasha Lewis (Lewis et al., 2016) using 2.05 mg/ml rat-tail collagen type I (First Link UK Ltd.) through controlling the pH with NaOH (Sigma-Aldrich). For the soft gels, 1ml of collagen type I was first put in a vial containing 0.2ml of ADSC media (listed above), 0.2ml FBS and 0.1ml 10x DMEM (First Link UK Ltd.). The phenol red pH indicator showed a yellow colour indicating a pH lower than 6. 0.1M NaOH (400-500µl) was then added rapidly until a bright pink colour was achieved indicating that a pH of ~7-8

which is suitable for collagen I self-assembly (Yan et al., 2012). For stiff gels, the protocol was slightly modified by increasing the molarity of NaOH to 1M, thereby gelation required only ~50µl NaOH. Setting time at room temperature was around 2-5 mins for soft whilst stiff gels were setting faster, at 30- 60 seconds. The gels were immediately added to the device or well plate by Pasteur pipette, taking care to avoid entrapping gas bubbles.

For collagen deformation analysis, a smartphone camera (Samsung S7) was used to capture an image per day and a ruled mat was used as a guide to allow comparative measurements. The physical properties of soft and stiff hydrogels (3 repeats) were measured with help from Dr Manlio Tassieri (UofG School of Engineering), to assess their elastic modulus using a rheological measurement, performed using a stress-controlled rotational rheometer (Anton-Paar Instrument MCR-302), able to detect torque values down to ~0.1 µNm. The rheometer was equipped with parallel plates geometry of 25mm diameter. Measurements were performed at a constant temperature of 23°C ± 0.01°C.

3.2.4. Sonotweezer operation

Three devices were used in this project with each having differences to the protocol of operation. Each device was sterilized by EtOH submergence for a 20-minute period. The heptagonal device required a foundation layer of agar to bring the particles into the correct field height. Agar was first dissolved in water (1.5g/ 100ml) in a beaker under moderate heat (ca. 60 °C) using a hotplate. Upon cooling, the agar gel formed in a bottle (for storage) and when required for use, this was reverted back to solution by a conventional microwave appliance at: “High” power/ 800W, 15-30 seconds. The gel was then applied to the desired location/device etc. and re-set with a time of ~2-3 minutes. The transducer field was switched on, ca. ~300 µl of the hydrogel added to the device, followed by 25 µl droplet of cells/10 µm polymer beads (Polysciences, Inc.) and left undisturbed until setting.

In the case of the 3-D printed device, a 3.5 cm petri dish was placed into the holding chamber and the transducer arm inserted into the culture dish. Magnets held both parts of the device together, locking the petri dish in place. Upon initiation of collagen hydrogel gelation, ~1ml of collagen solution was added into the dish whilst

the transducers were active, ensuring that all surfaces of the dish were covered. ADSC were then added to the collagen (25 μ l) and if required, the DRG explant as well, as soon as possible. Upon completion of the gelling process, the transducer setup was cut free from the collagen and dish by scalpel and removed, leaving the collagen construct inside the dish ready for culture.

The Octagonal device began with the creation of an agar mould through polytetrafluoroethylene (PTFE, Teflon®) blocks measuring 1 cm². In this, Aclar (Agar Bioscience, UK) was cut in rectangles (~1x3cm) and scored by scalpel blade twice to allow and facilitate accurate folding into a basic tray shape (1x1x1 cm) (shown within device in Figure 39A). This tray was then covered over the bottom surface of the PTFE block, and both inserted into the device, followed by the agar solution (until transducer line was reached (~1ml)). The side handle flaps of the Aclar tray were placed such as to ensure free acoustic pathways, as are necessary for the formation of the patterning field. Upon agar setting, the PTFE block was removed with minimal resistance leaving a cavity in the agar for the formation of square shaped collagen constructs. This agar cavity could be used repeatedly if proper care was taken through addition of a new Aclar tray. The transducer was then activated in preparation for the hydrogel formation. Collagen solution was then added to the agar cavity (~300 μ l) followed immediately by the ADSC (25 μ l) and then if required; the DRG using forceps. Partial setting occurred within ~1min however, the gel was left to sit for 4 mins to ensure complete setting and strengthen gel integrity. The gel could then be removed by gently lifting each flap of the Aclar tray simultaneously from the tomb and if required, incisions could be made to remove collagen/agar adhesions. The tray-gel was then placed in a culture plate with media and delicately moved until the gel appeared to slide with respect to the Aclar tray, indicative of being free-floating. The Aclar tray was left in during culture to provide an additional gauge for the initial direction of the alignment field and also to help protect the gel from excessive movement.

The transducers were driven using arbitrary waveform generator (TGA12104, Thurlby Thandar Instruments Ltd, UK). The settings for each device used were as follows:

- Heptagonal: 4 MHz Frequency/ 8 VppK, ~192 μ m pattern
- 3-D Printed: 6.88 MHz Frequency/ 5 VppK, ~107.5 μ m pattern

- Octagonal: 2, 4 MHz/ 6 VppK, ~ 375/ 185 μm respectively

For conduit trials, the alignment setup was very similar to the standard protocol. Micro-pored and micro-grooved (12.5 μm) PCL rolled conduits (~1 cm length) (Fabrication and characterisation described in detail in: (Thomson, 2018), obtained from Dr Suzanne Thomson, were cut to reveal a small gap for the addition of ADSC/ DRG and placed in the Aclar tray. Collagen solution was added whilst the conduit was held steady until fully submerged at which point the transducers were activated. The cells and DRG were added and alignment occurred to the chosen direction as the microporous PCL tube did not inhibit the formation of standing waves, even within the conduit (see Figure 51).

3.2.5. DRG/ ADSC collagen construct culturing

DRG extraction followed the same protocol used in Chp. 2. Cell culture was carried out in incubation providing a constant 37°C, 5% CO₂ in 1 ml / 22.5 mm diameter well (12 well plate) L15 media (Sigma, UK) supplemented with 10 % FBS, 50 $\mu\text{g}/\text{ml}$ n-acetylcysteine, and 1% antibiotic mixture (L-glutamine, penicillin streptomycin and fungizone) (PAA p11-002, UK). The volume of NGF 2.5S (Invitrogen, UK) was added to a concentration of 2ng/ ml. Cultures were split/ fed every second day for a period of 6-days at which point fixation was carried out.

3.2.5.1. Time-lapse culturing

Time-lapse cultures were carried out in a hot room of 37°C under CO₂ independent media (L15 media as above). Sterilised water filling remaining unused wells of the culture plate was done to ensure humidity. Images were captured (per 2 min) with an Axiovert 25 (Zeiss), with a 5x/ NA 0.12 objective lens (Zeiss), using a Guppy Pro camera and LabView Software (National Instruments).

3.2.6. Immunostaining

The protocol used bears similarity to that of Chp 2 however, longer incubation periods and more intensive wash steps were carried out due to the larger distances and longer diffusion times in the collagen hydrogel. Upon completion of the allotted culture period, constructs were fixed in 4% formaldehyde/PBS solution for 1 hour at 37°C.

This was followed by a permeabilisation stage through application of a buffer (per 100 ml PBS: 10.3g sucrose, 0.292g NaCl, 0.06g MgCl₂, 0.476g HEPES, 0.5% Triton X-100) for 1 day, incubated at 4°C. This was then removed and blocking solution (1% BSA/PBS) was added at 37°C for 1 hour under agitation. The blocking solution was then replaced with a 1 % BSA/ PBS containing the primary antibody anti-neurofilament heavy polypeptide (1:50, Abcam) and actin was labelled with Oregon green phalloidin (1:100, ThermoFisher Scientific). Samples were then incubated at 37°C for 6 hours followed by overnight agitation at room temperature. A wash step was then carried out involving 5 washes with PBS/ 0.5% Tween20 (Sigma, UK) solution for 20 mins under agitation each pass. Following this, samples were then incubated for 6 hours in PBS/BSA solution containing Texas Red conjugated anti-rabbit antibody (1:50, Vector Laboratories) and an overnight agitation period at room temperature. The previous wash step was then repeated. To image nuclei, a small drop of mounting medium containing DAPI (Vectorshield-DAPI) was dabbed on the surface of the substrate. Samples were viewed on an Olympus BX51 fluorescent microscope using 2.5, 5x and 100x objective lenses (Zeiss). Images were acquired using high resolution camera (QImaging), automated stage movement (Prior Scientific UK) combined with the auto-stitching of mosaic images with Surveyor Viewer software (Objective Imaging). For 3-D imaging, z-stacks consisting of 25 µm slices usually within a depth of 600 µm (adjusted if required).

3.2.7. Birefringence analysis of hydrogels

Analysis of collagen alignment was carried out using an Axioplan2 (Zeiss) microscope modified with polarization fittings involving a binocular crosshair gauge and rotatable stage. Gels were carefully placed onto a quartz glass microscope slide for analysis. Objective lenses (x4 (Motic), x10/ 0.3 Pol (Zeiss), x20/ 0.5 Pol (Zeiss)) were used to focus on points of the gel and videos were captured whilst slowly rotating the stage using a QImaging MicroPublisher 3.3RTV camera and QCapture software (QImaging). Image frames were taken the brightest point and its 45° rotation of each culture video and were analysed using ImageJ: Density Plot (~230 µm length, 75 µm thick), at 3 different points within the culture. These were then averaged and compared through a subtraction of mean grey value of light and dark to give the increase in grey value upon rotation and as a result the degree of birefringence/ collagen alignment.

3.2.8. Data analysis

3.2.8.1. Time-lapse cell tracking

Time-lapse videos of each culture were cut down to 12-13 hours for consistency and altered from 2 to 20 mins/ frame. Using FIJI (Schindelin et al., 2012) a stack was created and the Plugin: Manual Tracking was used to map a chosen point through the stack. For cell alignment tracking, the stack was first rotated to 90°. Then 4-6 cells were chosen at different regions of the pattern and then followed to provide a data set consisting of XY coordinates and distance travelled. The distance was then used to calculate the speed (per min) and the coordinates; the direction. To reduce comparative complexity and provide a simplistic gauge on cell-cell behaviour between or within lines of the pattern, the directions were split into 3 bins: Lateral (Perpendicular to pattern): 0-40°, Longitudinal (along pattern): 50-90° and equiangular (both): 40-50°. The average velocity was used in this chapter as a proxy to measure for the contractile strength of the cellular pattern and direction of pull. This was done on the presumption that greater contraction force between pattern lines/ cells will cause faster movement of neighbouring cells.

3.2.8.2. Axon network directionality analysis

From the 3-D fluorescent images, a single image of the entire stack was obtained using the Extended Depth of Field ImageJ Plugin (Forster et al., 2004) under “Easy Mode”/ High quality settings. The “pancaking” of images was possible due to the relatively planar growth of the. Each image was then rotated until the alignment pattern pointed horizontally to 0°. Following creation of the rotated EDF image, the Filament sensor software (Eltzner et al., 2015) was used with the “Filament Tracer” command (detailed in Section: 2.2.7.3). Averages were aggregated into a histogram. Randomly seeded cultures were rotated to their maximum Ferret’s diameter for comparison.

3.2.8.3. Statistical analysis

Graph creation and statistical analysis was performed using GraphPad Prism version 6 (GraphPad Software). The difference in gel deformation analysed by a paired Two-

way ANOVA with a Tukey post-hoc test for multiple comparisons and for the effect of uADSC/dADSC on contraction; an unpaired two-tailed Student's t-test was used. Micro-rheology results for elastic modulus was tested across 3 separately made gels and analysed for significance by Pearson's coefficient correlation. Analysis of DRG results were gained from a minimum of 3 explants from different rats. Birefringence and time-lapse tracking analysis was carried out with 3 different regions of each gel and 4-6 different cells respectively, from one biological repeat. Statistical significance was determined by $p < 0.05$, and presented by * $p < 0.05$, ** $p < 0.01$, *** $p < 0.001$ and **** $p < 0.0001$ complete with standard deviation bars.

3.3. Results

3.3.1. Method development

3.3.1.1. Acoustic standing waves pattern particles and cells in 3-D collagen hydrogels

The very nature of this chapter was unexplored territory, delving into the use of sonotweezers for the alignment of cells in a 3-D setting. Initial results obtained by Dr Frank Gesellchen during his postdoc had been discouraging with the forces that arise during gelation, disturbing any pattern that had been attained by acoustic tweezing (pers. Communication, Dr Mathis Riehle). Coupled to this was the necessity for the material to remain in liquid phase for the initial alignment followed by solidification to create the solid construct product. A description of device modifications, protocol alterations and their outcomes is described in Figure 38 and listed in Table 2 and Table 3, complementary to the text below.

Confirmation of the working theory was acquired using the older device model: the heptagonal sonotweezer, which successfully aligned micro-beads within the rapid setting agar gel to a pattern width of $\sim 200 \mu\text{m}$ (Figure 38B). Following this, an attempt was made to align cells within a biocompatible gel. Starting with immortalised human fibroblasts (hTERT) within a collagen type I gel, which had a much longer setting time ($\sim 5-10$ mins) than the agar used for the beads. As a result, alignment was observed however cells appeared to reside predominantly at the

bottom of the gel and no further analysis was carried out as the gel could not be extracted from the device (not shown).

In order to rectify the shortcomings of the heptagonal device, a slightly different approach was taken involving a switch to a two-piece, 3-D printed device (Figure 37C and Figure 38B). This setup consisted of a transducer arm (with oppositely positioned transducers) and a holding station which locked together magnetically (Figure 37C, orange arrows). Longer, narrower transducers were incorporated (1x0.25cm) in efforts to attain a wider area of acoustic field. Alignment/ hydrogel formation took place within the culture plate (petri dish) and following gelation, the perimeter of the gel was then cut (via scalpel) from the transducer arm of the device. This left the aligned gel construct within the dish ready for culture with some success. Issues arose regarding reproducibility and gel robustness due to the dimensions of the gel formed (shallow depth, large area; ca. 2mm x 20x20mm, shown: Figure 38D). Pattern damage was also likely as the act of cutting stretched the gel.

The octagonal sonotweezer was the final device iteration and was selected for experiments in this study (Figure 37B and Figure 38E). This design followed a reversion back to the heptagonal setup in which the gel was formed within the device and had to be transported for culture. Elements of the 3-D printed device were incorporated such as: the oppositely placed transducers, a slightly larger chamber size and an open top for ease of handling. However, a reversion back to wider, shorter (0.5x0.5cm) PZT (as used in heptagonal device) was implemented as a means to maximise the alignment zone through the entire depth of the gel. In addition to the device modifications, alterations to the mode of handling the gel were made through the creation of an agar mould and an Aclar tray holder. This proved to be extremely successful both: in the creation of hydrogels with highly reproducible dimensions, and a convenient transport mechanism to the desired culture dish. As a result of this, gels could be assessed accurately for variations in shape or size in the presence of ADSC.


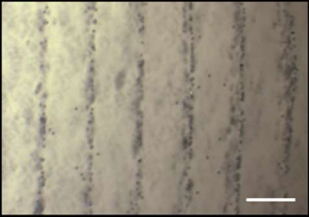
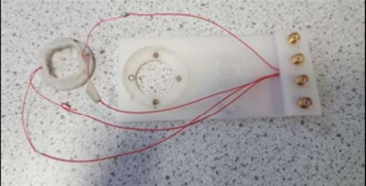

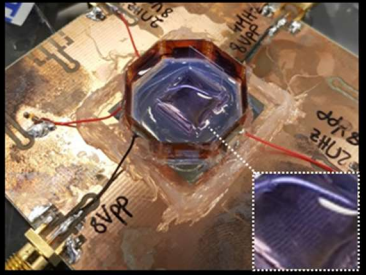
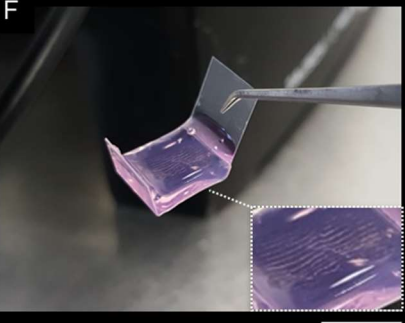
Acoustic Device	Method Iteration	Aligned Gel	Progress/ Issues
<p>A Heptagonal</p> 	<p>Initial attempts consisted of filling the chamber with collagen upon a pre-set agar bed (for correct field height) followed by dropwise addition of cells/ beads. Cells cultured within device.</p>	<p>B</p> 	<ul style="list-style-type: none"> • Alignment (95 μm) of beads/ cells • Unable to remove finished gel • Small pattern area • Difficulties in handling due to narrow lid gap
<p>C 3-D Printed</p> 	<p>Two part device consisting of PZT (inserted into petri dish) and the dish holder clamped together magnetically. The gel was made within the culture dish with the device then cut from the hydrogel with a scalpel.</p>	<p>D</p> 	<ul style="list-style-type: none"> • Alignment of beads/ cells/ silk + DRG (107.5 μm) within petri dish • Large pattern area • Requires gel to be cut out from device with scalpel: reproducibility and gel/ pattern damage • Gel transport not possible
<p>E Octagonal</p> 	<p>Reversion back to gel formation within the device following modification to the larger octagonal setup with easy access. Agar was molded using PTFE blocks and Aclar sheet was cut to create the hydrophobic trays holding the collagen. Gels were then transported to a well plate for culture.</p>	<p>F</p> 	<ul style="list-style-type: none"> • Alignment of beads/ cells/ silk + DRG (185/ 375μm) within free gel • Sufficient pattern area • Consistent gel size allowing deformation analysis • Robust gel thickness for handling • Gel transport possible using Aclar tray

Figure 38: Method Development for Sonotweezer Creation of Nerve Guidance Scaffolding. Image (A) shows the heptagonal setup with transducers situated slightly askew and the resulting alignment of 10 μm polystyrene microspheres (B). The 3-D printed device (C) shows the 2-part design, with the large rectangular holding station for the petri-dish and the smaller circular transducer arm which gets inserted to the dish for alignment. Image (D) shows a typical gel construct formed from the printed device following successful device removal. The gels created were flimsy due to their high surface area to low height and had high shape variations. The octagonal device depicted (E) with agar, aclar tray and collagen gel shows construct fabrication during alignment (silk microfiber (Chp. 4)) and the very same gel following extraction (F). White dotted insets magnify for clarity. This gives an insight into the ease of handling and transportability. Scale A, D, E: 1 cm, Scale B: 200 μm , Scale C: 500 μm

Device	Device Modification	Outcome
Heptagonal	Alignment hTert/ Collagen, square PZT	Successful alignment, unable to remove gel from device
Heptagonal	Culture within device	Contamination issues, visualisation difficulties
3-D Printed	Functioning altered to pattern inside culture well	No requirement for transfer to culture dish required separation of gel from device which causes pattern disruption, problems with robustness of wires due to mobility of transducer arm, stability issues keeping PZT in single plane
3-D Printed	Magnets inserted to device	Stability issues resolved
3-D Printed	Larger device cavity for holding gel	Larger and thinner gels, robustness issues at centre of gel
3-D Printed	Rectangular PZT, Larger length but shorter height	Larger pattern field, less acoustic streaming issues due to smaller working depth
3-D Printed	PZT situated opposite	Greater alignment precision
3-D Printed	PZT depth lowered to surface of well	No discernible effect
Octagonal	Reversion to alignment within device cavity chamber, mid cavity size	Better alignment quality, acceptable gel dimensions
Octagonal	PZT reverted to square, situated opposite	Greater alignment quality through depth, less streaming
Octagonal	Removal of device lid	Slightly less robust device, much better gel accessibility

Table 2: List of modifications to devices and progressive outcomes

Entity	Protocol alteration	Outcome
Collagen	Preparation on ice	Long setting time (>10 mins), cell/ particle sedimentation at bottom of gel
Collagen	Preparation at room temperature	Shorter gelation time (~ 3-5 mins), gel robustness issues
Collagen	NaOH molarity increased	Acceptable and predictable gelation time (30- 60s), robust gels, requires efficient handling
Collagen	High collagen solution concentration (ca. 5 mg/ ml)	Rapid gelation, viscosity too high for patterning
Agar	Moulded cavity of agar within device	Allowed reproducible gel dimensions and a controllable shape
Aclar	Tray created from aclar sheet placed within agar cavity	Allowed transport of gel with minimal pattern disruption, hydrophobic surface minimized collagen adhesion
Cells	Addition to collagen solution before sonotweezer device	Very poor pattern, extensive streaming and cells residing in outside edges or the bottom of device
Cells	Addition to device approx. 30 secs after collagen gel solution	Consistent depth of cell suspended
DRG	DRG added before cell patterning	DRG and cell depth inconsistent, DRG sinking to bottom
DRG	DRG added after cell patterning	Greater depth consistency of DRG and cells, possible pattern disruption with DRG addition
Operation Parameters	Alignment tested at a variety of voltages and harmonics	Optimal found, High Vppk resulted in high acoustic pressure/ sedimentation of cells. Deviations in frequency reduced patterning accuracy

Table 3: List of protocol alterations in pursuit of optimal method

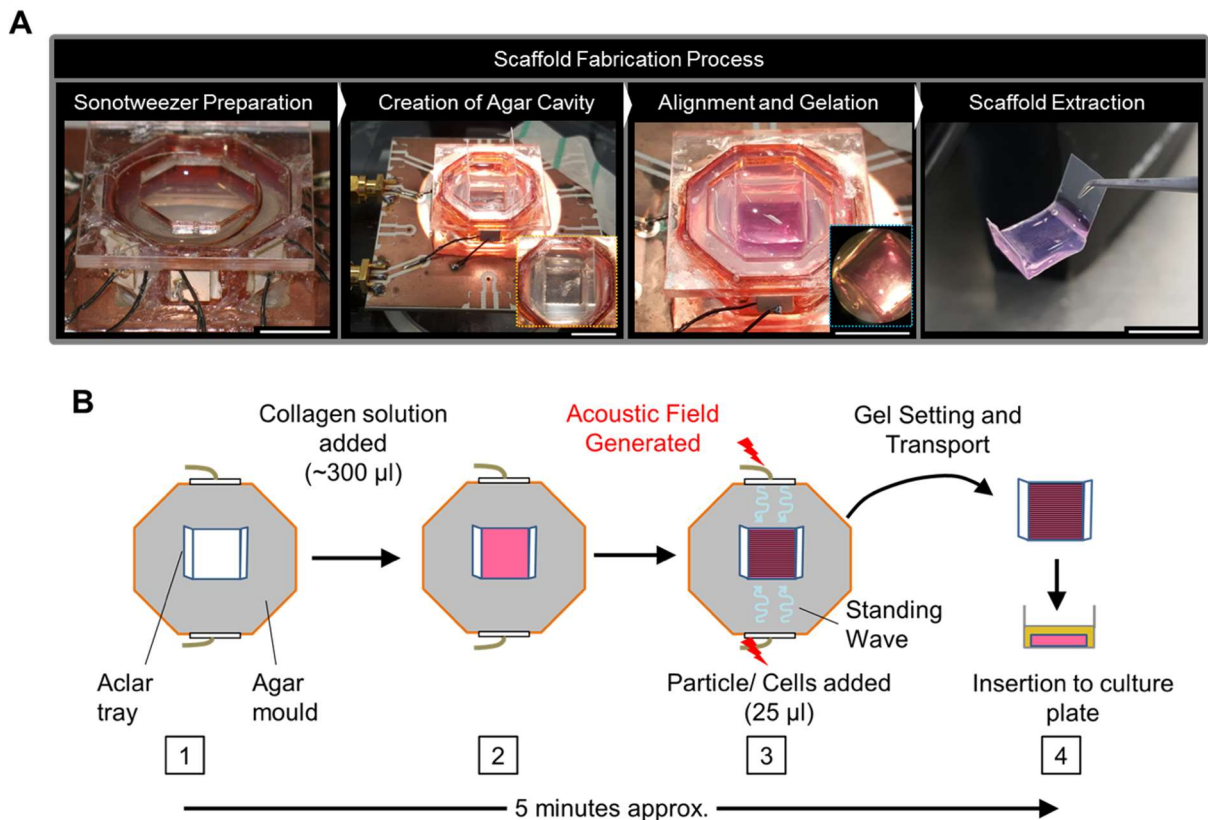


Figure 39: A visual schematic for the fabrication of aligned constructs. The method is described in detail within section: 3.2.7. Image-set (A) shows the process in practice with insets to give a detailed image from above the device (orange: agar cavity with Aclar tray, blue: magnified image of aligned particles). The procedure begins (1) with the creation of a cavity for the hydrogel to set in, within the field of transducers. In this agar was moulded using PTFE, leaving space for the Aclar tray to sit in which was inserted with handles facing the non-transducing sides. Collagen gelation was initiated in a vial and then $\sim 300 \mu\text{l}$ was put into the tomb (2) and the acoustic field was switched on. A $25 \mu\text{l}$ droplet of cells to a known concentration (12.5k or 25k) was then applied to the surface of the unset gel and alignment occurred (3). Gel setting occurs within ~ 1 min and a further ~ 3 -5 mins was used to further ensure complete gelation. After, the aclar tray- hydrogel construct was removed from the agar/ device by forceps carefully and put into a well plate for culture. Media was added and the tray/gel was agitated slightly to separate from one-another. Scale (excluding insets): 1 cm

3.3.1.2. Soft collagen gels lack mechanical strength to withstand uADSC contractile forces

Upon alignment of ADSC within the initial “soft” collagen type I gels created by the conventional method (described in section 3.2.3), a massive reduction in gel size was observed within 24 hours. Phase contrast images revealed that all patterning that had been applied to the cells had been lost over the same period. On closer inspection, a dense cell cluster was found in each gel with evidence of collagen alignment seen around the cell aggregation perimeter (Figure 40: right).

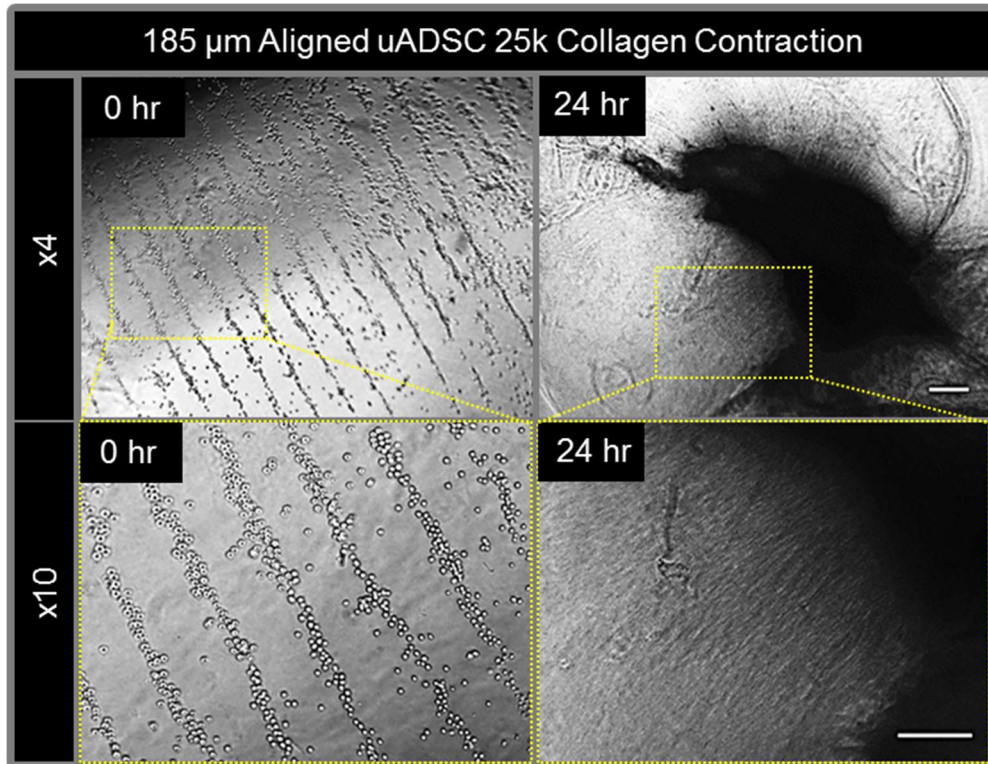


Figure 40: Initial soft hydrogel contraction by aligned uADSC. A typical collagen hydrogel with aligned uADSC using the octagonal sonotweezer to a pattern width of 185 μm seen at both x4 and x10 magnification at 0 hrs. Following a day of culture, it was found that cultures lost all alignment, clustering together with an excessive loss in hydrogel size. From the higher magnification, fibres of collagen can be seen surrounding the cluster, suggesting a contraction and remodelling, instead of motile congregation. Scale: 200 μm

3.3.1.3. Stiffer, faster setting collagen hydrogels allow reliable 3-D patterning

As key constraints for the use of the gels as nerve guidance constructs is in their robustness and maintained length across the lesion site, tougher gels were investigated. This involved increasing the concentration ratio of collagen to bulk solution through increasing the molarity of NaOH added. By using a lower volume of NaOH to neutralise, the final concentration of collagen type I increased from ca. 1 to 1.3 mg/ml. Through micro-rheological testing (Figure 41b), the gels produced using this method were found to be 2-3x stiffer than those made using more dilute collagen type I solution. Further, the higher concentration of collagen resulted in a more rapid setting time (from 4-5min to <1min) which was advantageous for the trapping of cells

as these remained suspended because they could no longer settle at the bottom of the dish.

3.3.1.4. Cell density is more important than collagen stiffness for shape retention of 3-D constructs

Analysis of gel deformation (images: Figure 41 and data: Figure 42) on soft collagen showed that the cell-free control gel had negligible difference to gel size whilst 25k ADSC resulted in a reduction of (approx. -0.9cm^2 / -80%) on average. In contrast to this, the stiff collagen showed significantly higher size and shape retention than soft (25k: approx. -0.45cm^2 / -40%), with 12.5k cells showing very little difference to the soft cell-free control. Further, a difference between aligned/random distributions was only found for 12.5k/ stiff collagen and none of the others (25k soft, 25k stiff).

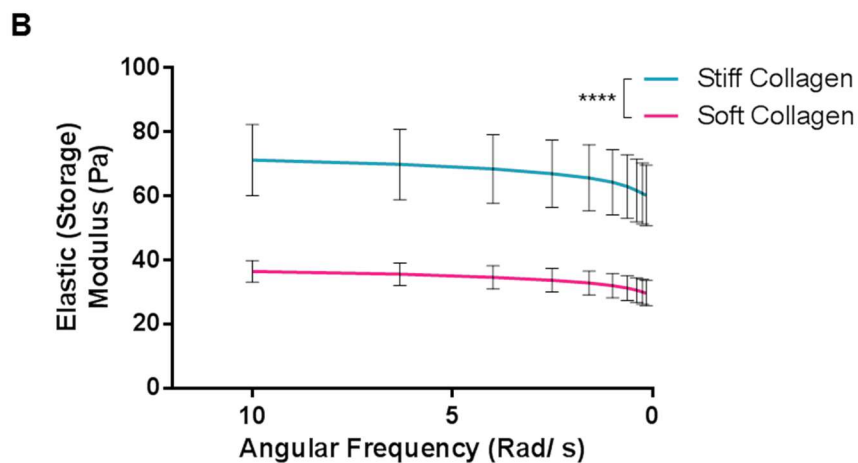
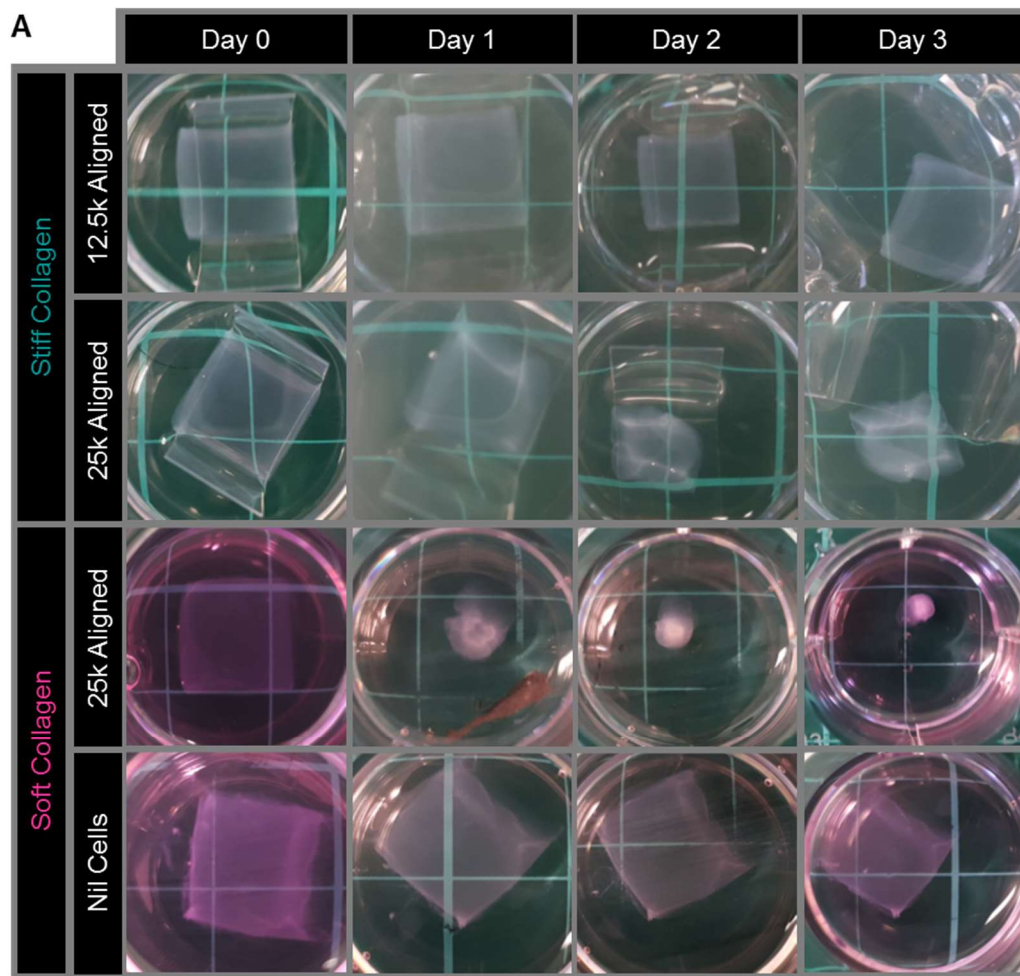
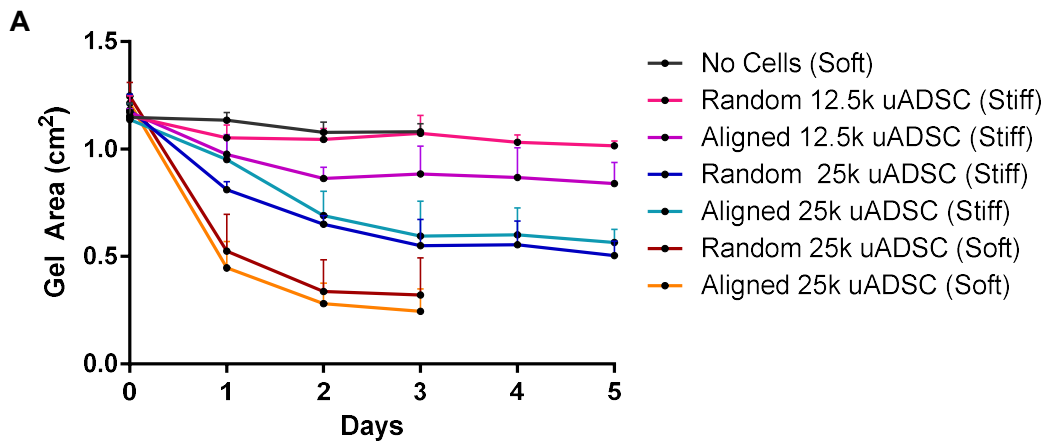


Figure 41: Mechanical strength comparison between stiff/soft collagen hydrogels. From the visual comparison (A), it can be seen that the stiff collagen hydrogels are able to withstand the contractile force of the uADSC in comparison to soft hydrogels which experience overwhelming contraction to an excessive loss in hydrogel size. Without uADSC, the soft hydrogel does not increase or decrease in size, indicating that the contraction is a result of ADSC and not through natural structure changes within the collagen. Further, it can be seen that the greater amount of cells results in more contraction serving as further confirmation of the above. Finally, micro-rheological analysis (B) of each type of hydrogel shows the stiffer to have 2-3x significantly greater elastic modulus than the soft. Micro-rheological analysis on 3 technical repeats of each gel and averaged, with significance determined by Pearson's Correlation where **** $P < 0.0001$. The bars indicate standard deviation. Scale Grid: 1cm^2



B

Significance Comparison			Day 1	Day 2	Day 3	Day 4
Aligned 25k uADSC (Stiff)	vs.	Aligned 12.5k uADSC (Stiff)	ns	ns	ns	*
Aligned 25k uADSC (Stiff)	vs.	Aligned 25k uADSC (Soft)	ns	****	****	***
Aligned 25k uADSC (Stiff)	vs.	Random 25k uADSC (Stiff)	ns	ns	ns	ns
Aligned 25k uADSC (Stiff)	vs.	Random 12.5k uADSC (Stiff)	ns	ns	***	****
Aligned 25k uADSC (Stiff)	vs.	Random 25k uADSC (Soft)	ns	****	***	*
Aligned 25k uADSC (Stiff)	vs.	No Cells (Soft)	ns	ns	**	****
Aligned 12.5k uADSC (Stiff)	vs.	Aligned 25k uADSC (Soft)	ns	****	****	****
Aligned 12.5k uADSC (Stiff)	vs.	Random 25k uADSC (Stiff)	ns	ns	ns	***
Aligned 12.5k uADSC (Stiff)	vs.	Random 12.5k uADSC (Stiff)	ns	ns	ns	ns
Aligned 12.5k uADSC (Stiff)	vs.	Random 25k uADSC (Soft)	ns	****	****	****
Aligned 12.5k uADSC (Stiff)	vs.	No Cells (Soft)	ns	ns	ns	ns
Aligned 25k uADSC (Soft)	vs.	Random 25k uADSC (Stiff)	ns	***	***	**
Aligned 25k uADSC (Soft)	vs.	Random 12.5k uADSC (Stiff)	ns	****	****	****
Aligned 25k uADSC (Soft)	vs.	Random 25k uADSC (Soft)	ns	ns	ns	ns
Aligned 25k uADSC (Soft)	vs.	No Cells (Soft)	ns	****	****	****
Random 25k uADSC (Stiff)	vs.	Random 12.5k uADSC (Stiff)	ns	*	****	****
Random 25k uADSC (Stiff)	vs.	Random 25k uADSC (Soft)	ns	**	**	*
Random 25k uADSC (Stiff)	vs.	No Cells (Soft)	ns	**	****	****
Random 12.5k uADSC (Stiff)	vs.	Random 25k uADSC (Soft)	ns	****	****	****
Random 12.5k uADSC (Stiff)	vs.	No Cells (Soft)	ns	ns	ns	ns
Random 25k uADSC (Soft)	vs.	No Cells (Soft)	ns	****	****	****

Figure 42: Comparative analysis of collagen hydrogel deformation by uADSC. (A) shows a line graph of average gel size deformation over time, comparing soft/ stiff gels, cell concentrations (12.5k/25k) and distribution (Aligned/ Unaligned). It can be seen clearly that soft gels (carried out in standard uADSC media) experience massive contraction whilst the stiffer gels (carried out in 2 ng/ml⁻¹ DRG media) support a greater mechanical strength. Also, the doubling the cell concentration was found to result in a significant increase in deformation to the gel. Table (B) compares each culture group, revealing at which time point (if any) there becomes a statistically significant difference. No significant difference was seen between aligned/ unaligned cultures except with the lower cell density on stiff in which, aligned exerted greater contraction of the gel. Significance was determined by paired two-way ANOVA with a Tukey post hoc test *p<0.05, **p<0.01, ***P<0.001 and ****P<0.0001 where n≥3 across 3 biological repeats excepting the No Cells (soft) where n=2 technical repeats. The bars indicate standard deviation.

3.3.2. Collagen embedded aligned ADSC behaviour within 3-D collagen (I) hydrogels

The creation of reproducible, ADSC aligned collagen hydrogels able to withstand the force of cell contraction/ remodelling prompted the further investigation into how the ADSC behave when aligned in a 3-D collagen environment. From the birefringence analysis of low and high density aligned (375 μ m width) ADSC gels (Figure 43), alignment of collagen fibres was found between the pattern lines in a perpendicular direction. Further, the gels seeded with the higher cell concentration/ number of cells showed a greater degree of fibre alignment (as shown by LUT). No birefringence/ fibre alignment was observed on nil-cell collagen gels that were formed within the acoustic field.

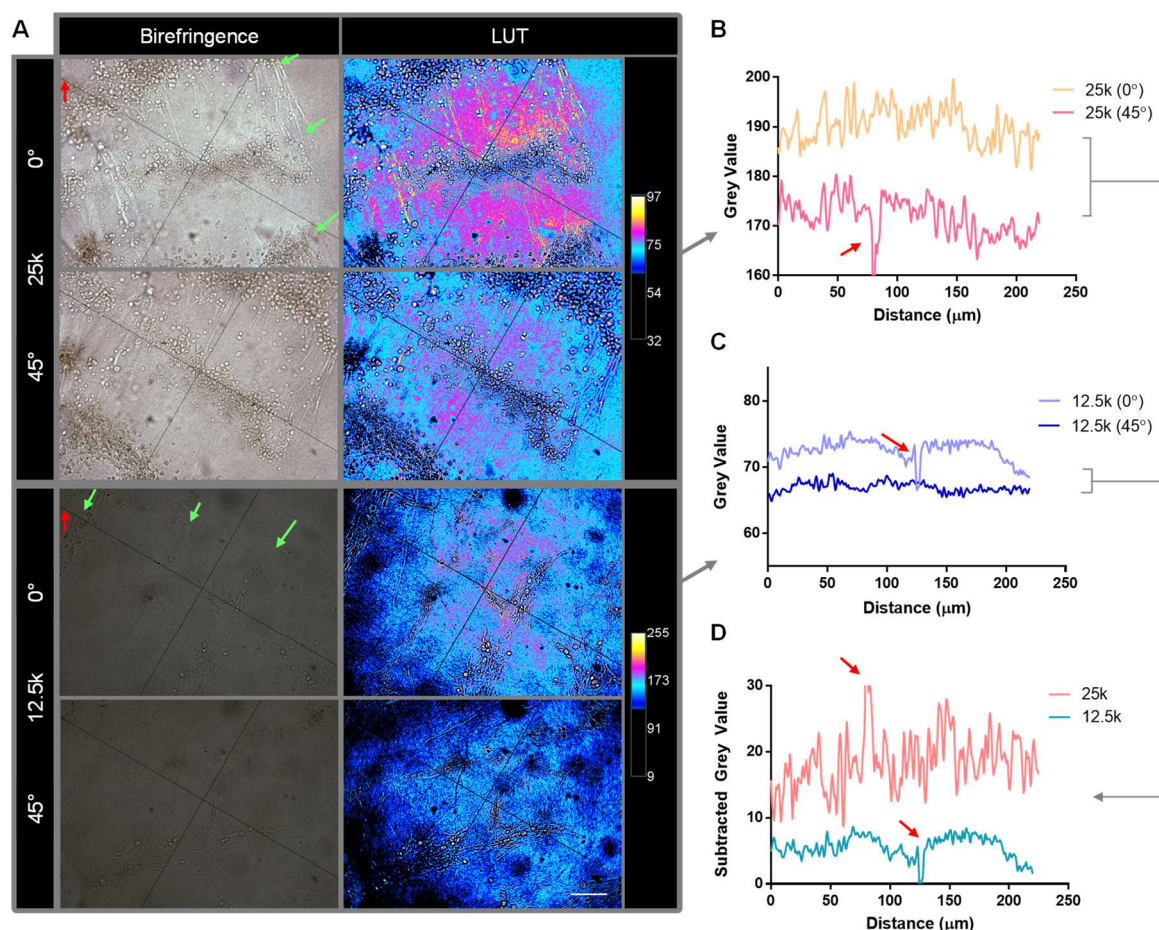


Figure 43: Birefringence analysis of 375 μ m aligned uADSC hydrogel contraction from 6-day cultures. A polarised microscope was used to reveal the alignment of collagen fibres within the gel by contraction (A). Higher cell densities were found to exhibit greater polarisation of light (Pink: bright, black: dark) upon rotation and thus a greater level of alignment of collagen fibres by contractile forces. As each had image initially had different brightness levels (due to: size of gel, brightness of microscope etc.) different LUTs grey levels had to be used. However, this was calibrated through a subtraction of light-

dark for each and provided a comparison of differences (B). Green arrows highlight the pattern lines/ direction and red Arrows Indicate points which analysis was influenced by the orientation gauge. For analysis, the average histogram was created from 3 separate areas (~200x75 μm) of a single culture. Scale 100 μm

To visualise ADSC behaviour, time-lapse phase contrast microscopy were used both: at low and high densities two different pattern widths (185 and 375 μm). This confirmed that contraction of the hydrogel instigated was instigated by ADSC. A kymograph (FIJI, Kymograph Builder plugin) (Figure 44 and Figure 45) was created from a 1 mm line across the pattern indicating that with higher cell densities, the pattern condenses laterally via contraction. Using Manual Tracking Analysis in FIJI, the movement of randomly selected individual cells (4-6) were followed giving a contraction velocity which for this chapter was assumed to be an indicator for contraction force. Upon comparison, it was found that within the initial few hours, a large spike in contraction occurs in the direction of the pattern lines, with the larger cell amounts producing greater contractile force. Patterns with a higher number of nodes, less separation also showed an increasing speed of contraction indicating that the force applied on the gel may have increased. At the high cell density with a velocity average of 5 μm / min, whilst the less densely seeded gels showed an average of 3 μm / min. This could also be seen in pockets of dense cell populations in which pattern was disrupted or by random occurrence which can override the alignment directed contraction creating issues. Following ~three hours, lateral contraction became a competitive force across each group and dominant at the narrow pattern/ high cell density which contrasted the wide pattern/ high cell density showing a relatively balanced force.

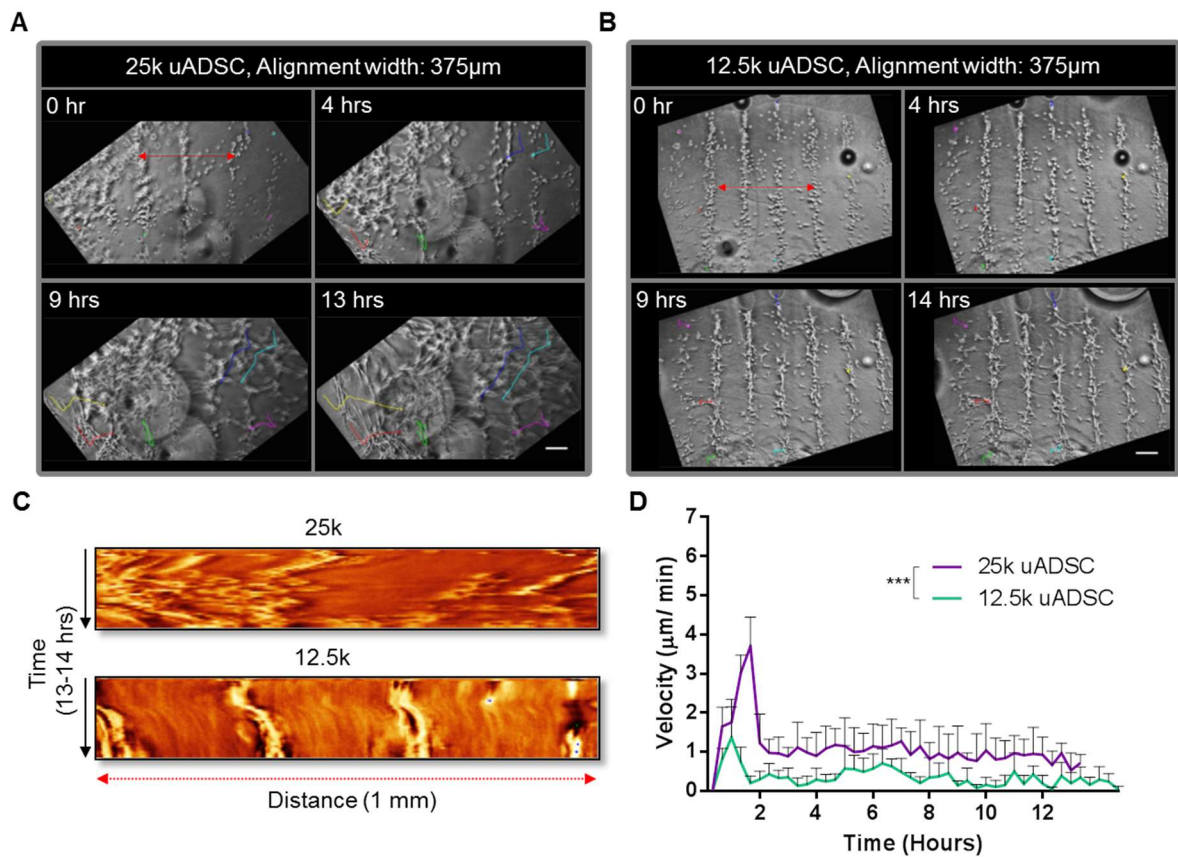


Figure 44: Manual tracking analysis of pattern contraction by 375 μ m aligned uADSC (13-14hrs) time-lapse image-sets. From time-lapse recordings of high (A) and low (B) density ADSC alignments, ImageJ plugin "Manual Tracking" was used to map cell movement (gel contraction). Each cell tracked for analysis can be seen by each line colour. Higher ADSC amounts can be seen to result in greater pattern distortion and the resulting pattern by the end of the time-lapse there is a stark contrast in pattern retention. From the kymograph (C) images of a line across 1mm of pattern (A, B: location shown by red dotted arrows), pattern lines of the high conc. ADSC gels contracted together whilst the lower conc. remained separated with a small reduction in width. From the average velocity analysis comparing both high and low conc. of ADSC gels, there was a spike in the velocity from 0-2 hours, followed by a relatively consistent rate of contraction with double the ADSC conc. generally doubling the velocity. Statistical significance of manual tracking was determined by a two-way ANOVA with a Tukey post hoc test for multiple comparisons (also including Figure 45, 185 μ m velocities). * p <0.05, ** p <0.01, *** P <0.001 and **** P <0.0001 (1 biological repeat, 4-6 cells tracked) and bars (D) indicate standard deviation. Scale A, B: 250 μ m

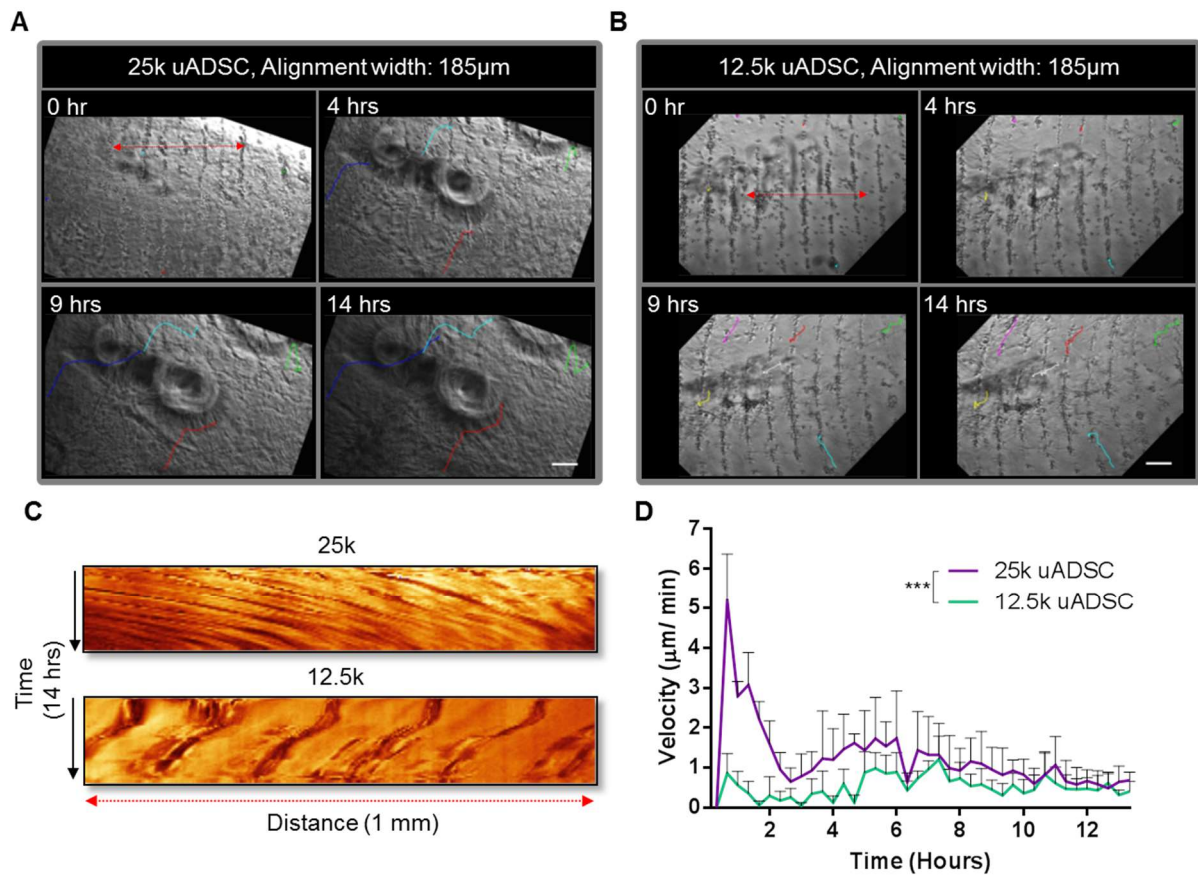


Figure 45: Manual tracking analysis of pattern contraction by 185 μm aligned uADSC (14hrs) time-lapse image-sets. From time-lapse recordings of high (A) and low (B) density ADSC alignments, ImageJ plugin “Manual Tracking” was used to map cell movement (gel contraction). Each cell tracked for analysis can be seen by each line colour. Similar to 375 μm pattern width (Figure 44), higher ADSC amounts can be seen to result in greater pattern distortion, with high conc. showing extreme contraction (although slightly out of focus towards end of time-lapse). From the kymograph (C) images of a line across 1mm of pattern (A, B: location shown by red dotted arrows), pattern lines of the high conc. ADSC gels merged together whilst the lower conc. showed some degree of contraction but remained relatively separate. From the average velocity analysis comparing both high and low conc. of ADSC gels, there was a large spike in the velocity from 0-3 hours on high conc. which was absent at the lower conc. This was followed by a more constant rate of contraction which steadily reached similar velocities for both ADSC conc. after ~6 hours. Statistical significance of manual tracking was determined by a two-way ANOVA with a Tukey post hoc test for multiple comparisons (also including Figure 44, 375 μm velocities). * $p < 0.05$, ** $p < 0.01$, *** $P < 0.001$ and **** $P < 0.0001$ (1 biological repeat, 4-6 cells tracked) and bars (D) indicate standard deviation. Scale A, B: 250 μm.

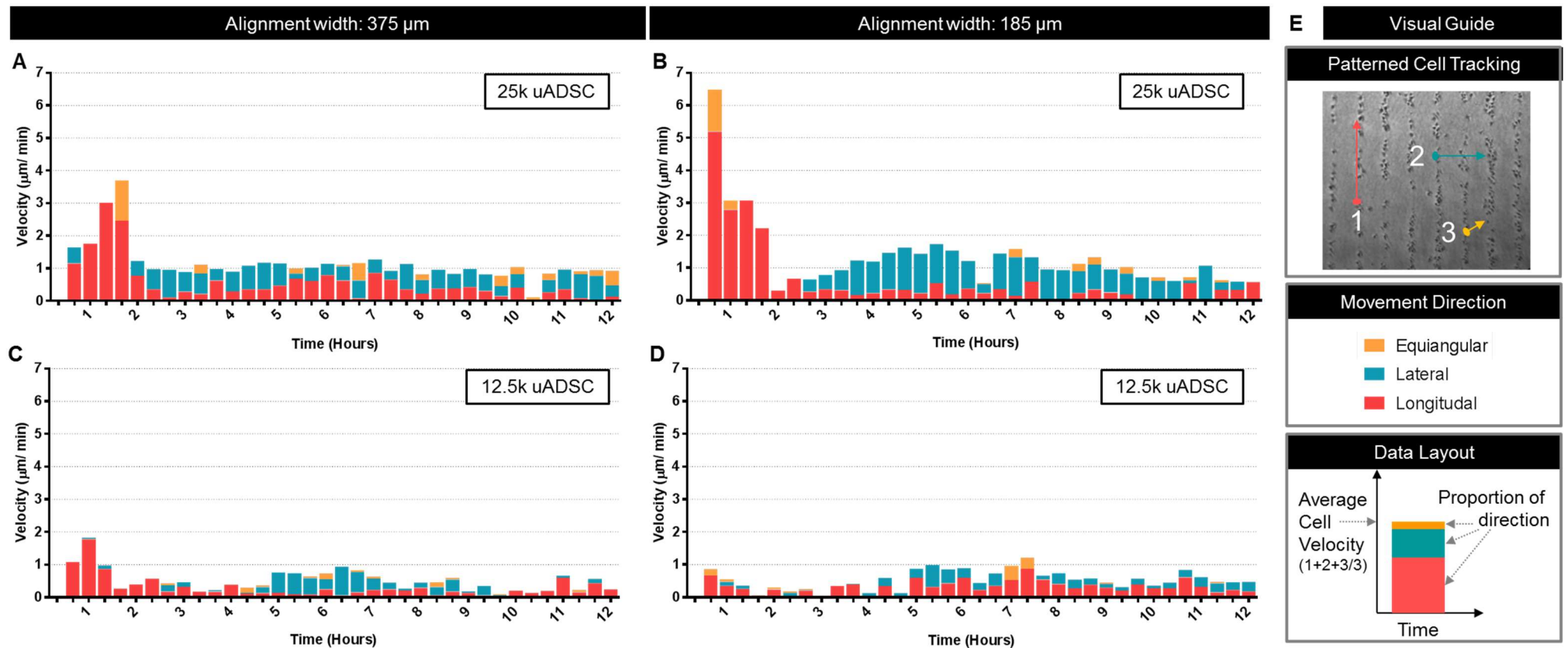


Figure 46: Average directional velocity of pattern contraction over a period of 13-14 hrs. From time-lapse recordings of high (A, C) and low (B, D) density ADSC alignments, ImageJ plugin “Manual Tracking” (Figure 44 and Figure 45) with the direction of movement calculated from co-ordinates. Average orientation was sectioned into 3 bins: equiangular (orange: 40-50°), lateral (blue: 0-40°) and longitudinal (red: 50-90°) in which the direction of pattern alignment was set to 90°. The graphs show the proportion of each direction making up the average over time. Across all but 1 group, the initial ~3 hours show a high rate of contraction which is predominantly longitudinal which was followed by more lateral contraction between pattern lines. Narrow alignment width exhibited greater contractile forces (1 biological repeat for each condition, 4-6 cells tracked).

3.3.3. Behavior of patterned dADSC in collagen I hydrogels

The next step was to determine the response of differentiated ADSC to alignment within the collagen matrix and whether they could serve as a pseudo alternative to bands of Büngner. Differentiation of cells was carried out using the protocol according to Kingham et al. (2007) with the confirmation of key markers by Dr Suzanne Thomson: p75, S100, GFAP. Prior to experiments, a flask of dADSC were checked for the typical spindle like morphology and elevated expression of S100 protein (Figure 47). There was no apparent difference in the ability to create alignment patterns with the switch to dADSC as expected however, cell behaviour showed a remarkable difference, with cell proliferation and/ or migration instead of gel contraction. Within a day, all pattern alignment had been lost with very little gel contraction occurring (see: Figure 48). Additionally, trial cultures of dADSC seeded collagen gels with a DRG showed no changes to survival rates. In consideration of dADSC; their use requires a lengthy initial differentiation culture (ca. 18 days), yet rapidly de-differentiation (ca. 1-3 days) without inducement (Faroni et al., 2016). As dADSC did not provide any collagen alignment or improvements to DRG survival, it was deemed that the use of dADSC would not be suitable for the work carried out in this chapter and thus their investigation discontinued.

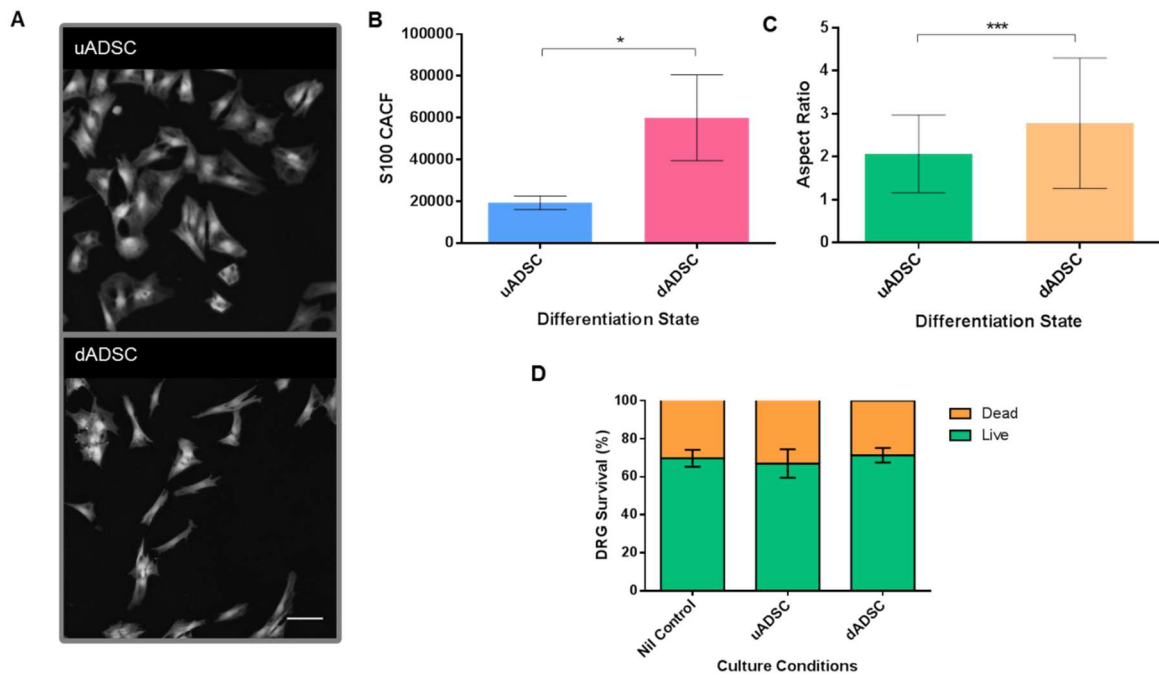


Figure 47: Verification and comparison of uADSC and dADSC. Image set (A) shows a visual comparison of uADSC and dADSC (tagged with Calcein). Differences in morphology can be seen with uADSC spreading evenly whilst dADSC show more spindle-like morphology. Graph (B) gives a relative comparison of average S100 fluorescence per cell, consistent with literature; dADSC shows a much greater level of S100 expression. Aspect ratio analysis of cell morphology (C) determined by ImageJ particle analysis command of 150-500 cells and shows dADSC to be on average more elongated in shape by a significant amount. Finally, a live-dead viability assay comparing the effects of each cell type (25k cells) on survival rate of a DRG, no significant increase in using either cell type over nil cells control. Significance (B, C) was determined two-tailed students t-test where n (B, C) = uADSC: 3 measured regions/ 1 biorepeat, dADSC: 3 measured regions, 28 cells/ 2 biorepeats. Significance (D) by paired two-way ANOVA with a Tukey post hoc test where $n=9$ technical repeats spread across ≥ 3 biological repeats. The bars indicate standard deviation. Scale: 100 μm

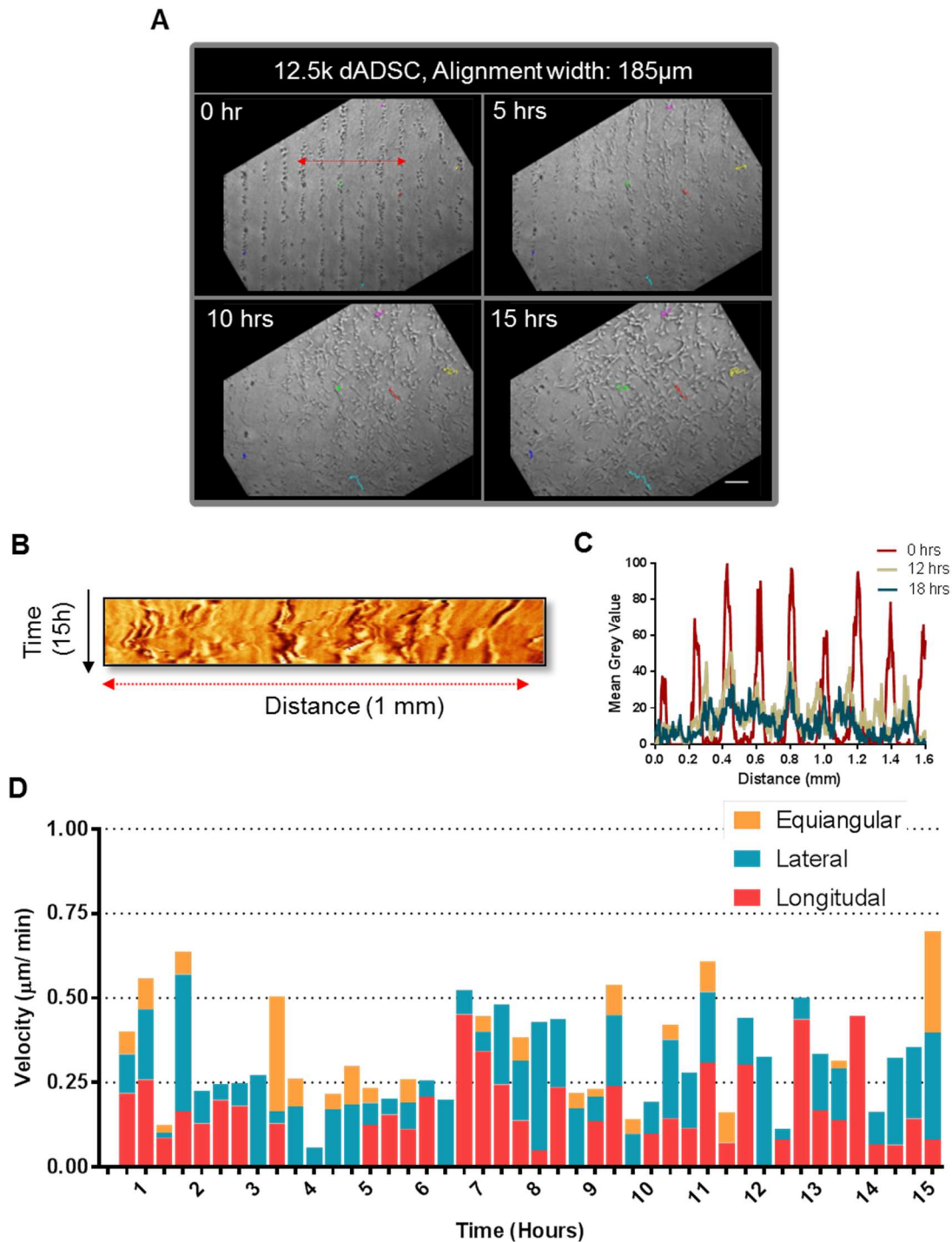


Figure 48: Time-lapse images of aligned dADSC cell behaviour in collagen hydrogel and cell tracking analysis. From a 15-hr time-lapse recording of 12.5k dADSC cells aligned (185 μ m) within the hydrogel, it became apparent that when differentiated, there is very little pattern contraction. Instead, cells proliferate and migrate and forgo the constraints of initial alignment. Manual Cell tracking (ImageJ plugin) revealed little displacement of each cell from its origin, creating an “undecided” path with no apparent purposeful direction. The kymograph (B) shows a loss in pattern but in a random orientated fashion i.e. not a consistent blur from right to left. Plot density profile of a distance (red dotted arrow shows) shows complete loss of the pattern over 18 hrs as cells migrate between bands. Finally, the average velocity of cell movement generally lies between 0.2 and 0.5 μ m/ min with what appears to be randomly directed. Manual tracking analysis was carried out on 6 separate dADSC cells from one time-lapse recording.

3.3.4. Neurite guidance by collagen embedded, aligned ADSC

After creation of a reliable method for successful, aligned seeding of ADSC within 3-D collagen, investigations began to assess the benefits of these constructs as scaffolding for regenerating nerves. This involved the use of organotypic DRG explants as an experimental model which was also inserted to the collagen during gelation. Initially, extreme difficulties were experienced when trying to image the neurite outgrowth using conventional fluorescence microscopy as immunolabelling of axons largely resulted in failure (B3-tubulin, S100). This difficulty is not uncommon, and protocols generally tackle the issue through longer antibody incubation and wash steps which are carried out under agitation. Many suggestions from various sources to reliably stain the neurites within the collagen gels were attempted and some success was found with a simple, one-step phalloidin tag for the actin cytoskeleton. However, this was not selective for axons, causing fluorescence of both support cells and ADSC. Towards end of the allotted project time, immunolabelling with neurofilament heavy subunit was attempted and resulted in reliable axon visualisation.

DRG were cultured for 6-days within aligned/ randomly distributed ADSC constructs at two different cell densities (12.5k/ 25k). Nil ADSC control DRG resulted in an overall even, radial shape, whilst the presence of ADSC resulted in greater bundling to form overall polarised network shapes (Figure 49 and Figure 50). No apparent difference or trend was seen with network size; however, the greater ADSC concentration resulted in an increased directional outgrowth. With regards to the pattern achieved by aligned seeding, directional outgrowth generally occurred perpendicular to the rows of ADSC. Random cell distribution also promoted neurite organisation; however, this was completely unpredictable. For the purposes of comparison, network directionality analysis was carried out with the Ferret's diameter of the network residing at 90° on the histograms.

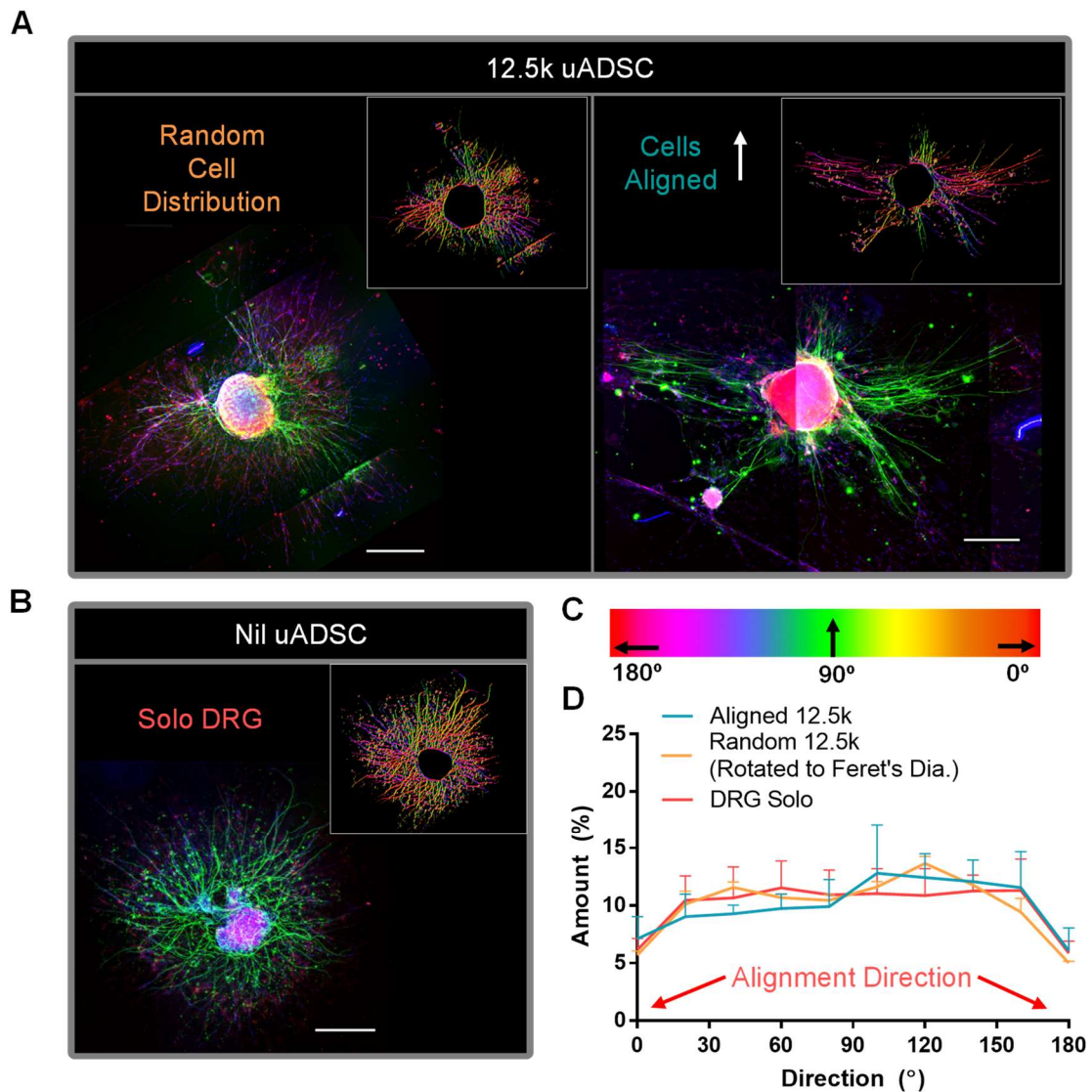


Figure 49: Directionality analysis of DRG networks cultured in 12.5k uADSC-collagen constructs. DRGs were cultured for 6-days with 2ng/ ml NGF-DRG media, within high conc. (12.5k) uADSC aligned (375 μ m) collagen hydrogels. Fluorescent images (A, B) of cultures immunostained with axons: green (anti-neurofilament heavy sub-unit), actin/cells: red (phalloidin), nuclei: blue (DAPI) and the resulting filament sensor eLoG image (white inset). Image set (A) shows the flattened DRG outgrowth promoted by uADSC in random (Orange/ left) and aligned (verticle) (turquoise/ right). It can be seen that there is greater directionality of growth when compared to the nill uADSC DRG flattened outgrowth (B) and alignment was found to promote axons to grow slightly perpendicular to the pattern although there remains some un/ misguided axons. The colour guide (C) provides the colour-orientation for directionality analysis (top right, inset images: A, B). In the histogram (D) of average network directionality, aligned cultures were rotated (pattern direction: 0/180°) for peak clarity and randomly distributed cell cultures were rotated to the Feret's diameter for comparison of potential. This revealed the overall network guidance to result in a similar orientation regardless of uADSC although there is the slight presence of peak 90-130° indicating a slight degree of directionality. Analysis was carried out on DRGs explants where $n \geq 3$ biological repeats. Scale: 500 μ m

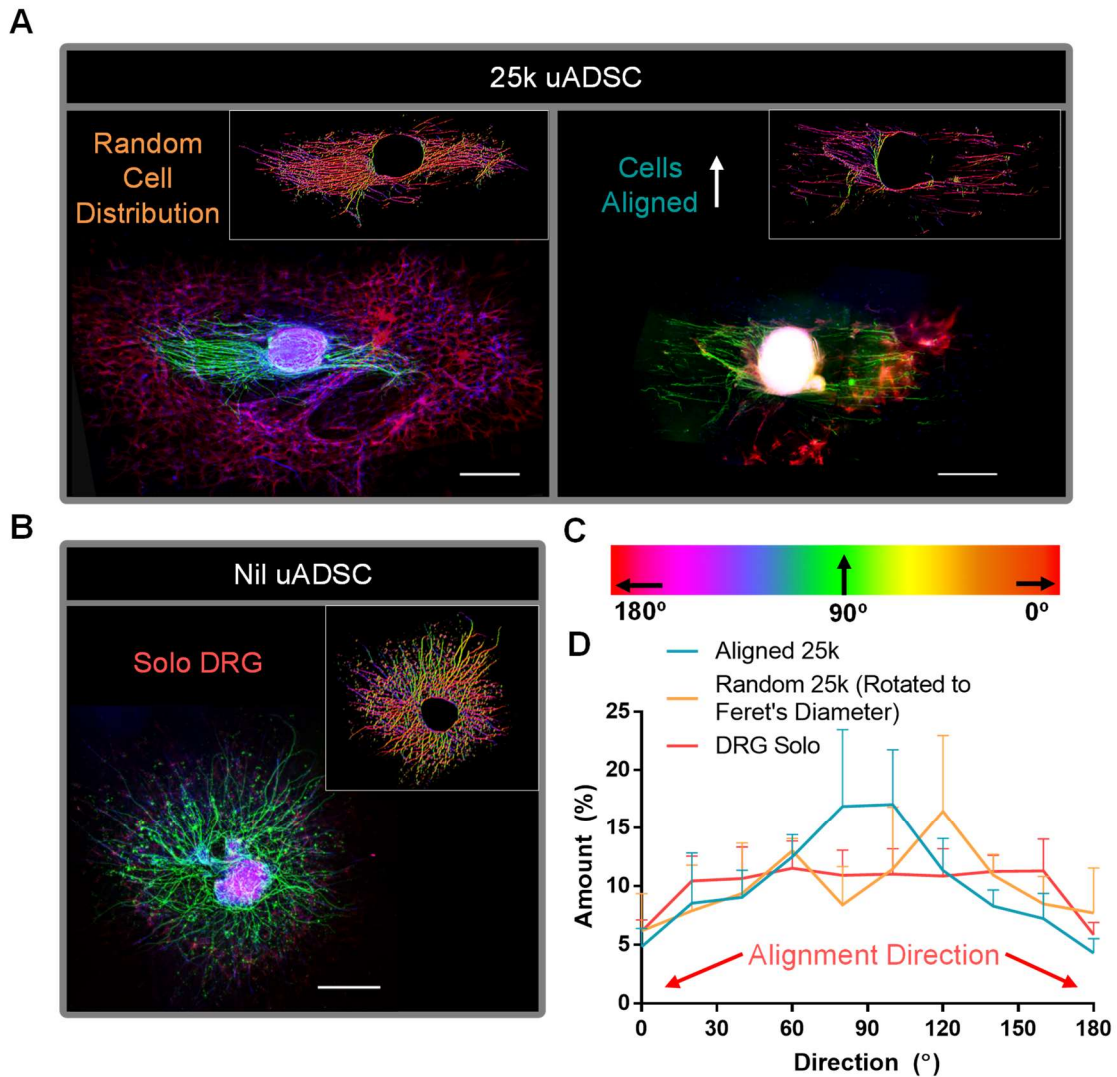


Figure 50: Directionality analysis of DRG networks cultured in 25k uADSC-collagen constructs. DRGs were cultured for 6-days with 2ng/ ml NGF-DRG media, within high conc. (25k) uADSC aligned (375 μ m) collagen hydrogels. Fluorescent images (A, B) of cultures immunostained with axons: green (anti-neurofilament heavy sub-unit), actin/cells: red (phalloidin), nuclei: blue (DAPI) and the resulting filament sensor eLoG image (white inset). Image set (A) shows the flattened DRG outgrowth promoted by uADSC in random (Orange/ left) and aligned (verticle) (turquoise/ right). Both random and aligned cell distributions provide an elongated network shape with much greater directionality of axon growth when compared to the nill uADSC DRG flattened outgrowth (B). Alignment was found to promote axons to grow relatively perpendicular to the pattern. The colour guide (C) provides the colour-orientation for directionality analysis (top right, inset images: A, B). In the histogram (D) of average network directionality, aligned cultures were rotated (pattern direction: 0/180°) for peak clarity and randomly distributed cell cultures were rotated to the Feret's diameter for comparison of potential. This revealed the overall network guidance of aligned uADSC to be substantial, promoting an average orientation of ~70-110°. Randomly distributed uADSC still promoted direction, but on average this was inconsistent, even upon rotation to the Feret's diameter. Analysis was carried out on DRGs explants where $n \geq 3$ biological repeats. Scale: 500 μ m

3.3.5. A brief assessment of the potential for creating lumen of a NGC using sonotweezers

To gain an insight into the translatability and as an indication to the potential for use of aligned ADSC seeded collagen constructs to serve as the inner lumen of a NGC, a premade rolled-PCL micro-grooved/pored conduit was used to house the cell seeded collagen gel. ADSC were successfully aligned within the NGC and these then co-cultured with a DRG in accordance to the pre-existing protocol (outlined in section 3.2.5). Axons were seen to regenerate within the conduits; however, of the two conduits tested, only one showed promising directionality of outgrowth.

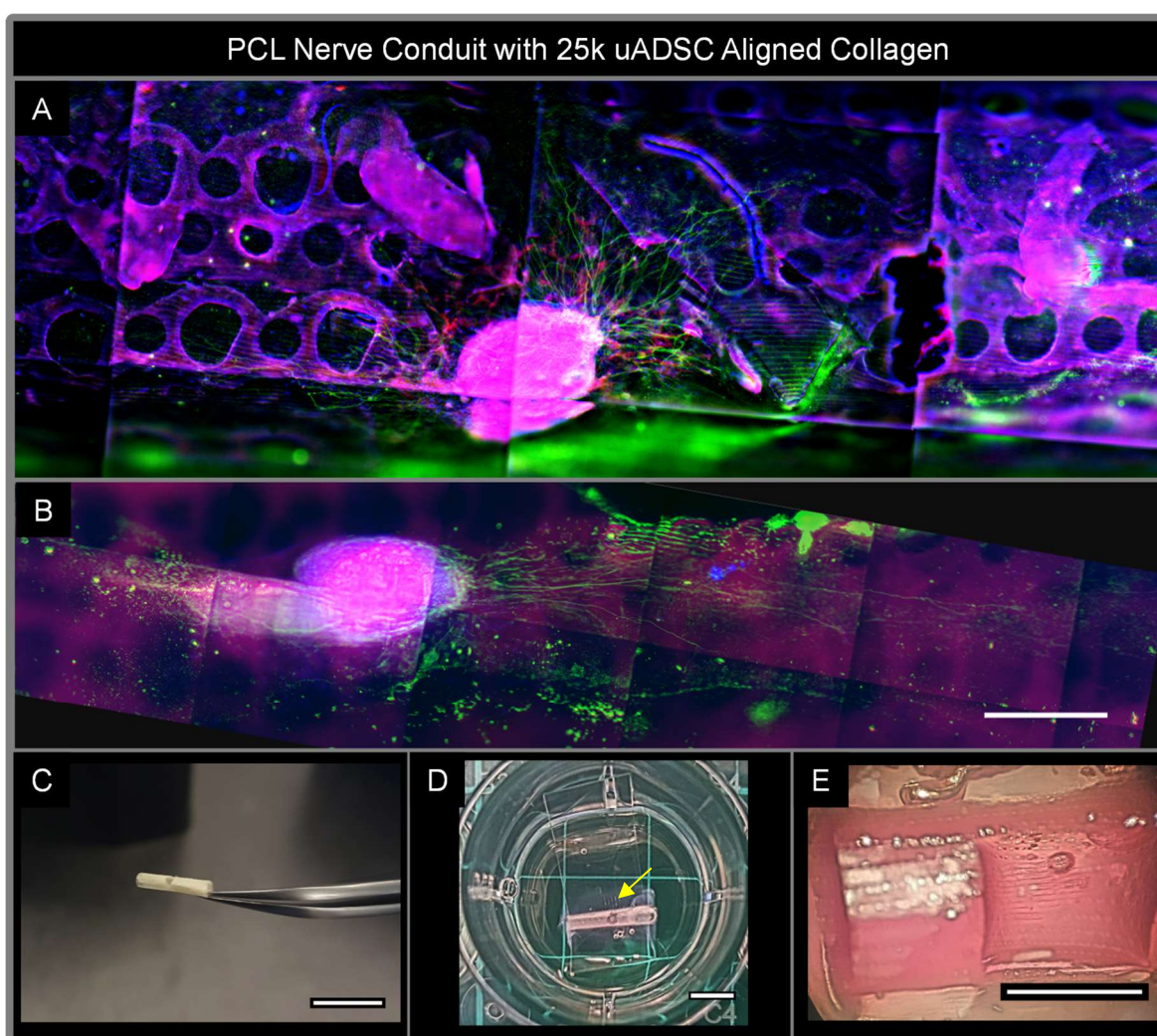


Figure 51: A brief test for the translatability and effectiveness of aligned uADSC within an NGC. Fluorescent images (A, B) of cultures immunostained with axons: green (anti-neurofilament heavy subunit), actin/cells: red (phalloidin), and nuclei: blue (DAPI). The PCL conduit used contained grooves (12.5 μm grooves, 200 μm pillars and pores) showed auto-fluorescence (purple/ red). Image (A) shows a poorly guided axon growth combined with some damage to the NGC. Image (B) displays much greater directional growth along the majority of the conduit (~1cm) with axons remaining above/ below the depths of the conduit, indicating cellular guidance. Camera images (C-E) provide insight into the

adaptation of the working protocol for use as a neurite guidance construct within an NGC. Image (C) shows the bare conduit and following alignment of 25k uADSC (perpendicular to conduit: yellow arrow) which was used for culture of a DRG explant. Alignment can also be done parallel to the conduit sides depicted by (E) although this was not used for DRG culture. Scale: A, B: 500 μ m, C, D, E: 5 mm

3.4. Discussion

3.4.1. Current Approaches to 3-D scaffold fabrication

There is a growing body of research carried out with the aim of providing non-invasive means for particle manipulation and sorting for biological applications (Atajanov et al., 2018, Ren et al., 2015). One approach in particular lies in the use of ultrasound (Bernassau et al., 2013) which has been used to manipulate micro-particles with controlled precision through the use of devices termed “sonotweezers”. Recently, the sonotweezer device has been used to align SC for the encouragement of directional DRG axon growth on 13mm diameter glass coverslips (Gesellchen et al., 2014). The directive of the work in this chapter was to translate this technique for cell alignment from a 2-D to a 3-D system in an effort to create precisely designed constructs serving as the inner scaffolding for NGC.

In the body, cells are arranged in intricate functional patterns including strings of cells that align for mutual guidance (bands of Büngner in regenerating nerve), form penetrating structures (vascular sprouting, cancer metastasis) or maintain functional tissue (tenocytes in tendon) (Weiss et al., 1988, Dorta et al., 2018, Kishore et al., 2012). To mimic these intricate linear strings of cells and achieve the reliable structured deposition of cells within three dimensions has been of interest especially for peripheral nerve repair. Free form added manufacturing methods have made great strides in recent years; these techniques rely on layer by layer deposition of cell filled gels - a drawback here is that the density of cells that would be required to achieve immediate strings to be formed are not attainable. Alternatively, the group of James Phillips at UCL have developed the EngT system, where cell filled collagen gels are aligned by the joined action of the cells contracting the gels and then transformed into useful tissue equivalents by plastic compression (Georgiou et al., 2013). To reliably manipulate cells optical, electric and acoustic methods could be applied.

Optical tweezer based methods could be used to assemble individual cells, but suffer from the high energy gradient that would need to be applied and their superior accuracy, individual cells could be placed - to manipulate whole strings of 100s of cells over large areas within a temperature sensitive gel would be pushing beyond the current state of the art (Atajanov et al., 2018). Acoustic methods have the advantage that these work over large areas, in three dimensions and can reliably manipulate hundreds of cells at once shown by Bazou et al. (2008) et al with levitation and positioning control of cell clusters and by Armstrong et al. (2018) for cellular alignment.

3.4.2. Challenges faced in 3-D patterning of ADSC within collagen during gelation

3.4.2.1. Cells are suspended at a consistent depth

The first challenge of this endeavour was to establish whether 3-D cellular patterning was possible with the sonotweezer and to what outcome i.e. can the pattern be reliably suspended, and will it remain singular or multi-planer through depth? In actuality, the alignments of cells and beads were found to reliably suspend inside the gel, creating a pattern on a single plane with low depth dispersion (ca. 100 μm). Multiple planes were seen to be produced in different areas of the gel but, were never present directly above or below other alignments. During writing of this thesis (post experimental stage), Armstrong et al (2018) published a sonotweezer approach for 3-D patterning of myoblasts suspended in collagen I and gelatine methacryloyl hydrogels with a view to create aligned fibrous muscle tissue. This method is remarkably similar to that used in this thesis (which is reasonable considering this device was based on that of the Drinkwater group in Bristol), and also resulted very little depth dispersion of the pattern alignments through the gel (ca. 20 μm). In early research for 3-D microparticle manipulation using standing waves, Kozuka et al. (2000) employed a transducer situated above a medium of polystyrene particles (100-500 μm), which trapped the particles at a controlled depth in an array of circular aggregates across the entire surface. Following on from this, Bazou et al. (2008) created a similar setup (instead moving the depth transducer to below the sample) allowing the levitation of a single aggregate of immortalized human liver carcinoma

cells (HepG2) inside an alginate medium. Upon alginate gelation, the aggregate was encapsulated at the specified depth. Although incorporation of additional transducer in the z-axis allows the trapping of aggregates at a controlled depth, the formation of linear patterns has not been achieved. Instead of this setup, the experiments of this PhD maintained a reproducible depth of suspended ADSC patterns through calibration of the setup parameters (viscosity, cell weight, transducer driven voltage and collagen formation protocol) in order to achieve a synergetic balance between the cell sinking rate and the collagen gelation time.

3.4.2.2. Consistent depth of pattern is maintained by collagen gelation time

The standard protocol for collagen hydrogel formation is carried out on ice to maximise operation time. Initial experiments quickly indicated that this was unsuitable for this project as long gelation period allowed the cells/ objects to sink to the bottom of the device. This gives a fundamental insight into the inner complexities of this project: particle weight, size, shape, buoyancy, vortex forces, solution/ gel viscosity and hydrogel setting time, further defining the scope of challenge within this project. A modification to the collagen hydrogel protocol was to carry it out at room temperature ($\sim 20^{\circ}\text{C}$) altered the setting time to $\sim 2\text{-}3$ mins which was sufficient to restrict excessive sinking. Generally, this produced adequate constructs (termed: “soft” in this thesis) but was prone to occasional failure.

Recently, Gong et al. (2018) applied a similar strategy of controlling the sinking and gelation rates in order to embed cells and cell-clusters in a 3-D at a specified depths within a collagen I or matrigel matrices. Through transfer from microwell arrays to the gel by inverting the device, designed configurations of nodes of cells or cell clusters could be formed and locked at a depth within the gels. Another inversion of the device ensured that cells did not settle at the bottom of the coverslip. The entire process took around 45 minutes however and cell patterns had a degree of variance in cell counts per node. Further, the depth at which cells were embedded was approximated to be on the same focal plane which is consistent with the findings of this thesis for the sinking/ gelation cell encapsulation approach.

3.4.2.3. Can this approach be improved?

Theoretically, it may be possible to incorporate aspects from both setups (utilizing an additional transducer and the sinking/ gelation strategy), as a means for greater depth control or even multi-layered alignments. This would likely require delicate fine tuning of the transducer, and possibly continued addition of the cells to the pre-set gel whilst voltage supplied to the PZT is modulated (steadily decreased). This could slow the sinking rate of cells over time and may increase the dispersion of depth, producing continued alignment through the entire gel which could be more beneficial for nerve repair in 3-D. Another way to create continuous alignment through the gel depth would be to successively add additional patterned layers of collagen akin to construction of EngNT (Georgiou et al., 2015) or stereolithography (Lee et al., 2016). This would however have the drawback of taking much longer for gel fabrication and thus lower throughput for scaffold production.

3.4.2.4. Collagen shape can be designed and readily transported

The next challenge lay in the handling and formation of suitable collagen hydrogels, a known issue in their use, which has resulted in a number of efforts to improve the mechanical robustness through incorporation of strengthening agents (Yu et al., 2017). In this case, the production of reproducible and transferrable gels was achieved through an agar mould and make-shift Aclar tray (shown in Figure 39A) in combination with stiffer resultant hydrogels (Figure 41). This simple method presents an extremely practical way to fabricate collagen hydrogels with specified dimensions which is beneficial for investigating gel contraction or possibly permeability/ diffusion.

3.4.2.5. This model can be used for organotypic DRG culturing

The final challenge lay in the requirement for a reliable protocol for DRG outgrowth investigations, overcome through careful insertion of the DRG into the gel immediately after cell alignment. This helped to prevent the explant body from interfering with the standing wave field during initial alignment of cells and as this was carried out during gelation, any pattern disruption was able to reorganise before complete setting. Post-patterning addition of the DRG also served to utilise its

weight, forcing the explant to promptly sink to the alignment layer depth; a fortunate occurrence for this experimental setup. It should also be remembered that this difficulty is a repercussion from the experimental setup. This issue would therefore not be present in actual scaffold fabrication and thus; quality and performance of the scaffold would likely increase.

Overall, these challenges were overcome through an intensive trial-and-error process involving countless attempts, parameter tweaks and sequences. Ultimately, this effort was met with success, with the final method providing a promising approach to the fabrication of precisely designed ADSC-collagen hydrogel scaffolds which are both reproducible and readily transportable.

3.4.2.6. Optimisation of device configuration to improve practicality and scaffold quality

Three devices were used over the course of this work in attempts to optimise the setup in order to produce alignment constructs of sufficient quality. The first: a heptagonal setup of transducers which did not have exactly opposite PZT plates. This device managed to trap beads and hTERT within agar and collagen successfully, but a cumbersome lid and small patterning chamber size together made for impossible gel extraction undamaged. Alongside this, there was a desire to move to oppositely placed PZT for theoretically better particle trapping potential. The second device was designed with Autocad software to bear similarity to that used previously (Courtney et al., 2011) and 3-D printed. Modifications to the PZT length gave a larger area of pattern and slightly greater aligning band width. This device was designed to allow for easily reproducible gels set within the culture dish, following which; the transducer arm could be removed to allow for typical culture undisturbed. In practice however, the large chamber area of patterning created flimsy gels that could not be handled and as the PZT resided on the inside of the alignment chamber, there was the added complications of hydrogel removal. For the gel to be removed, the outer perimeter had to be cut free from the device using a scalpel blade, with the majority of efforts resulting in degradation of pattern, damage to the gel yielding inconsistent gel shapes/ sizes and removing all possibility for accurate gel deformation studies. The final device used: the octagonal sonotweezer was akin to the device used in (Bernassau et al., 2013) with the exception of differing pattern band widths and

exclusion of the top lid for ease of access. This device demonstrated the greatest success and potential, aligning cells at 185 μm and 375 μm within gels that could be reproduced reliably, consistently and with suitable dimensions for gel exportation. Theoretically, all devices may achieve this and that this was simply the tweaked finished project tailored for this experimental modal.

3.4.3. Behaviour of patterned ADSC within a 3-D collagen matrix environment

In general, the use of ultrasound in medicine is well established to be relatively non-invasive, highly beneficial and most applications show minimal biological side effects (Miller et al., 2012). Studies have validated this claim at the cellular level, with no detrimental effects to cell proliferation or metabolic activity following application of standing acoustic waves generated by sonotweezers (Bazou et al., 2008, Armstrong et al., 2018). Gene and protein expression also showed no significant difference following being subject to the acoustic field. From these findings, it can be assumed that the application of the acoustic field does not alter the cell behaviour of ADSC (such as contractile force), instead these can be attributed to the result of embedded the cells in a pattern formation.

The soft collagen gels were found to near completely contract in the presence of 25k indicating the integrity of the gel was in question for these experiments and for use as nerve guidance constructs in general. Although, this posed the requirement of forming stiffer gels, it was recognised that with the proper collagen properties, contraction of the gel could be exploited to create guidance cues through collagen fibre alignment. An important factor to consider in this was in maintaining the ability for cells to migrate through the collagen matrix. Cell migration is heavily influenced by the matrix permeability, a property which decreases as the fibres become more densely packed to form the stiffer gels, which impedes cell penetration through the matrix (Kim et al., 1993). Tuning of collagen hydrogel properties is well documented (Antoine, et al., 2014); however, the delicate balance between creating stiffer gels that could withstand excessive cellular contraction, whilst maintaining the functionality of sonotweezer alignment and allowing cell migration, severely limited the variation of parameters.

Primarily, an increase in collagen concentration was attempted (5 mg/ ml) which is a well-known route to stiffer gels. This resulted in: very stiff gels, an extremely quick setting time and the inability to align cells; likely due to viscosity. In retrospect, it may be possible to manipulate cells in such viscosities through an increase in the voltage supplied to the PZT to provide greater alignment force. Instead of continuing down this route, an alternative means to increase the stiffness was carried out. In this, the starting collagen solution concentration was kept at 2.05 mg/ml; however, the NaOH was increased ten-fold (0.1 to 1M). This had the effect of increasing the resultant gel collagen over the 'soft' gels (ca. +30%), but, maintained a lower viscosity and a comfortable setting time (30- 60 secs) than using the high concentration collagen solution (5mg/ ml). Overall these findings were in agreement with Armstrong et al. (2018) and O'Rourke et al. (2015), who found that gels above 5mg/ml are too viscous for patterning whilst gels below 1 mg/ ml are too fragile. The gels formed from this protocol achieved the optimal balance for the sonotweezer setup and the resultant gel robustness was greatly improved, showing a relatively acceptable gel construct size after a period of at least five days. This reached a key requirement when considering these the approach of using these gels as a choice for scaffolding for the inner lumen filler of NGC, as the gel must maintain the length across the lesion site.

Anisotropic materials have been used extensively in nerve repair with aligned matrices of collagen or laminin showing great success in particular, through promoting reinnervation and function return over 6 mm gaps, a length considered limiting in regeneration of the rat sciatic nerve (Verdu et al., 2002, Ceballos et al., 1999). Alignment of collagen fibres is usually obtained through magnetic, freezing or plastic compression. Application of the sonotweezer induced acoustic field on collagen during gelation was seen to have no effect on fibre alignment across a range of different frequencies and voltages (i.e. pattern width, pressure differential respectively). However, upon embedding ADSC, a reduction in gel size and collagen fibre alignment was observed through birefringence (Figure 43). This was deemed to be generated by cellular contraction.

A number of different cell types have been assessed (in a similar way as those in the gel deformation study of section: Figure 41) for their ability to contract of collagen hydrogels including corneal stroma stem cells (Mukhey et al., 2018), glioma cells and

astrocytes (O'Rourke et al., 2015). These assays were carried out on free-floating collagen (ca. 1-5 mg/ ml) gels and analysed over a period of 24 hours. Interestingly, for 1-2 mg/ ml collagen gels, contraction was seen to be relatively consistent between these studies, showing around 80-95% gel size reductions arising from cell seeding densities in the range of $0.5-4 \times 10^6$ cells/ ml gel. Higher concentration of gels (4-5 mg/ ml) reduced the size decrease of astrocyte embedded gels (other cells not tested) to ~35%. These assays convey remarkably similar characteristics to the findings of section: Figure 42 in which 'soft' gels contracted by around 80%. In converse; the 'stiff' gels which have a collagen concentration of ca. 1.3mg/ ml instead managed to maintain the gel size for a longer period (5 days) and to an even greater extent than the higher concentration collagen gels (4 and 5 mg/ ml) of (O'Rourke et al., 2015). Reasoning for this can be attributed to either: the contractile force of ADSC is lower than other cell types or the more likely, seeding density of ADSC. In this study, the seeding density is much lower (12,5k: 41.25k/ ml gel, 82.5k: 60k/ ml gel) than those employed in elsewhere.

Of the two cell amounts added (12.5k, 25k), the lower concentration was seen to exhibit lower contraction forces indicated through the overall gel structure (deform) following 5 days of culture. When patterned however, there was a significant decrease in gel size over the randomly distributed ADSC gels and nil cell control gel (soft). At the higher concentration of ADSC caused significantly higher deformation of the hydrogel structure than both the lower and nil cells groups however there was no observed difference between gel sizes of aligned and random distributions at this higher ADSC concentration. Taking account of these results, it can be deduced that greater cell numbers will exhibit greater contractile forces on the 3-D collagen substrate to which, cell-cell proximity plays a major role. This can be reasoned for the low cell concentration random distribution findings where there is a greater distance between cells, whereas alignment causes cells to have closer neighbouring cells residing along the pattern. This results in higher contractile forces attributed to the combination of cells clustered together. Conversely, the higher cell population causes random distribution to have closer neighbouring ADSC which can interact and pull the gel together, similarly to that of the aligned cultures and as a result, very little difference was observed.

For the application of the cell mediated contraction, the strategy used in this study synergises the use softer gels alongside lower stem cell numbers. This approach could prove extremely beneficial in clinical applications when considering that the stem cells may be in limited supply. Furthermore, as shown in Figure 46 contraction velocity showed an initial burst of contractile force within the first 3-4 hours of culture. This was mirrored in other research (O'Rourke et al., 2015, Mukhey et al., 2018), where contraction was observed to occur predominantly within the first 2-5 hours although no reasoning was given. It can be proposed that this is likely a result of either: a result of the initial adherence of cells having greater contractile force than cell motility or further behavioural contraction, or that the initial gel is soft but becomes stiffer as cells contract the fibres together.

In addition to gel deformation, higher ADSC concentrations also provided a greater alignment of collagen fibres, visualised through a polarized microscope: a common practice to detect alignment within materials (Geary et al., 1987). In concordance with gel deformation results, higher ADSC concentrations caused significantly higher fibre alignment. The issue with employing cellular generated collagen alignment with conventional seeding procedures is that there is very little control over the direction at which fibres will organise. Through acoustic patterning, the direction of collagen fibre organisation could be induced, with collagen fibre alignment seen to occur between bands of the alignment pattern in a perpendicular direction. The alignment of individual cells (i.e. the cellular extension, aspect ratio) was not determined due to their density within the pattern and staining/ visualisation difficulties. This is contradictory to the alignments produced by tethering the collagen, a method used for production of EngNT (Georgiou et al., 2013) and of the study by Armstrong et al. (2018). In the tethering approach, an axis of tension is maintained between the points of anchored gel. During culture, cells contract the gel orthogonally to the tension axis, creating collagen and cellular alignment in the direction of the tension load. Used in combination with acoustically patterned myoblasts, tethering the collagen along the direction of pattern reduces interaction and movement between arranged lines of cells. This promotes the creation of muscle tissue with organized fibres orientated along the axis of tension with greater anisotropic tensile strength than cell patterns perpendicular to the clamped ends of the gel.

For the free-floating gels in this thesis, it is inconclusive whether collagen alignment is a result of longitude (along pattern direction) or lateral (perpendicular) contraction as either pulling direction could theoretically create perpendicular fibres. However, considering that alignment occurs in the direction of tension load upon tethering the gel (i.e. the direction that cells do not contract), whilst taking into account the initial preference for contraction to the direction of the pattern (displayed in Figure 46 and discussed in detail below) in free-floating collagen gels in this study, it can be proposed that collagen fibre alignment occurs through cells contracting together in a longitudinal direction, along the pattern lines.

To visualise the contractile behaviour of acoustically aligned ADSC embedded in collagen and investigate interaction between the pattern lines, cultures were recorded using a time-lapse coupled brightfield microscope. Both low and high cell densities were examined at two different pattern widths: wide (375 μm) and narrow (185 μm). Velocities of individual cell movement (randomly selected, 4-6 per culture) were tracked and gave a relative measurement of the strength and direction of contraction over time. From this analysis, greater pattern contraction was observed with higher ADSC concentration and/ or narrower alignment width. Also, it was revealed that within the initial 3 hours of culture, the ADSC exert a phase of strong contractile force near-entirely in the direction of alignment, likely as a result of adhesion to the collagen matrix/ other cells and intercellular communication. Generally, this period was then followed by an increase in lateral pattern contraction which resulted in no apparent preference in contraction direction on average (calculated from 4-6 cells residing in different regions of the gel). However, one exclusion to this was in the culture of the smaller pattern width (185 μm) seeded with the high ADSC density (25k), in which lateral contraction became predominant. In reasoning, it is possible that this is a result of closer proximity between neighbouring lines providing more potential for their interaction which a greater cell density would further contribute to. Another consideration is in the limits of acoustic patterning. It is not perfected; the narrower pattern lines will reduce the margin for error which again, higher cell seeding densities can influence as spatial competition occurs. Following on from this, another factor that must be accounted for is with the formation and effect of dense pockets of congregated cells, formed either by: contraction, pattern disruption or initial alignment failures. The presence of these irregularities were seen to overcome the more delicate forces exhibited by the

patterned cells. Overall, this analysis is further evidence that the contraction of the gel and alignment of collagen is a result of the uADSC behaviour. The degree of contraction is not only determined by the cell concentration but also the distribution and local densities of cells as neighbouring cells contract more when together than at a longer distance i.e. The nature of this force is a result of more than the sum of the individual cells.

3.4.4. Scaffolds in practice

3.4.4.1. Aligned dADSC do not retain pattern

The initial idea was that the alignment of ADSC in the presence of neuronal culture media may promote the differentiation to a SC phenotype akin to bands of Büngner; however, no evidence was found to this occurrence. Despite a relatively recent findings, ADSC when differentiated to a glial lineage are believed to hold a promising SC alternative for use as support cells within NGC. When differentiated, dADSC can provide neurotrophic support to regenerating neurites (Kingham et al., 2007) although to maintain this state, a selection of growth factors must be present. This presented the prospect of alignment of the dADSC within the matrix in order to utilize the collagen fibre alignment of uADSC, yet also release neurotrophic growth factors promoting faster rates of regeneration and proliferation.

Time-lapse recordings revealed cell behaviour of dADSC when aligned to be vastly different to that of the undifferentiated, with very little contraction and extensive motility and/or proliferation. Further, test cultures with a DRG showed that no increase was observed with using dADSC or uADSC with respect to nil-cell collagen matrices, indicating that no apparent benefit from neurotrophic factor release and that the hydrogel coupled with 2 ng/ ml NGF media was sufficient for adequate cell survival (Figure 48). As the dADSC were seen to neglect the pre-organised pattern, provide no collagen alignment and no increase in cell survival, coupled to the increasing demands for culture, it was deemed that dADSC was not the correct cell for this approach to scaffold fabrication. This is in complete contrast to their activity in tethered collagen of EngNT (Georgiou et al., 2015), which show dADSC to align towards the clamped ends and promoted neuron viability, although this could be an outcome of the continued supply of dADSC differentiating GF during culture. One

prospect which was not investigated could be to differentiate the cells via. typical culture recipe after alignment within the gel. As differentiation takes ~2-3 weeks, this environment may speed up the process as 3-D culturing has been shown to affect the differentiation state of ADSC with studies revealing the promotion to a neural lineage (Gao et al., 2014) and in addition, providing the collagen alignment for contact guidance of axons.

3.4.4.2. Collagen scaffolds with embedded, aligned uADSC direct nerve growth in 3-D

To investigate the effectiveness of uADSC constructs for nerve guidance, DRG were cultured within the pattern of the gel. Also, DRG growth was seen to maintain a relatively flat depth of network (~100 μm) allowing the use of EDF plugin (ImageJ) to “pancake” the network for a planar analysis for a relative approximation and comparison. High and low cell densities were used for this experiment in aligned (375 μm) and random distribution. As expected, the nil-uADSC DRG control exhibited a very even, radial growth with a flat histogram. In contrast, the presence of uADSC showed greater polarity of network directionality and shape across all groups indicating that the cellular contractions were playing a role in directing neurites. In-line with previous results and expectations, higher cell densities increased network directionality which was seen to occur relatively perpendicular to the alignment pattern. There was no apparent difference in network size between each scaffold. Although randomly distributed ADSC also encouraged directional growth and fasciculation (particularly at high cell concentration), the orientation was completely unpredictable. For the purposes of a visual/ histographical comparison, random networks were rotated to their Ferret’s diameter; however, aligned constructs reigned superior for directional nerve guidance.

Herein lies the essence of the work carried out in this chapter and the potential benefits for use of the sonotweezer in the creation of nerve guidance scaffolding: unaided, uADSC will intrinsically guide neurites through the remodelling of collagen matrix by contraction of the collagen gel, remodelling the matrix to create aligned fibres. By utilizing the sonotweezer device, the direction of remodelling can be controlled with moderate reliability. This approach was found to provides similar effectiveness in neurite guidance as EngNT scaffolds (compared visually within final

discussion, section: Figure 64) without the employment of more demanding cell types (SC, dADSC) and at much lower seeding densities. Further, additional steps are not carried out such as plastic compression, which could improve neurite guidance found through more pronounced fibre alignment.

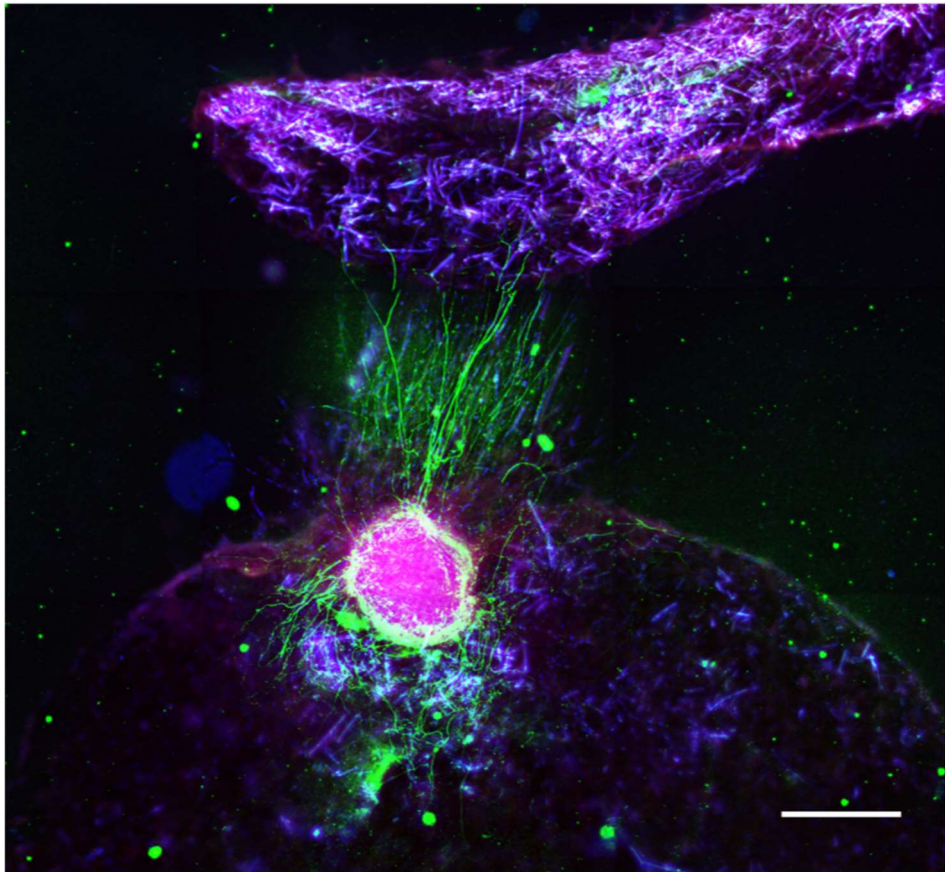
3.4.4.3. 3-D aligned strings of cells can be created within a NGC

To provide a brief insight into the practicality of using sonotweezers for the creation of precisely designed inner NGC scaffolding, the protocol was attempted within a hollow PCL-NGC (as used in: (Thomson, 2018)). The presence of the NGC tube did not have any noticeable interference to the acoustic alignment; however, it did complicate matters with the addition of another moving part. This complication is likely to have amounted to cell pattern disruptions which would not be an issue in actual scaffold production which would not require the inclusion of a DRG. Following alignment and setting, the conduit could be transported easily to where desired, in this case; a well plate for a six-day culture. For the entire period of culture, the gel maintained the length of the NGC and DRG outgrowth showed some degree of promise with one culture in specific showing impressive directionality and length. This approach of fabricating precisely designed scaffold lumen whilst inside the NGC to current knowledge has not been done before. Generally, incorporation of the inner scaffolding material will be fabricated before incorporation to the NGC with the process generally involving the layering or rolling of the scaffold before insertion to the NGC structure (Petcu et al., 2018a). This highlights the versatility of using ultrasound created scaffolds and the intricate advantages of the hydrogel formulation and transport protocol outlined in section: 3.2.3 and 3.2.4.

In conclusion, this chapter has laid the groundwork for the fabrication of gels precisely designed collagen hydrogel constructs with a view to be utilized as the inner lumen of an NGC. This study contributes to the promising potentials of ADSC as a suitable working alternative for SC and although current literature usually focuses on the benefits of glial lineages, here instead demonstrates the effectiveness of using the undifferentiated form for the promotion of nerve growth in a 3-D setting. Guidance of axons was found to be a result of ADSC contraction, heavily relying on the distribution of neighbouring cells. As sonotweezer created patterns of ADSC increases cell density differentials, the direction of contraction and thus; the

orientation of collagen fibres. This can promote directional neurite guidance perpendicular to the pattern. Finally, this is an extremely convenient method for creation of nerve scaffolding when considering ease of translation, modification and transportation of gels. This is further amplified when taking into account the efficiency of the fabrication, which requires much lower cell densities of a relatively accessible cell line.

4. Guiding Axons in 3-D: Fabrication of Arrayed Silk Microfibre Hydrogel Scaffolds Using Octagonal Sonotweezers



“First Contact” A 6-day DRG culture within a uADSC/NGF-silk collagen hydrogel. Fluorescent image, Green: Neurofilaments, Red: actin/ silk, Blue: Nuclei/ silk. 25k uADSC conc. Scale: 500 μ m

4.1. Introduction

Biomaterials are a central aspect to cell engineering strategies for improving nerve repair and are continuously evaluated and optimised. Silk fibroin is one such biomaterial which can be derived from the produce of various insects such as spiders webs and silkworm cocoon (Numata and Kaplan, 2010) and has attracted a lot of attention because of its exceptional mechanical properties, versatility, biocompatibility and biodegradability (Farokhi et al., 2017). In the context of nerve repair, silk fibroin hydrogels have been shown to serve as a more robust material for 3-D matrices than commonly used alternatives (i.e. collagen), whilst maintaining a positive neurite response in chick DRGs through stiffness modulated axon outgrowth (Hopkins et al., 2013) and through alignment of silk-fibroin fibres on a 2-D substrate by electrospinning, guidance of neurites is observed (Xue et al., 2017).

Analogous to the experiments carried out in Chp.3.2, this work utilised the sonotweezer device and protocols for the formation of precisely aligned 3-D nerve repair constructs. The main exception to this being that the majority of work was carried out aligning silk micro-fibres instead of uADSC. The mechanical properties of a substrate are known to have a substantial impact on cell behaviour (Gu et al., 2012, Doyle and Yamada, 2016, Dalby, 2005) including neurons, which are influenced heavily with respect to axonal outgrowth (Athamneh and Suter, 2015, Kerstein et al., 2015). Recently, axon growth was shown to exhibit recognition and pathfinding within 3-D stiffness gradients (Sundararaghavan et al., 2009).

As shown previously in Chp. 2 and elsewhere (Pfister et al., 2007), the presence of GF can have a substantial impact on nerve regeneration, making a strong argument for their application during the treatment of nerve injuries. In practice, supplying the regenerating nerve with consistent doses of neurotrophic support remains a challenge (Madduri and Gander, 2012). Generally, strategies involve incorporating drug delivery agents (biomaterial or cellular) into the NGC (for recap, see: Section: 1.7.4 and 1.7.5). The use of silk-fibroin as a biomolecular delivery agent is well established (Catrina et al., 2013, Kundu et al., 2010, Seib and Kaplan, 2012) and is a particularly exciting candidate for drug delivery. Upon NGC integration, functionalised fibroin can accomplish a number of different roles in nerve repair, serving as a combined structural, guidance and neurotrophic support material.

4.1.1. What are the physical limitations for sonotweezer alignment of silk microfibres?

Microparticles can be trapped in acoustic fields, but control is limited when the size of the particles approaches the half wavelength of the applied acoustic field; on the other hand, longer fibres are better placed to support regeneration as the number of disruptions is lower. Here the dimensional limitations on the silk microparticles limitations for reliable trapping and alignment were investigated.

4.1.2. Is durotaxis a suitable way to guide regenerating nerve fibres?

To guide regeneration topographic patterns, gradients of chemicals, and immobilised haptotactic chemical cues have been used. Quite a few different cell types, including neurons are guided by mechanical cues; termed durotaxis by (Lo et al., 2000), in which, the guidance of cells or in this case neurons by gradients or differences in local apparent stiffness. The stiffness of a hydrogel may be varied by a difference in fill factor, when a hard, particulate material is mixed in with the soft one; but the effectiveness of this patterning depends on: the differential stiffness as well as the extend of deformation that is applied to the material. Here it was hypothesized that through the embedding of aligned, stiffer silk micro-fibres within the relatively soft collagen, local stiffness gradients can be formed, which may serve as guidance cues for growing neurites.

4.1.3. Can silk microfibres be used for localised NGF release?

Growth factors, whose beneficial effect on peripheral nerve regeneration (introduced in section 1.5) have been supplied systemically, but then their effect can be dominated by unwanted side-effects on other targets such as in brain function, behavioural activity and pain sensation (Liu et al., 2014, Eriksdotter Jonhagen et al., 1998, Weissmiller and Wu, 2012). This has led to targeted delivery and suppository systems. One way to supply GFs locally is by exploiting the differential adsorption of these to materials which then can be used as GF release systems. A range of polymers have been investigated and used in this way include fibrin, silicone and collagen; through cross-linking, affinity based approaches for the delivery of neurotrophic

factors (e.g. NGF, GDNF) (for review: (Ramburrun et al., 2014). Here the hypothesis was that silk microfibrils could act to locally supply NGF to support regeneration over a well-defined period of time, guiding axons and promoting more extensive outgrowth.

The aims for this chapter of the thesis are to address the following questions:

- Is it possible to reliably manipulate and trap silk fibres within collagen hydrogels during gelation using sonotweezers?
- Will the size/ shape of the silk particles affect their placement and orientation in the acoustic field?
- Can the silk fibres direct neurite growth by proxy of a mechanical gradient or directly?
- Can the silk fibres be used as a delivery agent for growth factors e.g. NGF?

4.2. Methods

Protocols for DRG extraction, cell culture, immunostaining and time-lapse cell tracking were the same as used previously and are described in detail in Section: 3.2. Sonotweezer device operation was carried out as previously described, but here replacing cells with particles. Collagen hydrogels were formed using the “stiff” method, outlined in Section: 3.2.3. All work used the final octagonal sonotweezer device except in (Figure 53) which was done using the “3-D printed” device.

4.2.1. Silk Fibre Production and Processing

The production of silk fibroin and silk solution was carried out in collaboration with and under the supervision of Dr Philipp Seib (Strathclyde Institute of Pharmacy and Biomedical Sciences, University of Strathclyde).

4.2.1.1. Initial Silk Fibroin Extraction and Rinsing

Silk fibroin was extracted from the cocoons of *Bombyx mori* as previously described (Rockwood et al., 2011). In brief, cocoons were cut into ~25mm² pieces and boiled for 60 mins in 0.02M sodium carbonate solution and rinsed in deionized (DI) water to remove serum proteins, a process known as “degumming”. The extracted silk fibroin was then air dried to yield the degummed silk fibres.

4.2.1.2. Preparation of silk fibroin solution and hydrogel formation

Dry silk fibres were created as described above(4.2.1.1), their weight determined and then dissolved in a 60° C warm 9.3 M LiBr solution to yield a 20% w/v solution over a period of 4 hours. To remove LiBr salts, the solution dialysed (3.5kDa MW cut off tubing) against DI water over 48hrs. The DI water was changed 6 times (1/3/6 /18/36/48 hrs). The resultant silk fibroin solution was then twice centrifuged for 20mins at 5-10° C/ 9000rpm. The polymer concentration of the silk solution was measured by drying a known volume and weighing the resultant fibroin.

Silk hydrogel formation was achieved through sonication (Branson Ultrasonics, Danbury USA) of a 3% silk solution at high power (45%) for a period of 30-90 seconds. This resulted in a 1-2-hour gelation time required for sonotweezer alignment.

4.2.1.3. Preparation of silk microfibers

This work used a well-established protocol ((Mandal et al., 2012) for the fabrication of silk microfibers using alkaline hydrolysis. Briefly, 1g of dried, degummed silk fibres, created as described above (4.2.1.1), were submerged in 15ml of 17.5M NaOH (NaOH pellets, Sigma Aldrich UK.) solution for a period of 10 mins. Fibre size consistency and rate of hydrolysis was aided by stirring using a spatula. The hydrolysis was quenched with the addition of DI water (150 ml) followed by centrifugation at 2800x g for 5 mins. The supernatant was then discarded, and the fibres were suspended in 50 ml of water, stirred and centrifuged again. This step was repeated 6 times further and the pH measured before being adjusted to 7.0 by the dropwise addition of HCl. The neutralised silk fibre solution was centrifuged again for 5 mins before resuspension in 10 ml of PBS (repeated another 2 times). The silk fibres were then filtered to create a relative monodispersity/ majority fibre size <200 µm by passing the solution through a

100 µm strainer. A rough estimation of the concentration and size dispersion was attained by pipetting a known volume and viewing under a microscope before longer term storage (4 °C).

4.2.1.4. Preparation of sterilised silk microfiber solution

For cell culture, ~ 1ml of silk microfiber stock solution was sterilised through 30 min incubation within 70% ethanol and left in a laminar flow hood until complete evaporation/ drying had occurred. The dry, sterile fibres were then re-suspended in the ~5ml of media (DRG media (Section: 2.2.3)) and the concentration measured. From this the volume of solution was increased (as above) until a consistent fibre concentration was created, relative to other experiments (Figure 59). The resultant solution was used within the sonotweezer device in 25 µl aliquots and kept for a maximum of 2 weeks.

4.2.1.5. Preparation of carbon microrod solution

Carbon microrods were obtained as a gift from Prof. Jürg Dual's group at the Institute for Mechanical Systems, ETH Zürich. Firstly, the carbon microrods were sterilised by submergence in 70% ethanol for 30 mins before being left to dry in a laminar flow cabinet. To reduce the average rod size and provide greater monodispersion, rods were grinded using a spatula. Finally, the rods were suspended in media and heavily shaken before use. The concentration was not determined as this particle was employed merely to test although was seen to be comparable to the silk fibre solutions.

4.2.2. Analysis of particle alignment

Footage of particle alignment was recorded using a microscope with adjustable magnification (1-3x) adapted with a MikrOkular Full HD eyepiece camera (Bresser). This was situated within an open laminar flow cabinet in order to maintain sterile conditions for culture.

4.2.3. Preparation of NGF loaded silk microfibers (NGF-silk)

A general schematic of the protocol can be found (Figure 58). Initially, 1 ml of silk microfiber stock solution was centrifuged at 4000 rpm for 10mins and the supernatant removed. The fibres were then resuspended in 100 ng/ml NGF, DRG media and placed within the fridge overnight. Following this incubation, the fibres were again centrifuged at 4000 rpm and the NGF containing supernatant removed. NGF-loaded silk sediment fibres were then re-suspended in DRG media (nil NGF) and transferred to a fresh vial, completing the first wash cycle. To ensure sufficient NGF removal from the solution, this wash step was carried out 4 additional times. Finally, the silk fibres were adjusted to approximately the same concentration (as used above 4.2.1.3 and 4.2.1.4). To gain an insight into the consistency of fibre concentration, 2-3 droplets (2 or 5 μ l) were applied to a microscope slide and imaged under a microscope at (385nm excitation). Filament sensor: trace filaments (Eltzner et al., 2015) was then used to count and then calculate the average fibre concentration. Silk fibre solutions with/ without NGF were used immediately with any excess discarded to ensure consistency between experiments.

4.2.4. Enzyme-linked immunosorbent assay (ELISA) of NGF-silk

To assess the quantity of NGF released from the loaded NGF-silk fibres, a β -NGF rat ELISA kit (ERNGFCL, ThermoFisher Scientific) was used. Although this was originally intended for cell lysates, this kit was selected for its broad sensitivity range (15-15000 pg/ ml) and the possibility that it may not be as susceptible silk fibroin protein fragments blocking the assay. The assay was carried out as instructed within the given protocol (ERNGFCL)(ThermoFisher UK) which included the generation of a standard curve for NGF solution versus absorbance. Analysis of the plate was carried out on a Multiskan plate reader (ThermoScientific) (settings: Fast, 5 seconds-continuous shake (medium), 450/570 nm with no pathlength correction).

4.2.4.1. ELISA sample preparation and experimentation

NGF-silk solutions (3 solutions) were prepared as stated previously and their filament concentrations measured. High and low fibre concentrations were created for each sample through dilution before transferring ~110 μ l of each into Eppendorf for each

experimental condition. Following completion of each experiment, the Eppendorf was shaken (to disperse the eluted NGF), then centrifuged (500rpm/ 10 secs) before carefully siphoning the supernatant. This was then placed in a fresh Eppendorf and frozen (-80 °C) for storage until analysed.

For assessing the quantity of NGF release from the NGF-silk after a 3 days periods (Figure 59 B, D and E), Eppendorfs at low and high conc. were placed in cell culture incubator (37 °C, 5% CO₂) and the former placed in the fridge (4 °C). Time-interval analysis (Figure 59C) comprised of removing the media at each time point (outlined above) and replaced with fresh media, shaken and replaced under their respective experimental conditions. Analysis of untreated silk and 2 ng/ ml NGF-DRG media was carried as above with the former obviously under exclusion of silk steps.

Experiments were carried out in triplicate, with exception of the wash eluent (orange dashes), DRG media concentrations (blue, red lines) and silk (green line) which were singular. Each analysis for ELISA was carried out in duplicate.

4.2.5. Data analysis

4.2.5.1. Interpretation of ELISA results

Using excel software (Microsoft), the average absorbance of the blanks (450 nm) (nil NGF standard) were subtracted from all absorbance values (450 nm) of each well result (to correct for background). The duplicate standard and sample well readings were then transferred to Graphpad 6 software (Prism) to create an XY plot. Together with their known concentrations, the standard abs values were used to create the standard curve (below) using hyperbola interpolation (equation in determined by the shape of data) with a 95% confidence band. From this, the NGF concentration values of each well sample were then interpolated and averaged across duplicates to provide comparative values between experiments.

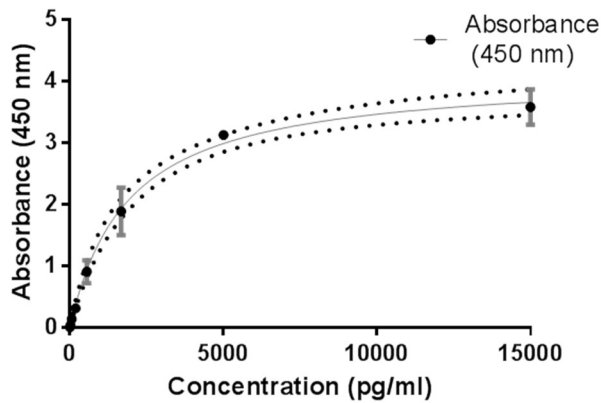


Figure 52: Standard curve for ELISA interpolation. Following background correction, the standard curve was generated from 450nm absorbance values of standard controls in the range of 15-15000pg/ml NGF. Interpolation was carried out using Graphpad 6 software through hyperbola curve fitting which was then used to extrapolate the concentration of each sample. Analysis of each sample was carried out in duplicate which was averaged for comparisons.

4.2.5.2. Determination of silk concentration and estimation of NGF concentration within NGF-silk cultures

Fluorescent images (excitation 385nm) of silk droplets were taken as stated previously of 2-3 droplets (for measurement repeats) per silk solution (6 repeats). To assess the total fibre length for a given volume, the droplet images were first processed via CLAHE (ImageJ) and CamRaw (Photoshop CC) (Section: 2.2.6.2) to create clean images devoid of speckles etc. which would provide false positive results. The fibre length was calculated using Filament Sensor: Trace filaments command under default, auto settings. The length for each filament detected in pixels was then totalled and converted to mm. Filament sensor accurately calculated the total length; however, individual fibre lengths sometimes comprised of 2 or more filaments and therefore this data could not be used to calculate the average fibre size. The total filament length was then calculated with reference to the volume used (for sonotweezer droplet: 25 μ l, for ELISA: 100 μ l).

The estimated NGF concentration in media (initial 24 hours) of the NGF-silk cultures was then calculated using the average calculated fibre length added to each culture (above) multiplied by the average NGF elution (pg/ mm) derived from the ELISA results. This was then calibrated for 400 μ l of media within the culture well. This was done with the assumption that the widths of all fibres are the same (based on

observations of the fibres) and thus, the surface area for NGF adsorption is consistently proportional to the fibre length in this study.

4.2.5.3. Quantification of axon network and silk alignment lengths/directionalities

For this the immunolabelled axon fluorescent images also contained silk fibres due to their autofluorescent nature. To separate axons from silk fibres, images were first flattened from their 3-D z-stack to 2-D using extended depth of field plugin (Forster et al., 2004). Then, the UV excitation (395 nm) image (which shows the autofluorescent silk and nuclei, but no axons) was subtracted from the red channel (excitation: 520 nm) channel which contained both neurofilaments (axon network) as well as silk autofluorescence using an ImageJ process: Image Calculator (subtraction). This resulted in an adequate separation without compromising the shape and density of the axon network. The images were then processed (CLAHE/ CamRaw) and analysed with Filament sensor: trace filaments command and the total length of axons and/ or silk measured as described in detail in section: 2.2.6.3.

For relative comparison of axon length: silk fibre length, the entire silk scaffold was not measured as it was assumed that diffusion of NGF from farther silk fibres did not reach or influence the migrating axons. Instead, a circle was fitted to the size of the network, cropped and the fibre length quantified as above. This was then calculated as length of silk per area of network to normalise the discrepancies of scaffold quality. Finally, this was displayed as a ratio of axon length: silk length per area (Figure 60).

For directionality guidance analysis of the silk scaffolds for axons (Figure 61), the scaffold was cropped exactly around the perimeter of the network (i.e. not a fitted circle) and measured as above. The guidance provided was then calculated comparing the neurite and silk directionality histograms (9 bins) as a Pearson's correlation graph using Excel software (Microsoft).

4.2.5.4. 3-D reconstruction of neural network using Neuromantic Software

To visualise the network of a DRG growth in 3-D, the z-stack was loaded into Neuromantic software (Myatt et al., 2012). Neurites were traced (under the “axons” setting) by hand through the depths in semi-automatic mode (which calibrates depth between nearby slices). The DRG body was included using the “soma” setting. The final 3-D reconstruction was then rotated, and snapshots captured for images shown in Figure 63.

4.2.5.5. Statistical analysis

Graph creation and statistical analysis was performed using GraphPad Prism version 6 (GraphPad Software). Analysis of cell survival (Figure 60) was carried out Two-way ANOVA with a Tukey post-hoc test for multiple comparisons. Due to unequal sample sizes and variances, network outgrowth analysis was carried out using non-parametric One-way ANOVA with Dunn’s test for multiple comparisons. Alignment speed analysis was tested across 6-10 different tracked particles within a single alignment recording and determined significant by Pearson’s coefficient correlation (Figure 61). Analysis of DRG results were gained from a minimum of 3 explants from different rats unless otherwise stated. Statistical significance was determined by $p < 0.05$, and presented by * $p < 0.05$, ** $p < 0.01$, *** $p < 0.001$ and **** $p < 0.0001$ complete with standard deviation bars.

4.3. Results

4.3.1. Silk Micro-Fibres Alignment Testing

In order to realise the potential of aligned silk fibres in 3-D, the trapping ability and quality of pattern had to be assessed first. Although these experiments were aligned within the stiffer collagen hydrogels created previously, a small number of attempts were made to carry out the procedure in silk fibroin hydrogels. However, this

required much more gelation, setting time and cell survival would have needed to be addressed, which was not possible within the time frame of this work.

4.3.1.1. Initial particle alignment attempts

Following the creation of silk fibres (described in section: 4.2.1) the fibres were chemically cleaved with NaOH, sterilized and re-suspended in solution. Initial attempts to align the silk particles within collagen yielded slight success with the indication that the silk fibres could be manipulated (Figure 53A) however, pattern disruption was caused due to larger filaments which could not be trapped. With the inclusion of a filtration step using a 100 µm strainer, much greater alignment quality was observed. As an alternative to silk, carbon micro-rods were also aligned (Figure 53B) and again, the larger rods inhibited patterning. This was counteracted through a grinding step using a spatula and resulted in moderately better alignment capabilities.

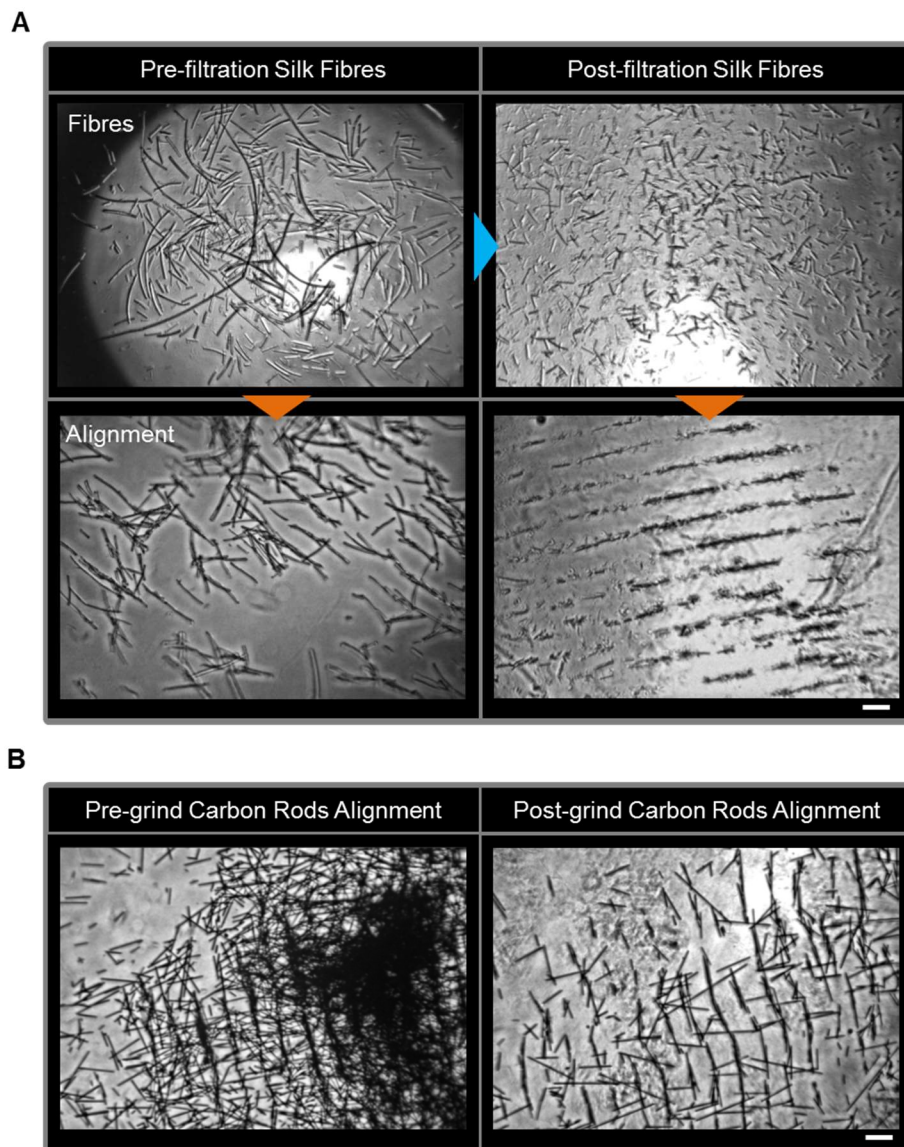


Figure 53: Pre-processing of silk fibres and carbon rods to trapping ability. Alignment was carried out using Chp. 3: “3-D printed sonotweezer device” to create a pattern width of $\sim 105\mu\text{m}$. Image set A shows: silk fibres left unfiltered in which fibres are sized between $\sim 50\mu\text{m}$ -2mm, causing difficulties with alignment (orange arrow) as larger fibres are unable to be manipulated. This pushes smaller alignments out of the field etc. and results in poor patterning. Following a $100\mu\text{m}$ filtration, there is a much more homogenous size dispersion of silk fibres and as a result, alignment is of a greater quality. Similar to silk, patterns of carbon rods were heavily disrupted by the presence of larger rods. Through the grinding of the rod solution using a spatula, many of the larger rods were broken down and as a result; greater trapping is observed. Scale: $100\mu\text{m}$

4.3.1.2. Characteristic alignment based on particle properties

Despite some success with alignment of objects, differences to cell manipulation were noted such as slower alignment speeds, poorer pattern quality and more rapid sinking rates. Through video recordings of each alignment and analysis using ImageJ Manual Tracking, the speed of particle movement was calculated (Figure 54).

Generally, across all particles, when the sonotweezer was activated, some alignment was seen immediately with addition of the droplet however remaining areas of the pattern had to “catch up” to complete alignment. The uADSC cells aligned near instantly and could not be tracked accurately. Silk fibres took ~7 secs settle into complete alignment whilst carbon rods required ~14 secs, which was also in agreement with the particle velocity measurements (B) indicating that the particle dimensions and weight were playing a role. Further, carbon microrods were found to rapidly sediment to the bottom of the gel, allowing almost no disruption (such as from DRG inclusion, or accidental device agitation) to the pattern during setting. These disruptions would cause very poor-quality patterning as the rods could not be re-manipulated fast enough before sedimentation at the bottom of the gel where surface friction likely inhibited further movement.

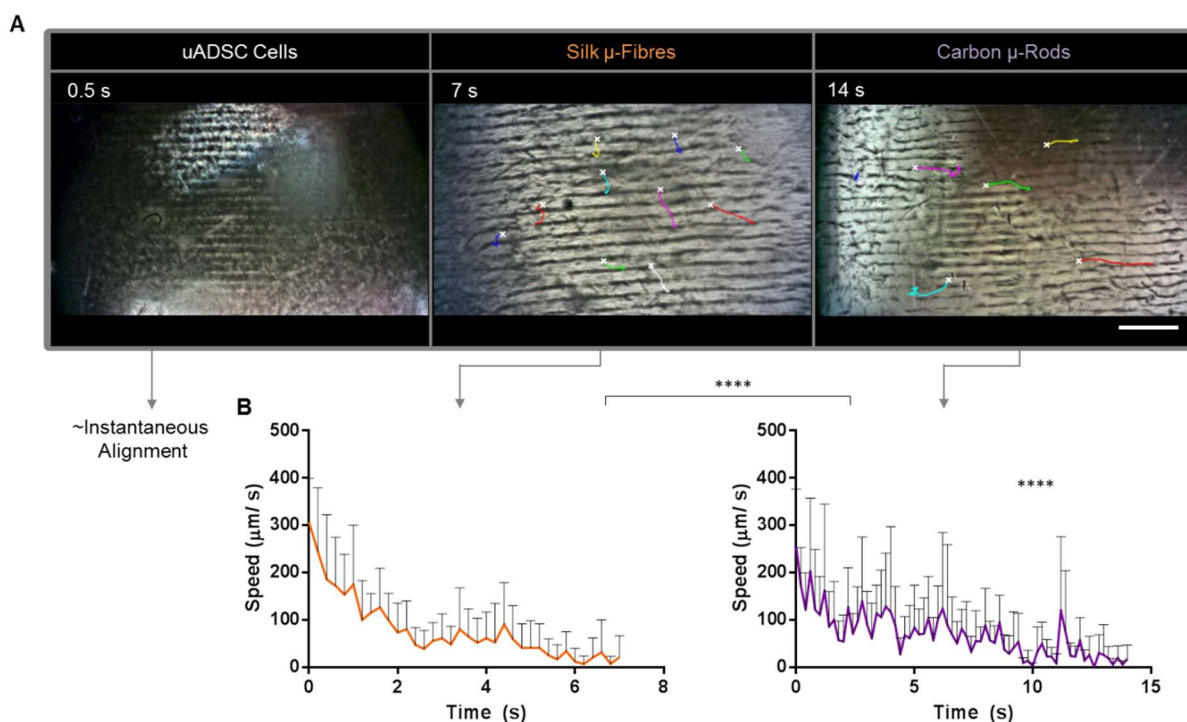


Figure 54: Alignment Speed and Time Comparison. The 185 μm alignment speed of each particle was calculated using the manual tracking plugin of ImageJ. The image-set (A) shows the route (coloured lines) individual particles take (originating from white cross). Overall, all particle alignments have some degree of initial alignment upon application of the droplet; however, the time taken for completed, unsettled alignment differs. Left: uADSC pattern alignment occurred almost immediately and could not be tracked (also due to the size of cell). Middle: silk micro-fibres were completely aligned by 7 seconds and right: carbon micro-rods took ~14 seconds. The speed of particles (B: silk/ orange, carbon/ purple) graphs show the silk fibres to travel ~100 μm faster than the carbon rods initially and plateau (alignment completion) at a faster rate. Statistical analysis carried out on 6-10 tracked particles from a single alignment recording, by Pearson's coefficient where $P^{****}<0.0001$. Scale: 1mm, x1 Mag.

4.3.1.3. Quality assessment of silk fibre-collagen alignment

To assess the overall quality of aligned silk micro-fibre scaffolding, the average direction of fibres over the entirety of 3 independent gels was calculated using Filament Sensor “trace filaments” command (Figure 55). The orientation was found to be predominantly in the direction of alignment to a pattern width $\sim 375\mu\text{m}$ as expected. The acoustic trapping field generated by the sonotweezer device created an alignment area of $\sim 25\text{mm}^2$, outside of which the fibres seemed disorganised (yellow arrow). Larger fibres with a length that was approximately the same as the spacing of the acoustic nodes were seen to orient perpendicular to the pattern (blue arrows). The finished hydrogels then could be readily transported to the culture well, as in Chp. 3.

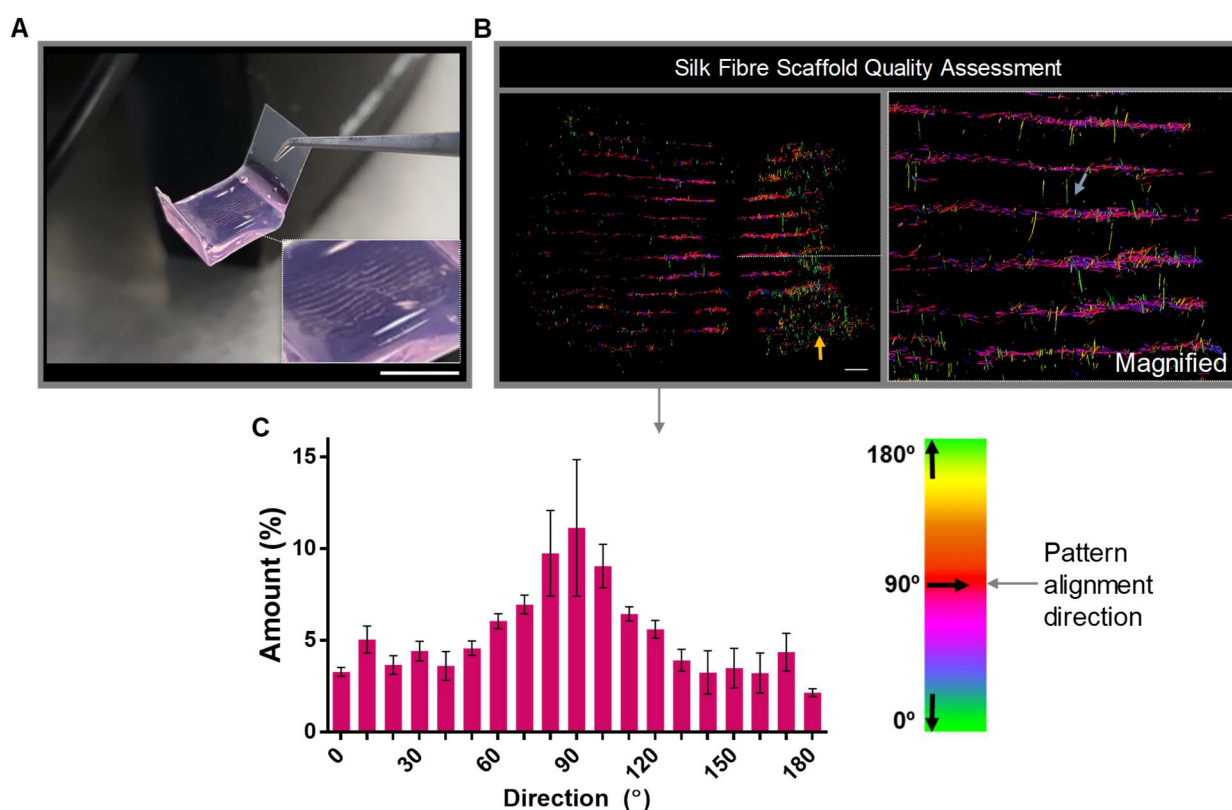


Figure 55: Aligned silk scaffolding reproducibility assessment. For this analysis, silk micro- fibres suspended as an array within collagen hydrogel during gelation to a pattern width of $375\mu\text{m}$ and relatively singular plane of alignment ($\sim \pm 50\mu\text{m}$ depth dispersion). (A) shows the macroscale image of the silk suspended within the finished gel construct, accompanied with an inset showing a zoomed-in view (white dashes, re-used from Chp. 3: Figure 38). Imageset (B) shows a Filament Sensor eLoG output of an entire fabricated scaffold with magnification for detailed visualisation of silk microfibre alignment. Silk microfibres were seen to be predominantly aligned in accordance with the directionality of the pattern lines. Alignment was consistent through the entire area of the predicted pattern field ($\sim 4\text{mm}^2$) with its outer perimeter visible where fibre disorganisation occurred (yellow arrow). Also, despite the filtration step, inevitably some larger fibres were present, which was seen

to reside perpendicular to pattern direction, between the bands (blue arrow). The colour wheel (C), ties the directionality histogram (Filament Sensor) to the eLoG images. The directionality histogram shows the average histogram result from the analysis of 3 scaffold repeats, revealing a prevalence for the direction of alignment (~red/ 90°). Scale A: 500µm, D: 1cm

4.3.2. Aligned Silk Micro-fibres for Nerve Growth

4.3.2.1. 3-D Guidance of DRG neurites with silk microfibres

Returning to the overall goal in using combined collagen type I/-silk microfiber constructs to enhance current nerve repair strategies, DRG explants were cultured for 6-days/ NGF (2 ng/ ml) within the gels as described earlier in section 3.2.5. Both collagen type I gels with aligned and with random distributions of silk microfibers were investigated (Figure 56) and compared against the growth of DRG cultures on collagen type I gels without silk microfibers (also used in section: 3.3.4). The image analysis of axon networks showed that only a small aspect of the axon networks were directed by the silk microfibre pattern. However, a more uneven histogram than the nil silk control may indicate that the aligned silk microfibers could possibly play some role in axon guidance.

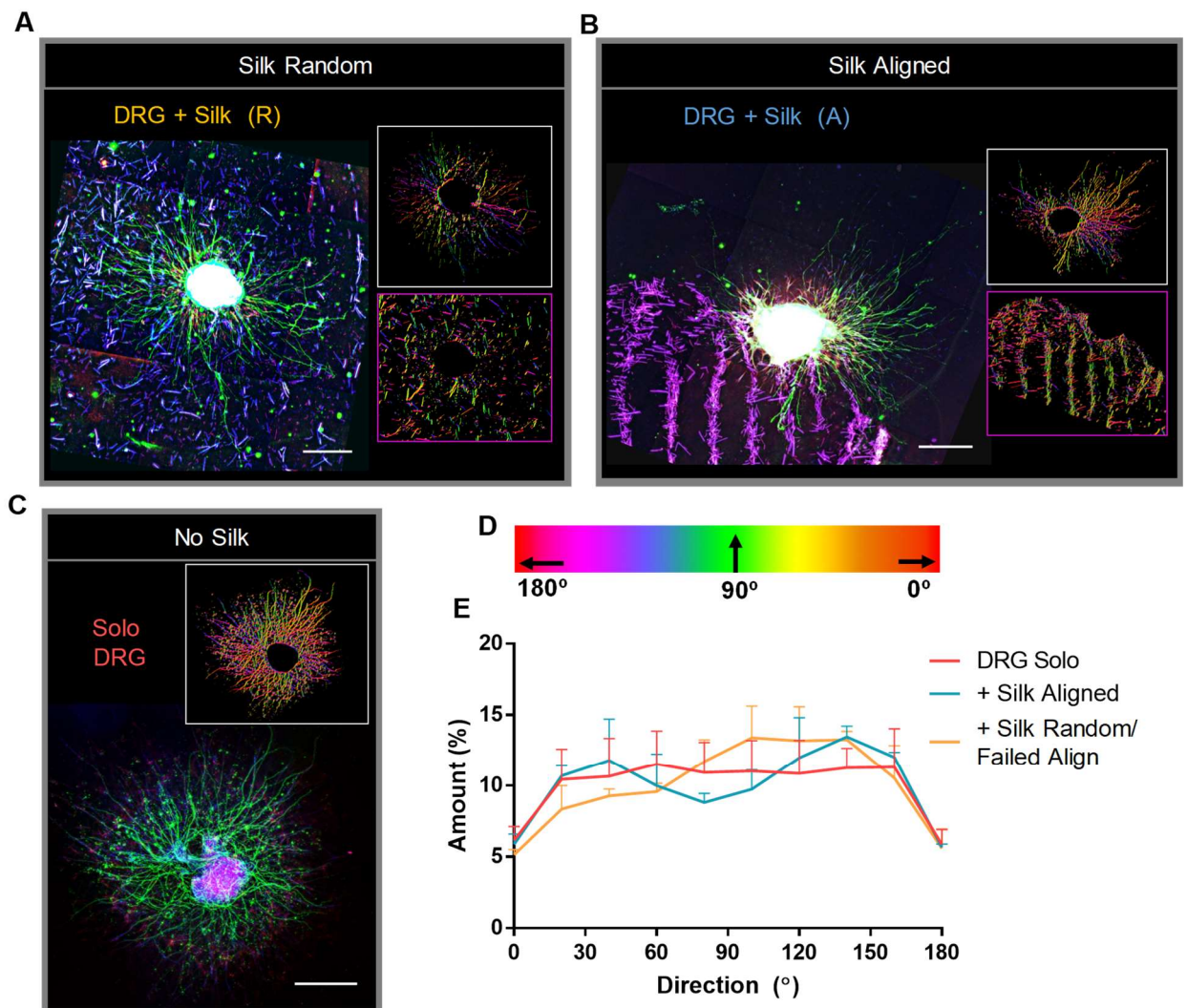


Figure 56: Analysis of DRG axon guidance by aligned silk micro-fibres suspended in collagen at 2 ng/ml NGF. Fluorescent image-set (A-C) visualised through immunostaining of axons (Neurofilament heavy chain, green), actin (phalloidin, red) and nuclei (DAPI, blue). Silk is auto-fluorescent, showing up as the blue/ purple fibres. Unaligned silk microfibres were not patterned. In comparison to the solo DRG cultures, axons of DRG cultured within the silk microfibre scaffolds were seen to exhibit a slightly less even outgrowth. However, DRG grown on collagen gels with aligned silk showed no apparent alignment of axons compared to the collagen gels with unaligned-random silk microfibres. These observations were further confirmed through Filament Sensor directionality analysis (inset boxes: white/ neurites, pink/scaffold), showing some peak formations within the histogram, although overall: very minor differences compared to the nil silk control. Analysis was carried out on 6-day DRG explants; solo DRG $n \geq 3$ and silk fibre DRG cultures (aligned/ unaligned) $n = 2$ independent biological repeats with bars to indicate the standard deviation (E). Scale: 500 μ m

4.3.2.2. Visualising the interaction between GC and silk

To gain an insight into the possibility of an interaction, a culture was recorded using a time-lapse microscope (Figure 57). From this video, the majority of axons were seen to neglect the presence of the silk, growing in the typical fashion of a singular DRG culture in 3-D (Figure 56). Despite this, a minority of axons exhibited an interaction

with the silk, which generally involved the growth cone travelling alongside the silk, or deviating akin to the typical behaviour of GCs meeting repulsive cue (e.g. semaphorin 3 (Hung and Terman, 2011)), as depicted by the manual tracking colour paths.

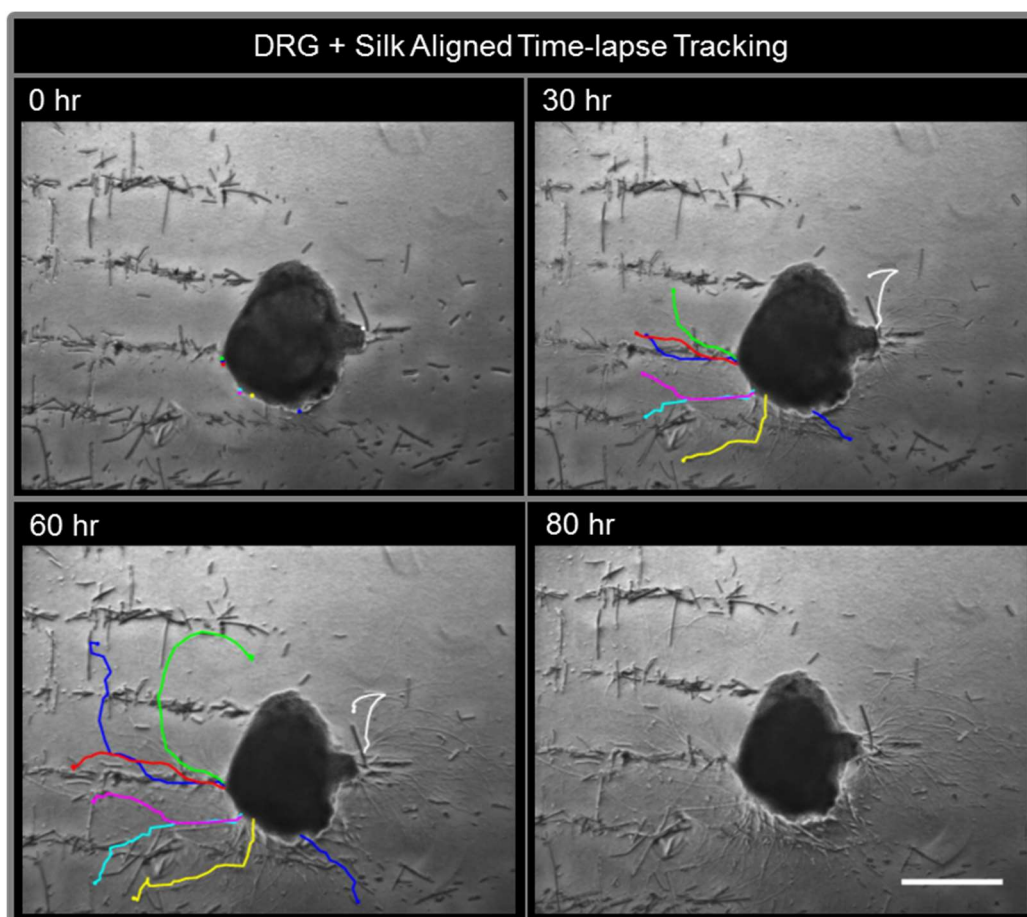


Figure 57: Time-lapse tracking of DRG axon outgrowth within the silk fibre scaffold at 2 ng/ml NGF. The neurite growth of a DRG was recorded over a period of 80 hours using a brightfield microscope and camera setup mentioned previously. Tracking of axon pathfinding (0-60hr) was carried out using Manual Tracking plugin (ImageJ) and is depicted as coloured trails within the image-set. Axons can be seen to have a marginal interaction with the silk fibres, with the majority apparently regardless. Tracked neurites highlights the minority of axons which have some interaction that can be seen, in which upon meeting the silk fibres, they either: deviate around it or are repulsed by it. An image at 80 hrs (bottom right) is shown to give a later fuller network growth. Scale bar: 500µm

4.3.3. NGF loaded silk microfibers (NGF-silk)

4.3.3.1. Creation of NGF-silk

As there was very little neurite guidance by the native silk, investigation began into the use of silk microfibres as delivery agents for local NGF release for chemotactic neurite guidance. This was attempted through the loading of the fibres with NGF

(Figure 58) through an overnight incubation step within a concentrated NGF solution (100 ng/ ml) which was presumed to lead to NGF ad or absorption to the silk microfibres, bearing similarity with the work of Kundu et al. (2010) for the loading of silk nanoparticles with VEGF. To ensure that the remaining NGF within the bulk solution was removed, an intensive wash step was carried out (Figure 58 (4)).

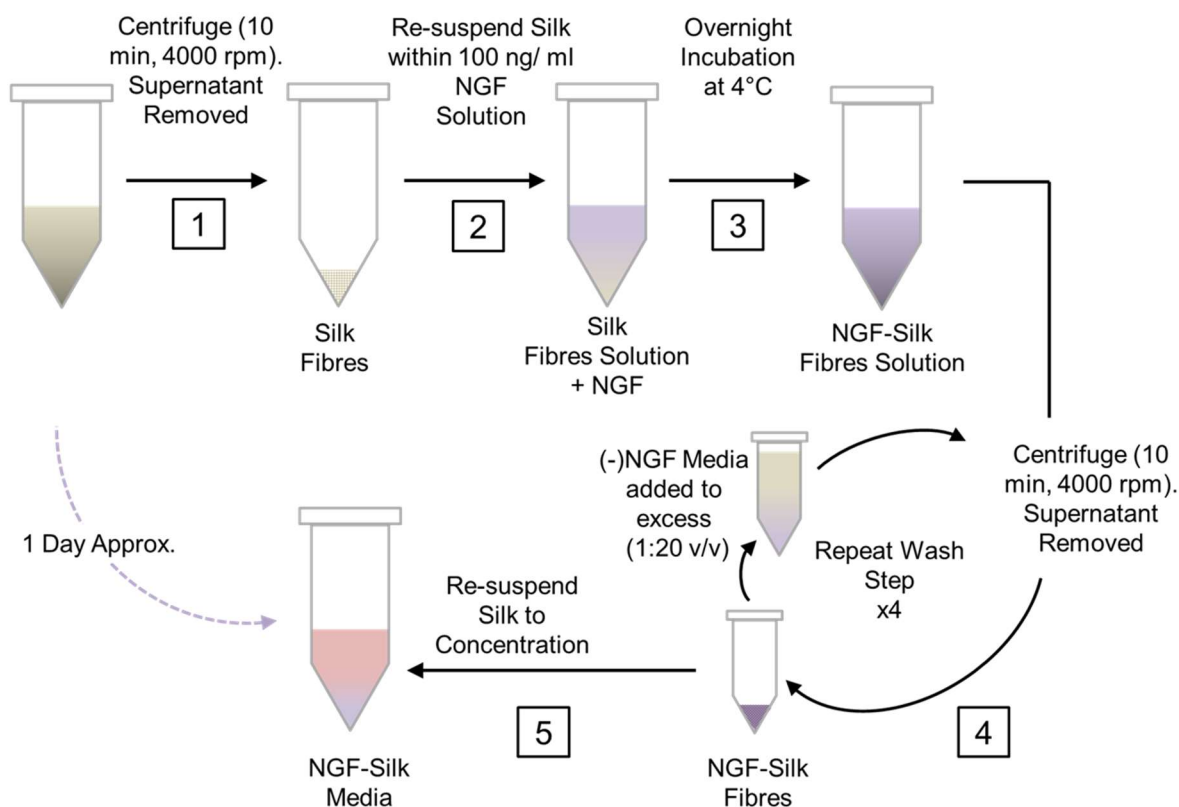


Figure 58: Schematic of process for the creation of NGF functionalised silk micro-fibres. An in-depth protocol is disclosed in the methods (section: 4.2.3). Briefly, following the micro-fibre production and sterilisation, the suspension was centrifugated and the supernatant removed (1) leaving a dense, silk/ liquid mass. This was then re-suspended in excessive 100 ng/ ml NGF DRG media by shaking and incubated in the fridge (4°C) overnight (3), serving as the “NGF steep” step. This was then transferred to a fresh vial and centrifuged with supernatant removal to leave the dense NGF-silk/ NGF-liquid residue. This was then re-suspended in excess base DRG media (nil NGF) to an equivalent volume of 20 times the residue volume and shaken. This was considered the “wash step” and was repeated 4 further times from the point of transference to a fresh vial (4). Finally, upon completion of the intensive wash step, the NGF-silk was suspended within the chosen media (in this case DRG media) (5). The entire process was completed over 24 hours; however, this was largely dependent on the length of the NGF incubation step.

4.3.3.2. ELISA quantification of NGF release from loaded silk

To investigate the effectiveness of the incubation step in loading the silk microfibers with NGF, an ELISA was carried out of the media/ NGF-loaded-silk microfibre solutions at low and high (x2) concentrations and a standard curve used to

extrapolate the data (Figure 59). Following a three day incubation, 0.03 pg/ ml of NGF was found to be eluted per mm of NGF-Silk microfiber (Figure 59B) (Two results averaged, one result discounted from analysis but kept in graphs for transparency :black arrows with red asterisk, orange data points). This omission was done on the basis that it was an error/outlier due to similarity to regular silk. A control was taken as the final wash from the NGF-silk wash step and shown to only contain a negligible amount of NGF (gold dashes).

The amount of NGF that eluted from NGF-loaded-silk fibre samples kept at 37°C were found to decrease at a rate of about 400-500 pg/ ml per day eventually reaching a plateau after two to three days (Figure 59C). Also, Samples of NGF-loaded-silk maintained a higher NGF elution concentration when kept at 4°C, than when incubated at 37°C for a 3-day total period (Figure 59D), providing an indication to the relatively rapid rate at which NGF degrades within culture conditions. The 2 ng/ ml NGF media controls kept in fridge/ incubator further validated this occurrence, with the incubated media providing very little NGF detected after 24 hours (Figure 59C, black triangles). A discrepancy arose regarding the base DRG media controls, in which they show an approximate value of ~600 pg/ ml of NGF instead of the expected 2 ng/ ml. It was inconclusive if this is a result of poor media formulation, degraded stock or poor ELISA detection.

Finally, an estimate the NGF concentration within typical media conditions through the presence of NGF-silk (Figure 59E) was done by calculating the amounts eluted after 24 hours incubation of the NGF-loaded-silk samples relative to their total silk length and applying the NGF per mm to numerous droplet silk concentration tests (section: 4.2.5.2) taken throughout the entire study (6 tech repeats, 2/3 measured repeats). This found that on average, NGF-loaded-silk scaffolds kept within ca. 400 µl of culture media (as used in this work), produce an estimated ~60 pg/ ml NGF culture concentration within the initial day. However, this does not consider the diffusion of rate NGF through the collagen matrix, which is likely to produce much higher concentrations locally, and lower in the bulk media outside of the gel.

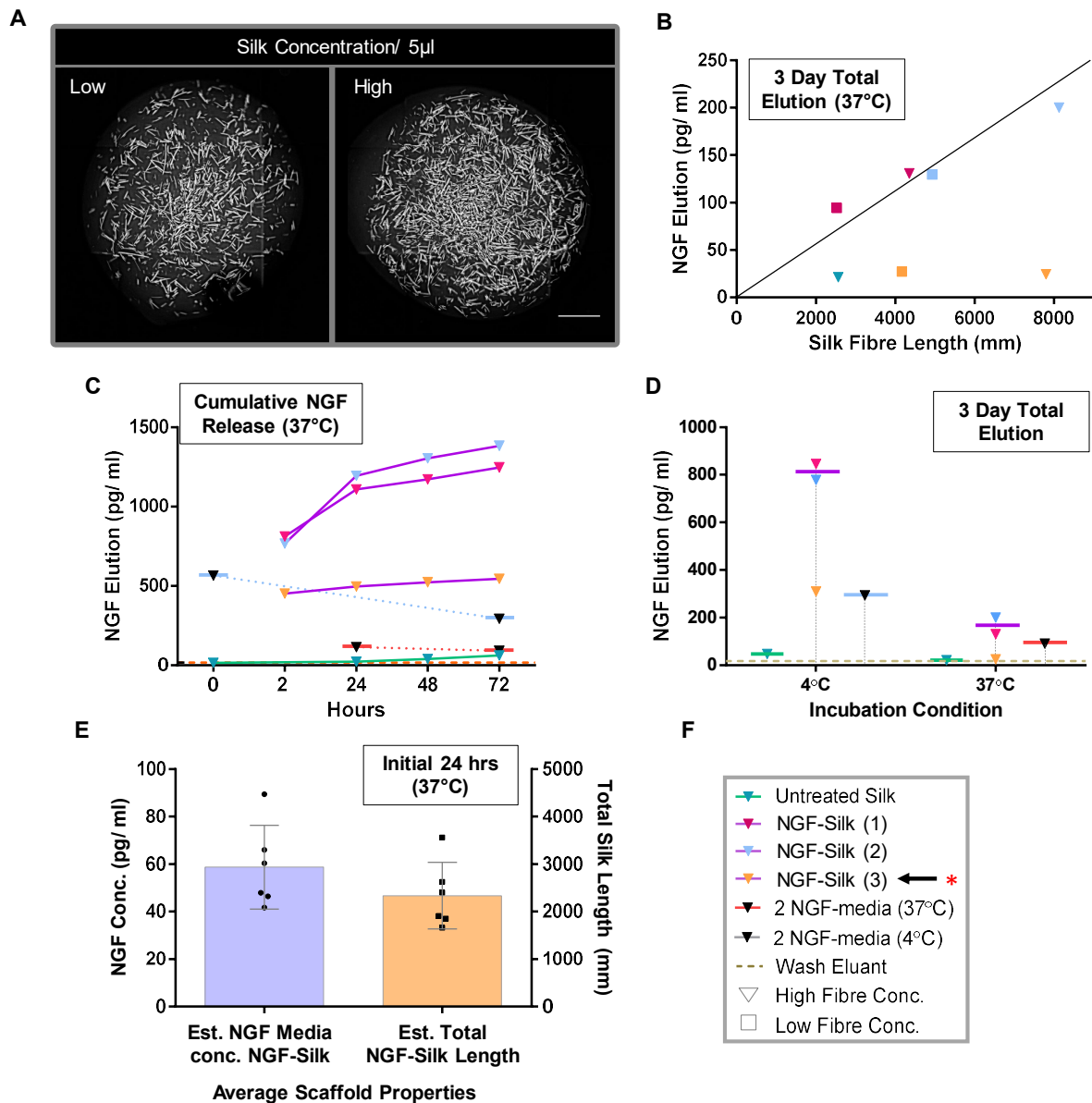


Figure 59: Investigation into the extent of NGF release from NGF-silk using ELISA. Analysis was carried out using an NGF sandwich ELISA kit (detection range: 15-15000 pg/ml) to generate an interpolated standard curve for extrapolation of data. Each NGF-silk sample was suspended in base DRG growth media under different conditions. Of the 3 repeats, one showed extremely poor performance and was considered an error (orange data points, red asterisk in (F)) but included for visual transparency. Quantity of NGF-silk was calculated (A) by imaging a 5 μ l droplet and using Filament Sensor software to measure total fibre length/ μ l. The elution of each repeated silk loading process (F: Untreated/ NGF- Silk (1-3)) is graphed with comparison to the length of silk in each sample at two different silk concentrations (high (triangles): ca. 2x low(circles)) (B). From this, it was found that the total length of NGF-silk present in solution correlated to the amount of NGF eluted into the media with an average of 0.03 pg/ml of NGF per mm of silk. This was much higher than that of untreated silk (green triangle) calculated at 0.008 pg/ml NGF per mm of silk. A day-by-day, cumulative analysis (C) of the eluted NGF in media of the NGF-silk and untreated silk shows the rate of degradation and/or elution of NGF from the silk fibres. For comparison, a non-cumulative, measured concentration of base culture media (2 ng/ml NGF) following timed incubations (blue lines: fridge, red lines: culture incubator) are included in the graph alongside the wash eluent (taken from the final wash step supernatant: gold dashed line). The amount of NGF eluted was seen to reduce by ~400-500 pg/ml per day to eventually plateau after 2 days, approaching levels like that of the incubated 2 ng/ml NGF media. Graph (D) compares the levels NGF eluted from NGF-silk, untreated silk and base 2 ng/ml NGF

media following incubation within the fridge and under culture conditions after a total of 3 days. This indicated that culture condition vastly reduced NGF levels; however, NGF-loaded silk fibres acted to provide higher NGF concentrations detected than that of the base culture media. Untreated silk showed minimal NGF presence and a negligible difference between each environment. Finally, to contextualise the results, an estimate of media NGF concentration within NGF-silk scaffold over the first 24 hours of culture using average 2hr+ 24hr elution (C) and total silk lengths per scaffold, revealing an average effective concentration of ~60pg/ ml. Experiments were carried out in triplicate, with exception of the wash eluent (orange dashes), DRG media concentrations (black triangles/ blue, red lines) and silk (green line) which were singular. Each sample for ELISA was carried out in duplicate.

4.3.3.3. NGF-silk scaffolds promote DRG outgrowth

Application of the NGF-Silk constructs for nerve regeneration was investigated as in previous experiments with DRGs cultured for a period of 6-days. To assess if the NGF-loaded-silk microfibers changed DRG response, these were cultured in media without any NGF, comparing cultures growing on treated and untreated silk microfiber embedded collagen gels (Figure 60). From the viability assay, NGF-silk was seen to have a slightly positive effect on cell survival (+~5%) over untreated silk, to reach a similar survivability as that of DRGs cultured in 2 ng/ ml NGF. However, this increase was not deemed to be statistically significant. Analysis of the network size (total axonal length) carried out using Filament Sensor, revealed the NGF-silk to promote a much greater average size than untreated, again showing comparable results to the 2 ng/ ml NGF cultures. Incorporating the length of NGF-fibres (and thus the NGF eluted) present in the vicinity of the network revealed axons to reach ~20% of the silk fibre length, further mirrored the previous results.

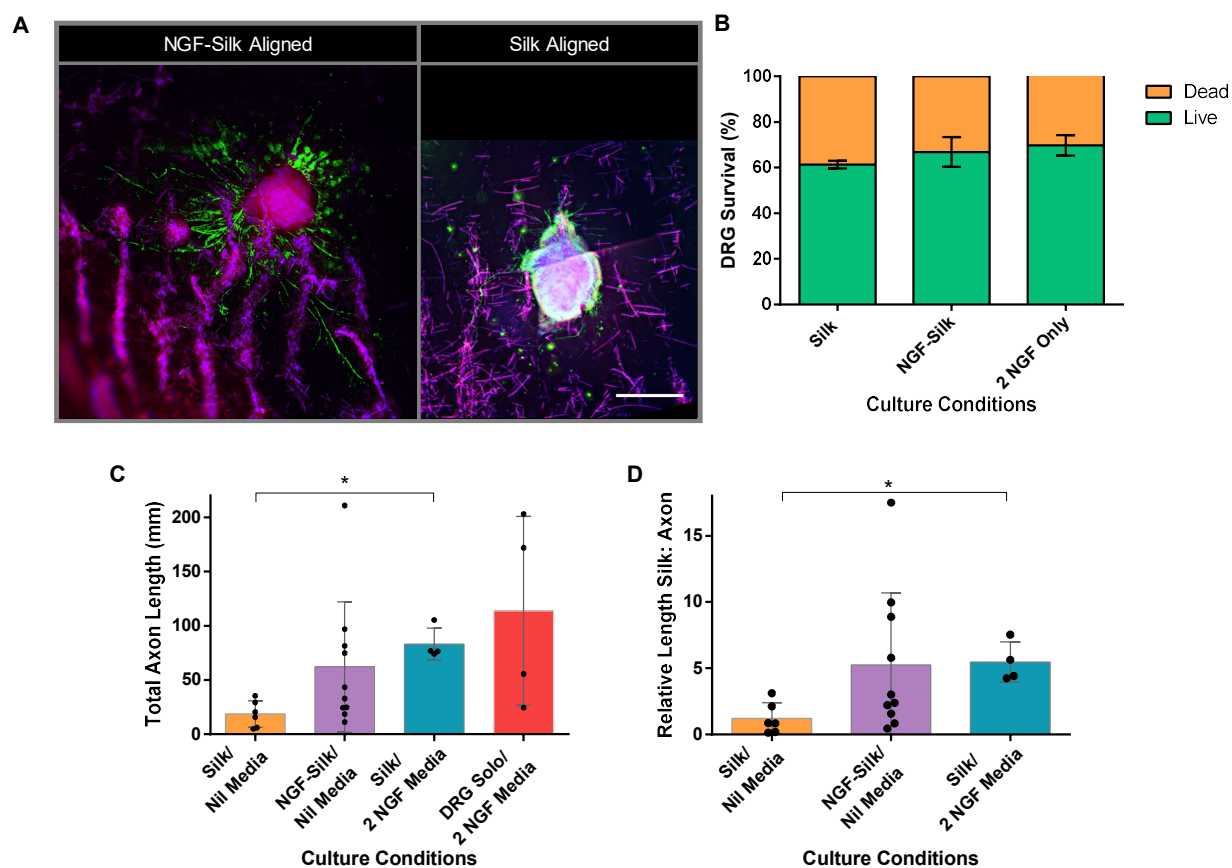


Figure 60: Analysis of DRG survivability and outgrowth within NGF-silk constructs at nil NGF media. Fluorescent image-set of each experimental setup (A) was visualised through immunostaining of axons (Neurofilament heavy chain, green), actin (phalloidin, red) and nuclei (DAPI, blue). Silk is auto-fluorescent, shown as the blue/ purple fibres. For outgrowth and survivability analysis, aligned and random cultures were grouped together. The DRG viability assay (B) showed no significant difference between each condition; however, on average NGF-silk increased survival by ~6% relative to untreated silk, reaching similar levels to that of 2 ng/ ml DRG cultures. The total axon length (calculated by Filament Sensor, (C)) of each culture condition revealed a large average increase in network length of DRG cultured in of NGF-silk over untreated silk, although this remained slightly lower than 2 ng/ ml NGF DRG cultures. Graph (D) compares the average ratio of axon network size to amount of silk per area (calculated: silk fibre length/area of network). This showed over a fourth-fold increase of NGF-silk to the regular untreated silk, and comparable levels to the 2 ng/ ml NGF cultures. This provided further confirmed the growth promoting effects of NGF-silk micro-fibres. Experiments were carried out on 6-day DRG explants. Statistical significance was determined by non-parametric, one-way ANOVA with Dunn's correction for multiple comparisons where $n \geq 4$ independent biological repeats. Bars indicate the standard deviation. Scale: 500 μ m

4.3.3.4. Investigating neurite guidance of aligned NGF-loaded-silk

Axon alignment was found to be reduced in the presence of any NGF source, whether by external media supply (2 ng/ ml) or that of the collagen embedded NGF-loaded-silk microfibre array (Figure 61). No apparent difference in network directionality was observed between DRG grown on collagen gels with either aligned or random NGF-loaded-silk microfibrils; however, untreated silk microfibrils/ nil NGF cultures did show more of a peak indicating that axons aligned along the pattern direction to

some. This was further confirmed through a Pearson's correlation analysis between silk microfibre direction (restricted to the filaments in the vicinity of the axon network section: 4.2.5.3) and axon direction, which was seen to be greatest at nil NGF/ untreated silk (-0.8) over that of the NGF-silk and untreated/ 2 ng/ ml (-0.6).

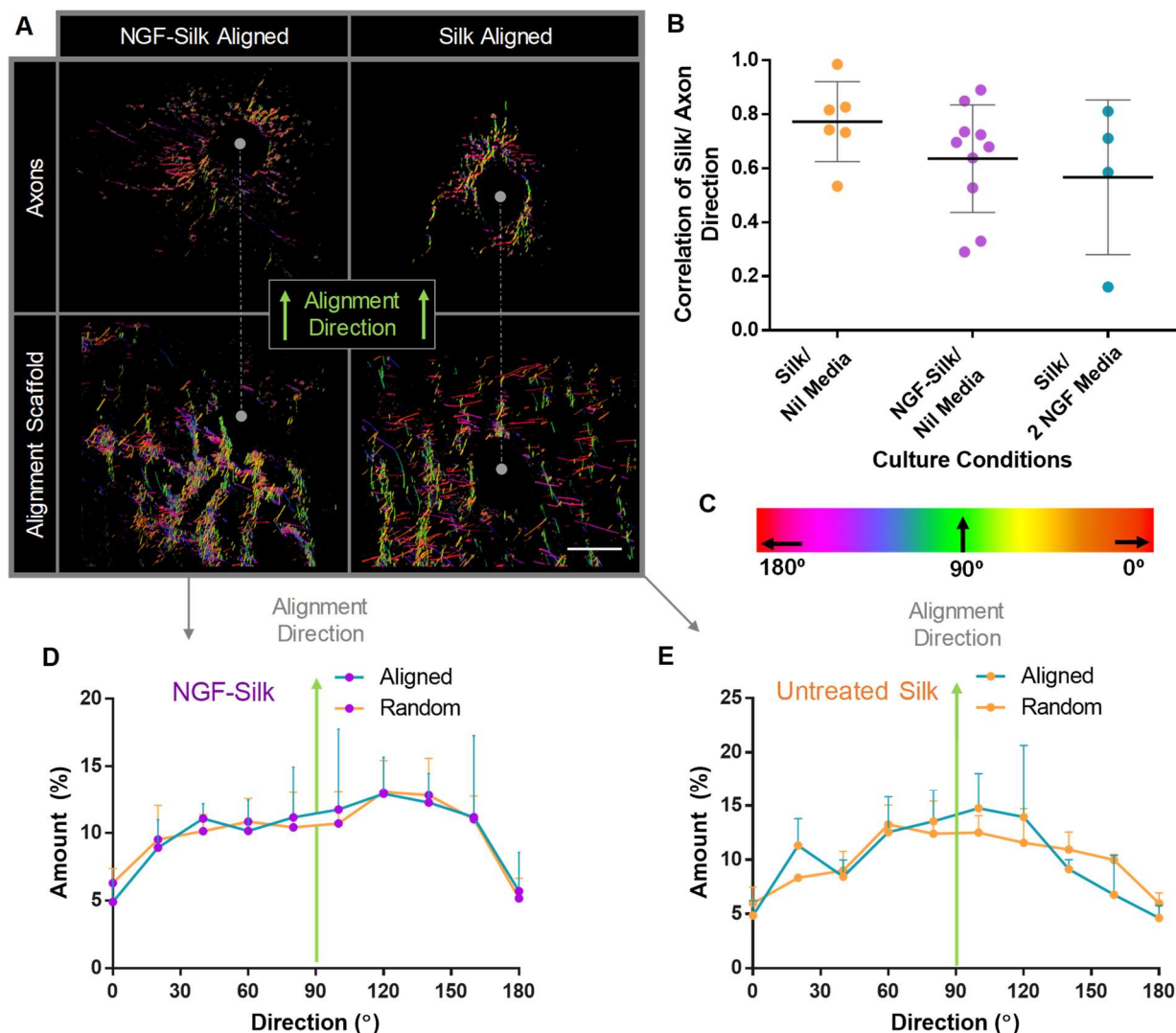


Figure 61: Analysis of directional neurite guidance of DRG explants within aligned NGF-silk fibre constructs at nil NGF media. Directionality of axons/ fibres (A) was found through EDF flattening of the 3-D image followed by image subtraction (axons (Neurofilament heavy chain) - silk (DAPI)) using ImageJ to separate each prior to analysis (Filament Sensor). The colour bar (C) gives direction: colour for Filament Sensor images. Graph (B) shows the correlation of silk: axon directionalities (silk analysis carried out within the region of the network only) to give a comparison between each scaffold. Of this, untreated silk without NGF supplied proved to rank the highest Pearson's coefficient by a relatively moderate margin, followed by NGF-silk and untreated/ 2 ng/ ml NGF which were comparable. Graphs (D) and (E) show the average orientation of axons within aligned and random fibre distributions for NGF-loaded silk and untreated silk cultures. The NGF-loaded silk histogram (purple data points) showed very little directional guidance by the silk relative to the randomly distributed constructs. In contrast, alignment of untreated silk microfibrils (orange data points) was found to provide a slight peak presence along the pattern direction (green arrow) over that of randomly distributed fibres. Experiments were carried out on 6-day DRG explants where $n \geq 4$ independent biological repeats. Bars indicate the standard deviation (E). Scale: 500 μ m

4.3.4. Composite Alignment of uADSC and NGF-Silk for Nerve Regeneration

4.3.4.1. Improved alignment and outgrowth with composite scaffolds

As explained within the introduction, effective nerve repair requires improvements in two key criteria; increased rates of regenerating axons and greater directional growth. Using the NGF-loaded-silk microfibrils, the former was reached to some extent; however, there was no impact of the embedded, aligned microfibrils on the guidance of neurites. As shown in Figure 50, ADSC can direct axonal outgrowth within 3-D collagen I hydrogels with predictability. In attempting to incorporate both: promotion of neurite outgrowth (from NGF-loaded-silk microfibrils). This led to experiments investigating the incorporation of uADSC in combination to the NGF-silk fibres in attempts to retain growth rates while harnessing the increased network directionality found in Chp 3. For this, aligned constructs were created by aligning 25k uADSC and NGF-silk fibres and the DRG explants grown successfully for 6-days within media absent of NGF. Of the 5 cultures, two were secluded and analysed separately as exceptions due to only partial alignment (described below). Of the other cultures (Figure 62), it was found that the total axon length was comparable to previous results of the functionalized silk, vastly increased over untreated silk and slightly lower than the DRG grown in 2 ng/ ml NGF. Network directionality also was more aligned, showing a similar directionality of outgrowth on to the aligned uADSC constructs described in Figure 51, however with a slight shift to the left from 90° alignment direction.

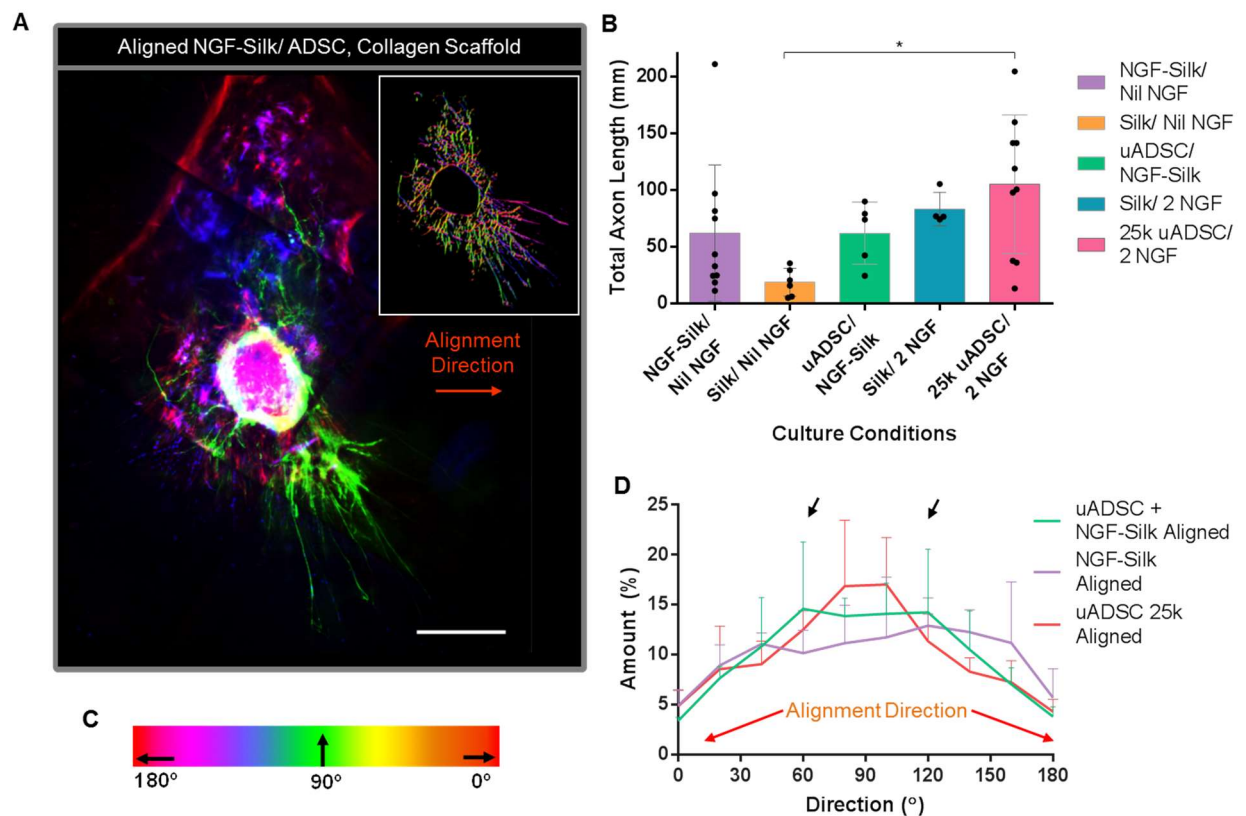


Figure 62: Analysis of DRG outgrowth within combined NGF-silk/ uADSC collagen constructs in nil NGF media. Fluorescent imaging of networks (A) were visualised through immunostaining of axons (Neurofilament heavy chain, green), actin (phalloidin, red) and nuclei (DAPI, blue). Silk is auto-fluorescent, shown as the blue/ purple fibres. Filament Sensor was used for directionality analysis (white inset, colour bar (C)) to create an average histogram comparing each construct (D). With the combination of uADSC and NGF-silk, it was found that axons exhibited greater axon alignment over sole NGF-silk constructs however, the average network direction was slightly more disperse at ~10-30° (D, black arrows) showing a small deviation from the axis perpendicular to the uADSC alignment (red arrows) and giving a slightly wider peak. Calculation of total axon length also showed that the combined culture had retained the growth promoting effect of the sole NGF-silk cultures (nil NGF media). Again, this was seen to be slightly lower than the 2 ng/ ml media cultures. Two specific cultures were excluded from these results and are described below (section: 4.4.6.5) based on their exceptional initial alignment quality. Experiments were carried out using DRG explants where $n \geq 3$ independent biological repeats. Statistical significance was determined by one-way ANOVA of unequal variance and Dunn's correction for multiple comparisons where $P^* < 0.05$. Bars indicate the standard deviation. Scale: 500 μ m

4.3.4.2. Excluded cultures highlighting potential

The excluded cultures (Figure 63) showed remarkably aligned growth surprisingly in the direction of alignment, which contrasted the results found with uADSC experiments. In closer examination of these cultures, it was found that although partial alignment occurred around the DRG, this alignment was largely disrupted at either side of the DRG. This created two dense regions of random cell distributions (yellow arrows), which were visible as intense clusters in the fluorescent images

obtained after the allotted 6-day culture period. Using Neuromantic software (Myatt et al., 2012) the axons were traced to further understand the nature of the network outgrowth in this case and highlighted the planar growth of network in a 3-D reconstruction.

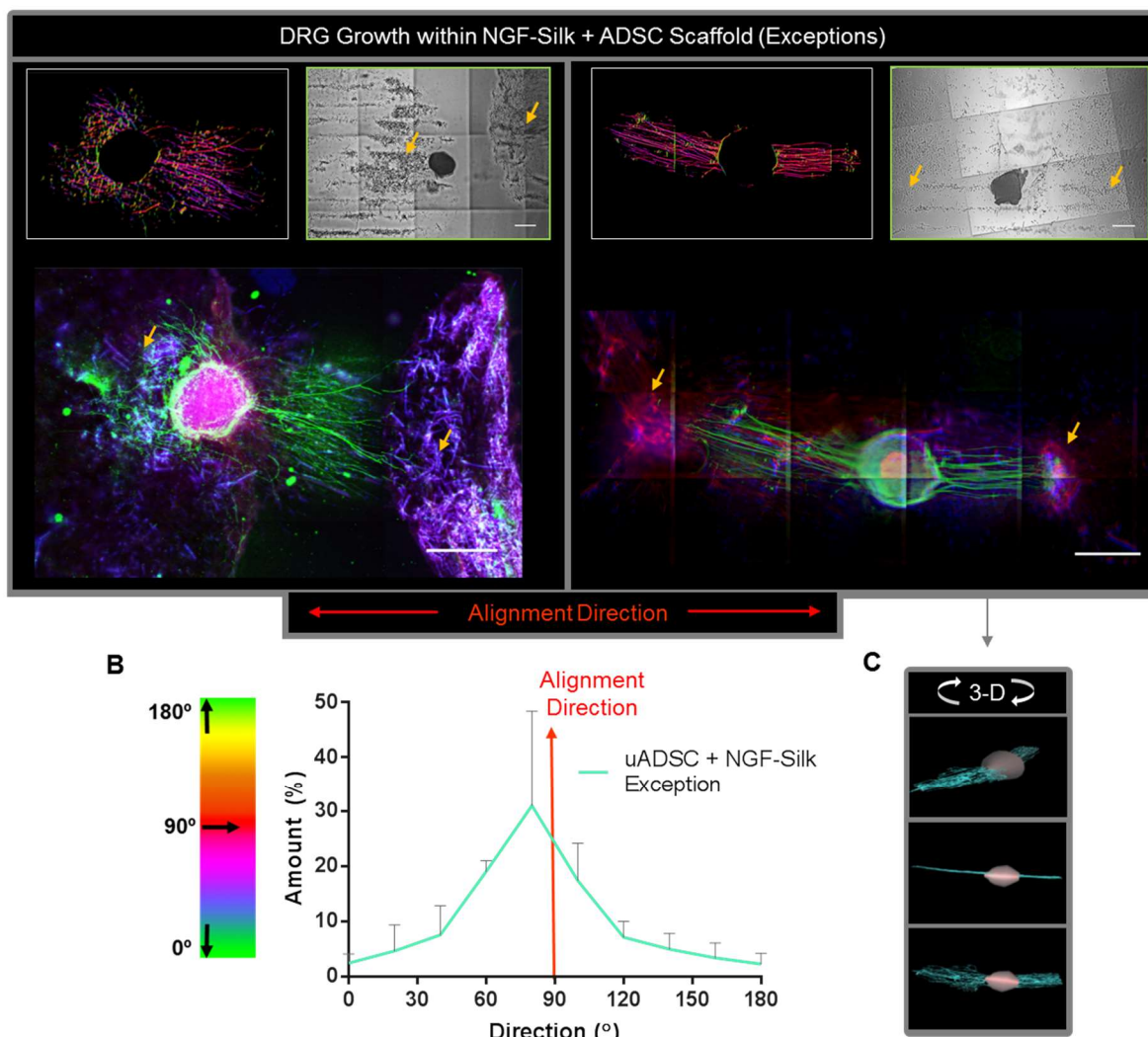


Figure 63: DRG outgrowths examination of exceptional NGF-silk/uADSC collagen scaffold at nil NGF media. Fluorescent imaging of networks (A) were visualised through immunostaining of axons (Neurofilament heavy chain, green), actin (phalloidin, red) and nuclei (DAPI, blue). Silk is auto-fluorescent, shown as the blue/ purple fibres. Filament Sensor was used for directionality analysis (Image and colour bar (B)) to create a histogram profile (C) showing directionality of network growth in relation to the pattern orientation (red arrow). These cultures showed extreme alignment of axons parallel to the direction of the pattern which was in stark contrast to previous experiments with uADSC aligned constructs. On closer examination of the initial scaffolding (brightfield image, green inset), it could be seen that partial alignment had occurred in the vicinity of the DRG however, at opposite poles there was dense regions of disorganised cells/ silk (yellow arrows). This can be seen following 6-days of culture from the fluorescent images, by the intense clusters of uADSC and silk (yellow arrows). To further investigate the nature of the networks arising from these irregularities, axons (from A: right) were traced and reconstructed in 3-D (C) using Neuromantic software. This revealed a highly planar outgrowth. Due to the character of the initial scaffolds, these cultures were treated as outliers although included for transparency and further insight into the potentials of utilising NGF-silk/ uADSC collagen constructs. Analysis carried out on 2 biological repeats, bars indicate standard deviation. Scale: 500µm

4.4. Discussion

4.4.1. Particle aligned scaffolds

Previously in chapter 3, the sonotweezer device was successfully used to create precisely designed, cellular-collagen constructs which showed benefits for nerve guidance, opening up exciting potentials (upon optimisation) for serving as nerve repair scaffolding. This sparked the idea of a different approach to neurite guidance through the fabrication of precisely formed stiffness differentials within a 3-D collagen matrix. Mechanosensing of substrate cues such as stiffness gradients are known to have a large impact on cell behaviour and in particular, axon pathfinding for growing neurites termed “durotaxis” (Athamneh and Suter, 2015, Wrobel and Sundararaghavan, 2014, Lo et al., 2000). Further, substrate adhesion interactions become more complex in 3-D systems (Doyle and Yamada, 2016) and there is little in the literature about the way by which stiffness gradients influence neuronal behaviour within a 3-D setting; although in one study (Willits and Skornia, 2004), axons of dissociated DRG neurons were seen to extend faster in softer collagen than stiffer. This was also observed by Sundararaghavan, et al. (2009), in which DRG neurites exhibited preference to follow stiffness gradients set up within collagen hydrogels. In this, the stiffness gradient was generated through increasing the concentration of cross-linking agent at one side of the gel. However, chemical approaches (e.g. cross-linking concentration or hydrogel concentration) to modify the hydrogel stiffness may not always be suitable (such as in operation of the sonotweezer device which cannot manipulate particles within high collagen concentrations and viscosities). Recently, research carried out by Mandal, et al. (2012) showed that the mechanical strength of silk fibroin hydrogels could be reinforced by the addition of silk microfibrils. This brings the assumption that through patterned alignment of microparticles, stiffness gradients may be produced within the collagen hydrogels, which also may affect the mechanical strength or stiffness of the entire gels.

Here, two materials were chosen: synthetic carbon micro-rods and silk fibroin microfibrils processed from the silk fibroin cocoons of *Bombyx mori*. These materials were assumed to have greater stiffness/ be harder than the softer collagen hydrogels, based on evidence from the study by Mandal et al. (2012). In the mentioned study, the stiffness of silk hydrogels without silk-fibre incorporation was much stiffer than

the collagen hydrogels in this thesis (average silk hydrogel: ca. 85kPa, collagen hydrogel used here: ca. 0.08 kPa). However, upon incorporation of the silk-microfibres to the silk fibroin hydrogels, a 50 to 100-fold increase in resistance to compression was found indicating that the silk fibroin was reinforced by the inclusion of silk microfibers which was determined by the size and amount of fibres present. Thus; it may be assumed that the silk microfibers are of a greater stiffness than both the collagen (I) and silk fibroin hydrogels and their inclusion. However, it is not known by how much, as the stiffness increase is can also be attributed to the covalent interactions between the silk hydrogels and silk fibres. On account of this study, it was deemed that silk microfibres would serve as suitable particles for the creation of stiffness cues dispersed as an array within the 3-D collagen matrices.

4.4.2. Sonotweezing of microparticles can be used to create anisotropic collagen hydrogel scaffolds

4.4.2.1. Acoustic alignment of carbon microrods and silk microfibres is size dependent

Initial attempts at alignment of these elongated/ high aspect ratio particles proved difficult (Figure 53). This issue was considered a possibility beforehand, as the size dimensions, shape, weight, buoyancy and electrostatic properties of these particles were likely to be different from that of to that of the cells/ beads that had been used before in Chp. 3. To address this, the first alteration of reducing the particle size (which inherently changed weight etc.) proved to be successful allowing each the alignment of each species to ~105µm pattern width. Unfortunately, any remaining particles of sufficient length (approx. $\geq 200\mu\text{m}$) which bypassed the filtering/ grinding process, were seen to interfere with the alignment of more suitably sized particles, leading to disruptions to the pattern if concentrated enough.

Separation of microparticles based on size using acoustic standing waves has been well studied (for review: (Trujillo et al., 2014)). In this, it is stated that manipulative ability is determined mainly by the particle size through affecting the following: acoustic pressure force, drag force and buoyancy, all of which increase as the microparticles get larger. From this conclusion, although the fibres may experience greater force, the drag and buoyancy of the larger particles inside the viscous

medium of collagen ultimately restrict their movement (such as those of ca. $\geq 200\mu\text{m}$ oriented orthogonally to the pattern Figure 55) producing a slower alignment velocity over a longer time (Figure 54). Also described in this review, is the effect of spatial saturation of an area by the microparticles as they form lines within the pattern. This reasons that the acoustic field cannot move microparticles into an already occupied space if the amount of particles in that space is greater than the 'saturation concentration'. Applying this concept to the observations of Figure 53 and in which unprocessed fibres and rods show difficulty in patterning due to aggregation, the force required to overcome the movement of the larger particles such as those pre-filtered (especially when aggregated), in order align the more suitably sized particles, is likely too considerable for this sonotweezer setup.

However, these conclusions have been formed from equations based on spherical microparticles, however with silk microfibres and carbon microrods, the dimensions are instead asymmetric and thus; likely to act differently to ultrasonic standing waves. From a study investigating polystyrene microfibres orientation in response to acoustic standing waves, fibres were seen to orient based on their fibre length and wavelength of propagation through the medium. (Syojiro Yamahira et al., 2000). Taking this into account, it can be reasoned that the larger silk microfibres and carbon rods may cause disruptions to the pattern due to their alignment resulting from drag forces. This may reveal the upper limitations to particle size of the sonotweezer setup used in this thesis. To circumvent this, a more refined filter process would be advantageous in order to exclude the larger, unsuitable microparticles although this would likely also reduce the yield.

4.4.2.2. Quality analysis of silk scaffolds

Assessment of the quality of aligned ($375\ \mu\text{m}$) silk collagen scaffolds without any interference arising from inclusion of DRG explant (Figure 50). effectively gauged the method reproducibility and quality of constructs for the intended nerve repair applications outside the experimental setup conditions. Fibres were found to be predominantly orientated in the direction of the pattern. In the images, a small number of individual fibres were seen to reside between alignment bands (marked with blue arrows) perpendicular to the direction of the pattern. This occurrence is also documented in the research carried out by Syojiro Yamahira et al. (2000), with

polymer fibres aligning in aqueous sugar solution, indicating that this is likely to be intrinsic to the fibre shape of the particle. In their study, orientation of fibres of a length greater than $\frac{1}{4}$ to $\frac{1}{2}$ of wavelength of the standing wave (sinusoidal, and therefore 1λ creates 2 pressure nodes/ 2 pattern widths) were found to orientate in parallel to the wave propagation (perpendicular to pattern). In contrast fibres with a length less than $\frac{1}{4} \lambda$ orientated perpendicular to the wave propagation, i.e. parallel to the pattern. Reasoning for these findings were calculated and found to be as a result of the drag forces applied to the long dimension of the fibre, the resultant torque force and the moment of inertia created by residing in two pressure nodes. This aptly explains the orientation of fibres with lengths approx. $\geq 200\mu\text{m}$, which orientate perpendicular to the $375\mu\text{m}$ pattern lines (Figure 55, blue arrows). For alignment of a pattern with a width of $375\mu\text{m}$ spacing, a propagating λ of $\sim 750\mu\text{m}$ (equivalent to double the pattern width) is required. Therefore, fibres of a length of less than $\frac{1}{4} \lambda$: $187.5\mu\text{m}$ were seen to be aligned as expected along the pattern direction; however, fibre lengths of greater than $\frac{1}{4} \lambda$ i.e. $\geq 187.5\mu\text{m}$ instead were seen to align perpendicular to the pattern.

Areas of disorganisation (Figure 55, yellow arrows) can be explained by the working field of the sonotweezer device, consistent with expectations of $\sim 4 \times 4 \text{ mm}^2$ for this setup (Dr. Anne Bernassau, as per comm.). The perpendicularly orientated fibres and regions of disorganisation will have influenced the average directionality histogram; however, these were included to give an idea of the technical performance and the limitations of this method holds. This however could be circumvented simply through altering the size of PZT transducers to produce a larger field across the entire gel, hereby removing/ reducing the loss of patterning regions.

4.4.2.3. Alignment in acoustic fields is particle size, density and shape dependent

To further investigate the characteristic differences of these objects to cells, a comparative analysis was carried out involving microscope-camera recordings of the alignment process (Figure 54). Across all particles, some initial alignment occurred at the application point of the droplet however, the settling time for completed patterning was vastly different. The uADSC could not be tracked due to their size and thus visibility; however, they could be seen to align near immediately. Silk micro-

fibres completed alignment within 7 seconds and carbon micro-rods took double the time of silk at 14 seconds. This could be seen from the speed of particles graph, in which the initial silk rate was $\sim 100\mu\text{m/s}$ higher than carbon and experienced a much faster decline as alignment occurred.

Overall due to the prototypical nature of this work, comparisons for particle manipulations remains difficult; however, in relation to 3-D trapping using standing surface acoustic waves, the particle movement speed observed with the sonotweezer was higher at ca. $>300\mu\text{m/s}$ ($\sim 20\text{-}150\mu\text{m}$ asymmetric particles) over $2.5\mu\text{m/s}$ ($10\mu\text{m}$ particle) (Guo et al., 2016). In contrast, manipulation within a 2-D acoustic tweezer setup was shown to be in the range of $2000\mu\text{m/s}$ ($90\mu\text{m}$ particle) (Courtney et al., 2014). Another important consideration is the medium which the sonotweezer device manipulates the particles within collagen I during gelation. This means that as the collagen cross-links, it will become increasingly more viscous, producing greater drag forces on particles, and thus reduce their movement velocities. It can be assumed that the velocity of each particle is likely to be higher when aligned in more simple media e.g. water.

Other issues which became apparent during alignments of carbon micro-rods was their rapid sedimentation to the bottom of the gel and problems with pattern resilience and stability. These can be attributed to their larger density than the silk-fibres (observed through rapid sedimentation at rest). These issues invalidated the prospective use of carbon rods in these experiments as the goals for acceptable construct creation required particles to be both; suspended to a suitable depth within the gel and certain degree of allowance for reformation which would be required to counteract disruptions which inevitably arise from the addition of the DRG through the experimental setup. In theory, it could be argued that a faster setting gel and the intended use of construct for nerve repair being absent of the DRG addition and thus could create an acceptable construct; however, faster setting gels would likely have increased viscosity, requiring a field strength. These arguments reveal a potential which could not be determined within the time constraints of this project.

4.4.3. Aligned silk fibre scaffolds in practice for nerve growth

4.4.3.1. Collagen scaffolds with aligned silk microfibres provide insufficient influence on DRG outgrowth

The aligned silk/ collagen constructs were investigated as scaffolds for culturing DRG (2 ng/ml NGF) and providing durotactic guidance to regenerating axons. Minimal impact to the directional aspect of the axon network was observed; however, a slightly greater unevenness to the histogram profile than that of the solo DRG cultures was given (Figure 56). Although no apparent difference was found over randomly distributed cultures, this did indicate that axons may interact with the silk fibres slightly. The images also show less network symmetry and possibly an avoidance of the alignment region. From these data, it can be concluded that any stiffness differential attributed to the inclusion of silk fibres was insufficient for axons to migrate towards or remain guided by.

4.4.3.2. Axon growth cones did not align to the patterned silk microfibres

To visualise the nature of any interactions by the axons with the silk fibres, a time-lapse microscope recording was setup over a period of ~80 hrs (Figure 57). From this, a number of axons could be seen to meet silk fibres within the alignment and deviate from their path confirming that the silk fibres require functionalisation with neural adhesion molecules (e.g. Poly-D-lysine (Chwalek et al., 2015)) in order to act as a substrate for axons and indicating that a kind of repulsive cue was at play which is consistent with the directionality results/ images (Figure 56). A wide range of studies have reported that silk fibroin is supportive of axon adhesion and outgrowth (Hopkins et al., 2013, Farokhi et al., 2017), which is in contradiction to the results observed here. In these studies, the silk fibroin is the sole material available for axons/ GC to interact with, whereas here: collagen could offer an alternative, better suited substrate for growth and adhesion, leading to the perceived 'avoidance' seen. Thus, it may be reasoned that the stiffness gradients of the scaffold are working against the initial intended function. This complies with the work carried out by Koser et al. (2016) where axons of retinal ganglion cells were seen to grow in towards softer tissue; and of Sundararaghavan et al. (2009) which showed that neurons from chick

DRG grow towards the region of lower stiffness of collagen in 3-D set up with stiffness gradient across a single gel.

4.4.4. NGF-releasing silk microfibres to stimulate and direct axonal regeneration

Growth factor supply to the regenerating front is essential to support the regenerative phenotype of neurons (Allodi et al., 2012). As injections are not a sustainable way to continuously deliver growth factors, silk microfibres were investigated as an alternative means to deliver NGF locally. This is based on numerous studies (for review: (Wenk et al., 2011) that show that silk-fibroin is a very good material for GF adsorption and slow release (Uebersax et al., 2007). Further, silk fibroin is an exceptionally versatile material for this purpose, as it can allow different routes for loading such as by direct binding of drugs through functionalization of the protein or by adsorption through hydrophobic or electrostatic interaction (Wenk et al., 2011). The silk micro-fibres with adsorbed NGF form a reservoir that would slowly (over at least three days (Figure 59)) release an appropriate amount of NGF to support the continued outgrowth of the DRG axons. In this approach, NGF-loaded-silk microfibres would deliver NGF for the axons to sustain their outgrowth and follow. This potentially directional, NGF gradient based signal would be reinforced by the topographic/ durotactic signal that confines the growing axons to the pattern direction, guiding growth.

4.4.4.1. Loading silk microfibres with NGF

The protocol of loading the silk microfibres with NGF was formulated in a similar process has shown success previously, to which VEGF was loaded to silk fibroin nanoparticles through an overnight steep within 100 ng/ ml VEGF and later used for cellular uptake and a controlled VEGF release (Kundu et al., 2010). It is plausible that loading is achieved by electrostatic interactions between each species at the pH during incubation and cell culture (pH 7.4), as silk fibroin has a net negative isoelectric point (pH 3.6-5.2) (Dyakonov et al., 2012) whereas NGF is positive (pH 9.3) (Harper et al., 1982). Finally, an intensive wash cycle was carried out to ensure that NGF present within the final solution would be presumably negligible.

4.4.4.2. ELISA: outline

This loading process on was based upon logical assumption however the effectiveness was unknown, thus; and an ELISA was carried out to assess the quantity of NGF eluted from the silk. As the amount of NGF released was could reside between 0 and 100 ng/ml, an ELISA kit with a wide detection range had to be utilized and the chosen kit in question was intended for use on cell lysates.

4.4.4.3. ELISA: 3-day total NGF elution (37 °C)

The ELISA indicated that two samples of silk had been successfully loaded with NGF with one sample showing very poor NGF release rates and thus deemed a failure (Figure 59, orange data points highlighted with red asterisk). Whether this perceived failure arose from an initial steeping error (incorrect NGF media concentration added) or by unsuccessful NGF steep remains inconclusive. The results are thereby mainly discussed with exclusion of this repeat in mind; however, the consideration remains that this process requires further investigation, optimisation and tuning, to increase reliability.

The level of NGF eluted after 3 days within cell culture conditions was seen to directly correlate with the total length of fibres present (at an average of 0.0296 pg/ml NGF per mm of silk fibre) which is in agreement with the research of Lammel et al. (2010) who found that the release kinetics of the drug: crystal violet from silk fibroin particles (loaded electrostatically) was dependent on the particle size. The relation of NGF to fibre length provided confirmation that NGF detected was a direct result of fibre release and not due to an incomplete wash step. Also, this was not attributed to false-positive ELISA detection as it showed greater NGF elution than that of the untreated silk solution 0.0083pg/ml NGF per mm silk. The untreated silk elution is likely occurring as a result of false positive detection of proteins within media/ silk or possibly cross-contamination issues.

4.4.4.4. ELISA: Environmental impact (4 °C vs 37 °C)

Incubation conditions were found to have a drastic effect on NGF elution concentration of all samples (2NGF DRG media and NGF-loaded silk microfibre) as aliquots kept at 4°C for 3 days exhibited between 4-6 times higher NGF elution

concentrations than aliquots of the same sample kept at 37°C, in the cell culture incubator. Although it has been known for some time that temperature has a direct effect on protein degradation rate following first order kinetics (Chaloupka et al., 1980), protection from protein degradation can be achieved through the addition of stabilizing agents such as the carrier protein BSA (Checa-Casalengua et al., 2011). In addition to this, temperature can also affect the kinetics of protein adsorption/ desorption and; can be generalised to increase adsorption with increasing temperature (Rabe et al., 2011). Without the impact of culture (temperature mediated affinity between the NGF and silk fibroin or the rising pH of media during cell culture), the actual release of the silk fibres over 3 days at 4°C is approx. 0.12pg/ mm. In essence, it may be reasoned that these data may indicate that the adsorption of NGF to the silk fibroin does not protect or stabilise the NGF at 37°C or in contrast; it may be argued that: as it is inconclusive how much of the initial NGF was adsorbed onto the silk, the opposite may be occurring; in which the NGF may be simply eluting at a slower rate over a longer period. In agreement of the latter, a study on NGF release from silk fibroin matrices and films (electrostatically adsorbed) show that only 0.3-13% of the total NGF adsorbed is released over 23 days. Furthermore, the release profile of NGF over time bears characteristic similarity of that of the NGF-loaded-silk ELISA, in which an initial burst of NGF release was apparent followed by a more plateaued consistent rate. Overall, by comparison to the effect of temperature on 2NGF DRG-media, which provided a lower detected NGF concentration in samples kept in 37°C than 4°C, it can be deduced that NGF stability will become an issue upon its release from the silk.

4.4.4.5. ELISA: NGF release per day

As stated above, the amount of NGF eluted was seen to reduce rapidly (~50%, 400-500 pg/ ml/ day) with each day until day 2 which generally plateaued the release amount to around 60-110 pg/ ml NGF but does not decrease to further towards 0. In comparison to the 2 ng/ ml NGF media (37°C), the elution from NGF-silk was seen to consistently be higher from the initial sample (taken after 2 hours) by ~200pg/ ml. Again, this contrasted the results of 2 ng/ ml (4°C) which maintained a slower decline; however, the ELISA detection/ graph interpolation of standard curve calculated these 2 ng/ ml NGF controls to be in the region of ~600 pg/ ml which may indicate stock solution error or detection error of the assay. As a result, it remains unclear whether the actual elution of NGF from the silk is ~4 times higher or is

accurately assessed, although, the response of DRG cultured within scaffolds incorporating the NGF-loaded-silk microfibres indicate that this is a detection issue.

An estimation was made to quantify the approximate NGF concentration supplied by the NGF-silk within the first 24 hours of DRG cultures carried out in this chapter was calculated to be ~60pg/ ml NGF. This concentration is comparable to normal human sera (Bonini et al., 1996) although less than the levels present within a nerve wound provided by natural cellular support (rat sciatic nerve lesion day 1: ~490pg/ ml) (Liu et al., 1995).

It can be therefore be concluded that within the cultures of this project, NGF-silk releases a high concentration of NGF over the course of the initial two days followed by a sustained lower concentration for at least another two days. This is consistent with Uebersax, et al. (2007) and indicates that the NGF-loaded-silk may allow for NGF delivery over a number of weeks. However, this assumes that release kinetics will be similar between silk gels or films and silk microfibres. In their study, the rate of NGF release was found to be largely dependent on the conditions during silk fibroin matrix formation, in particular: temperature, which can alter the physical properties of silk, i.e. pore size. Further, the adsorption/ desorption process was deemed to not impact NGF bioactivity. This was reflected on cell behaviour, with matrix formation that was seen deliver larger amounts of NGF were also shown to provide a greater increase PC12 differentiation.

Experimentally, the actual concentration in culture would be reduced over the culture period through cell uptake, degradation or dilution with fresh media during feeding. Herein lays a disparity between the normal cultures, where fresh NGF-supplemented media is added every 2 days and the cultures where NGF-loaded-silk microfibres are the sole supply of NGF available to the DRG. The NGF concentration around the DRG is therefore more consistent (although this may also depend on porosity of the collagen hydrogel for diffusion of the NGF) if this is contained in the media supplied. This is reflected in the different degree of outgrowth between NGF supplementation through media and NGF delivered internally through NGF-silk microfibres, observed in Figure 60 and also well represented in the literature (Liu et al., 2013a, Mohtaram et al., 2013).

In a clinical setting, NGF-loaded-silk could prove useful approach to nerve repair, with its inclusion to NGC providing an initial boost to the injury site with high concentration of NGF followed by sustained release for longer periods of time. If the above deductions are correct, NGF-loaded-silk microfibre scaffolds would then require no further involvement once applied as treatment for nerve injury.

4.4.5. Investigating DRG neurite growth within NGF-silk/ collagen scaffolding

4.4.5.1. NGF-loaded-silk microfibres promote DRG neurite outgrowth

The inclusion of NGF-loaded-silk microfibres in the collagen gels was found to produce greater overall outgrowth (~3x higher total axon length) than that of collagen gels with embedded native silk microfibre controls (Figure 60). The axon: silk length graph (D) gives an idea of the influence that the NGF-loaded-silk microfibres provide. Relative to the cultures in collagen gels with silk microfibres supplemented with media without or with 2 ng/ ml NGF, the cultures with NGF-loaded-silk microfibres showed an increase in outgrowth over the former NGF0free, becoming comparable to the cultures supplied with 2 ng/ ml NGF media. This demonstrates that NGF-loaded-silk microfibres have a positive effect on DRG outgrowth which is dependent on the length of silk fibre present in the vicinity of growing axons, further validating the ELISA conclusions. Taking the estimated NGF concentration of media within NGF-silk cultures (Figure 59) it can be assumed that the 3-D axon growth does not increase in a manner directly proportional to the NGF concentration (similar to 2-D growth, as in Chp. 2).

4.4.5.2. Reduced axon guidance in collagen gels with aligned NGF-loaded-silk microfibres

Analysis of the directionality of networks cultured within NGF-silk scaffolds shows no apparent positive effect between aligned and random silk distributions. Instead, a correlation of axon direction to silk direction (taken within the vicinity of network only) showed that neurite guidance by the silk is highest when NGF is absent. This may be explained by both the findings by Turney *et al.* (2016) and Chp. 2 of this

thesis, in which NGF inhibits contractility, which reduces mechanosensing and may result in the inability to follow stiffness cues. Also, it is known that NGF increases exploratory nature of axons such as branching (Ketschek et al., 2015), Chp. 2) thus, they are less likely to become contented within a specific direction (i.e. along the silk fibre), instead opting to deviate and branch. This gives a slight insight that on occasions where silk is the sole guidance cue provided, it may slightly enhance directionality of growth, albeit insufficiently relative to current advancements in 3-D neurite guidance (Nguyen et al., 2017).

4.4.5.3. Remarks on NGF-loaded-silk microfibres to support nerve regeneration

Taken together; the NGF loaded silk was found to be largely beneficial for the improvement to neurite outgrowth when compared to nil NGF controls although this sacrificed a slight directionality loss. It also provided a further confirmation that the loading of silk with NGF was at least a partial success although still resulting in relatively small amounts of NGF eluted. Nevertheless, there is potential for optimisation or a switch to an alternative biomolecule, silk fibroin particle shape or biomaterial entirely to create aligned scaffolding.

4.4.6. DRG outgrowth within uADSC/ NGF-silk composite- collagen scaffolds

4.4.6.1. Initial prospect: uADSC guidance/ NGF-silk growth

Recently, pre-aligned collagen constructs containing SC (Georgiou et al., 2013) and dADSC (Georgiou et al., 2015) were shown to provide directional guidance and neurotrophic support for regenerating axons of primary sensory neurons and the sciatic nerve. Efforts into understanding and controlling cellular contraction for orientation of collagen fibres have been made through tethering the collagen at high C6 cell numbers ($\sim 0.5-6 \times 10^6$ cells/ gel) (O'Rourke et al., 2015). Previously in this thesis, uADSC were employed to provide an aligned structure of collagen fibrils through contraction which served direct neurite outgrowth. Using the sonotweezer device, this could be controlled to some degree; however, no apparent improvement to outgrowth was observed.

To assess any synergistic effects aligned collagen scaffolds containing both: uADSC (growth directing) and NGF-loaded-silk microfibrils were created. Interestingly, the nature of this approach reversed the conventional idea of an NGC make-up (de Ruiter et al., 2009), with ADSC providing guidance, instead of promoting growth through GF release and silk microfibrils providing NGF release, instead of structural support or guidance of axon outgrowth. Here, two hydrogels had obvious poor particle alignment as well as dense regions of particles at opposite poles of the DRG' these data are therefore excluded from the analysis and discussed separately.

4.4.6.2. NGF-silk-microfibrils do not interfere with ADSC mediated collagen contraction

It was unknown how the ADSC would behave when seeded with NGF-loaded-silk fibres during alignment, e.g. would they adhere onto the silk fibres and not provide the collagen contraction previously observed to guide neurites Chp. 2. This is plausible when considering that ADSC have been shown to have good biocompatibility with silk fibroin/ chitosan scaffolds displaying high adhesion rates for the biomaterial (Ji et al., 2013). Despite this, a predominant adherence to silk over collagen does not appear to be the case in these experiments, as guidance of axons remained relatively consistent with previous work carried out in Chp.3. This does not rule out the possible adhesion of the ADSC to the silk fibres but, shows that any interaction that they share does not have a large detrimental effect on the function of ADSC for controlled collagen fibre alignment. Furthermore, from the collagen contraction speed analysis of aligned ADSC (Figure 46), most of the contraction for alignment was concluded to be carried out during the first 2-4 hours following seeding. Taking this into account provides the reasoning as to why the leading statement does not apply, i.e. the silk microfibrils do not inhibit ADSC contraction.

However, it should be noted that in ADSC/NGF-silk microfibril composite scaffolds, the axon network growth was not as precisely perpendicular to the initial pattern alignment than scaffolds containing only with ADSC. Instead, average axon direction was slightly askew ($\sim 10-30^\circ$) to the ADSC/ NGF-loaded-silk microfibril pattern orientation. As a result, a wider peak distribution ($\sim 60^\circ$) was found in comparison to only ADSC ($\sim 40^\circ$), as the average was plotted from both right and left directed cultures. In theory, this could be due to a small amount of interaction between ADSC

and silk; however, it seems more likely that this was a result of poorer pattern quality (seen in Figure 63) arising from the incorporation of three separate entities to the collagen during gelation (cells, silk fibres and the DRG explant) which can obstruct the acoustic field or interfere together.

4.4.6.3. ADSC does not appear to differentiate when cultured with NGF-silk-microfibres for six days

Another subject for discussion in relation to the ADSC response to the NGF-loaded-silk microfibres is in the possible stimulation to induce differentiation to other lineages. The first consideration is in the physical and mechanical nature of the silk fibre alignment. The approach for scaffold function was to create anisotropic gels with aligned physical cues and local stiffness gradients in efforts to guide neurites; however, this can also guide other cells, promoting their alignment. Anisotropic guidance cues (collagen II alignment) have been shown promote differentiation of BMSC to tenocyte lineage (Gigante et al., 2009) and stiffness has been found in a number of studies to initiate the differentiation to (Engler et al., 2006). Another study investigating the response of ADSC when cultured films of silk fibroin and collagen I fabricated with 2-D patterns (microchannel or micropillar) showed that the combination of cellular alignment and extracellular matrix composition promoted differentiation to an osteogenic lineage (Sayin et al., 2015). The elution of NGF from the NGF-loaded-silk may also play a role in stimulating ADSC differentiation within the construct. In this regard, silk fibroin has previously been used as a TGF- β delivery agent through composition with decellularised cartilage ECM and was proven to be effective at inducing ADSC towards chondrocyte lineage (Yang et al., 2017). Taking these findings into account, it can be understood how the combined alignment of NGF-loaded-silk with ADSC inside collagen I hydrogels may stimulate their differentiation to other lineages, particularly glial. However, within the six day cultures of this research, this is not likely to be the case as all observed differentiations require weeks of inducement (Kingham et al., 2007). Also, as there was no apparent increase in DRG outgrowth, differentiation to dADSC is not evident.

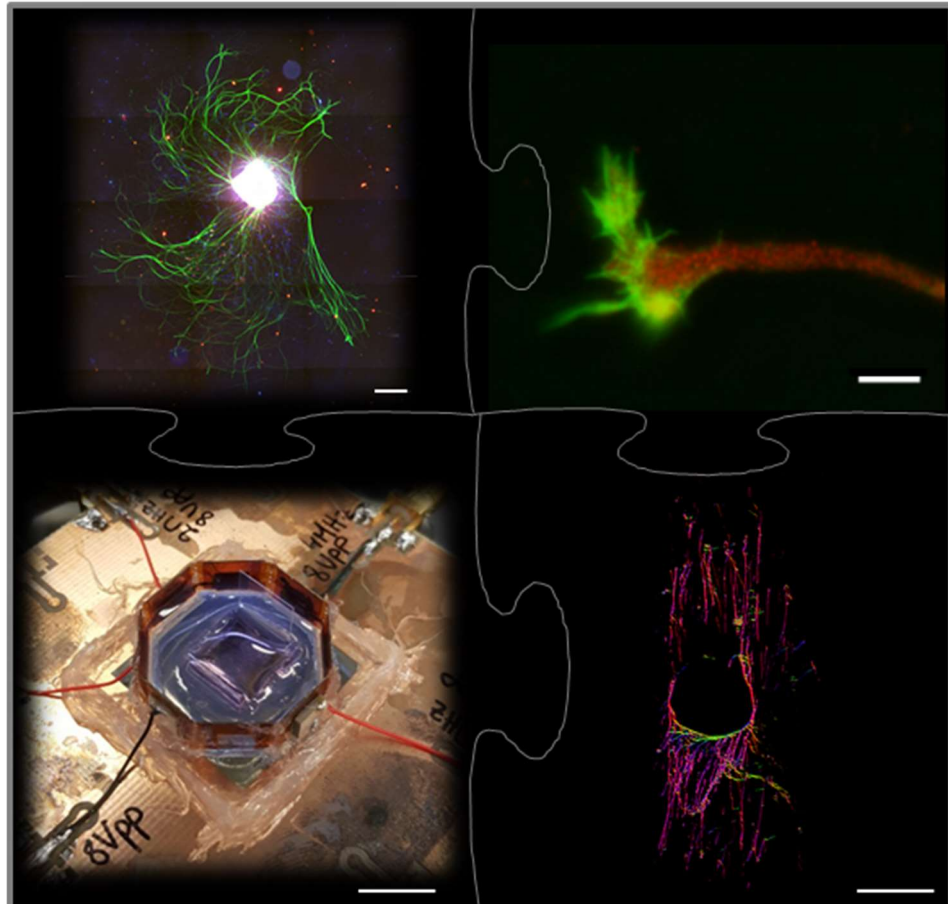
4.4.6.4. ADSC/ NGF-loaded-silk microfibre embedded collagen scaffolds promote and guide DRG outgrowth

Overall, from the fluorescent images of the DRG axon networks Figure 63, it could be seen that the network growth adopts characteristics from either separate scaffold type (NGF-silk/ ADSC). Total neurite outgrowth was no different on average to that of NGF-silk scaffolds, showing much greater lengths than untreated silk, but less than that of 2 ng/ ml NGF cultures. In essence, the combined ADSC/NGF-silk scaffolds proved to incorporate the majority of positive aspects to nerve growth from their individual performance.

4.4.6.5. Excluded cultures in greater detail: directed growth by diametric pattern disruptions

Both exclusions were seen to promote highly directed axon alignment, parallel to the pattern, contrasting previous work. On closer examination of initial alignment images, it can be deduced that this highly aligned growth is resulting from the clustering of cells situated at opposite poles of the DRG. It is likely that the contraction arising from these clusters work in tandem together, creating much higher alignment of collagen fibres and thus; greater neurite guidance. Although this does seem to be the key to directed nerve growth, one must remember that cell clustering would be difficult to reliably control, as unpredictable cell behaviours could deviate the intended growth path.

5. Final Discussion



“Piecing together the bigger picture.” Top left: Immunofluorescent image of DRG growth on flat substrate from topographical/NGF interaction studies. Top right: Actin (green), Myosin IIA (red) growth cone from the GC inhibitory studies. Bottom left: sonotweezer alignment of silk within collagen for neurite outgrowth investigation. Bottom right: Directionality of neurite outgrowth within aligned uADSC embedded collagen scaffold. Individually, each piece contributes to understanding nerve regeneration and methods which to more suitable materials for influence neuronal behaviour. Together these pieces enhance both knowledge and application which are essential to forming the optimum nerve injury repair strategy. Scale: top left, bottom right: 500 μ m, top right: 5 μ m, bottom left: 1 cm

5.1. General Discussion

Cell engineering approaches for the improvement of peripheral nerve regeneration may be loosely summarised as the effort to control cell/ axon behaviour through the inclusion of supportive influences to the injury environment. Currently, the autologous nerve graft remains the leader for healing potential although this is not for lack of research directed into a suitable alternative (O'Rourke et al., 2018, Levi et al., 2016, Moore et al., 2011, Arslantunali et al., 2014). Improvement to current nerve repair strategies relies on:

- A) a deepened understanding of cellular mechanisms/ interactions,
- B) maintaining a cellular environment supportive of repair for extended period of time by the inclusion of cells.
- C) the creation of more effective environmental conditions through better scaffold properties and character, and

Overcoming all of these challenges together is the key to reaching and surpassing the standards set by the autologous nerve graft (Isaacs and Browne, 2014).

The work carried out in this thesis attempted to address these issues through three separate approaches (discussed in detail in 5.2, 5.3 and 5.4).and thus provide the basis for a future comprehensive improvement to regenerative strategies.

The first investigation highlighted and attempted to explain the interactions in signalling arising from exposure to both neurotrophins and topographical cues.

The second investigation formulated a new method for the fabrication of organised ADSC collagen scaffolding and evaluated their effectiveness in promoting neurite outgrowth and guidance in 3-D with the ambition that they may serve as the inner lumen of a NGC.

The third investigation combined silk fibroin microfibres aligned by sonotweezers as a means to create a structured, growth factors releasing, system to support nerve regeneration.

5.2. Investigating the axon behaviour and signalling interactions arising from neurotrophic factors and topographical cues

To summarise the results of chapter 2; NGF, but not other neurotrophins initiates a signalling response that interacts with signalling initiated by placement of DRG explants on an anisotropic surface that confines and aligns outgrowth. The signalling pathways activated by topography and by NGF lead to increased fasciculation and reduce outgrowth. The underpinning mechanism seems to be an increased build-up of tension on linear topographies and with increasing NGF concentrations with the involvement of the regenerating axon growth cone. This has implications for the design of NGC and GF therapy to support regeneration through a scaffold after PNS injury.

Current NGC strategies consist of employing topographical/ structural cues for neurite guidance and/ or neurotrophic growth factor delivery for improved rates of regeneration. For the former, this may be in the form of biomaterials with anisotropic, porous, inclusive objects (fibres, rods etc.) or patterns on the inner side of the surrounding conduit tube (Petcu et al., 2018b, Arslantunali et al., 2014). The latter may be with the supplementation of NGF or other neurotrophic support (BDNF, GDNF, NT-3 etc.) through numerous delivery strategies (Liu et al., 2013a) including cellular (SC, dADSC, fibroblast)(Madduri and Gander, 2012, Pfister et al., 2007). In the field of therapeutics, the delivery of controlled concentrations of NGF over longer periods of time remains a difficult challenge however (Madduri and Gander, 2012), and the its use in combination with guidance cues is not considered.

Research carried out in Chp. 2 addressed this in a 2-D approach to reduce experimental complexity (e.g. reliable topographical fabrication, network imaging and analysis) and separate the actions of each cue. In continuation from the findings of Déjardin (2013) which found that higher NGF produced lower axon network sizes from DRG cultured on grooved surfaces, this research provided further confirmation of the observed trend through expanding the range of NGF concentration investigated. This trend has also been shown to occur in singular DRG neurons (Kredi, 2016) however, there have been very few studies revealing the detrimental effects of

excessive NGF exposure on regenerating DRG explants and none in relation to topographical cues. One study attributes the over-fasciculation of axons resulting from the increase in neurite counts (Rutishauser and Edelman, 1980) as the reasoning for poor growth at excess NGF levels. Other investigations have shown that modulation of NGF response is dependent on the type of ECM protein with each mediating different processes involving: RhoA, Vinculin dependent cytoskeletal-adhesion coupling and both Myosin IIA/B isoforms (Turney et al., 2016, Liu et al., 2002). In general, these processes amount to a regulation in the retrograde flow of actin which promotes the initiation or arrest of axon extension. In a study by Liu, et al. (2002), it was observed that synthetic polymers had no effect on the neuron response to differing NGF concentrations which directly contradicts the findings of this thesis. Taking this into account, it can be concluded that the NGF-level modulation in growth is a result of the topographical influence and not from a signalling cascade instigated by substrate chemistry. The findings of this thesis reveal that aspects of each evaluation (i.e. over-fasciculation, myosin IIA blocking) play a role, acting together in a concerted fashion to impact the overall axon network size.

In summation, the entire process may be explained by the occurrence of the following events: excessive NGF levels provide an increase neurite outgrowth numbers whilst also restricting myosin IIA activity which promotes axon extension whilst reducing adhesion strength. Taken together with the narrow confinement of axons created by the microgrooved topography, over-fasciculation occurs and eventually leads to adhesion loss as underneath axons cannot maintain a sufficient binding force to withstand the combined contraction of multiple axons above.

5.2.1. Myosin II mediates fasciculation

Blebbistatin was seen to block the effect of NGF on myosin II, which is in agreement with the study by Shin et al. (2014). Further, as it has been established that fasciculation is mediated by myosin II (Liu et al., 2013c), it was concluded that myosin IIB promotes fasciculation of axons whilst myosin IIA; de-fasciculation. This was based upon the morphological differences between NGF conc. (extent of myosin IIA inhibition) and blebbistatin (myosin IIA, B inhibition). Interactions between axons and the mechanistic determination of fasciculation is still largely unknown; however, homophilic binding of L1CAM and of NCAM are known to be required for fasciculation

to occur (Rutishauser, 1992) and thus may be involved in the observed trend. This conclusion is in agreement with the findings by Liu, et al (2002), who showed, that axon lengths of sensory neurons cultured on L1(L1CAM ligand) were reduced when in the presence of NGF. Their work also showed that L1CAM-enabled RhoA activity inhibited NGF induced outgrowth. Additionally, the directionality analysis of DRG networks cultured with blebbistatin reported here showed that axons ignore the confinements of the microgrooves (average $\sim 7^\circ$ shift in orientation histograms). Although this did not occur when the DRG were cultured with the high concentration of NGF without blebbistatin; morphologies could be seen to disobey the confinements of microgrooves and considering the findings of the myosin IIA intensity study, it may be possible that contact guidance involves myosin IIA. However, high fasciculation can also produce this effect as densely packed axons can mask the surface topography.

5.2.2. The interaction is exclusive to NGF

Upon investigating other neurotrophic GF (FGFb, BDNF, FGFa and to a small extent: SDF1 α), the trend was not observed indicating that the response to NGF is likely a result of signalling cascades generated by its binding to TrkA or that it is as a result of the axon morphological characteristics induced exclusively by NGF or both. This is consistent with previous investigations of other neurotrophins BDNF and NT-3 (Conti et al., 1997) and may be explained by the conclusions of (Gehler et al., 2004c) which found BDNF signalling to be independent of Myosin II activity.

5.2.3. The interaction between NGF and topography signalling takes several days to establish

The time-series study over ten days (DRG fixed for analysis every two days) indicates that this interaction becomes more evident as time goes on, with a minimal difference present at four DIV whilst at six DIV, the trend begins to manifest and finally at ten DIV, which show the greatest difference in network length on grooves at low and high NGF concentrations. Taken together with the data that shows blebbistatin to have: little effect at four DIV (where the trend is not occurring) and a large effect at six DIV (where the trend becomes apparent), this implies that myosin II is involved in reducing the axon network sizes observed. As myosin II is a mediator of fasciculation, this data provides further evidence that fasciculation is a key player;

initially, growth cones and axons will have space to extend; however, over time they will begin to saturate the available surface before they start adhering to each other. This may account for the data, where no apparent trend in other studies investigating DRG response to NGF which use shorter culture periods e.g. 36-40hrs: (Rosoff et al., 2004). Overall, this could be indicative of the potential ramifications in the treatment of nerve injuries which can last several months (Sulaiman and Gordon, 2013).

5.2.4. Considering the experimental setup

It must be remembered that the results of Chp 2 are experimentally based on the restriction of axons to a 2-D substrate and the behaviour within 3-D environment may be different (Ko and Frampton, 2016). In 3-D reality (injury site/ NGC), the axons will have more surrounding opportunities to form adhesion complexes and therefore may not fasciculate as heavily whilst also experiencing a difference in mechanosensing mediated contractility. This is likely to heavily depend on the microstructure of the scaffold however and it is currently unknown to what effect this will modulate NGF induced outgrowth. Overall, this may shed light on why current NGC perform poorer than autologous nerve grafts and indicate routes in which to improve them.

5.3. Ultrasonically aligned uADSC/ silk microfibers in collagen for nerve repair

To summarise the results of chapters 3 and 4, a method was developed for patterning of cells (discussed in sections 5.3.2-5.3.4) and/ or silk fibroin microfibres (discussed in section 5.4) embedded within collagen hydrogels using ultrasound. This showed the sonotweezer to be a suitable platform for the design and creation of 3-D nerve scaffolds.

Hydrogel deformation and collagen fibre alignment was observed in those seeded with uADSC which was concluded to be as a result of cell contraction. Patterning of the uADSC using the sonotweezer device allowed some control over cell-mediated orientation of collagen fibres in comparison to the random directionality without patterning. A seeding density of 25k cells/ gel, pattern width of 375 μm was seen to be most effective in orientating collagen fibres without compromising the gel

superstructure. Consistent directional guidance of DRG axons was apparent in patterned scaffolds; however, no axon length was observed.

In contrast, silk fibroin microfibres were seen to be ineffective for DRG neurite guidance. A method was developed for the loading of silk microfibres with NGF which was seen to release over the course of 3-days validated by ELISA. Upon embedding the NGF-loaded silk microfibres in the collagen hydrogels, DRG cultured in absence of NGF outgrowth was improved to be comparable with those supplied with 2 ng/ ml NGF externally.

This research presents the sonotweezer an effective approach for efficient NGC creation achieving two key requirements of directional guidance and improved outgrowth. By alignment of uADSC, a significant reduction in support cell requirements can be gained in comparison to other methods and cell types. Through incorporation of NGF-loaded silk microfibres, a continuous administration of trophic support can be achieved, removing or minimising the requirement of external GF delivery during treatment. Utilising both uADSC and NGF-loaded silk accomplished the outcomes of both although further work is required for optimisation.

5.3.1. Comparative approaches to particle manipulation

In this thesis, a novel approach to 3-D nerve scaffold fabrication was carried out by utilizing the sonotweezer device to construct collagen hydrogel matrices with ADSC and/or silk microfibre arrays. Acoustic trapping of cells and particles provides exciting potential owing to its high resolution, rapid throughput and non-invasiveness (lack of damaging effects on the cells relative to other methods to manipulate cells such as optical tweezers) (Feng et al., 2005). Although cellular patterning has been accomplished in 3-D with acoustics with basic control over cell/ particle movement, these have mostly been restricted to simplistic experimental approaches to understand cellular behaviour (Feng et al., 2005, Garvin et al., 2013) with none translated into a working nerve scaffold. This is mainly due to the sonotweezer remaining in the early stages of development and thus has so far been used predominantly for 2-D patterning experiments (Bernassau et al., 2014, Bernassau et al., 2013). This work started off from successful guidance of regenerating DRG neurites by proxy of acoustically patterned SC (Gesellchen et al., 2014). This is

changing however, as evidenced by creation of organized muscle fibres by patterning of myoblasts within collagen, with sonotweezer devices emerging as a prominent route for 3-D cell engineering applications (Armstrong et al., 2018). Overall, this brings attention to the sonotweezer device as a platform for 3-D scaffold fabrication providing a promising alternative to 3-D printing, which currently remains restricted to a lower precision, as determined by the resolution which is, with respect to cell printing, limited to about 150µm (Petcu et al., 2018b, Armstrong et al., 2018).

5.3.2. 3-D patterning was seen to be in one plane

The results of Chp. 3 demonstrated the ability to align uADSC cells in 3-D collagen hydrogels at varying pattern widths using the operating protocol and setup developed for the octagonal sonotweezer (section: 3.2.2-3.2.4). Aligned cells were seen to be deposited within a layer, at a depth within the gel that was determined by the gelation time of the hydrogel and the time the cells took to sediment. These gel embedded strings of cells are quite similar to those created by Armstrong et al.(2018) which also exhibit a mainly 2-D spatial organisation instead of full 3-D dispersion. Also, section 3.2.4 demonstrated the ability to create gels of various shapes and sizes which could be readily transported. The tray system enables handling to overcome the lack of sufficient mechanical strength of the collagen hydrogel (Hopkins et al., 2013). Alternatively, the plastic compression method, as first introduced by Brown et al. (2005) could be applied to create transferable collagen systems with better mechanical properties; but these are quite different with respect to collagen density and dimensions. Further, the ability to align uADSC within collagen gels that are formed within a PCL scaffold was shown (Figure 51). This shows that this scaffold is very versatile and has application for cell positioning within sufficiently porous scaffolds.

5.3.3. Alignment of uADSC within collagen allows for controlled fibre alignment through contractile forces

It is well known that collagen gels have robustness issues (Hopkins et al., 2013, Mandal et al., 2012), which can be problematic when considering the mechanical requirements of an NGC (Arslantunali et al., 2014). Here, gels of insufficient mechanical robustness were completely contracted, whilst stiffer gels allowed for

some contraction however maintained the overall gel dimensions, shape and cell positions within acceptable standards (Figure 41 and Figure 42). Despite its many advantages, collagen is well known to have robustness issues which can be problematic when considering the mechanical requirements of an NGC. The trade-off when creating stiffer gels is a reduced pore size in the matrix, which can impede cellular penetration, a property which has been shown to result in an even poorer nerve repair than hollow NGC tubes (Petcu et al., 2018b, Mandal et al., 2012). On the other hand, a certain degree of deformability is sought to allow the cellular mediated contractile alignment of collagen fibres. Organised collagen fibres are a long-established motif for neurite guidance (Yoshii and Oka, 2001), with repair comparable to autologous nerve grafts across <20mm distances. To date, there are only three methods regularly used for the manufacture of aligned collagen (Petcu et al., 2018b): magnetic (Torbet and Ronzière, 1984), moulding (Naik et al., 2014) and freeze drying (Lowe et al., 2016). Although not commonly used, cellular alignment through contractile behaviour has been known for some time (Eppenberger and Zuppinger, 1999), however is only recently becoming a popular route for production (O'Rourke et al., 2018), although in these approaches the collagen is tethered. To current knowledge, this is the first reported instance in directional control over cellular contraction generated matrix fibre alignment in free-floating collagen gels.

One recent study has investigated the cellular induced contraction of collagen hydrogels in an attempt to assess the potential for nerve growth applications (O'Rourke et al., 2015). No control was gained over the direction of resulting fibre alignment, however. This distinguishes the results of cell behaviour undertaken studies in section 3.3.2 which consistently showed alignment of collagen fibres perpendicular to the pre-ordained pattern direction. Higher cell seeding densities promoted greater contraction and collagen fibre alignment. From the time-lapse tracking studies, this behaviour was consistently initiated by a high degree of contraction in the direction of the pattern. This was likely instigated by the abundant cell densities within the pattern bands contracting together as adhesions complexes to the surrounding matrix are made. The consistency in this observation indicates that this initial contraction may serve as the initial foundation for controlled, cellular mediated, collagen fibre alignment.

5.3.4. Scaffolds with aligned uADSC guide neurite outgrowth

Directionality analysis of DRG outgrowth of cultures within aligned uADSC-collagen scaffolds (Figure 49 and Figure 50) demonstrated a axon network organisation perpendicular to the initial direction of the cell pattern over random cellular distributions. This gave further confirmation to the birefringence analysis (carried out on singular bio-repeats for each cell density) (Figure 43) of the cellular behaviour and the reliable alignment of collagen fibres through an initial cellular pattern formation. A recent collagen NGC which has attracted a lot of attention is the EngNT (O'Rourke et al., 2018) due to its promising clinical potential for increasing outgrowth whilst promoting a high degree of neurite organisation through directed outgrowth both *in vivo* and *in vitro studies*. In EngNT seeded with SC (Georgiou et al., 2013) or dADSC (Georgiou et al., 2015), cells were seen to elongate in the direction of the tethered edges of the gel and the collective contractile forces exerted by the cells aligned the collagen fibres. Although mechanistically; this approach is similar to the one taken in Chp.3, there are a number of distinct differences (here, EngNT): cell type (uADSC versus SC or dADSC), hydrogels (remain free floating and fully hydrated versus tethered and plastic compressed), direction of contraction (orthogonal compared to along the initial alignment). Further, the seeding density in EngNT is substantially higher (~1000k cells/ 1 ml gel) than with the sonotweezer fabrication described here (41.25-82.5k/ 1 ml gel) which highlights an impressive advantage when considering the difficulties in harvesting/ cultural maintenance of SC/dADSC. In performance, the directionality of neurite outgrowth showed similar frequency distributions (Figure 64) indicating that the uADSC patterned collagen hydrogels have the potential to be comparable in axon guidance. For these comparisons, it must also be taken into account that each scaffold investigated a different neuronal culture type (EngNT: primary rat sensory neurons, sonotweezer: DRG explant) and orientation analysis was not the same. This may explain the larger dispersion towards 90° in the histogram for the organotypic DRG explant, as neurites migrate from all directions around the DRG before guidance occurs.

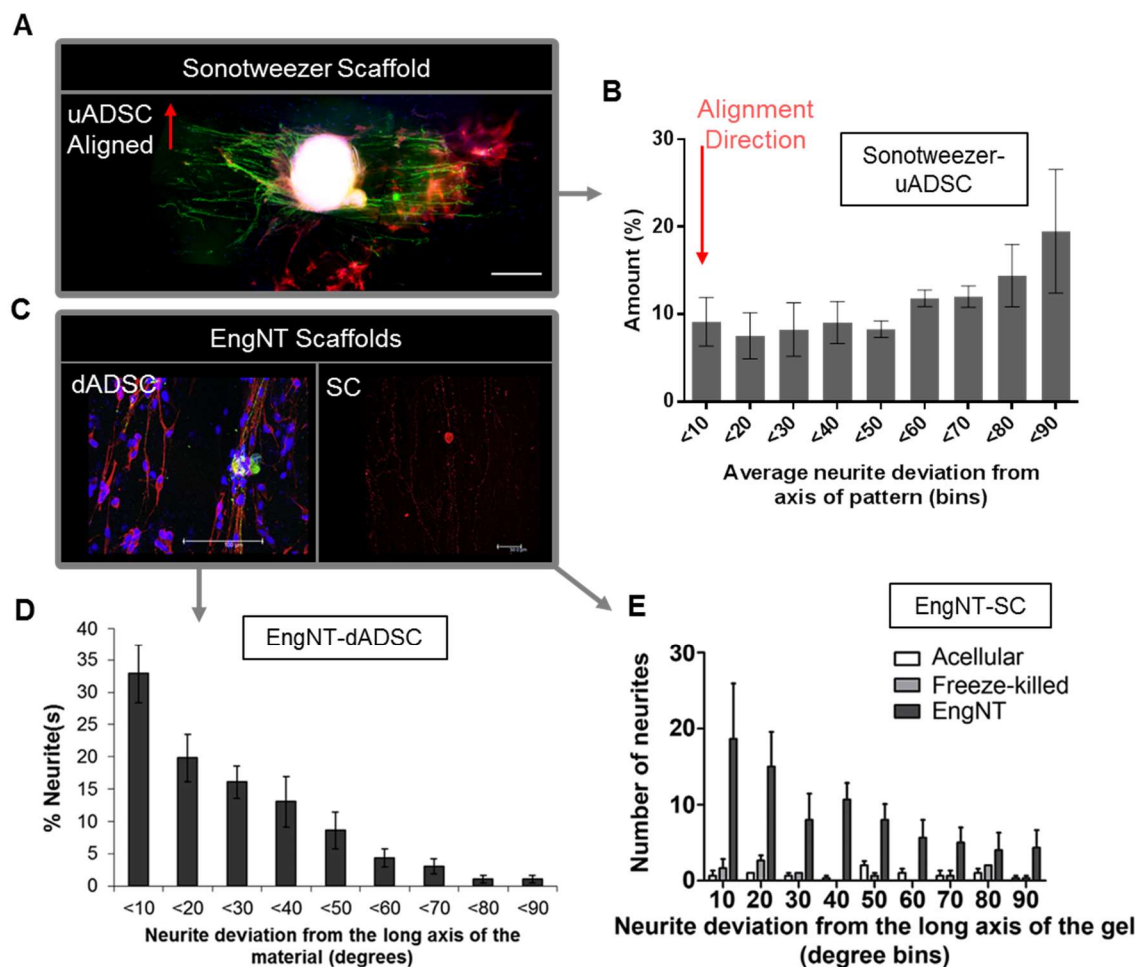


Figure 64: Comparison of uADSC aligned scaffolds and EngNT in directional guidance of axons. Image-set A and C shows a visual comparison of axon growth using immunofluorescent labelling of the following: top: green: neurofilaments (axons), red: actin (uADSC), blue: DAPI (nuclei), bottom-left: green: B3-tubulin (axons), red: S100(SC), blue: Hoechst (nuclei), bottom-right: red: B3-tubulin (axons). Axons of the sonotweezer scaffold can be seen to grow perpendicular to the initial pattern direction (red arrow), conversely; EngNT promotes axon growth in the direction of cellular alignment. Directionality analysis (B-C) shows similar profile of histograms with a predominant alignment for all at less than 10 bins from the intended direction. Aligned uADSC showed slightly poorer performance through higher variation across scaffolds although this may also be a result of using DRG explants or different methods for calculating orientation C: filament sensor. Bars indicate standard deviation. Image adapted from: (Georgiou et al., 2013, Georgiou et al., 2015). Scale: top: 500 μ m, left-bottom: 100 μ m, right-bottom: 50 μ m

5.4. Silk fibroin microfiber scaffolds

Silk fibroin/ collagen hydrogel composites constructs for tissue engineering have been investigated for a variety of applications in regenerative medicine (Yeo et al., 2008), in particular; for nerve repair (Xu et al., 2016), in order to utilise the mechanical, structural and chemical properties of a composite. Most of these studies employed both proteins as constituent copolymer materials. The initial aim of Chp. 4 was to harness the different mechanical properties of each protein preparation as separate

entities within a single construct in order to create an anisotropic composite scaffold. The initial intention was to improve the directionality of neurite outgrowth through the stiffness differential, a guidance cue which has been previously established on both 2-D and 3-D (Déjardin, 2013, Sundararaghavan et al., 2009). Functionally, this is a similar approach to the scaffolds constructed by Chwalek et al.(2015) in which collagen hydrogel and silk fibroin sponge are combined to produce a model which mimics the mechanical properties of white (soft) and grey matter (stiffer) of the brain to investigate the behaviour of rat brain derive neurons. However, the structural architecture is vastly different, between this brain model ('donut shaped'- porous silk sponge immersed within collagen matrix) and the scaffolds fabricated here (silk microfibrils imbedded in aligned formation within collagen matrix. Neurons were observed to growth within the collagen filled central region of the scaffold and the silk fibroin was considered to serve as the structural support to the construct.

5.4.1. The sonotweezer allows for a unique approach to pattern silk microfibrils within collagen I hydrogels

Prior to nerve growth studies, the quality of silk aligned scaffolds was assessed without the inclusion of a DRG explant. The majority of silk microfibrils were seen to align along the direction of the pattern within the region of acoustic force, however, some microfibrils of greater lengths than ca. 200 μ m, approximately the spacing between acoustic nodes perpendicular to the node pattern. This has been observed by Syojiro Yamahira, et al. (2000) and was calculated to be resultant of the drag and torque forces applied to the fibre and the moment of inertia created by residing in two pressure nodes.

In literature, no other research could be found on the creation of 3D collagen matrices with aligned anisotropic particles using acoustic waves, making comparisons to other scaffold fabrication methods difficult. The closest similarities to this protocol are: the sonotweezer aligned myoblasts within collagen matrices recently published (Armstrong et al., 2018), plastic compression or electrospinning and 3-D printing approaches.

The first is a cellular alignment for application in muscle and therefore does not compare in either functionality or in the resulting scaffold structure. Brown, et al.

(2005) showed that plastic compression could be used as a method to produce collagen matrices reinforced with aligned PGA fibres, which promote fibroblast proliferation. Over time these fibres hydrolyse resulting in a gradual decrease in stiffness of the composite, to levels of stiffness of collagen seen *in vivo*. This approach has elements, which are similar to those used in this thesis (e.g. fibre align, collagen hydrogel, stiffness induced cell response). However, as this work targeted connective tissue its application to nerve regeneration remain to be elucidated.

Electrospinning is a well-established technique to produce aligned micro and nanofibrous substrates for improved neurite growth (GF delivery) and guidance (fibre alignment) in 2-D (Liu et al., 2018, Xie et al., 2014). The formation of 3-D nerve guidance tubes has been achieved through rolling/ folding the electrospun substrate membrane (Du et al., 2018) although this technique is probably better suited to provide internal guidance by topography/ chemical properties of the NGC tube rather than a filler for the lumen. Approaches for the creation of aligned 3-D scaffolding using electrospinning have involved cutting and twisting together of PCL electrospun microfibres (Daud et al., 2012, Behbehani et al., 2018) or electrospinning under water vortex of poly(lactic-co-glycolic acid) (PLGA) (Zamani et al., 2014), each methods carried out before manual insertion into a conduit tube. Proof of action was found as neurite guidance was directly relative to fibre size (Daud et al., 2012); however, as this was the sole material inside the conduit, it is more reflective of aligned collagen lumen than the composite scaffolds created in Chp. 4.

The last relevant approach to cell/ material patterning is additive manufacturing processes, particularly 3-D printing, a relatively recent breakthrough in scaffold design and fabrication, reviewed by Petcu, et al. (2018b)). Bioprinting has undergone an explosive research output owing to its continuously advancing, accessible technology, intricate scaffold production, bio-ink versatility, rapid throughput and low cost. However, no research could be found on 3-D printing of microparticles within a hydrogel matrix. Generally, this method is utilized for accurate cell seeding, creation of biomolecular concentration gradients, and the NGC inner architecture macrostructure, but a lower resolution remains one of the key issues (Petcu et al., 2018b, Graham et al., 2017) in comparison to the alignment capabilities of the sonotweezer.

Overall, each of these methods are not mutually exclusive, with recent strategies incorporating both electrospinning and 3-D printed constructions (Lee et al., 2016, Vijayavenkataraman et al.). Herein lays the potential for the sonotweezer method of scaffold fabrication which can be used in conjunction with other construction methods. Through a complementary setup of these methods, the creation of precisely designed e.g. with cell and/ or particle patterns lumen which can be readily inserted into or formed within pre-fabricated conduits (see Figure 51).

5.4.2. Scaffolds with incorporated NGF loaded silk microfibres improves initial outgrowth

NGF loaded silk microfibers were created with the aim to provide local NGF delivery, at the site of need. The microfibres were seen to release an estimated average NGF culture concentration of ~60 pg/ ml within the initial 24 hrs and a further much lower but consistent amount eluted over a period of three days. This release profile was consistent with theory of release from adsorbed monolayers (Matsumoto et al., 2004) and silk fibroin in particular (Uebersax et al., 2007). The former is of particular interest as it revealed that only 0.3-13% of the initially loaded NGF silk matrices was released after 23 days. This may indicate that the consistent NGF release from NGF-loaded-silk microfibres post 24 hrs may be sustained for a number of weeks depending on the conditions. Temperature is one such condition that is to mediate adsorption affinities (Rabe et al., 2011) giving reasoning as to why samples kept at 37°C released less NGF than 4°C. However, another probable factor is that the released NGF was impacted by protein denaturing and degradation at culture conditions (as evidence by elution difference between silk-free, 2 ng/ ml NGF-media samples kept at 4 and 37°C), despite the stabilising presence of foetal bovine serum (carrier protein). Protection from protein degradation has been achieved through the addition of stabilizing agents such as the carrier protein BSA (Checa-Casalengua et al., 2011) or detergent additives Tween 20/40 (Kraskiewicz et al., 2013). Other methods have been investigated in efforts to prolong both delivery and bioactivity of neurotrophins such as hydrogel or microsphere encapsulation (Piantino et al., 2006, Checa-Casalengua et al., 2011). Despite some success (for review: (Liu et al., 2013a, Madduri and Gander, 2012) this hurdle currently remains a substantial challenge for sustained delivery in a clinical setting.

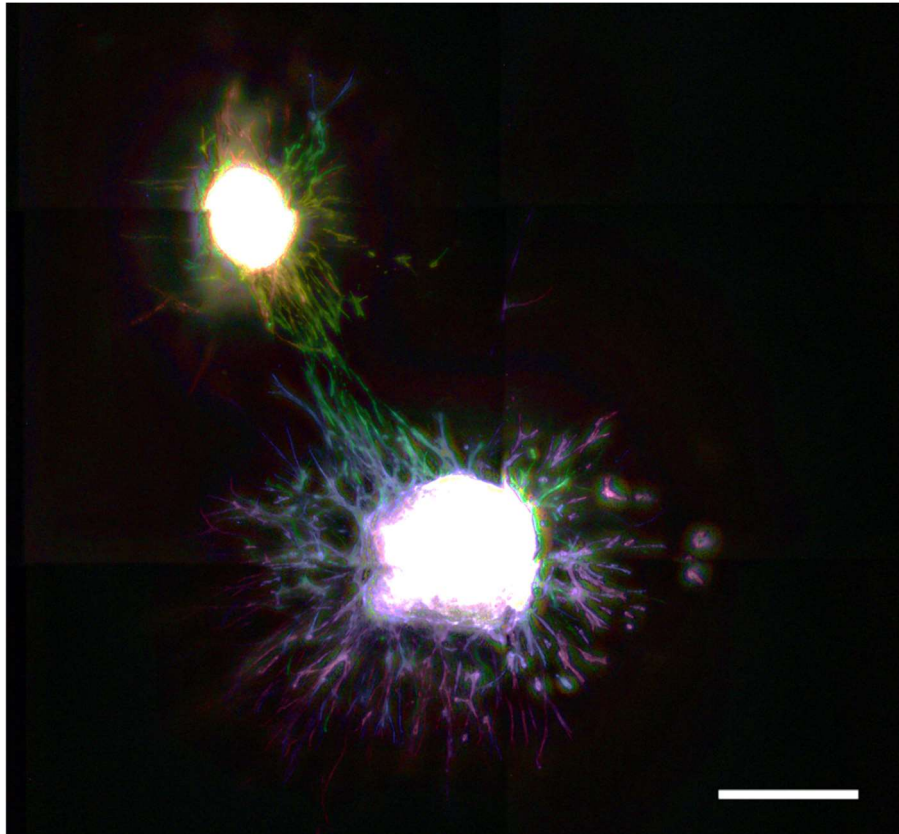
The NGF loading method of Chp. 4 focused on the adsorption of NGF through electrostatic attraction between silk and NGF in a very similar process detailed for VEGF loading of silk nanoparticles (Kundu et al., 2010). This maintains the advantage that there is minimal influence to biological function (Liu et al., 2013a) (which was also observed in adsorption of NGF by silk fibroin matrices of (Uebersax et al., 2007)) and an allowance for passive diffusion into the surrounding gel/tissue over other more permanent immobilisation motifs such as with covalent bonding (McCormick et al., 2013). As there is no solid binding to the adsorbed NGF and silk fibroin relatively rapid initial delivery release rates were observed which is consistent with the findings of (Pakulska et al., 2016) which showed protein release rates from poly(lactic-co-glycolic acid) (PLGA) nanoparticles (NP). Also, this was found to be directly related to the surface area (determined by the NP size). Nanoparticles are well known to have vastly increased surface areas over their bulk counterparts and in relation to microparticles (such as the silk microfibrils in this thesis). This could explain the rapid elution of NGF from the silk as an occurrence resulting from the fibres size occupying microscale dimensions; leaving a low surface area is exposed for NGF adsorption but also highlights routes for improvement.

The alignment of silk microfibers was seen to have very little effect on axon growth (Figure 56), especially in the presence of NGF, which instead promoted a more branching, exploratory outgrowth instead of an organized axon alignment. This indicated that any durotactic effect instigated by the stiffness differential between collagen and silk was not profound enough to overcome minimal amounts of NGF. Also, generally the peripheral nerve environment is considered soft (in the region of 150-300kPa) which may reason for the preferred growth through the softer collagen matrix. Despite these findings, DRG outgrowth on or within collagen gels with NGF loaded silk showed higher total axon lengths than in collagen gels with incorporated untreated silk. The DRG outgrowth approached levels similar to cultures supplied cultures with 2 ng/ ml NGF (Figure 60). In summation, NGF-silk may provide an alternative for NGF delivery for shorter periods of time. A longer release is still up for debate however if this approach is limited short term NGF provision, culture periods could be increased through improving NGF stability and by including slow release systems until the local cell population would adapt to provide sufficient levels.

5.4.3. Combined collagen scaffolds with aligned NGF-silk microfibres/ uADSC improve outgrowth and directionality or regeneration

To complete the overall study of sonotweezer fabricated collagen scaffolds for enhancement of nerve regeneration, NGF-silk and uADSC were aligned together within a single gel. This increased complexity of alignment and introduced the possibility for uADSC to interact with the NGF-silk microfibres. This approach proved to be successful at incorporating both positive aspects of each entity: NGF-silk improved outgrowth and uADSC: directional guidance. It should be noted however that guidance was slightly lower than observed for scaffolds with aligned uADSC, which could be attributed to the presence of silk microfibres reducing patterning quality (see Figure 55). Interestingly, two cultures with highly aligned axon growth towards the direction of the pattern were found which completely contrasted results of sections 3.3.2, 3.3.4 and other cultures of section 4.3.4. Greater scrutiny revealed that regions of disorganisation had occurred at opposite sides of the DRG (yellow arrows/inset shown in Figure 63) which could contract and aggregate into two separate clusters. The clusters then further contract the gel and create a region of collagen fibre alignment path which caused impressive DRG axon directionality. As a result, this indicates that aggregation between two opposing uADSC clusters is likely a highly proficient route for aligning collagen fibres and directing neurite outgrowth.

6. Future Work



“A binary star in a dish” A fluorescent image of actin labelled (phalloidin) of an uADSC spheroid (top left) and DRG (bottom right) cultured within a collagen I matrix. Image consists of 10 colour co-ordinated 30 μ m slices, which are flattened to a single image using ImageJ: Extended Depth of Field plugin. Scale: 500 μ m

6.1. Antagonistic convergence of topographical and NGF signalling cascades

In Chapter 2 the work focused on determining the presence of an interaction between NGF and topography-initiated signalling and concluded that their combined inductive properties ultimately conflicted which had detrimental effect on the regeneration of DRG neurons. The results in section: 0 implicated that high NGF concentrations act as both: an inhibitor of the cytoskeletal tension activator myosin IIA as well as a promoter of fasciculation. Fasciculation, when confined by microgrooves was seen to cause loss of substrate adhesion and lead to network retraction. Although this data gives an initial insight into the combined processes involved, further work could follow a number of different directions. Either: to understand the occurrence in greater detail in vitro or investigate its presence or impact in setups closely resembling clinical approaches.

6.1.1. Target of key signalling mediators

Primarily, an inhibitory study could be carried out investigating myosin IIB to further pinpoint the signalling interaction. Additionally, an effort could be made to determine the effects of topography/ NGF on the retrograde flow actin, through tracking the movement/ localisation of MT/actin within the growth cones. Together, these results could lead to a confirmation of the conclusions in (section: 2.4) which hypothesize that topography may promote myosin IIB activity. Also, an inhibition to other targets may be worthwhile, specifically the GTPases: RhoA or Rac1 which are involved in the NGF signalling and contractility pathway interactions (Loudon et al., 2006, Yasui et al., 2001, Nusser et al., 2002, Shin et al., 2014, Liu et al., 2002). To demonstrate the effect topography has on axon tension , laser induced lesions could be performed to measure the tension release as shown by Vassalli et al., (2013). Signalling activity further down the axon to the microtubule cytoskeleton or even nuclear expression could be carried out in order to determine if the interaction occurs mainly at the growth cone or is present throughout the whole network. Nocodazole inhibition of dynien, a molecular motor for MT responsible for NGF retrograde transport (Wu and Mobley, 2009, Prokop, 2013), could be used to address the involvement of different signalling cascades by NGF under the modulation of surface

cues. Further, protein tracking/localisation studies on alternating topographies/NGF conc. could target Tau, the key binding protein linking the MT and actin filaments and largely responsible for axon cytoskeletal dynamics (Elie et al., 2015), or kinesin-1: another MT motor protein which functions in MT sliding and thus elongation (Prokop, 2013). Altogether, these studies would tie in well with the recent study by Thomson et al. (2017) which implicates mTOR as a downstream mediator of the neuronal response to topographical cues. Evidence has shown mTOR to be regulated by dynein transport (Clippinger and Alwine, 2012) and is known to be a downstream effector of Rac and RhoA in PI3K/Akt signalling pathway (Thomson et al., 2017). Thus, it is unclear whether the observed expression of mTOR serves to effect or is affected by topographical MT or actin dynamics and further, to what extent NGF might modulate the response to topographical cues. Overall, addressing these unknowns would not only determine their contribution to the observed NGF-topographical trend but also aid in understanding the bigger picture of the underlying signalling instigating the antagonistic effect on axon growth. With this knowledge, a greater clarity on which signalling mediators are responsible and should be potentiated in order to reduce the observed impact on neurite outgrowth at higher NGF concentrations.

6.1.2. Substrate chemistry

Another facet of the signalling interaction which has not born much discussion in this thesis is the chemical nature of the substrate. As noted by Turney, et al. (2016), substrate bound proteins can provoke vastly different signalling responses, with synthetic polymers deemed as being inert (Liu et al., 2002) providing a good indication that the microgrooves are key to the NGF conc. trend (Figure 14 and Figure 15). To confirm this, the substrate could be modified with different proteins i.e. Collagen, laminin and fibronectin separately or in combination. Laminin has previously been used in a previous study involving singular DRG neurons (Kredi, 2016) to which NGF-topography interaction was not active; however, this did not encompass other characteristics of the organotypic DRG culture such as overwhelming fasciculation and supportive cell presence which are central to the proposed hypothesis in this thesis.

6.1.3. Investigation on how topography influences tension and promotes fasciculation

An effort could be made to separate the fasciculation effect and signalling interaction through culturing the DRG on the centre of multi-directional grooved surface (akin to wheel spokes). This in theory should reduce fasciculation whilst keeping all other parameters consistent. Additionally, it may also provide an insight into the chiral morphologies of DRG networks cultured within blebbistatin (Figure 24) which could only be discussed theoretically. The main plausible limitation to this approach may be in the overall axonal network tension vector which may spread in all directions as oppose to the bipolar nature presumed in cultures of this thesis. This may have an impact when considering that tension plays an intrinsic role in the hypothesized events whilst also possibly placing mechanical strain on a soma/ nuclei within the DRG which can lead to a deformation and the alteration of structure/functioning (Martins et al., 2012). Also, this work focuses on the actin mechanics within the growth cone; however, as suggested above, there may be other factors at play further down the axon such as the MT. As a result, the multi-directional model could also influence this and provide a discrepancy between the conventional, unidirectional grooved surfaces.

6.1.4. Translation to a 3-D model

The final suggestion for further work in this section is in the shift to a 3-D system. This would provide a more indicative model for the impact of this interaction within current nerve repair strategies and overall; a stronger case for more scrutiny in combinatorial approaches. Alongside this, the involvement of substrate chemical properties would have to be investigated to serve as a suitable comparison and ensure that the interaction (or lack of) observed is not solely as a result of the chemical influence of the chosen substrate/ matrix. Upon switching to a 3-D setup, the motif for tropic guidance will have to be evaluated although two obvious structures are in the alignment of biomaterial fibres (aligned col/ alginate etc.) or in organised tubes (Petcu et al., 2018b).

6.2. Sonotweezer aligned scaffolding

In both chp.3 and 4, the sonotweezer device was successful in the fabrication of precisely designed, aligned cells/ silk fibres within 3-D collagen matrix, which was seen to provide a positive influence on DRG nerve regeneration. This work was extremely prototypical and thus; there remains a vast opening for optimisation of nearly every parameter. Briefly, these may include: the pattern width, gel concentration, cell seeding density, gelation time, PZT/ acoustic field dimensions and sonotweezer operational settings. Another key suggestion is in the 3-D characterisation of gels and axon outgrowths which could be carried out simply using confocal microscopy.

6.2.1. Use of other biomaterials

Firstly, the use of a different hydrogel biomaterial may be of interest as there is a variety of other suitable alternatives to collagen, which may produce better results for neurite outgrowth e.g. alginate (Grulova et al., 2015), silk fibroin (Floren et al., 2016). Each would likely require alterations to the prescribed protocol (section: 3.2.4) and/ or device settings. Undisclosed previously in this thesis, silk fibroin was attempted but required a much greater effort to produce reliable gel-setting. Of the gels which did set, cracks were seen to form within the gel possibly as a result of dehydration or the application of continued acoustic field. Overall, aligned particles within silk fibroin is possible; however, remains more challenging than the simplicity of collagen hydrogel formation and would require extensive time out-with the constraints of this PhD.

6.2.2. Alternative to uADSC for alignment

Alternatively, the employment of uADSC for the controlled contraction and matrix fibre alignment could be forgone to investigate other cell types instead. The most obvious choice would be with SC alignment in an effort to create true bands of Büngner. Although, if the behaviour of SC is found to bear any similarity to that of dADSC, this endeavour may prove fruitless as mass cellular migration occurs. Recent understandings of the intrinsic mechanisms and events of nerve regeneration (Cattin and Lloyd, 2016b) reveal that during reprogramming for a regenerative response, SC are attracted to EphB released by fibroblasts. Also, in this paper, the importance of

endothelial cells through the formation blood vessels was explained through serving as the foundation for directed migration for SC, crucial for bands of Büngner formation. Taking these findings into account, the use of a complementary cell type which secretes EphB such as fibroblasts and/or endothelial cells may provide the incentive for SC to anchor more permanently to the prescribed pattern until the cells are locked as bands of Büngner. A scaffold constructed in this manner would serve to further mimic the make-up and components of the natural neuro-regenerative environment.

6.2.3. Improving NGF-silk

With regards to silk fibroin incorporation, no major benefits for alignment were found and further; the fibre dimensions made for greater difficulty in sonotweezer manipulation and patterning. The NGF-silk did show to improve outgrowth and thus may be applied to silk nanoparticles which would not experience any acoustic forces due to the working size of the acoustic field. This would also remove any barrier effect they would present during the combined alignment of other objects/ cells. Moving to the nanometre scale would also create the opportunity for greater NGF adsorption due to vast increases in surface area and likely more sustained NGF release (Pakulska et al., 2016).

6.2.4. Material reinforcement through silk fibre alignment

Additionally, outside the context of nerve repair, silk microfibres have been incorporated into silk hydrogels to provide an increase in mechanical strength to the overall gel properties (Mandal et al., 2012). In theory, this strategy could be applied to the use of the sonotweezer induced alignment of silk microfibres to create mechanically anisotropic material which exhibits both a stiff and soft direction. This may find applications outside cell/ tissue engineering (e.g. shock absorbers (Lethbridge et al., 2010) or hydraulics (Matthias and Marion, 2018)) which requires differing structural support and compressibility in orthogonal directions.

6.2.5. Translation to in vivo models

Overall, sonotweezer aligned scaffold research should aim to progress into NGC incorporation and in vivo experimentation in order to provide a true insight of the

scaffold performance for nerve repair. The collagen moulding process detailed in section 3.2.4 allows the alteration to produce any shape or size required and the absence of the DRG explant body (for practical in vivo experiments) should improve scaffold quality considerably.

6.2.6. A spheroidal approach

Finally, the last suggestion does not involve signalling interactions or acoustic aligned scaffolds but draws on the findings of the exceptional scaffolds shown in Chp 4. Here impressive neurite guidance was observed to arise from regions of uADSC disorganisation in the gel indicating that dense, cellular clustering is highly effective for directional outgrowth. However, this is difficult to reliably produce under conventional seeding procedures. One such route which may circumvent this issue is through spheroid formation. Spheroids are dense clusters of cells which have adhered together as a result of aggregation followed by no available substrate for adhesion (Lewis et al., 2016). With spheroidal derivation of stem cells, interesting cell behaviours have been presented in comparison to their singular cell counterparts such as their inherent quiescence and migratory and differentiation upon receiving an injury signal. During this work, a small number of experiments were carried out examining spheroidal ADSC and DRG co-cultures within collagen I hydrogels, showing a high degree of interaction between the two. Due to time-constraints, this could not be properly investigated; although, it did indicate that this could be another route to neurite guidance using ADSC.

7. References

- AHMED, E. M. 2015. Hydrogel: Preparation, characterization, and applications: A review. *Journal of Advanced Research*, 6, 105-121.
- AHMED, F. A. K. M., INGOGLIA, N. A. & SHARMA, S. C. 2001. Axon Resealing Following Transection Takes Longer in Central Axons Than in Peripheral Axons: Implications for Axonal Regeneration. *Experimental Neurology*, 167, 451-455.
- ALLODI, I., UDINA, E. & NAVARRO, X. 2012. Specificity of peripheral nerve regeneration: Interactions at the axon level. *Progress in Neurobiology*, 98, 16-37.
- ANTOINE, E. E., VLACHOS, P. P. & RYLANDER, M. N. 2014. Review of Collagen I Hydrogels for Bioengineered Tissue Microenvironments: Characterization of Mechanics, Structure, and Transport. *Tissue Engineering. Part B, Reviews*, 20, 683-696.
- ARMSTRONG, J. P. K., PUETZER, J. L., SERIO, A., GUEX, A. G., KAPNISI, M., BREANT, A., ZONG, Y., ASSAL, V., SKAALURE, S. C., KING, O., MURTY, T., MEINERT, C., FRANKLIN, A. C., BASSINDALE, P. G., NICHOLS, M. K., TERRACCIANO, C. M., HUTMACHER, D. W., DRINKWATER, B. W., KLEIN, T. J., PERRIMAN, A. W. & STEVENS, M. M. 2018. Engineering Anisotropic Muscle Tissue using Acoustic Cell Patterning. *Advanced Materials*, 0, 1802649.
- ARSLANTUNALI, D., DURSUN, T., YUCEL, D., HASIRCI, N. & HASIRCI, V. 2014. Peripheral nerve conduits: technology update. *Medical Devices (Auckland, N.Z.)*, 7, 405-424.
- ATAJANOV, A., ZHBANOV, A. & YANG, S. 2018. Sorting and manipulation of biological cells and the prospects for using optical forces. *Micro and Nano Systems Letters*, 6, 2.
- ATHAMNEH, A. I. M. & SUTER, D. M. 2015. Quantifying mechanical force in axonal growth and guidance. *Frontiers in Cellular Neuroscience*, 9, 359.
- BAIN, J. R., MACKINNON, S. E., HUDSON, A. R., FALK, R. E., FALK, J. A. & HUNTER, D. A. 1988. The peripheral nerve allograft: an assessment of regeneration across nerve allografts in rats immunosuppressed with cyclosporin A. *Plast Reconstr Surg*, 82, 1052-66.
- BARRAL, J.-P. & CROIBIER, A. 2009. Chapter 1 - Some preliminary thoughts. *Manual Therapy for the Cranial Nerves*. Edinburgh: Churchill Livingstone.
- BASAK, S., DESAI, D. J., RHO, E. H., RAMOS, R., MAUREL, P. & KIM, H. A. 2015. E-cadherin enhances neuregulin signaling and promotes Schwann cell myelination. *Glia*, 63, 1522-36.
- BAZOU, D., COAKLEY, W. T., HAYES, A. J. & JACKSON, S. K. 2008. Long-term viability and proliferation of alginate-encapsulated 3-D HepG2 aggregates formed in an ultrasound trap. *Toxicology in Vitro*, 22, 1321-1331.
- BEHBEHANI, M., GLEN, A., TAYLOR, C. S., SCHUHMACHER, A., CLAEYSSENS, F. & HAYCOCK, J. W. 2018. Pre-clinical evaluation of advanced nerve guide conduits using a novel 3D in vitro testing model. *International Journal of Bioprinting*, 4.
- BEN-YAAKOV, K., DAGAN, S. Y., SEGAL-RUDER, Y., SHALEM, O., VUPPALANCHI, D., WILLIS, D. E., YUDIN, D., RISHAL, I., ROTHER, F., BADER, M., BLESCH, A., PILPEL, Y., TWISS, J. L. & FAINZILBER, M. 2012.

- Axonal transcription factors signal retrogradely in lesioned peripheral nerve. *The EMBO Journal*, 31, 1350.
- BERNASSAU, A. L., COURTNEY, C. R. P., BEELEY, J., DRINKWATER, B. W. & CUMMING, D. R. S. 2013. Interactive manipulation of microparticles in an octagonal sonotweezer. *Applied Physics Letters*, 102, 164101.
- BERNASSAU, A. L., GLYNNE-JONES, P., GESELLCHEN, F., RIEHLE, M., HILL, M. & CUMMING, D. R. S. 2014. Controlling acoustic streaming in an ultrasonic heptagonal tweezers with application to cell manipulation. *Ultrasonics*, 54, 268-274.
- BETZ, T., KOCH, D., LIM, D. & KÄS, J. A. 2009. Stochastic Actin Polymerization and Steady Retrograde Flow Determine Growth Cone Advancement. *Biophysical Journal*, 96, 5130-5138.
- BIELA, S. A., SU, Y., SPATZ, J. P. & KEMKEMER, R. 2009. Different sensitivity of human endothelial cells, smooth muscle cells and fibroblasts to topography in the nano–micro range. *Acta Biomaterialia*, 5, 2460-2466.
- BONINI, S., LAMBIASE, A., ANGELUCCI, F., MAGRINI, L., MANNI, L. & ALOE, L. 1996. Circulating nerve growth factor levels are increased in humans with allergic diseases and asthma. *Proc Natl Acad Sci U S A*, 93, 10955-60.
- BOUQUET, C. & NOTHIAS, F. 2007. Molecular Mechanisms of Axonal Growth. In: BAGNARD, D. (ed.) *Axon Growth and Guidance*. New York, NY: Springer New York.
- BRANDT, J., DAHLIN, L. B. & LUNDBORG, G. 1999. AUTOLOGOUS TENDONS USED AS GRAFTS FOR BRIDGING PERIPHERAL NERVE DEFECTS. *The Journal of Hand Surgery: British & European Volume*, 24, 284-290.
- BROWN, J. A. & BRIDGMAN, P. C. 2009. Disruption of the cytoskeleton during Semaphorin 3A induced growth cone collapse correlates with differences in actin organization and associated binding proteins. *Dev Neurobiol*, 69, 633-46.
- BROWN, R. A., WISEMAN, M., CHUO, C.-B., CHEEMA, U. & NAZHAT, S. N. 2005. Ultrarapid Engineering of Biomimetic Materials and Tissues: Fabrication of Nano- and Microstructures by Plastic Compression. *Advanced Functional Materials*, 15, 1762-1770.
- BUNNELL, B. A., FLAAT, M., GAGLIARDI, C., PATEL, B. & RIPOLL, C. 2008. Adipose-derived Stem Cells: Isolation, Expansion and Differentiation. *Methods (San Diego, Calif.)*, 45, 115-120.
- BURNETTE, D. T., JI, L., SCHAEFER, A. W., MEDEIROS, N. A., DANUSER, G. & FORSCHER, P. 2008. Myosin II activity facilitates microtubule bundling in the neuronal growth cone neck. *Dev Cell*, 15, 163-9.
- CAI, Y., BIAIS, N., GIANNONE, G., TANASE, M., JIANG, G., HOFMAN, J. M., WIGGINS, C. H., SILBERZAN, P., BUGUIN, A., LADOUX, B. & SHEETZ, M. P. 2006. Nonmuscle Myosin IIA-Dependent Force Inhibits Cell Spreading and Drives F-Actin Flow. *Biophysical Journal*, 91, 3907-3920.
- CAMPBELL, I. D. & HUMPHRIES, M. J. 2011. Integrin Structure, Activation, and Interactions. *Cold Spring Harbor Perspectives in Biology*, 3, a004994.
- CAO, J., SUN, C., ZHAO, H., XIAO, Z., CHEN, B., GAO, J., ZHENG, T., WU, W., WU, S., WANG, J. & DAI, J. 2011. The use of laminin modified linear ordered collagen scaffolds loaded with laminin-binding ciliary neurotrophic factor for sciatic nerve regeneration in rats. *Biomaterials*, 32, 3939-48.

- CATRINA, S., GANDER, B. & MADDURI, S. 2013. Nerve conduit scaffolds for discrete delivery of two neurotrophic factors. *Eur J Pharm Biopharm*, 85, 139-42.
- CATTIN, A.-L., BURDEN, JEMIMA J., VAN EMMENIS, L., MACKENZIE, FRANCESCA E., HOVING, JULIAN J. A., GARCIA CALAVIA, N., GUO, Y., MCLAUGHLIN, M., ROSENBERG, LAURA H., QUEREDA, V., JAMECNA, D., NAPOLI, I., PARRINELLO, S., ENVER, T., RUHRBERG, C. & LLOYD, ALISON C. 2015. Macrophage-Induced Blood Vessels Guide Schwann Cell-Mediated Regeneration of Peripheral Nerves. *Cell*, 162, 1127-1139.
- CATTIN, A.-L. & LLOYD, A. 2016a. *The multicellular complexity of peripheral nerve regeneration*.
- CATTIN, A.-L. & LLOYD, A. C. 2016b. The multicellular complexity of peripheral nerve regeneration. *Current Opinion in Neurobiology*, 39, 38-46.
- CEBALLOS, D., NAVARRO, X., DUBEY, N., WENDELSCHAFER-CRABB, G., KENNEDY, W. R. & TRANQUILLO, R. T. 1999. Magnetically Aligned Collagen Gel Filling a Collagen Nerve Guide Improves Peripheral Nerve Regeneration. *Experimental Neurology*, 158, 290-300.
- CHALOUPKA, J., PILLAI, K. R. & STRNADOVÁ, M. 1980. The complex effect of temperature on protein degradation in sporulating *Bacillus megaterium*. *FEMS Microbiology Letters*, 9, 107-110.
- CHANG, Y.-C., CHEN, M.-H., LIAO, S.-Y., WU, H.-C., KUAN, C.-H., SUN, J.-S. & WANG, T.-W. 2017. Multichanneled Nerve Guidance Conduit with Spatial Gradients of Neurotrophic Factors and Oriented Nanotopography for Repairing the Peripheral Nervous System. *ACS Applied Materials & Interfaces*, 9, 37623-37636.
- CHANGÉDE, R. & SHEETZ, M. 2017. Integrin and cadherin clusters: A robust way to organize adhesions for cell mechanics. *BioEssays*, 39, 1-12.
- CHAO, M. V. 2003. Neurotrophins and their receptors: A convergence point for many signalling pathways. *Nat Rev Neurosci*, 4, 299-309.
- CHECA-CASALENGUA, P., JIANG, C., BRAVO-OSUNA, I., TUCKER, B. A., MOLINA-MARTÍNEZ, I. T., YOUNG, M. J. & HERRERO-VANRELL, R. 2011. Retinal ganglion cells survival in a glaucoma model by GDNF/Vit E PLGA microspheres prepared according to a novel microencapsulation procedure. *Journal of Controlled Release*, 156, 92-100.
- CHERNOUSOV, M. A., ROTHBLUM, K., STAHL, R. C., EVANS, A., PRENTISS, L. & CAREY, D. J. 2006. Glypican-1 and alpha4(V) collagen are required for Schwann cell myelination. *J Neurosci*, 26, 508-17.
- CHIU, D. T. & STRAUCH, B. 1990. A prospective clinical evaluation of autogenous vein grafts used as a nerve conduit for distal sensory nerve defects of 3 cm or less. *Plast Reconstr Surg*, 86, 928-34.
- CHWALEK, K., SOOD, D., CANTLEY, W. L., WHITE, J. D., TANG-SCHOMER, M. & KAPLAN, D. L. 2015. Engineered 3D Silk-collagen-based Model of Polarized Neural Tissue. *Journal of Visualized Experiments : JoVE*, 52970.
- CIRILLO, V., BUSHMAN, J., GUARINO, V., KOHN, J. & AMBROSIO, L. 2018. 16 - 3D conduits for peripheral nerve regeneration. In: GUARINO, V. & AMBROSIO, L. (eds.) *Electrofluidodynamic Technologies (EFDTs) for Biomaterials and Medical Devices*. Woodhead Publishing.
- CLIPPINGER, A. J. & ALWINE, J. C. 2012. Dynein mediates the localization and activation of mTOR in normal and human cytomegalovirus-infected cells. *Genes & Development*, 26, 2015-2026.

- COHEN-CORY, S., KIDANE, A. H., SHIRKEY, N. J. & MARSHAK, S. 2010. Brain-Derived Neurotrophic Factor and the Development of Structural Neuronal Connectivity. *Developmental neurobiology*, 70, 271-288.
- CONTI, A. M., FISCHER, S. J. & WINDEBANK, A. J. 1997. Inhibition of axonal growth from sensory neurons by excess nerve growth factor. *Ann Neurol*, 42, 838-46.
- CORBIT, K. C., FOSTER, D. A. & ROSNER, M. R. 1999. Protein Kinase C δ Mediates Neurogenic but Not Mitogenic Activation of Mitogen-Activated Protein Kinase in Neuronal Cells. *Molecular and Cellular Biology*, 19, 4209-4218.
- COREY, J. M., LIN, D. Y., MYCEK, K. B., CHEN, Q., SAMUEL, S., FELDMAN, E. L. & MARTIN, D. C. 2007. Aligned electrospun nanofibers specify the direction of dorsal root ganglia neurite growth. *Journal of biomedical materials research. Part A*, 83, 636-45.
- COURTNEY, C. R. P., DEMORE, C. E. M., WU, H., GRINENKO, A., WILCOX, P. D., COCHRAN, S. & DRINKWATER, B. W. 2014. Independent trapping and manipulation of microparticles using dexterous acoustic tweezers. *Applied Physics Letters*, 104, 154103.
- COURTNEY, C. R. P., ONG, C.-K., DRINKWATER, B. W., BERNASSAU, A. L., WILCOX, P. D. & CUMMING, D. R. S. 2011. Manipulation of particles in two dimensions using phase controllable ultrasonic standing waves. *Proceedings of the Royal Society A: Mathematical, Physical and Engineering Science*.
- COVACEUSZACH, S., KONAREV, PETR V., CASSETTA, A., PAOLETTI, F., SVERGUN, DMITRI I., LAMBA, D. & CATTANEO, A. 2015. The Conundrum of the High-Affinity NGF Binding Site Formation Unveiled? *Biophysical Journal*, 108, 687-697.
- DALBY, M. J. 2005. Topographically induced direct cell mechanotransduction. *Med Eng Phys*, 27, 730-42.
- DALY, W., YAO, L., ZEUGOLIS, D., WINDEBANK, A. & PANDIT, A. 2012. A biomaterials approach to peripheral nerve regeneration: bridging the peripheral nerve gap and enhancing functional recovery. *Journal of the Royal Society Interface*, 9, 202-221.
- DAUD, M. F. B., PAWAR, K. C., CLAEYSSENS, F., RYAN, A. J. & HAYCOCK, J. W. 2012. An aligned 3D neuronal-glia co-culture model for peripheral nerve studies. *Biomaterials*, 33, 5901-5913.
- DE RUITER, G. C. W., MALESSY, M. J. A., YASZEMSKI, M. J., WINDEBANK, A. J. & SPINNER, R. J. 2009. Designing ideal conduits for peripheral nerve repair. *Neurosurgical focus*, 26, E5-E5.
- DÉJARDIN, T. P.-E. 2013. New Strategies for Nerve Regeneration. *Centre for Cell Engineering*, Doctor of Philosophy.
- DENT, E. W., GUPTON, S. L. & GERTLER, F. B. 2011. The Growth Cone Cytoskeleton in Axon Outgrowth and Guidance. *Cold Spring Harbor Perspectives in Biology*, 3, a001800.
- DEUMENS, R., BOZKURT, A., MEEK, M. F., MARCUS, M. A. E., JOOSTEN, E. A. J., WEIS, J. & BROOK, G. A. 2010. Repairing injured peripheral nerves: Bridging the gap. *Progress in Neurobiology*, 92, 245-276.
- DI SUMMA, P. G., KINGHAM, P. J., RAFFOUL, W., WIBERG, M., TERENGI, G. & KALBERMATTEN, D. F. 2010. Adipose-derived stem cells enhance peripheral nerve regeneration. *J Plast Reconstr Aesthet Surg*, 63, 1544-52.

- DITTY, B. J., OMAR, N. B. & ROZZELLE, C. J. 2015. Chapter 24 - Surgery for Peripheral Nerve Trauma A2 - Tubbs, R. Shane. *In: RIZK, E., SHOJA, M. M., LOUKAS, M., BARBARO, N. & SPINNER, R. J. (eds.) Nerves and Nerve Injuries*. San Diego: Academic Press.
- DOMENICONI, M. & FILBIN, M. T. 2005. Overcoming inhibitors in myelin to promote axonal regeneration. *Journal of the Neurological Sciences*, 233, 43-47.
- DONNELLY, C. J., FAINZILBER, M. & TWISS, J. L. 2010. Subcellular communication through RNA transport and localized protein synthesis. *Traffic (Copenhagen, Denmark)*, 11, 1498-1505.
- DORTA, M. P., DE BRITO, I. V., PEREIRA, A. C. & ALENCAR, A. M. 2018. Quantification of alignment of vascular smooth muscle cells. *Cytometry Part A*, 93, 533-539.
- DOYLE, A. D. & YAMADA, K. M. 2016. Mechanosensing via cell-matrix adhesions in 3D microenvironments. *Experimental cell research*, 343, 60-66.
- DRURY, J. L. & MOONEY, D. J. 2003. Hydrogels for tissue engineering: scaffold design variables and applications. *Biomaterials*, 24, 4337-4351.
- DU, J., CHEN, H., QING, L., YANG, X. & JIA, X. 2018. Biomimetic neural scaffolds: a crucial step towards optimal peripheral nerve regeneration. *Biomaterials science*, 6, 1299-1311.
- DUBEY, N., LETOURNEAU, P. C. & TRANQUILLO, R. T. 1999. Guided neurite elongation and schwann cell invasion into magnetically aligned collagen in simulated peripheral nerve regeneration. *Exp Neurol*, 158, 338-50.
- DYAKONOV, T., YANG, C. H., BUSH, D., GOSANGARI, S., MAJURU, S. & FATMI, A. 2012. Design and Characterization of a Silk-Fibroin-Based Drug Delivery Platform Using Naproxen as a Model Drug. *Journal of Drug Delivery*, 2012, 10.
- EBADI, M., BASHIR, R. M., HEIDRICK, M. L., HAMADA, F. M., EL REFAEY, E., HAMED, A., HELAL, G., BAXI, M. D., CERUTIS, D. R. & LASSI, N. K. 1997. NEUROTROPHINS AND THEIR RECEPTORS IN NERVE INJURY AND REPAIR. *Neurochemistry International*, 30, 347-374.
- EDMONDSON, R., BROGLIE, J. J., ADCOCK, A. F. & YANG, L. 2014. Three-Dimensional Cell Culture Systems and Their Applications in Drug Discovery and Cell-Based Biosensors. *Assay and Drug Development Technologies*, 12, 207-218.
- ELIE, A., PREZEL, E., GUÉRIN, C., DENARIER, E., RAMIREZ-RIOS, S., SERRE, L., ANDRIEUX, A., FOUREST-LIEUVIN, A., BLANCHOIN, L. & ARNAL, I. 2015. Tau co-organizes dynamic microtubule and actin networks. *Scientific Reports*, 5, 9964.
- ELTZNER, B., WOLLNIK, C., GOTTSCHLICH, C., HUCKEMANN, S. & REHFELDT, F. 2015. The Filament Sensor for Near Real-Time Detection of Cytoskeletal Fiber Structures. *PLOS ONE*, 10, e0126346.
- ENGLER, A. J., SEN, S., SWEENEY, H. L. & DISCHER, D. E. 2006. Matrix Elasticity Directs Stem Cell Lineage Specification. *Cell*, 126, 677-689.
- EPPENBERGER, H. M. & ZUPPINGER, C. 1999. In vitro reestablishment of cell-cell contacts in adult rat cardiomyocytes. Functional role of transmembrane components in the formation of new intercalated disk-like cell contacts. *Faseb J*, 13, 583-9.

- ERBA, P., MANTOVANI, C., KALBERMATTEN, D. F., PIERER, G., TERENGI, G. & KINGHAM, P. J. 2010. Regeneration potential and survival of transplanted undifferentiated adipose tissue-derived stem cells in peripheral nerve conduits. *J Plast Reconstr Aesthet Surg*, 63, 20.
- ERIKSDOTTER JONHAGEN, M., NORDBERG, A., AMBERLA, K., BACKMAN, L., EBENDAL, T., MEYERSON, B., OLSON, L., SEIGER, SHIGETA, M., THEODORSSON, E., VIITANEN, M., WINBLAD, B. & WAHLUND, L. O. 1998. Intracerebroventricular infusion of nerve growth factor in three patients with Alzheimer's disease. *Dement Geriatr Cogn Disord*, 9, 246-57.
- ERNGFCL, T. F. Invitrogen NGF beta-Cell Lysates Rat ELISA Kit Source: <https://assets.thermofisher.com/TFS-Assets/LSG/manuals/ERNGFCL .pdf> Downloaded on: 10/10/2017.
- ESPER, R. M. & LOEB, J. A. 2009. Neurotrophins Induce Neuregulin Release through Protein Kinase C δ Activation. *Journal of Biological Chemistry*, 284, 26251-26260.
- FAIRLESS, R., FRAME, M. C. & BARNETT, S. C. 2005. N-cadherin differentially determines Schwann cell and olfactory ensheathing cell adhesion and migration responses upon contact with astrocytes. *Mol Cell Neurosci*, 28, 253-63.
- FAROKHI, M., MOTTAGHITALAB, F., SHOKRGOZAR, M. A., KAPLAN, D. L., KIM, H.-W. & KUNDU, S. C. 2017. Prospects of peripheral nerve tissue engineering using nerve guide conduits based on silk fibroin protein and other biopolymers. *International Materials Reviews*, 62, 367-391.
- FARONI, A., MOBASSERI, S. A., KINGHAM, P. J. & REID, A. J. 2015. Peripheral nerve regeneration: Experimental strategies and future perspectives. *Advanced Drug Delivery Reviews*, 82-83, 160-167.
- FARONI, A., SMITH, R. J., LU, L. & REID, A. J. 2016. Human Schwann-like cells derived from adipose-derived mesenchymal stem cells rapidly de-differentiate in the absence of stimulating medium. *Eur J Neurosci*, 43, 417-30.
- FENG, S. Q., KONG, X. H., GUO, S. F., WANG, P., LI, L., ZHONG, J. H. & ZHOU, X. F. 2005. Treatment of spinal cord injury with co-grafts of genetically modified Schwann cells and fetal spinal cord cell suspension in the rat. *Neurotox Res*, 7, 169-77.
- FLOREN, M., MIGLIARESI, C. & MOTTA, A. 2016. Processing Techniques and Applications of Silk Hydrogels in Bioengineering. *Journal of Functional Biomaterials*, 7, 26.
- FORSTER, B., VAN DE VILLE, D., BERENT, J., SAGE, D. & UNSER, M. 2004. Complex wavelets for extended depth-of-field: a new method for the fusion of multichannel microscopy images. *Microsc Res Tech*, 65, 33-42.
- FRESE, L., DIJKMAN, P. E. & HOERSTRUP, S. P. 2016. Adipose Tissue-Derived Stem Cells in Regenerative Medicine. *Transfusion Medicine and Hemotherapy*, 43, 268-274.
- GALLO, G. 2006. RhoA-kinase coordinates F-actin organization and myosin II activity during semaphorin-3A-induced axon retraction. *J Cell Sci*, 119, 3413-23.
- GAO, S., ZHAO, P., LIN, C., SUN, Y., WANG, Y., ZHOU, Z., YANG, D., WANG, X., XU, H., ZHOU, F., CAO, L., ZHOU, W., NING, K., CHEN, X. & XU, J. 2014. Differentiation of human adipose-derived stem cells into neuron-like cells which are compatible with photocurable three-dimensional scaffolds. *Tissue Eng Part A*, 20, 1271-84.

- GAO, X., DAUGHERTY, R. L. & TOURTELLOTTE, W. G. 2007. Regulation of low affinity neurotrophin receptor (p75(NTR)) by early growth response (Egr) transcriptional regulators. *Mol Cell Neurosci*, 36, 501-14.
- GARCÍA, A. J. 2014. PEG-maleimide hydrogels for protein and cell delivery in regenerative medicine. *Annals of biomedical engineering*, 42, 312-322.
- GARVIN, K. A., DALECKI, D., YOUSEFHUSSIEN, M., HELGUERA, M. & HOCKING, D. C. 2013. Spatial patterning of endothelial cells and vascular network formation using ultrasound standing wave fields. *The Journal of the Acoustical Society of America*, 134, 1483-1490.
- GARY, D. S. & MATTSON, M. P. 2001. Integrin signaling via the PI3-kinase-Akt pathway increases neuronal resistance to glutamate-induced apoptosis. *J Neurochem*, 76, 1485-96.
- GAVAZZI, I., KUMAR, R. D., MCMAHON, S. B. & COHEN, J. 1999. Growth responses of different subpopulations of adult sensory neurons to neurotrophic factors in vitro. *Eur J Neurosci*, 11, 3405-14.
- GEARY, J. M., GOODBY, J. W., KMETZ, A. R. & PATEL, J. S. 1987. The mechanism of polymer alignment of liquid-crystal materials. *Journal of Applied Physics*, 62, 4100-4108.
- GEHLER, S., GALLO, G., VEIEN, E. & LETOURNEAU, P. 2004a. *p75 Neurotrophin Receptor Signaling Regulates Growth Cone Filopodial Dynamics through Modulating RhoA Activity*.
- GEHLER, S., GALLO, G., VEIEN, E. & LETOURNEAU, P. C. 2004b. p75 neurotrophin receptor signaling regulates growth cone filopodial dynamics through modulating RhoA activity. *J Neurosci*, 24, 4363-72.
- GEHLER, S., SHAW, A. E., SARMIERE, P. D., BAMBURG, J. R. & LETOURNEAU, P. C. 2004c. Brain-derived neurotrophic factor regulation of retinal growth cone filopodial dynamics is mediated through actin depolymerizing factor/cofilin. *J Neurosci*, 24, 10741-9.
- GEORGIU, M., BUNTING, S. C. J., DAVIES, H. A., LOUGHLIN, A. J., GOLDING, J. P. & PHILLIPS, J. B. 2013. Engineered neural tissue for peripheral nerve repair. *Biomaterials*, 34, 7335-7343.
- GEORGIU, M., GOLDING, J. P., LOUGHLIN, A. J., KINGHAM, P. J. & PHILLIPS, J. B. 2015. Engineered neural tissue with aligned, differentiated adipose-derived stem cells promotes peripheral nerve regeneration across a critical sized defect in rat sciatic nerve. *Biomaterials*, 37, 242-251.
- GERALDO, S. & GORDON-WEEKS, P. R. 2009. Cytoskeletal dynamics in growth-cone steering. *Journal of Cell Science*, 122, 3595-3604.
- GESELLCHEN, F., BERNASSAU, A. L., DEJARDIN, T., CUMMING, D. R. S. & RIEHLE, M. O. 2014. Cell patterning with a heptagon acoustic tweezer - application in neurite guidance. *Lab on a Chip*, 14, 2266-2275.
- GESS, B., HALFTER, H., KLEFFNER, I., MONJE, P., ATHAUDA, G., WOOD, P. M., YOUNG, P. & WANNER, I. B. 2008. Inhibition of N-cadherin and beta-catenin function reduces axon-induced Schwann cell proliferation. *J Neurosci Res*, 86, 797-812.
- GIGANTE, A., CESARI, E., BUSILACCHI, A., MANZOTTI, S., KYRIAKIDOU, K., GRECO, F., DI PRIMIO, R. & MATTIOLI-BELMONTE, M. 2009. Collagen I membranes for tendon repair: effect of collagen fiber orientation on cell behavior. *J Orthop Res*, 27, 826-32.

- GJOREVSKI, N. & LUTOLF, M. P. 2017. Synthesis and characterization of well-defined hydrogel matrices and their application to intestinal stem cell and organoid culture. *Nat Protoc*, 12, 2263-2274.
- GLASBY, M. A., GSCHMEISSNER, S. G., HITCHCOCK, R. J. & HUANG, C. L. 1986. The dependence of nerve regeneration through muscle grafts in the rat on the availability and orientation of basement membrane. *J Neurocytol*, 15, 497-510.
- GOLD, B. G. 1997a. Axonal regeneration of sensory nerves is delayed by continuous intrathecal infusion of nerve growth factor. *Neuroscience*, 76, 1153-1158.
- GOLD, B. G. 1997b. FK506 and the role of immunophilins in nerve regeneration. *Mol Neurobiol*, 15, 285-306.
- GOLDSHMIT, Y., SZTAL, T. E., JUSUF, P. R., HALL, T. E., NGUYEN-CHI, M. & CURRIE, P. D. 2012. Fgf-Dependent Glial Cell Bridges Facilitate Spinal Cord Regeneration in Zebrafish. *The Journal of Neuroscience*, 32, 7477.
- GONG, X. & MILLS, K. L. 2018. Large-scale patterning of single cells and cell clusters in hydrogels. *Scientific Reports*, 8, 3849.
- GORDON, T. 2015. Chapter 61 - The Biology, Limits, and Promotion of Peripheral Nerve Regeneration in Rats and Humans A2 - Tubbs, R. Shane. In: RIZK, E., SHOJA, M. M., LOUKAS, M., BARBARO, N. & SPINNER, R. J. (eds.) *Nerves and Nerve Injuries*. San Diego: Academic Press.
- GRAHAM, A. D., OLOF, S. N., BURKE, M. J., ARMSTRONG, J. P. K., MIKHAILOVA, E. A., NICHOLSON, J. G., BOX, S. J., SZELE, F. G., PERRIMAN, A. W. & BAYLEY, H. 2017. High-Resolution Patterned Cellular Constructs by Droplet-Based 3D Printing. *Scientific Reports* [Online], 7. Available: <http://europepmc.org/abstract/MED/28765636>.
- GRINSELL, D. & KEATING, C. P. 2014. Peripheral Nerve Reconstruction after Injury: A Review of Clinical and Experimental Therapies. *BioMed Research International*, 2014, 13.
- GRULOVA, I., SLOVINSKA, L., BLAŠKO, J., DEVAUX, S., WISZTORSKI, M., SALZET, M., FOURNIER, I., KRYUKOV, O., COHEN, S. & CIZKOVA, D. 2015. Delivery of Alginate Scaffold Releasing Two Trophic Factors for Spinal Cord Injury Repair. *Scientific Reports*, 5, 13702.
- GU, Y., JI, Y., ZHAO, Y., LIU, Y., DING, F., GU, X. & YANG, Y. 2012. The influence of substrate stiffness on the behavior and functions of Schwann cells in culture. *Biomaterials*, 33, 6672-81.
- GUO, F., MAO, Z., CHEN, Y., XIE, Z., LATA, J. P., LI, P., REN, L., LIU, J., YANG, J., DAO, M., SURESH, S. & HUANG, T. J. 2016. Three-dimensional manipulation of single cells using surface acoustic waves. *Proceedings of the National Academy of Sciences*, 113, 1522.
- HALL, A. & LALLI, G. 2010. Rho and Ras GTPases in Axon Growth, Guidance, and Branching. *Cold Spring Harbor Perspectives in Biology*, 2, a001818.
- HALL, S. 2005. The response to injury in the peripheral nervous system. *J Bone Joint Surg Br*, 87, 1309-19.
- HANANI, M. 2005. Satellite glial cells in sensory ganglia: from form to function. *Brain Research Reviews*, 48, 457-476.

- HARPER, G. P., GLANVILLE, R. W. & THOENEN, H. 1982. The purification of nerve growth factor from bovine seminal plasma. Biochemical characterization and partial amino acid sequence. *Journal of Biological Chemistry*, 257, 8541-8.
- HARRINGTON, A. W., HILLAIRE, C. S., ZWEIFEL, L. S., GLEBOVA, N. O., PHILIPPIDOU, P., HALEGOUA, S. & GINTY, D. D. 2011. Recruitment of actin modifiers to TrkA endosomes governs retrograde NGF signaling and survival. *Cell*, 146, 421-434.
- HARRINGTON, A. W., KIM, J. Y. & YOON, S. O. 2002. Activation of Rac GTPase by p75 is necessary for c-jun N-terminal kinase-mediated apoptosis. *J Neurosci*, 22, 156-66.
- HASS, R., KASPER, C., BÖHM, S. & JACOBS, R. 2011. Different populations and sources of human mesenchymal stem cells (MSC): A comparison of adult and neonatal tissue-derived MSC. *Cell Communication and Signaling : CCS*, 9, 12-12.
- HEMPSTEAD, B. L. 2002. The many faces of p75NTR. *Curr Opin Neurobiol*, 12, 260-7.
- HIGUCHI, M., ONISHI, K., MASUYAMA, N. & GOTOH, Y. 2003. The phosphatidylinositol-3 kinase (PI3K)-Akt pathway suppresses neurite branch formation in NGF-treated PC12 cells. *Genes to Cells*, 8, 657-669.
- HILL, R. E. & WILLIAMS, P. E. 2002. A quantitative analysis of perineurial cell basement membrane collagen IV, laminin and fibronectin in diabetic and non-diabetic human sural nerve. *Journal of Anatomy*, 201, 185-192.
- HIRASAWA, Y., ODA, R., NAKATANI, K., SHIKATA, Y. & MAKINO, T. 1976. *Statistical study on peripheral nerve injury*.
- HIRATA, A., MASAKI, T., MOTOYOSHI, K. & KAMAKURA, K. 2002. Intrathecal administration of nerve growth factor delays GAP 43 expression and early phase regeneration of adult rat peripheral nerve. *Brain Res*, 944, 146-56.
- HIROSE, M., KURODA, Y. & MURATA, E. 2016. NGF/TrkA Signaling as a Therapeutic Target for Pain. *Pain Pract*, 16, 175-82.
- HOFFMAN-KIM, D., MITCHEL, J. A. & BELLAMKONDA, R. V. 2010. Topography, Cell Response, and Nerve Regeneration. *Annual review of biomedical engineering*, 12, 203-231.
- HONG, K., NISHIYAMA, M., HENLEY, J., TESSIER-LAVIGNE, M. & POO, M. 2000. Calcium signalling in the guidance of nerve growth by netrin-1. *Nature*, 403, 93-8.
- HOPKINS, A. M., DE LAPORTE, L., TORTELLI, F., SPEDDEN, E., STALL, C., ATHERTON, T. J., HUBBELL, J. A. & KAPLAN, D. L. 2013. Silk Hydrogels as Soft Substrates for Neural Tissue Engineering. *Advanced Functional Materials*, 23, 5140-5149.
- HORSTKORTE, R. & FUSS, B. 2012. Chapter 9 - Cell Adhesion Molecules A2 - Brady, Scott T. In: SIEGEL, G. J., ALBERS, R. W. & PRICE, D. L. (eds.) *Basic Neurochemistry (Eighth Edition)*. New York: Academic Press.
- HORTON, A., LARAMEE, G., WYATT, S., SHIH, A., WINSLOW, J. & DAVIES, A. M. 1997. NGF binding to p75 enhances the sensitivity of sensory and sympathetic neurons to NGF at different stages of development. *Mol Cell Neurosci*, 10, 162-72.

- HOULE, J. D. & JOHNSON, J. E. 1989. Nerve growth factor (NGF)-treated nitrocellulose enhances and directs the regeneration of adult rat dorsal root axons through intraspinal neural tissue transplants. *Neuroscience Letters*, 103, 17-23.
- HUNG, R.-J. & TERMAN, J. R. 2011. Extracellular Inhibitors, Repellents, and Semaphorin/Plexin/MICAL-mediated Actin Filament Disassembly. *Cytoskeleton (Hoboken, N.J.)*, 68, 415-433.
- ISAACS, J. & BROWNE, T. 2014. Overcoming short gaps in peripheral nerve repair: conduits and human acellular nerve allograft. *Hand (New York, N.Y.)*, 9, 131-137.
- IWAN, J., N., N. L., N., N. L., MONIKA, R., ANDREAS, U., MIKAEL, W., LEIF, C. & J., K. P. 2018. Regenerative effects of human embryonic stem cell-derived neural crest cells for treatment of peripheral nerve injury. *Journal of Tissue Engineering and Regenerative Medicine*, 12, e2099-e2109.
- JANG, S. Y., SHIN, Y. K., PARK, S. Y., PARK, J. Y., RHA, S.-H., KIM, J. K., LEE, H. J. & PARK, H. T. 2015. Autophagy Is Involved in the Reduction of Myelinating Schwann Cell Cytoplasm during Myelin Maturation of the Peripheral Nerve. *PLOS ONE*, 10, e0116624.
- JAWORSKI, J. & SHENG, M. 2006. The growing role of mTOR in neuronal development and plasticity. *Mol Neurobiol*, 34, 205-19.
- JESSEN, K. R. & MIRSKY, R. 2016. The repair Schwann cell and its function in regenerating nerves. *The Journal of Physiology*, 594, 3521-3531.
- JI, W., ZHANG, Y., HU, S. & ZHANG, Y. 2013. Biocompatibility study of a silk fibroin-chitosan scaffold with adipose tissue-derived stem cells in vitro. *Experimental and Therapeutic Medicine*, 6, 513-518.
- JI, Y., LU, Y., YANG, F., SHEN, W., TANG, T. T.-T., FENG, L., DUAN, S. & LU, B. 2010. Acute and gradual increases in BDNF concentration elicit distinct signaling and functions in neurons. *Nature Neuroscience*, 13, 302.
- JULLIEN, J., GUILI, V., REICHARDT, L. F. & RUDKIN, B. B. 2002. Molecular kinetics of nerve growth factor receptor trafficking and activation. *The Journal of biological chemistry*, 277, 38700-8.
- KAMIGUCHI, H. 2007. The role of cell adhesion molecules in axon growth and guidance. *Adv Exp Med Biol*, 621, 95-103.
- KAWABUCHI, M., TAN, H. & WANG, S. 2011. Age affects reciprocal cellular interactions in neuromuscular synapses following peripheral nerve injury. *Ageing Research Reviews*, 10, 43-53.
- KELLY, C. M., ZIETLOW, R., DUNNETT, S. B. & ROSSER, A. E. 2003. The effects of various concentrations of FGF-2 on the proliferation and neuronal yield of murine embryonic neural precursor cells in vitro. *Cell Transplant*, 12, 215-23.
- KERSTEIN, P., H NICHOL IV, R. & M GOMEZ, T. 2015. *Mechanochemical regulation of growth cone motility*.
- KETSCHKE, A., JONES, S., SPILLANE, M., KOROBOVA, F., SVITKINA, T. & GALLO, G. 2015. Nerve growth factor promotes reorganization of the axonal microtubule array at sites of axon collateral branching. *Dev Neurobiol*, 75, 1441-61.
- KIM, D. H., CONNOLLY, S. E., ZHAO, S., BEUERMAN, R. W., VOORHIES, R. M. & KLINE, D. G. 1993. Comparison of macropore, semipermeable, and nonpermeable collagen conduits in nerve repair. *J Reconstr Microsurg*, 9, 415-20.

- KIM, S. A., TAI, C.-Y., MOK, L.-P., MOSSER, E. A. & SCHUMAN, E. M. 2011. Calcium-dependent dynamics of cadherin interactions at cell–cell junctions. *Proceedings of the National Academy of Sciences*, 108, 9857-9862.
- KING, R. 2013. Chapter 2 - Microscopic anatomy: normal structure. In: GÉRARD, S. & CHRISTIAN, K. (eds.) *Handbook of Clinical Neurology*. Elsevier.
- KINGHAM, P. J., KALBERMATTEN, D. F., MAHAY, D., ARMSTRONG, S. J., WIBERG, M. & TERENGI, G. 2007. Adipose-derived stem cells differentiate into a Schwann cell phenotype and promote neurite outgrowth in vitro. *Exp Neurol*, 207, 267-74.
- KIRSCH, M., TERHEGGEN, U. & HOFMANN, H.-D. 2003. Ciliary neurotrophic factor is an early lesion-induced retrograde signal for axotomized facial motoneurons. *Molecular and Cellular Neuroscience*, 24, 130-138.
- KISHORE, V., BULLOCK, W., SUN, X., VAN DYKE, W. S. & AKKUS, O. 2012. TENOGENIC DIFFERENTIATION OF HUMAN MSCs INDUCED BY THE TOPOGRAPHY OF ELECTROCHEMICALLY ALIGNED COLLAGEN THREADS. *Biomaterials*, 33, 2137-2144.
- KLEIN, M., HEMPSTEAD, B. L. & TENG, K. K. 2005. Activation of STAT5-dependent transcription by the neurotrophin receptor Trk. *J Neurobiol*, 63, 159-71.
- KLOSS, C. U., WERNER, A., KLEIN, M. A., SHEN, J., MENUZ, K., PROBST, J. C., KREUTZBERG, G. W. & RAIVICH, G. 1999. Integrin family of cell adhesion molecules in the injured brain: regulation and cellular localization in the normal and regenerating mouse facial motor nucleus. *J Comp Neurol*, 411, 162-78.
- KO, K. R. & FRAMPTON, J. P. 2016. Developments in 3D neural cell culture models: the future of neurotherapeutics testing? *Expert Review of Neurotherapeutics*, 16, 739-741.
- KOLEGA, J. 2004. Phototoxicity and photoinactivation of blebbistatin in UV and visible light. *Biochem Biophys Res Commun*, 320, 1020-5.
- KOOPMANS, G., HASSE, B. & SINIS, N. 2009. Chapter 19: The role of collagen in peripheral nerve repair. *Int Rev Neurobiol*, 87, 363-79.
- KOSER, D. E., THOMPSON, A. J., FOSTER, S. K., DWIVEDY, A., PILLAI, E. K., SHERIDAN, G. K., SVOBODA, H., VIANA, M., COSTA, L. D. F., GUCK, J., HOLT, C. E. & FRANZE, K. 2016. Mechanosensing is critical for axon growth in the developing brain. *Nature Neuroscience*, 19, 1592.
- KOVACS, M., TOTH, J., HETENYI, C., MALNASI-CSIZMADIA, A. & SELLERS, J. R. 2004. Mechanism of blebbistatin inhibition of myosin II. *The Journal of biological chemistry*, 279, 35557-63.
- KOZUKA, T., TUZIUTI, T., MITOME, H., ARAI, F. & FUKUDA, T. Three-dimensional acoustic micromanipulation using four ultrasonic transducers. MHS2000. Proceedings of 2000 International Symposium on Micromechatronics and Human Science (Cat. No.00TH8530), 22-25 Oct. 2000 2000. 201-206.
- KRAMES, E. S. 2014. The Role of the Dorsal Root Ganglion in the Development of Neuropathic Pain. *Pain Medicine*, 15, 1669-1685.
- KRASKIEWICZ, H., BREEN, B., SARGEANT, T., MCMAHON, S. & PANDIT, A. 2013. Assembly of Protein-Based Hollow Spheres Encapsulating a Therapeutic Factor. *ACS Chemical Neuroscience*, 4, 1297-1304.

- KREDI, D. 2016. Improving interfaces for nerve repair. PhD thesis, University of Glasgow. Published online: <http://theses.gla.ac.uk/7255/>.
- KUBEK, T., GHALIB, N. & DUBOVÝ, P. 2011. Endoneurial extracellular matrix influences regeneration and maturation of motor nerve axons—A model of acellular nerve graft. *Neuroscience Letters*, 496, 75-79.
- KUCENAS, S. 2015. Perineurial Glia. *Cold Spring Harbor Perspectives in Biology*, 7, a020511.
- KUNDU, J., CHUNG, Y.-I., KIM, Y. H., TAE, G. & KUNDU, S. C. 2010. Silk fibroin nanoparticles for cellular uptake and control release. *International Journal of Pharmaceutics*, 388, 242-250.
- L3224, T. F. LIVE/DEAD Viability/Cytotoxicity Kit for mammalian cells, source: <https://assets.thermofisher.com/TFS-Assets/LSG/manuals/mp03224.pdf> downloaded on 10.10.2017.
- LACKINGTON, W. A., RYAN, A. J. & O'BRIEN, F. J. 2017. Advances in Nerve Guidance Conduit-Based Therapeutics for Peripheral Nerve Repair. *ACS Biomaterials Science & Engineering*, 3, 1221-1235.
- LAMMEL, A. S., HU, X., PARK, S.-H., KAPLAN, D. L. & SCHEIBEL, T. R. 2010. Controlling silk fibroin particle features for drug delivery. *Biomaterials*, 31, 4583-4591.
- LAVDAS, A. A., FRANCESCHINI, I., DUBOIS-DALCQ, M. & MATSAS, R. 2006. Schwann cells genetically engineered to express PSA show enhanced migratory potential without impairment of their myelinating ability in vitro. *Glia*, 53, 868-878.
- LEE, S.-J., NOWICKI, M., HARRIS, B. & ZHANG, L. G. 2016. Fabrication of a Highly Aligned Neural Scaffold via a Table Top Stereolithography 3D Printing and Electrospinning. *Tissue Engineering Part A*, 23, 491-502.
- LETHBRIDGE, Z. A. D., WALTON, R. I., MARMIER, A. S. H., SMITH, C. W. & EVANS, K. E. 2010. Elastic anisotropy and extreme Poisson's ratios in single crystals. *Acta Materialia*, 58, 6444-6451.
- LEVI, A. D., BURKS, S. S., ANDERSON, K. D., DIDIDZE, M., KHAN, A. & DIETRICH, W. D. 2016. The Use of Autologous Schwann Cells to Supplement Sciatic Nerve Repair With a Large Gap: First in Human Experience. *Cell Transplant*, 25, 1395-403.
- LEWIS, E. E. L., WHEADON, H., LEWIS, N., YANG, J., MULLIN, M., HURSTHOUSE, A., STIRLING, D., DALBY, M. J. & BERRY, C. C. 2016. A Quiescent, Regeneration-Responsive Tissue Engineered Mesenchymal Stem Cell Bone Marrow Niche Model via Magnetic Levitation. *ACS Nano*, 10, 8346-8354.
- LEWIS, G. M. & KUCENAS, S. 2014. Perineurial glia are essential for motor axon regrowth following nerve injury. *J Neurosci*, 34, 12762-77.
- LI, N. & FOLCH, A. 2005. Integration of topographical and biochemical cues by axons during growth on microfabricated 3-D substrates. *Experimental cell research*, 311, 10.1016/j.yexcr.2005.10.007.
- LI, Q., CHEN, J., CHEN, Y., CONG, X. & CHEN, Z. 2016. Chronic sciatic nerve compression induces fibrosis in dorsal root ganglia. *Molecular medicine reports*, 13, 2393-2400.
- LI, Q., PING, P., JIANG, H. & LIU, K. 2006. Nerve conduit filled with GDNF gene-modified Schwann cells enhances regeneration of the peripheral nerve. *Microsurgery*, 26, 116-21.

- LIN, C. H., ESPREAFICO, E. M., MOOSEKER, M. S. & FORSCHER, P. 1996. Myosin drives retrograde F-actin flow in neuronal growth cones. *Neuron*, 16, 769-82.
- LIN, Y.-L., JEN, J.-C., HSU, S.-H. & CHIU, I.-M. 2008. Sciatic nerve repair by microgrooved nerve conduits made of chitosan-gold nanocomposites. *Surgical Neurology*, 70, Supplement 1, S9-S18.
- LINDWALL, C. & KANJE, M. 2005. Retrograde axonal transport of JNK signaling molecules influence injury induced nuclear changes in p-c-Jun and ATF3 in adult rat sensory neurons. *Molecular and Cellular Neuroscience*, 29, 269-282.
- LIU, C., LI, X., XU, F., CONG, H., LI, Z., SONG, Y. & WANG, M. 2018. Spatio-temporal release of NGF and GDNF from multi-layered nanofibrous bicomponent electrospun scaffolds. *Journal of Materials Science. Materials in Medicine*, 29, 102.
- LIU, H., ZHOU, Y., CHEN, S., BU, M., XIN, J. & LI, S. 2013a. Current sustained delivery strategies for the design of local neurotrophic factors in treatment of neurological disorders. *Asian Journal of Pharmaceutical Sciences*, 8, 269-277.
- LIU, H. M., LEI, H. Y. & KAO, K.-P. 1995. Correlation between NGF levels in wound chamber fluid and cytological localization of NGF and NGF receptor in axotomized rat sciatic nerve. *Experimental Neurology*, 132, 24-32.
- LIU, R. Y., SCHMID, R. S., SNIDER, W. D. & MANESS, P. F. 2002. NGF enhances sensory axon growth induced by laminin but not by the L1 cell adhesion molecule. *Mol Cell Neurosci*, 20, 2-12.
- LIU, W., XING, S., YUAN, B., ZHENG, W. & JIANG, X. 2013b. Change of laminin density stimulates axon branching via growth cone myosin II-mediated adhesion. *Integrative Biology*, 5, 1244-1252.
- LIU, W., ZHENG, W., YUAN, B. & JIANG, X. 2013c. A micropatterned coculture system for axon guidance reveals that Slit promotes axon fasciculation and regulates the expression of L1CAM. *Integr Biol*, 5, 617-23.
- LIU, X., ZHANG, T., HE, S., HONG, B., CHEN, Z., PENG, D., WU, Y., WEN, H., LIN, Z., FANG, Y. & JIANG, K. 2014. Elevated serum levels of FGF-2, NGF and IGF-1 in patients with manic episode of bipolar disorder. *Psychiatry Res*, 218, 54-60.
- LO, C. M., WANG, H. B., DEMBO, M. & WANG, Y. L. 2000. Cell movement is guided by the rigidity of the substrate. *Biophys J*, 79, 144-52.
- LOUDON, R. P., SILVER, L. D., YEE, H. F. & GALLO, G. 2006. RhoA-Kinase and Myosin II Are Required for the Maintenance of Growth Cone Polarity and Guidance by Nerve Growth Factor. *Journal of neurobiology*, 66, 847-867.
- LOWE, C. J., REUCROFT, I. M., GROTA, M. C. & SHREIBER, D. I. 2016. Production of Highly Aligned Collagen Scaffolds by Freeze-drying of Self-assembled, Fibrillar Collagen Gels. *ACS Biomaterials Science & Engineering*, 2, 643-651.
- LOWERY, L. A. & VACTOR, D. V. 2009. The trip of the tip: understanding the growth cone machinery. *Nature Reviews Molecular Cell Biology*, 10, 332.
- LUCA, A. C. D., RAFFOUL, W., GIACALONE, F., BERTOLINI, M. & SUMMA, P. G. D. 2015. Tissue-engineered constructs for peripheral nerve repair: current research concepts and future perspectives. *Plastic and Aesthetic Research; Vol 2, No 4 (2015)*.

- MA, T. C. & WILLIS, D. E. 2015. What makes a RAG regeneration associated? *Frontiers in Molecular Neuroscience*, 8, 43.
- MACKINNON, S. E., DELLON, A. L., HUDSON, A. R. & HUNTER, D. A. 1984. Chronic nerve compression--an experimental model in the rat. *Ann Plast Surg*, 13, 112-20.
- MADDURI, S. & GANDER, B. 2012. Growth factor delivery systems and repair strategies for damaged peripheral nerves. *Journal of Controlled Release*, 161, 274-282.
- MANDAL, B. B., GRINBERG, A., SEOK GIL, E., PANILAITIS, B. & KAPLAN, D. L. 2012. High-strength silk protein scaffolds for bone repair. *Proceedings of the National Academy of Sciences of the United States of America*, 109, 7699-7704.
- MARSICK, B. M., FLYNN, K. C., SANTIAGO-MEDINA, M., BAMBURG, J. R. & LETOURNEAU, P. C. 2010. Activation of ADF/cofilin mediates attractive growth cone turning toward nerve growth factor and netrin-1. *Developmental neurobiology*, 70, 565-588.
- MARTINS, R. P., FINAN, J. D., GUILAK, F. & LEE, D. A. 2012. MECHANICAL REGULATION OF NUCLEAR STRUCTURE AND FUNCTION. *Annual review of biomedical engineering*, 14, 431-455.
- MATHESON, C. R., CARNAHAN, J., URICH, J. L., BOCANGEL, D., ZHANG, T. J. & YAN, Q. 1997. Glial cell line-derived neurotrophic factor (GDNF) is a neurotrophic factor for sensory neurons: comparison with the effects of the neurotrophins. *J Neurobiol*, 32, 22-32.
- MATSUMOTO, T., OKAZAKI, M., INOUE, M., YAMAGUCHI, S., KUSUNOSE, T., TOYONAGA, T., HAMADA, Y. & TAKAHASHI, J. 2004. Hydroxyapatite particles as a controlled release carrier of protein. *Biomaterials*, 25, 3807-3812.
- MATTHIAS, L. & MARION, M. 2018. Improvement of the drawing ratio of the anisotropic material behaviour under near plane strain conditions for DP600 characterized in elliptic hydraulic bulge test. *Journal of Physics: Conference Series*, 1063, 012161.
- MCCLOY, R. A., ROGERS, S., CALDON, C. E., LORCA, T., CASTRO, A. & BURGESS, A. 2014. Partial inhibition of Cdk1 in G2 phase overrides the SAC and decouples mitotic events. *Cell Cycle*, 13, 1400-1412.
- MCCORMICK, A. M., WIJEKOON, A. & LEIPZIG, N. D. 2013. Specific Immobilization of Biotinylated Fusion Proteins NGF and Sema3A Utilizing a Photo-Cross-Linkable Diazirine Compound for Controlling Neurite Extension. *Bioconjugate Chemistry*, 24, 1515-1526.
- MEDEIROS, N. A., BURNETTE, D. T. & FORSCHER, P. 2006. Myosin II functions in actin-bundle turnover in neuronal growth cones. *Nat Cell Biol*, 8, 215-26.
- MENORCA, R. M. G., FUSSELL, T. S. & ELFAR, J. C. 2013. Peripheral Nerve Trauma: Mechanisms of Injury and Recovery. *Hand Clinics*, 29, 317-330.
- MICHAELVSKI, I., MEDZIHRADESKY, K. F., LYNN, A., BURLINGAME, A. L. & FAINZILBER, M. 2010. Axonal Transport Proteomics Reveals Mobilization of Translation Machinery to the Lesion Site in Injured Sciatic Nerve. *Molecular & Cellular Proteomics*, 9, 976-987.
- MILLER, D., SMITH, N., BAILEY, M., CZARNOGA, G., HYNYNEN, K., MAKIN, I. & AMERICAN INSTITUTE OF ULTRASOUND IN MEDICINE BIOEFFECTS, C. 2012. Overview of Therapeutic Ultrasound Applications and Safety Considerations. *Journal of ultrasound in medicine : official journal of the American Institute of Ultrasound in Medicine*, 31, 623-634.

- MITRE, M., MARIGA, A. & CHAO, M. V. 2017. Neurotrophin signalling: novel insights into mechanisms and pathophysiology. *Clinical science (London, England : 1979)*, 131, 13-23.
- MOHAMMADI, R., AZIZI, S. & AMINI, K. 2013. Effects of undifferentiated cultured omental adipose-derived stem cells on peripheral nerve regeneration. *J Surg Res*, 180, 27.
- MOHIUDDIN, L., FERNYHOUGH, P. & TOMLINSON, D. R. 1996. Acidic fibroblast growth factor enhances neurite outgrowth and stimulates expression of GAP-43 and T α 1 α -tubulin in cultured neurones from adult rat dorsal root ganglia. *Neuroscience Letters*, 215, 111-114.
- MOHTARAM, N. K., MONTGOMERY, A. & WILLERTH, S. M. 2013. Biomaterial-based drug delivery systems for the controlled release of neurotrophic factors. *Biomed Mater*, 8, 1748-6041.
- MONK, K. R., WU, J., WILLIAMS, J. P., FINNEY, B. A., FITZGERALD, M. E., FILIPPI, M.-D. & RATNER, N. 2007. Mast cells can contribute to axon-glia dissociation and fibrosis in peripheral nerve. *Neuron glia biology*, 3, 233-244.
- MOORE, A. M., MACEWAN, M., SANTOSA, K. B., CHENARD, K. E., RAY, W. Z., HUNTER, D. A., MACKINNON, S. E. & JOHNSON, P. J. 2011. Acellular nerve allografts in peripheral nerve regeneration: a comparative study. *Muscle Nerve*, 44, 221-34.
- MOSAHEBI, A., WIBERG, M. & TERENCEHI, G. 2003. Addition of Fibronectin to Alginate Matrix Improves Peripheral Nerve Regeneration in Tissue-Engineered Conduits. *Tissue Engineering*, 9, 209-218.
- MUHAMMAD, R., PEH, G. S. L., ADNAN, K., LAW, J. B. K., MEHTA, J. S. & YIM, E. K. F. 2015. Micro- and nano-topography to enhance proliferation and sustain functional markers of donor-derived primary human corneal endothelial cells. *Acta Biomaterialia*, 19, 138-148.
- MUHEREMU, A. & AO, Q. 2015. Past, Present, and Future of Nerve Conduits in the Treatment of Peripheral Nerve Injury. *BioMed Research International*, 2015, 6.
- MUKAI, J., SUVANT, P. & SATO, T.-A. 2003. Nerve Growth Factor-Dependent Regulation of NADE-Induced Apoptosis. *Vitamins & Hormones*. Academic Press.
- MUKHEY, D., PHILLIPS, J. B., DANIELS, J. T. & KURESHI, A. K. 2018. Controlling human corneal stromal stem cell contraction to mediate rapid cell and matrix organization of real architecture for 3-dimensional tissue equivalents. *Acta Biomaterialia*, 67, 229-237.
- MYATT, D. R., HADLINGTON, T., ASCOLI, G. A. & NASUTO, S. J. 2012. Neuromantic – from Semi-Manual to Semi-Automatic Reconstruction of Neuron Morphology. *Frontiers in Neuroinformatics*, 6, 4.
- NAIK, N., CAVES, J., CHAIKOF, E. & ALLEN, M. G. 2014. Generation of Spatially Aligned Collagen Fiber Networks through Microtransfer Molding. *Advanced healthcare materials*, 3, 367-374.
- NAVARRO, X., VIVÓ, M. & VALERO-CABRÉ, A. 2007. Neural plasticity after peripheral nerve injury and regeneration. *Progress in Neurobiology*, 82, 163-201.
- NECTOW, A. R., MARRA, K. G. & KAPLAN, D. L. 2012. Biomaterials for the Development of Peripheral Nerve Guidance Conduits. *Tissue Engineering. Part B, Reviews*, 18, 40-50.
- NGUYEN, L. H., GAO, M., LIN, J., WU, W., WANG, J. & CHEW, S. Y. 2017. Three-dimensional aligned nanofibers-hydrogel scaffold for controlled non-viral drug/gene delivery to direct axon regeneration in spinal cord injury treatment. *Scientific Reports*, 7, 42212.

- NIINEMETS, Ü., PORTSMUTH, A. & TOBIAS, M. 2006. Leaf shape and venation pattern alter the support investments within leaf lamina in temperate species: a neglected source of leaf physiological differentiation? *Functional Ecology*, 21, 28-40.
- NIKKHAH, M., EDALAT, F., MANOUCHERI, S. & KHADEMHOSEINI, A. 2012. Engineering microscale topographies to control the cell–substrate interface. *Biomaterials*, 33, 5230-5246.
- NUMATA, K. & KAPLAN, D. L. 2010. Silk-based delivery systems of bioactive molecules. *Advanced Drug Delivery Reviews*, 62, 1497-1508.
- NUSSER, N., GOSMANOVA, E., ZHENG, Y. & TIGYI, G. 2002. Nerve Growth Factor Signals through TrkA, Phosphatidylinositol 3-Kinase, and Rac1 to Inactivate RhoA during the Initiation of Neuronal Differentiation of PC12 Cells. *Journal of Biological Chemistry*, 277, 35840-35846.
- O’ROURKE, C., DAY, A. G. E., MURRAY-DUNNING, C., THANABALASUNDARAM, L., COWAN, J., STEVANATO, L., GRACE, N., CAMERON, G., DRAKE, R. A. L., SINDEN, J. & PHILLIPS, J. B. 2018. An allogeneic ‘off the shelf’ therapeutic strategy for peripheral nerve tissue engineering using clinical grade human neural stem cells. *Scientific Reports*, 8, 2951.
- O’ROURKE, C., DRAKE, R. A. L., CAMERON, G. W. W., JANE LOUGHLIN, A. & PHILLIPS, J. B. 2015. Optimising contraction and alignment of cellular collagen hydrogels to achieve reliable and consistent engineered anisotropic tissue. *Journal of Biomaterials Applications*, 30, 599-607.
- OAKLEY, R. A. & KARPINSKI, B. A. 2002. Target-Independent Specification of Proprioceptive Sensory Neurons. *Developmental Biology*, 249, 255-269.
- ORLOVA, I., SILVER, L. & GALLO, G. 2007. Regulation of actomyosin contractility by PI3K in sensory axons. *Dev Neurobiol*, 67, 1843-51.
- PAKULSKA, M. M., ELLIOTT DONAGHUE, I., OBERMEYER, J. M., TULADHAR, A., MCLAUGHLIN, C. K., SHENDRUK, T. N. & SHOICHET, M. S. 2016. Encapsulation-free controlled release: Electrostatic adsorption eliminates the need for protein encapsulation in PLGA nanoparticles. *Science Advances*, 2.
- PELTONEN, S., ALANNE, M. & PELTONEN, J. 2013. Barriers of the peripheral nerve. *Tissue Barriers*, 1, e24956.
- PENAZZI, L., LORENGEL, J., SUNDERMANN, F., GOLOVYASHKINA, N., MARRE, S., MATHIS, C. M. B., LEWEJOHANN, L., BRANDT, R. & BAKOTA, L. 2017. DMSO modulates CNS function in a preclinical Alzheimer's disease model. *Neuropharmacology*, 113, 434-444.
- PERLSON, E., HANZ, S., BEN-YAAKOV, K., SEGAL-RUDER, Y., SEGER, R. & FAINZILBER, M. 2005. Vimentin-dependent spatial translocation of an activated MAP kinase in injured nerve. *Neuron*, 45, 715-26.
- PETCU, E. B., MIDHA, R., MCCOLL, E., POPA-WAGNER, A., CHIRILA, T. V. & DALTON, P. D. 2018a. 3D printing strategies for peripheral nerve regeneration. *Biofabrication*, 10, 1758-5090.
- PETCU, E. B., MIDHA, R., MCCOLL, E., POPA-WAGNER, A., CHIRILA, T. V. & DALTON, P. D. 2018b. 3D printing strategies for peripheral nerve regeneration. *Biofabrication*, 10, 032001.
- PEZET, S. & MCMAHON, S. B. 2006. Neurotrophins: mediators and modulators of pain. *Annu Rev Neurosci*, 29, 507-38.

- PFISTER, L. A., PAPALOIZOS, M., MERKLE, H. P. & GANDER, B. 2007. Nerve conduits and growth factor delivery in peripheral nerve repair. *J Peripher Nerv Syst*, 12, 65-82.
- PIANTINO, J., BURDICK, J. A., GOLDBERG, D., LANGER, R. & BENOWITZ, L. I. 2006. An injectable, biodegradable hydrogel for trophic factor delivery enhances axonal rewiring and improves performance after spinal cord injury. *Experimental Neurology*, 201, 359-367.
- POLLERBERG, G. E., THELEN, K., THEISS, M. O. & HOCHLEHNERT, B. C. 2013. The role of cell adhesion molecules for navigating axons: Density matters. *Mechanisms of Development*, 130, 359-372.
- PREVITALI, S. C., FELTRI, M. L., ARCHELOS, J. J., QUATTRINI, A., WRABETZ, L. & HARTUNG, H.-P. 2001. Role of integrins in the peripheral nervous system. *Progress in Neurobiology*, 64, 35-49.
- PROKOP, A. 2013. The intricate relationship between microtubules and their associated motor proteins during axon growth and maintenance. *Neural Development*, 8, 17-17.
- PULJAK, L., KOJUNDZIC, S. L., HOGAN, Q. H. & SAPUNAR, D. 2009. Lidocaine Injection into the Rat Dorsal Root Ganglion Causes Neuroinflammation. *Anesthesia & Analgesia*, 108, 1021-1026.
- QI, L., LI, N., HUANG, R., SONG, Q., WANG, L., ZHANG, Q., SU, R., KONG, T., TANG, M. & CHENG, G. 2013. The Effects of Topographical Patterns and Sizes on Neural Stem Cell Behavior. *PLOS ONE*, 8, e59022.
- RABE, M., VERDES, D. & SEEGER, S. 2011. Understanding protein adsorption phenomena at solid surfaces. *Advances in Colloid and Interface Science*, 162, 87-106.
- RAIVICH, G. & MAKWANA, M. 2007. The making of successful axonal regeneration: Genes, molecules and signal transduction pathways. *Brain Research Reviews*, 53, 287-311.
- RAMBURRUN, P., KUMAR, P., CHOONARA, Y. E., BIJUKUMAR, D., DU TOIT, L. C. & PILLAY, V. 2014. A Review of Bioactive Release from Nerve Conduits as a Neurotherapeutic Strategy for Neuronal Growth in Peripheral Nerve Injury. *BioMed Research International*, 2014, 132350.
- REICHARDT, L. F. 2006. Neurotrophin-regulated signalling pathways. *Philosophical Transactions of the Royal Society B: Biological Sciences*, 361, 1545-1564.
- REN, L., CHEN, Y., LI, P., MAO, Z., HUANG, P.-H., RUFO, J., GUO, F., WANG, L., MCCOY, J. P., LEVINE, S. J. & HUANG, T. J. 2015. A high-throughput standing surface acoustic wave (SSAW)-based cell sorter. *Lab on a Chip*, 15, 3870-3879.
- REUSS, B. & VON BOHLEN UND HALBACH, O. 2003. Fibroblast growth factors and their receptors in the central nervous system. *Cell and Tissue Research*, 313, 139-157.
- REYNOLDS, M. L. & WOOLF, C. J. 1993. Reciprocal Schwann cell-axon interactions. *Curr Opin Neurobiol*, 3, 683-93.
- RISHAL, I., GOLANI, O., RAJMAN, M., COSTA, B., BEN-YAAKOV, K., SCHOENMANN, Z., YARON, A., BASRI, R., FAINZILBER, M. & GALUN, M. 2013. WIS-NeuroMath enables versatile high throughput analyses of neuronal processes. *Dev Neurobiol*, 73, 247-56.
- ROCKWOOD, D. N., PREDI, R. C., YÜCEL, T., WANG, X., LOVETT, M. L. & KAPLAN, D. L. 2011. Materials fabrication from Bombyx mori silk fibroin. *Nature Protocols*, 6, 1612.

- RODGER, J., GOTO, H., CUI, Q., CHEN, P. B. & HARVEY, A. R. 2005. cAMP regulates axon outgrowth and guidance during optic nerve regeneration in goldfish. *Mol Cell Neurosci*, 30, 452-64.
- RODRIGUES, M. C. O., RODRIGUES, A. A., GLOVER, L. E., VOLTARELLI, J. & BORLONGAN, C. V. 2012. Peripheral Nerve Repair with Cultured Schwann Cells: Getting Closer to the Clinics. *The Scientific World Journal*, 2012, 10.
- ROSOFF, W. J., URBACH, J. S., ESRICK, M. A., MCALLISTER, R. G., RICHARDS, L. J. & GOODHILL, G. J. 2004. A new chemotaxis assay shows the extreme sensitivity of axons to molecular gradients. *Nature Neuroscience*, 7, 678.
- ROUT, U. K. 2013. Roles of Integrins and Intracellular Molecules in the Migration and Neuritogenesis of Fetal Cortical Neurons: MEK Regulates Only the Neuritogenesis. *Neuroscience Journal*, 2013, 15.
- ROUX, P. P. & BARKER, P. A. 2002. Neurotrophin signaling through the p75 neurotrophin receptor. *Prog Neurobiol*, 67, 203-33.
- RUTISHAUSER, U. 1992. NCAM and its polysialic acid moiety: a mechanism for pull/push regulation of cell interactions during development? *Dev Suppl*, 99-104.
- RUTISHAUSER, U. & EDELMAN, G. M. 1980. Effects of fasciculation on the outgrowth of neurites from spinal ganglia in culture. *J Cell Biol*, 87, 370-8.
- SANTOSA, K. B., JESURAJ, N. J., VIADER, A., MACEWAN, M., NEWTON, P., HUNTER, D. A., MACKINNON, S. E. & JOHNSON, P. J. 2013. Nerve allografts supplemented with schwann cells overexpressing glial-cell-line-derived neurotrophic factor. *Muscle Nerve*, 47, 213-23.
- SAYIN, E., BARAN, E. T. & HASIRCI, V. 2015. Osteogenic differentiation of adipose derived stem cells on high and low aspect ratio micropatterns. *Journal of Biomaterials Science, Polymer Edition*, 26, 1402-1424.
- SCHINDELIN, J., ARGANDA-CARRERAS, I., FRISE, E., KAYNIG, V., LONGAIR, M., PIETZSCH, T., PREIBISCH, S., RUEDEN, C., SAALFELD, S., SCHMID, B., TINEVEZ, J.-Y., WHITE, D. J., HARTENSTEIN, V., ELICEIRI, K., TOMANCAK, P. & CARDONA, A. 2012. Fiji: an open-source platform for biological-image analysis. *Nat Meth*, 9, 676-682.
- SCHMIDT, H. & RATHJEN, F. G. 2010. Signalling mechanisms regulating axonal branching in vivo. *BioEssays*, 32, 977-985.
- SCHMIEG, N., MENENDEZ, G., SCHIAVO, G. & TERENCEIO, M. 2014. Signalling endosomes in axonal transport: Travel updates on the molecular highway. *Seminars in Cell & Developmental Biology*, 27, 32-43.
- SEIB, F. P. & KAPLAN, D. L. 2012. Doxorubicin-loaded silk films: Drug-silk interactions and in vivo performance in human orthotopic breast cancer. *Biomaterials*, 33, 8442-8450.
- SHIN, E.-Y., LEE, C.-S., YUN, C.-Y., WON, S.-Y., KIM, H.-K., LEE, Y. H., KWAK, S.-J. & KIM, E.-G. 2014. Non-Muscle Myosin II Regulates Neuronal Actin Dynamics by Interacting with Guanine Nucleotide Exchange Factors. *PLOS ONE*, 9, e95212.
- SHOULDERS, M. D. & RAINES, R. T. 2009. COLLAGEN STRUCTURE AND STABILITY. *Annual review of biochemistry*, 78, 929-958.

- SONG, H. J. & POO, M. M. 1999. Signal transduction underlying growth cone guidance by diffusible factors. *Curr Opin Neurobiol*, 9, 355-63.
- SOWA, Y., KISHIDA, T., IMURA, T., NUMAJIRI, T., NISHINO, K., TABATA, Y. & MAZDA, O. 2016. Adipose-Derived Stem Cells Promote Peripheral Nerve Regeneration In Vivo without Differentiation into Schwann-Like Lineage. *Plast Reconstr Surg*, 137, 36.
- SPIVEY, E. C., KHAING, Z. Z., SHEAR, J. B. & SCHMIDT, C. E. 2012. The fundamental role of subcellular topography in peripheral nerve repair therapies. *Biomaterials*, 33, 4264-4276.
- STOFFEL, W. & BOSIO, A. 1997. Myelin glycolipids and their functions. *Current Opinion in Neurobiology*, 7, 654-661.
- STRAUCH, B., RODRIGUEZ, D. M., DIAZ, J., YU, H. L., KAPLAN, G. & WEINSTEIN, D. E. 2001. Autologous Schwann cells drive regeneration through a 6-cm autogenous venous nerve conduit. *J Reconstr Microsurg*, 17, 589-95.
- SULAIMAN, W. & GORDON, T. 2013. Neurobiology of Peripheral Nerve Injury, Regeneration, and Functional Recovery: From Bench Top Research to Bedside Application. *The Ochsner Journal*, 13, 100-108.
- SUNDARARAGHAVAN, H. G., MONTEIRO, G. A., FIRESTEIN, B. L. & SHREIBER, D. I. 2009. Neurite growth in 3D collagen gels with gradients of mechanical properties. *Biotechnol Bioeng*, 102, 632-43.
- SYOJIRO YAMAHIRA, SHIN, ICHI H., MAMORU KUWABARA & SHIGEO ASAI 2000. Orientation of Fibers in Liquid by Ultrasonic Standing Waves. *Japanese Journal of Applied Physics*, 39, 3683.
- TERZIS, J. K. & KOSTOPOULOS, V. K. 2010. Vascularized Nerve Grafts and Vascularized Fascia for Upper Extremity Nerve Reconstruction. *Hand (New York, N.Y.)*, 5, 19-30.
- THOMSON, S. 2018. *PhD Thesis, Translational development of a three-dimensional bioactive conduit for peripheral nerve repair, through the application of topographical cues & stem cell support. Not yet publicly available.*
- THOMSON, S. E., CHARALAMBOUS, C., SMITH, C.-A., TSIMBOURI, P. M., DÉJARDIN, T., KINGHAM, P. J., HART, A. M. & RIEHLE, M. O. 2017. Microtopographical cues promote peripheral nerve regeneration via transient mTORC2 activation. *Acta Biomaterialia*, 60, 220-231.
- THORNTON, M. R., SHAWCROSS, S. G., MANTOVANI, C., KINGHAM, P. J., BIRCHALL, M. A. & TERENCE, G. 2008. Neurotrophins 3 and 4 differentially regulate NCAM, L1 and N-cadherin expression during peripheral nerve regeneration. *Biotechnol Appl Biochem*, 49, 165-74.
- TOFARIS, G. K., PATTERSON, P. H., JESSEN, K. R. & MIRSKY, R. 2002. Denervated Schwann cells attract macrophages by secretion of leukemia inhibitory factor (LIF) and monocyte chemoattractant protein-1 in a process regulated by interleukin-6 and LIF. *J Neurosci*, 22, 6696-703.
- TOGO, T. & STEINHARDT, R. A. 2004. Nonmuscle Myosin IIA and IIB Have Distinct Functions in the Exocytosis-dependent Process of Cell Membrane Repair. *Molecular Biology of the Cell*, 15, 688-695.
- TONI, T., DUA, P. & VAN DER GRAAF, P. H. 2014. Systems Pharmacology of the NGF Signaling Through p75 and TrkA Receptors. *CPT: Pharmacometrics & Systems Pharmacology*, 3, e150.

- TORBET, J. & RONZIÈRE, M. C. 1984. Magnetic alignment of collagen during self-assembly. *Biochemical Journal*, 219, 1057-1059.
- TOS, P., RONCHI, G., GEUNA, S. & BATTISTON, B. 2013. Chapter Eight - Future Perspectives in Nerve Repair and Regeneration. In: STEFANO GEUNA, I. P. P. T. & BRUNO, B. (eds.) *International Review of Neurobiology*. Academic Press.
- TRUJILLO, F. J., JULIANO, P., BARBOSA-CÁNOVAS, G. & KNOERZER, K. 2014. Separation of suspensions and emulsions via ultrasonic standing waves – A review. *Ultrasonics Sonochemistry*, 21, 2151-2164.
- TSE, K. H., NOVIKOV, L. N., WIBERG, M. & KINGHAM, P. J. 2015. Intrinsic mechanisms underlying the neurotrophic activity of adipose derived stem cells. *Exp Cell Res*, 331, 142-51.
- TUCKER, B. A., RAHIMTULA, M. & MEAROW, K. M. 2008. Src and FAK are key early signalling intermediates required for neurite growth in NGF-responsive adult DRG neurons. *Cellular Signalling*, 20, 241-257.
- TUNG, T. H. 2015. Clinical strategies to enhance nerve regeneration. *Neural Regeneration Research*, 10, 22-24.
- TURNER, S. G., AHMED, M., CHANDRASEKAR, I., WYSOLMERSKI, R. B., GOECKELER, Z. M., RIOUX, R. M., WHITESIDES, G. M. & BRIDGMAN, P. C. 2016. Nerve growth factor stimulates axon outgrowth through negative regulation of growth cone actomyosin restraint of microtubule advance. *Molecular Biology of the Cell*, 27, 500-517.
- UEBERSAX, L., MATTOTTI, M., PAPALOIZOS, M., MERKLE, H. P., GANDER, B. & MEINEL, L. 2007. Silk fibroin matrices for the controlled release of nerve growth factor (NGF). *Biomaterials*, 28, 4449-60.
- URBANČIČ, V., BUTLER, R., RICHIER, B., PETER, M., MASON, J., LIVESSEY, F. J., HOLT, C. E. & GALLOP, J. L. 2017. Filopodyan: An open-source pipeline for the analysis of filopodia. *The Journal of Cell Biology*.
- VALDEZ, G., PHILIPPIDOU, P., ROSENBAUM, J., AKMENTIN, W., SHAO, Y. & HALEGOUA, S. 2007. Trk-signaling endosomes are generated by Rac-dependent macroendocytosis. *Proc Natl Acad Sci U S A*, 104, 12270-5.
- VALENTE, P., LIGNANI, G., MEDRIHAN, L., BOSCO, F., CONTESTABILE, A., LIPPIELLO, P., FERREA, E., SCHACHNER, M., BENFENATI, F., GIOVEDÌ, S. & BALDELLI, P. 2016. Cell adhesion molecule L1 contributes to neuronal excitability regulating the function of voltage-gated Na⁺ channels. *Journal of Cell Science*, 129, 1878.
- VASSALLI, M., BASSO, M. & DIFATO, F. 2013. Measurement of Tension Release During Laser Induced Axon Lesion to Evaluate Axonal Adhesion to the Substrate at Piconewton and Millisecond Resolution. *Journal of Visualized Experiments : JoVE*, 50477.
- VERDU, E., LABRADOR, R. O., RODRIGUEZ, F. J., CEBALLOS, D., FORES, J. & NAVARRO, X. 2002. Alignment of collagen and laminin-containing gels improve nerve regeneration within silicone tubes. *Restor Neurol Neurosci*, 20, 169-79.
- VERDÚ, E. & NAVARRO, X. 1998. The Role of Schwann Cell in Nerve Regeneration. In: CASTELLANO, B., GONZÁLEZ, B. & NIETO-SAMPEDRO, M. (eds.) *Understanding Glial Cells*. Boston, MA: Springer US.

- VIJAYAVENKATARAMAN, S., THAHARAH, S., ZHANG, S., LU, W. F. & FUH, J. Y. H. 3D-Printed PCL/rGO Conductive Scaffolds for Peripheral Nerve Injury Repair. *Artificial Organs*, 0.
- VÖGELIN, E., BAKER, J. M., GATES, J., DIXIT, V., CONSTANTINESCU, M. A. & JONES, N. F. 2006. Effects of local continuous release of brain derived neurotrophic factor (BDNF) on peripheral nerve regeneration in a rat model. *Experimental Neurology*, 199, 348-353.
- WALMOD, P. S., KOLKOVA, K., BEREZIN, V. & BOCK, E. 2004. Zippers make signals: NCAM-mediated molecular interactions and signal transduction. *Neurochem Res*, 29, 2015-35.
- WANG, H., WANG, R., THRIMAWITHANA, T., LITTLE, P. J., XU, J., FENG, Z.-P. & ZHENG, W. 2014. The Nerve Growth Factor Signaling and Its Potential as Therapeutic Target for Glaucoma. *BioMed Research International*, 2014, 759473.
- WANG, Z., LIU, Y., TAKAHASHI, M., VAN HOOK, K., KAMPA-SCHITTENHELM, K. M., SHEPPARD, B. C., SEARS, R. C., STORK, P. J. & LOPEZ, C. D. 2013. N terminus of ASPP2 binds to Ras and enhances Ras/Raf/MEK/ERK activation to promote oncogene-induced senescence. *Proc Natl Acad Sci U S A*, 110, 312-7.
- WANNER, I. B. & WOOD, P. M. 2002. N-cadherin mediates axon-aligned process growth and cell-cell interaction in rat Schwann cells. *J Neurosci*, 22, 4066-79.
- WEISS, L. M., PICKER, L. J., COPENHAVER, C. M., WARNKE, R. A. & SKLAR, J. 1988. Large-cell hematolymphoid neoplasms of uncertain lineage. *Hum Pathol*, 19, 967-73.
- WEISS, P. 1934. In vitro experiments on the factors determining the course of the outgrowing nerve fiber. . *J Exp Zool*, 68, 393-448.
- WEISSMILLER, A. M. & WU, C. 2012. Current advances in using neurotrophic factors to treat neurodegenerative disorders. *Translational Neurodegeneration*, 1, 14.
- WENK, E., MERKLE, H. P. & MEINEL, L. 2011. Silk fibroin as a vehicle for drug delivery applications. *Journal of Controlled Release*, 150, 128-141.
- WESSBERG, G. A., WOLFORD, L. M. & EPKER, B. N. 1982. Experiences with microsurgical reconstruction of the inferior alveolar nerve. *J Oral Maxillofac Surg*, 40, 651-5.
- WHITWORTH, I. H., BROWN, R. A., DORÉ, C. J., ANAND, P., GREEN, C. J. & TERENCE, G. 1996. Nerve growth factor enhances nerve regeneration through fibronectin grafts. *The Journal of Hand Surgery: British & European Volume*, 21, 514-522.
- WILLITS, R. K. & SKORNIA, S. L. 2004. Effect of collagen gel stiffness on neurite extension. *Journal of Biomaterials Science, Polymer Edition*, 15, 1521-1531.
- WITT, K. A. & DAVIS, T. P. 2006. CNS drug delivery: Opioid peptides and the blood-brain barrier. *The AAPS Journal*, 8, E76-E88.
- WOLFORD, L. M. & STEVAO, E. L. L. 2003. Considerations in nerve repair. *Proceedings (Baylor University Medical Center)*, 16, 152-156.
- WOO, S.-H., LUMPKIN, E. A. & PATAPOUTIAN, A. 2015. Merkel cells and neurons keep in touch. *Trends in cell biology*, 25, 74-81.

- WROBEL, M. R. & SUNDARARAGHAVAN, H. G. 2014. Directed migration in neural tissue engineering. *Tissue Eng Part B Rev*, 20, 93-105.
- WU, C. & MOBLEY, W. C. 2009. Retrograde Neurotrophic Signaling. In: SQUIRE, L. R. (ed.) *Encyclopedia of Neuroscience*. Oxford: Academic Press.
- WYLIE, S. R. & CHANTLER, P. D. 2001. Separate but linked functions of conventional myosins modulate adhesion and neurite outgrowth. *Nat Cell Biol*, 3, 88-92.
- XIE, J., LIU, W., MACEWAN, M. R., BRIDGMAN, P. C. & XIA, Y. 2014. Neurite Outgrowth on Electrospun Nanofibers with Uniaxial Alignment: The Effects of Fiber Density, Surface Coating, and Supporting Substrate. *ACS Nano*, 8, 1878-1885.
- XIE, S., LU, F., HAN, J., TAO, K., WANG, H., SIMENTAL, A., HU, D. & YANG, H. 2017. Efficient generation of functional Schwann cells from adipose-derived stem cells in defined conditions. *Cell Cycle*, 16, 841-851.
- XU, Y., ZHANG, Z., CHEN, X., LI, R., LI, D. & FENG, S. 2016. A Silk Fibroin/Collagen Nerve Scaffold Seeded with a Co-Culture of Schwann Cells and Adipose-Derived Stem Cells for Sciatic Nerve Regeneration. *PLOS ONE*, 11, e0147184.
- XUE, C., ZHU, H., TAN, D., REN, H., GU, X., ZHAO, Y., ZHANG, P., SUN, Z., YANG, Y., GU, J. & GU, Y. 2017. Electrospun silk fibroin-based neural scaffold for bridging a long sciatic nerve gap in dogs. *J Tissue Eng Regen Med*, 9.
- YAN, M., LI, B., ZHAO, X. & QIN, S. 2012. Effect of concentration, pH and ionic strength on the kinetic self-assembly of acid-soluble collagen from walleye pollock (*Theragra chalcogramma*) skin. *Food Hydrocolloids*, 29, 199-204.
- YANG, Q., TENG, B.-H., WANG, L.-N., LI, K., XU, C., MA, X.-L., ZHANG, Y., KONG, D.-L., WANG, L.-Y. & ZHAO, Y.-H. 2017. Silk fibroin/cartilage extracellular matrix scaffolds with sequential delivery of TGF- β 3 for chondrogenic differentiation of adipose-derived stem cells. *International Journal of Nanomedicine*, 12, 6721-6733.
- YANO, H. & CHAO, M. V. 2000. Neurotrophin receptor structure and interactions. In: UGO GULINI, M. G. W. Q. & GABRIELLA, M. (eds.) *Pharmacochimistry Library*. Elsevier.
- YASUI, H., KATOH, H., YAMAGUCHI, Y., AOKI, J., FUJITA, H., MORI, K. & NEGISHI, M. 2001. Differential responses to nerve growth factor and epidermal growth factor in neurite outgrowth of PC12 cells are determined by Rac1 activation systems. *The Journal of biological chemistry*, 276, 15298-305.
- YEO, I.-S., OH, J.-E., JEONG, L., LEE, T. S., LEE, S. J., PARK, W. H. & MIN, B.-M. 2008. Collagen-Based Biomimetic Nanofibrous Scaffolds: Preparation and Characterization of Collagen/Silk Fibroin Bicomponent Nanofibrous Structures. *Biomacromolecules*, 9, 1106-1116.
- YORK, R. D., MOLLIVER, D. C., GREWAL, S. S., STENBERG, P. E., MCCLESKEY, E. W. & STORK, P. J. 2000. Role of phosphoinositide 3-kinase and endocytosis in nerve growth factor-induced extracellular signal-regulated kinase activation via Ras and Rap1. *Mol Cell Biol*, 20, 8069-83.
- YOSHII, S. & OKA, M. 2001. Collagen filaments as a scaffold for nerve regeneration. *Journal of Biomedical Materials Research*, 56, 400-405.

- YU, H., FISCHER, G., EBERT, A. D., WU, H.-E., BAI, X. & HOGAN, Q. H. 2015. Analgesia for neuropathic pain by dorsal root ganglion transplantation of genetically engineered mesenchymal stem cells: initial results. *Molecular Pain*, 11, 5.
- YU, H., ZHAO, H., HUANG, C. & DU, Y. 2017. Mechanically and Electrically Enhanced CNT–Collagen Hydrogels As Potential Scaffolds for Engineered Cardiac Constructs. *ACS Biomaterials Science & Engineering*, 3, 3017-3021.
- YU, L. M. Y., LEIPZIG, N. D. & SHOICHET, M. S. 2008. Promoting neuron adhesion and growth. *Materials Today*, 11, 36-43.
- ZAMANI, F., AMANI-TEHRAN, M., LATIFI, M., SHOKRGOZAR, M. A. & ZAMINY, A. 2014. Promotion of spinal cord axon regeneration by 3D nanofibrous core–sheath scaffolds. *Journal of Biomedical Materials Research Part A*, 102, 506-513.
- ZHANG, C., DENG, Y., DAI, H., ZHOU, W., TIAN, J., BING, G. & ZHAO, L. 2017. Effects of dimethyl sulfoxide on the morphology and viability of primary cultured neurons and astrocytes. *Brain Res Bull*, 128, 34-39.
- ZHANG, H. & LIU, K.-K. 2008. Optical tweezers for single cells. *Journal of the Royal Society Interface*, 5, 671-690.
- ZHOU, F., WATERMAN-STORER, C. & COHAN, C. 2002. *Focal loss of actin bundles causes microtubule redistribution and growth cone turning.*
- ZHU, J. & MARCHANT, R. E. 2011. Design properties of hydrogel tissue-engineering scaffolds. *Expert review of medical devices*, 8, 607-626.
- ZOCHODNE, D. W. *The challenges and beauty of peripheral nerve regrowth*, J Peripher Nerv Syst. 2012 Mar;17(1):1-18. doi: 10.1111/j.1529-8027.2012.00378.x.
- ZUIDERVELD, K. 1994. Contrast limited adaptive histogram equalization. In: PAUL, S. H. (ed.) *Graphics gems IV*. Academic Press Professional, Inc.